



Nuclear Reactions for Nuclear Astrophysics

Weak Interactions and Fission in Stellar
Nucleosynthesis

Dissertation for the degree
of Doctor of Philosophy



Nikolaj Thomas Zinner
Department of Physics and Astronomy

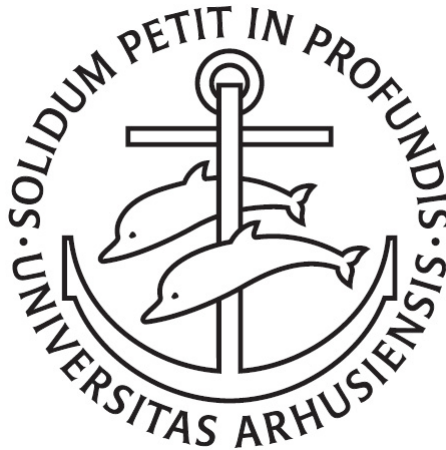
October 2007

Nuclear Reactions for Nuclear Astrophysics

Weak Interactions and Fission in Stellar
Nucleosynthesis

Nikolaj Thomas Zinner

Department of Physics and Astronomy
University of Aarhus



Dissertation for the degree of Doctor of
Philosophy

October 2007

@2007 Nikolaj Thomas Zinner
2nd Edition, October 2007
Department of Physics and Astronomy
University of Aarhus
Ny Munkegade, Bld. 1520
DK-8000 Aarhus C
Denmark
Phone: +45 8942 1111
Fax: +45 8612 0740
Email: zinner@phys.au.dk

Cover Image: The evolution of the Universe from the Big Bang to the emergence of complex chemistry and Life.
Printed by Reprocenter, Faculty of Science, University of Aarhus.

This dissertation has been submitted to the Faculty of Science at the university of Aarhus in Denmark, in partial fulfillment of the requirements for the PhD degree in physics. The work presented has been performed under the supervision of Prof. Karlheinz Langanke. The work was mainly carried out at the Department of Physics and Astronomy in Aarhus. Numerous short-term visits to Gesellschaft für Schwerionenforschung (GSI) in Darmstadt, Germany from 2005 to 2007 have been very fruitful toward the completion of the thesis. The European Center for Theoretical Studies in Nuclear Physics and Related Areas (ECT*) in Trento, Italy is also acknowledged for its hospitality during the summer of 2004.

*There is something fascinating about science.
One gets such wholesale returns of conjecture
out of such a trifling investment of fact.*

Mark Twain (1835 - 1910)

Contents

Outline	vii
Acknowledgements	viii
List of Publications	ix
1 Introduction	1
1.1 Children of the Stars	1
1.2 Stellar Evolution and Supernovae	2
1.3 Physics of Core-collapse Supernovae	3
1.4 Nucleosynthesis	5
1.5 Angle of this Thesis Work	9
2 Theoretical Nuclear Models	10
2.1 Weak Interactions	10
2.1.1 Weak Interactions in Nuclei	12
2.1.2 Cross Sections and Rates	15
2.2 Nuclear Structure Modeling	19
2.2.1 Independent Particle Model	21
2.2.2 Random Phase Approximation	25
2.2.3 Reduction of Transition Operators	37
2.2.4 Ground State and Model Space Considerations	41
2.2.5 Excitation Spectra Examples	42
2.2.6 Neutrino and Antineutrino Cross Section Comparison	44
2.3 Nuclear Decay Model	46
2.3.1 Particle Decay Rates and Fission	47
2.3.2 Fission Fragments	50
2.3.3 The Dynamical Code ABLA	52
2.4 Unified Nuclear Model	53
2.4.1 Energy Mesh	55
2.4.2 Monte Carlo and Statistics	56
2.4.3 Neutrino Spectra and Folding	57
2.4.4 Anisotropy and Exotica	60

3	Muon Capture	63
3.1	Introduction	63
3.1.1	Previous Studies	64
3.2	The Relativistic Muon	67
3.2.1	The Leptonic Current	68
3.2.2	The Non-Relativistic Limit	72
3.2.3	The Relativistic Rate Formula	74
3.3	Quenching of Multipoles	87
3.4	The Residual Interaction	88
3.5	Results and Discussion	89
3.6	Concluding Remarks	92
4	Neutrinos and Proton-Rich Ejecta	95
4.1	Introduction	95
4.2	Neutrino Reactions on Matter	96
4.3	Hydrodynamical Simulation	97
4.4	Network and Neutrinos	99
4.5	νp -process Nucleosynthesis	101
5	Neutrinos and the r-process	107
5.1	r -process Nucleosynthesis	107
5.1.1	General Conditions	107
5.1.2	The Neutrino-driven Wind	108
5.2	UMP Stars and Neutrino-induced Fission	111
5.3	Neutrino-induced Fission on r -process Nuclei	113
5.3.1	Initial Uranium Calculations	114
5.3.2	r -process Nuclei	118
5.3.3	Preliminary Conclusions	125
6	Fission and the r-process	127
6.1	Introduction	127
6.2	Nuclear Physics Input	127
6.2.1	β -delayed Fission	128
6.2.2	Neutron-induced and Spontaneous Fission	130
6.2.3	Fragment Distributions	131
6.3	r -process Simulation Model	133
6.4	Results	134
6.4.1	The Region and Role of Fission	134
6.4.2	The $N = 184$ Shell and Half lives	138
6.4.3	The $N = 82$ Shell Closure	139
6.4.4	Fission and Neutrinos	141
6.5	Nuclear Data Consistence	142
6.6	Concluding Remarks	143

7	Summary and Outlook	145
7.1	Outlook - Nuclear Physics	146
7.2	Outlook - Nuclear Astrophysics	148
A	Formalism and Conventions	150
A.1	Units and Definitions	150
A.2	Angular Momentum Coupling and Spherical Functions	151
A.3	Spherical Dirac Equation	154
B	Neutrino Capture Rate Formula	155
C	Nucleosynthesis and Entropy	157
	Bibliography	159

Outline

This thesis describes theoretical nuclear physics calculations for the purpose of expanding and improving the nuclear data input used in stellar nucleosynthesis modeling. In particular, the neutrino capture and β -decay weak interactions on a broad range of nuclei are considered. The decay of the daughter states resulting from the mentioned reactions are treated in a statistical model. The latter includes both particle emission and fission channels and provides fragments distributions for the fissioning nuclei based on a semi-empirical approach that agrees well with experimental data. These distributions have subsequently been implemented in simulations of the astrophysical r -process which is responsible for producing about half the heavy elements observed in nature. The neutrino capture processes on nuclei are also implemented in astrophysical modeling of ejected material from exploding stars. Here it is found that an entirely new nucleosynthesis process operates. It requires the abundances of antineutrinos and can produce many of the rare proton-rich elements whose origin is generally considered unknown. The nuclear physics results presented in the thesis are for reactions where very little experimental information is available. To ensure that the theoretical model used is not at odds with existing knowledge we have therefore also calculated total muon capture rates within the same framework. The capture rates have been measured in many nuclei across the nuclear chart and therefore provide a good benchmark to test the model against.

In chapter one we give an introduction to the Supernova environment which is the likely candidate site for the nucleosynthesis considered in later chapters. Chapter two introduces and describes the nuclear structure and statistical decay models that have been used in the calculations. Muon capture on nuclei is described in chapter three, including novel correction terms for relativistic effects that can influence the capture rate in heavy nuclei. Chapter four discusses the inclusion of neutrino and antineutrino reactions on nucleons and nuclei in nucleosynthesis calculations of early proton-rich ejecta from core-collapse Supernovae. In chapter five we discuss neutrino reactions in the r -process with particular emphasis on the role of neutrino-induced fission and neutron emission. Chapter six presents and discusses results from fully dynamical r -process simulations with all relevant fission channels and realistic fragment distributions included. Conclusions and outlook are given in chapter seven.

In the second edition (October 2007) misprints have been corrected and some statements have been clarified.

Acknowledgements

I would like to thank my adviser Karlheinz Langanke for proposing an interesting thesis project and for his continuous support and enthusiasm toward it. I am grateful to him for expanding my knowledge of physics, both from the academic point of view but surely also from a human perspective. Although most of his advise has proven invaluable there is one subject on which I strayed. Karlheinz once told me that I would never be able to finish a thesis without drinking coffee (as of this time I still do not drink it).

I wish to warmly thank Gabriel Martínez-Pinedo for his advise on nucleosynthesis issues discussed in this thesis and for providing the network calculations presented.

I wish to thank Carla Fröhlich, Darko Mocerlj, and F.-K. Thielemann in Basel for making our collaborations both pleasant and fruitful, and for taking care of me during my visit in early 2004. I warmly thank Petr Vogel from the California Institute of Technology for suggestions and discussions on muon capture and for a continued interest in its development. Furthermore, I owe a debt of gratitude to Aleksandra Kélic and K.-H. Schmidt for providing us with the ABLA code and for their help during its implementation. Thanks also goes to Ivan Borzov for various discussion on nuclear structure details.

Thanks goes to Hans Fynbo for reading the draft version and correcting a host of trivial and non-trivial mistakes.

I wish to thank my friends and colleagues at the university in Aarhus for providing a comfortable and interesting environment to work in. The bar on Friday was always fun. I also give many thanks to TÅGEKAMMERET and FC Nordbyen 1993 for providing the needed break from studies whenever necessary. I have many friends outside these places that have also been invaluable during the work, in particular Peter Busch Christiansen always provided comic relief and friendship in Vestervang for most of my life. I hope he will continue to do so in the future.

Lastly I want to thank my family for putting up with my dreadful schedule and continuous canceling of various events during the past years. You have always provided comfort and support during the brief periods I have actually been away from the university. Thanks to my mother, Inge Zinner, to whom my debt can never be repaid. Always remember that I am, and always was, first and foremost Your son.

A special thanks goes to Anne Sevelsted. Her seemingly unending tolerance for my less than perfect behavior and for my unrealistically involved schedule over the years is not taken lightly. I have no way to describe how grateful I am for your continued presence in my life.

List of Publications

- [I] A. Kélic, N. T. Zinner, E. Kolbe, K. Langanke, and K.-H. Schmidt:
Cross Sections and Fragment Distributions from Neutrino-induced Fission on r -Process Nuclei,
Physics Letters **B616** (2005) 48.
- [II] C. Fröhlich, P. Hauser, M. Liebendörfer, G. Martínez-Pinedo, E. Bravo, W. R. Hix, N.T. Zinner, and F.-K. Thielemann:
The Innermost Ejecta of Core Collapse Supernovae,
Nucl. Phys. **A758**, 27 (2005).
- [III] C. Fröhlich, P. Hauser, M. Liebendörfer, G. Martínez-Pinedo, F.-K. Thielemann, E. Bravo, N.T. Zinner, W.R. Hix, K. Langanke, A. Mezzacappa, and K. Nomoto:
Composition of the Innermost Core Collapse Supernova Ejecta,
Astrophysical Journal **637** (2006) 415.
- [IV] C. Fröhlich, G. Martínez-Pinedo, M. Liebendörfer, F.-K. Thielemann, E. Bravo, W. R. Hix, K. Langanke, and N. T. Zinner:
Neutrino-induced nucleosynthesis of $A > 64$ nuclei: The νp -process,
Phys. Rev. Lett. **96** (2006) 142502.
Featured in: *A New Way to Make Elements*,
Phys. Rev. Focus **17** (2006) story 14.
- [V] N. T. Zinner, K. Langanke, and P. Vogel:
Muon capture on nuclei: random phase approximation evaluation versus data for $Z=6-94$ nuclei,
Phys. Rev. C **74** (2006) 024326.
- [VI] G. Martínez-Pinedo, A. Kélic, K. Langanke, K.-H. Schmidt, D. Mochel, C. Fröhlich, F.-K. Thielemann, I. Panov, T. Rauscher, M. Liebendörfer, N. T. Zinner, B. Pfeiffer, R. Buras, and H.-Th. Janka:
Nucleosynthesis in neutrino heated matter: The νp -process and the r -process,
Invited talk at NIC-IX, International Symposium on Nuclear Astrophysics - Nuclei in the Cosmos - IX, CERN, Geneva, Switzerland, 25-30 June, 2006.
Proceedings contribution available through arXiv:astro-ph/0608490v1.
- [VII] C. Fröhlich, M. Liebendörfer, G. Martínez-Pinedo, F.-K. Thielemann, E. Bravo, N.T. Zinner, W.R. Hix, K. Langanke, A. Mezzacappa, and K. Nomoto:
Composition of the Innermost Core Collapse Supernova Ejecta and the νp -process,
AIP Conference Proceedings, Volume **847** (2006) 333.

- [VIII] C. Fröhlich, W. R. Hix, G. Martínez-Pinedo, M. Liebendörfer, F.-K. Thielemann, E. Bravo, K. Langanke, and N. T. Zinner:
Nucleosynthesis in Neutrino-Driven Supernovae,
New Astronomy Reviews, Volume **50**, Issue 7-8, p. 496 (2006).
- [IX] C. Fröhlich, M. Liebendörfer, F.-K. Thielemann, G. Martínez Pinedo, K. Langanke, N.T. Zinner, W.R. Hix, and E. Bravo:
The Role of Neutrinos in Explosive Nucleosynthesis,
Proceedings of the International Symposium on Nuclear Astrophysics - Nuclei in the Cosmos - IX. 25-30 June 2006, CERN., p.33.1.
- [X] I.N. Borzov, K. Langanke, G. Martínez-Pinedo, A. Kélic, and N.T. Zinner:
Neutrino-induced fission on nuclei,
Proceedings of the International Symposium on Nuclear Astrophysics - Nuclei in the Cosmos - IX. 25-30 June 2006, CERN., p.78.1.
- [XI] I. N. Borzov, J.J. Cuenca-Garcia, K. Langanke, G. Martínez-Pinedo, A. Kélic, and N.T. Zinner:
Beta-decay of very neutron-rich nuclei near exotic shell-closures,
EXON 2006 International Symposium on Exotic Nuclei,
Khanty-Mansiysk, Russia, 17-22 July, 2006.
- [XII] F.-K. Thielemann, C. Fröhlich, R. Hirschi, M. Liebendörfer, I. Dillmann, D. Mochelj, T. Rauscher, G. Martínez-Pinedo, K. Langanke, K. Farouqi, K.-L. Kratz, B. Pfeiffer, I. Panov, D.K. Nadyozhin, S. Blinnikov, E. Bravo, W.R. Hix, P. Höflich, and N.T. Zinner:
Production of intermediate-mass and heavy nuclei,
Prog. Part. Nucl. Phys. **59**, 74 (2007).
- [XIII] G. Martínez-Pinedo, D. Mochelj, N.T. Zinner, A. Kélic, K. Langanke, I. Panov, B. Pfeiffer, T. Rauscher, K.-H. Schmidt, and F.-K. Thielemann:
The role of fission in the r-process,
Prog. Part. Nucl. Phys. **59**, 199 (2007).
- [XIV] G. Martínez-Pinedo, D. Mochelj, N.T. Zinner *et al.*:
The role of fission and the $N = 82$ shell closure in r-process nucleosynthesis,
to be submitted to Phys. Rev. Lett.
- [XV] N.T. Zinner, A. Kelic *et al.*:
Fission fragment distributions for r-process nucleosynthesis,
in progress.

Chapter 1

Introduction

1.1 Children of the Stars

The beginning of the 21st century is a truly great time for science. Ideas, theories, measurements and observations are converging into what appears to be a unified picture of the Universe we live in, Nature around us and even our own existence. It is estimated that we have accumulated more scientific knowledge in the last 30-40 years than throughout the rest of our lifetime on this planet. One of the greatest outcomes of this process is undoubtedly that we can now explain the evolution of the universe from the time when it was a mere 10^{-43} seconds old and all the way up to the emergence of intelligent lifeforms. Although the answers obtained have brought along even more question and warrant continuing scientific efforts, we now have a remarkably insightful understanding of the laws of Nature. Our curiosity and thirst for knowledge has brought us a modern version of Genesis.

Our theories describe how the Big Bang started a Universe that would later form clusters, galaxies and seemingly endless amounts of stars. As these stars evolve, they process the light elements hydrogen and helium into the elements that we observe today. The very same elements that provide the conditions for life to develop. What this modern Genesis teaches us is that we are all children of the stars. As such, one is not too surprised that the synthesis of elements in stars is a hot topic. The basics are well understood but we still need to work on the accuracy of predictions. A mixture of large-scale hydrodynamical simulations, nuclear theories and experiments, knowledge of atomic transition lines, and an abundance of very accurate observations are needed to achieve this goal.

In this thesis we will be concerned with the nuclear modeling aspects of stellar nucleosynthesis. We wish to provide accurate nuclear physics input for simulations of element production. Before we embark on our journey into the details of the relevant nuclear physics, we will devote a few sections to explain basic features of the stellar environment that we consider.

1.2 Stellar Evolution and Supernovae

One of the greatest physicists of all time, the late Hans Bethe, pioneered the efforts to understand the reactions that power the stars in our night sky. He identified key fusion reactions that could produce the energy needed to balance a stars gravitation and emit the light we observe. In particular, he proposed the so-called p-p reaction where protons from ionized hydrogen are converted into helium. This is the main source of energy in stars with masses up to roughly that of our Sun. He also suggested what is known as the CNO-cycle of Hydrogen burning, a process that had also been considered earlier by Carl Friedrich von Weizsäcker and which also operates in the Sun at the percent level.

The crucial thing for these burning processes to ignite at all is that the initial cloud of gas that contracts to become a stellar object contains enough mass. The gravitational contraction will heat the material, and if enough mass is present the temperature will reach about 10^7 K needed for hydrogen burning to begin. This will happen when the protostar has mass in the range $M = 0.1 - 1.4 M_{\odot}$. Below this limit self-sustaining energy production will never be achieved and these objects become what is known as black dwarfs or dead stars. In the cited mass range, the star will evolve similarly to our Sun, burning hydrogen to helium for billions of years. As this is the longest period among stellar evolution processes, it is no wonder that most of the stars we observe are actually of mass close to M_{\odot} and in the hydrogen burning phase. These are known as main-sequence stars. When these stars finally exhaust their hydrogen, they will expand and cool, and in the core Helium burning starts. The light emitted will become more reddish and the stars are appropriately named Red Giants. They will presumably contract again through a series of luminosity fluctuations and violent ejection of outer material. This will leave behind a so-called white dwarf, which will gradually cool and fade on a very long time scale of hundreds of billions of years, leaving again an inert black dwarf. When the mass is below about $1.4 M_{\odot}$, the so-called Chandrasekhar mass limit (we will return to this limit in the next section), the star evolves essentially in the way described above. The details of intermediate mass star $M = 1.4 - 8 M_{\odot}$ are rather involved. They reach the Helium burning phase and through various mass-loss mechanism they eventually settle down in the white dwarf stage.

Stars of mass $M \geq 8 M_{\odot}$ have much shorter lifetimes. The larger gravitational energy released during contraction will lead to higher temperatures and this will make the burning of nuclear fuel faster. On top of that, these stars are capable of igniting the ashes of their previous burning stages through continual contraction. As the energy output of each stage of burning decreases compared to the previous stage, the star has to burn its fuel ever faster to balance gravity. This process of contraction and burning of ashes can continue up to the iron group, where the binding energy per nucleon has

a global maximum. The lifetime of a star is basically determined by the hydrogen burning time as mentioned above. The more massive stars are denser and burn at higher temperatures so the Hydrogen is exhausted in less than 10 million years. When the core reaches the iron group it cannot produce more energy and the inner parts of the star start to collapse. The star finally explodes in a cataclysmic event known as a core-collapse or Type II Supernova. This will eject the matter above the inner core into the interstellar medium and leave behind a neutron star. These are usually found observationally in the form of so-called pulsars which emit radiation at extremely precise intervals. If the protostar is very massive ($M \gtrsim 20 M_\odot$), matter will accrete on the neutron star in excess of the Chandrasekhar limit, making it collapse into a Black Hole (recent work indicates that above around $60M_\odot$ there will again be heavy mass loss to prevent the star from becoming a Black Hole).

1.3 Physics of Core-collapse Supernovae

Since we will be very concerned with the physical environment around a core-collapse Supernova, we will now describe the process in more detail. When the iron-group is reached and nuclear burning ceases to produce energy, the core of the star starts to collapse as mentioned above. This process is halted by the pressure of the degenerate electrons in the ionized material. Chandrasekhar showed that this can only stabilize a mass given by

$$M_{Ch} = 1.44(2Y_e)^2[1 + F(T)] M_\odot, \quad (1.1)$$

where Y_e is the electron fraction or number of electrons per baryon and $F(T)$ is a finite temperature correction which is usually $0.2 - 0.3$ for massive stars. This is the Chandrasekhar mass limit. As the core contracts the Fermi energy of the electrons increases, so electron capture on nuclei becomes energetically favorable. This lowers Y_e and thus also M_{Ch} . The captures also produce energetic electron neutrinos that escape the core. We thus have a reduction of energy and pressure and this will trigger almost free-fall collapse in the core.¹ When densities are in excess of a few 10^{11} g/cm^3 , the neutrinos are scattered so frequently on nuclei that they cannot diffuse out of the core and become effectively trapped. The inner $0.7 M_\odot$ now becomes equilibrated by electron-neutrino scatterings and collapses as a whole called the homologous core.

¹Electron capture rates on protons are actually larger than the capture rate per nucleon on most nuclei. However, the collapse proceeds at low entropy [1] and the temperature is kept low by neutrino losses, so most nucleons are bound in nuclei. It turns out that the low entropy and high density enable β -decays to actually compete against electron captures in the early stages of the collapse, so detailed studies have to take these into account also [2].

The collapse of the homologous core continues until nuclear densities of 10^{14} g/cm³ are reached where the incompressibility of nuclear matter halts the implosion. This sudden stop creates a shock wave that moves outward through the iron layers falling down from above. This will dissociate the matter and leave mostly free nucleons. One can make an estimate of the energy of the shock and the mass it has to traverse. In doing so, one quickly realizes that the energy is insufficient to cause an explosion of the star. Most likely the shock simply stalls and becomes an accretion shock at a radius of a few hundred kilometers. Matter will fall on it and be dissolved until it runs out of energy. So it seems that another mechanism is needed for successful explosions.

A likely candidate is the so-called delayed Supernova mechanism which is a way of reviving the shock by neutrinos. Electron captures on protons have by now turned the remains of the homologous core into a protoneutron star that attempts to cool as fast as possible. In doing so it emits huge amounts of neutrinos of all species. Furthermore there is a burst of neutrinos coming right when the shock moves through the core from electrons capturing on free protons. By neutrino absorption on free nucleons, energy can be transformed to the shock front, reviving it in less than a second by neutrino-nucleon reactions to produce a successful explosion.

To simulate this enormously complex stellar system is a great numerical problem. One needs accurate modeling of magneto-hydrodynamics, shock propagation, energy transport, lepton number tracking and neutrino diffusion. This naturally raises serious computational issues and consistent results are often hard to come by. It now seems clear, however, that consistent explosions cannot be achieved in realistic spherical one-dimensional models. Thus it would appear that we need multi-dimensional models where convection and rotational motion are handled properly. Studies where these effects are properly handled have been reported only very recently. Janka *et al.* have found consistent explosions in two-dimensional simulations through the neutrino-driven mechanism [3], whereas Burrows *et al.* now find explosions through acoustic oscillations (also in two dimensions) [4]. Both studies have been carried out for several different progenitor masses and the results appear robust. They do, however, indicate that there could be more than one mechanism that drives a Supernova explosion depending on the initial conditions. Models in three dimensions are underway and will likely teach us more about these newly discovered features.

As the solution of this problem could lie in accurate knowledge of the characteristics of this huge amount of neutrinos, people are also hoping for a galactic Supernova in the near future. By now, the detectors are ready for the task of measuring the neutrino blueprint for all species, so that plenty of things could be learned if a Supernova exploded in our part of the Universe.

1.4 Nucleosynthesis

The origin of the chemical elements have long been a grand challenge for astrophysics. The lightest elements, H, He and some Li, were produced in the early stage of the Big Bang. All other elements are produced in various kinds of stellar processes. Nuclear burning for energy production will only produce a limited range of species around the line of stability so the fact that many other elements are found in nature tells us that other mechanisms are operating. Since the coulomb barrier will hinder fusion of heavy nuclei one has to look for other means. The elemental abundance data of Suess and Urey [5] provided an answer since one could clearly see peaks at neutron numbers 50, 82 and 126 (see figure (1.1)). This suggested that neutron capture was responsible for heavy element synthesis and in two classical papers by Burbidge, Burbidge, Fowler, and Hoyle (B²FH) [6], and Cameron [7], the details of synthesis by neutron capture was described.

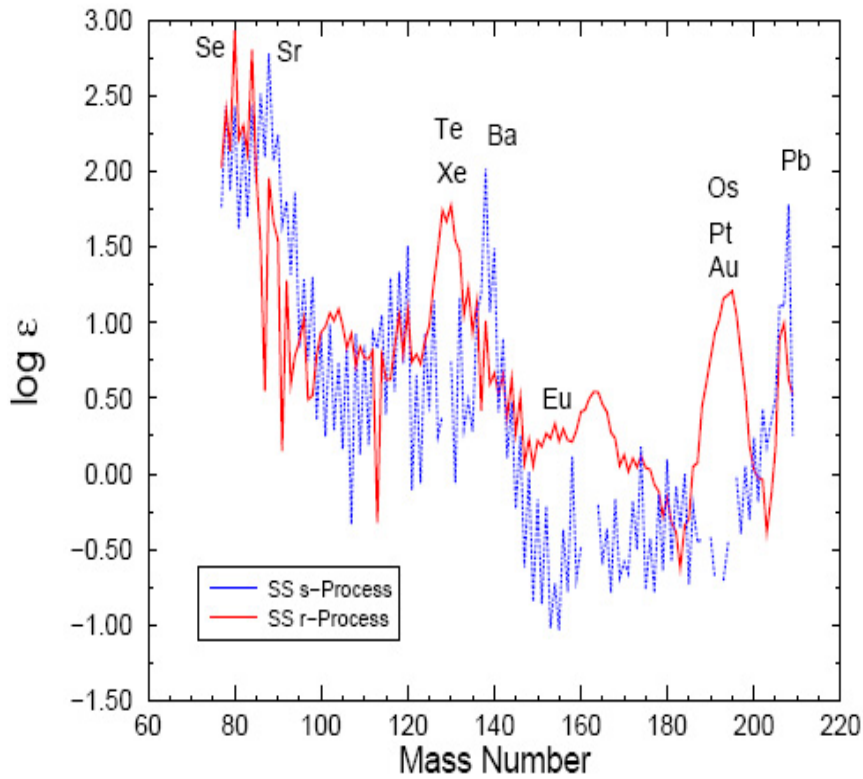


Figure 1.1: Breakdown of the solar system meteoritic neutron capture abundances for the *s*-process (red) and *r*-process (blue). Some prominent elements are noted at their approximate mass numbers. Adapted from [8].

Two main branches of heavy element production were identified: The

s-process (slow) and the *r*-process (rapid). The names indicate whether neutron capture proceeds slower or faster than β -decay. Each process is responsible for the production of about half the heavy elements, but there are several cases where a nucleus can only be produced by one of the two (see figure (1.2)). The species that can only be produced by either *s*- or *r*-process provide us with the ability to isolate the outcome of each mechanism in our experimental data. We can therefore get independent information about each process for use in model comparison.

Today the *s*-process is characterized by a weak (producing nuclei below ^{88}Sr) and a main component (producing those above) [9]. The weak *s*-process is believed to occur in massive stars, whereas the main *s*-process operates in so-called Asymptotic Giant Branch (AGB) star (which includes Red Giants). The *r*-process requires explosive conditions with large neutron fluxes and the favored scenario is the neutrino-driven wind that blows material of the newly-born neutron star in core-collapse Supernovae. Other places like neutron star mergers have been mentioned but they appear too rare to explain the entire *r*-process elemental abundance.

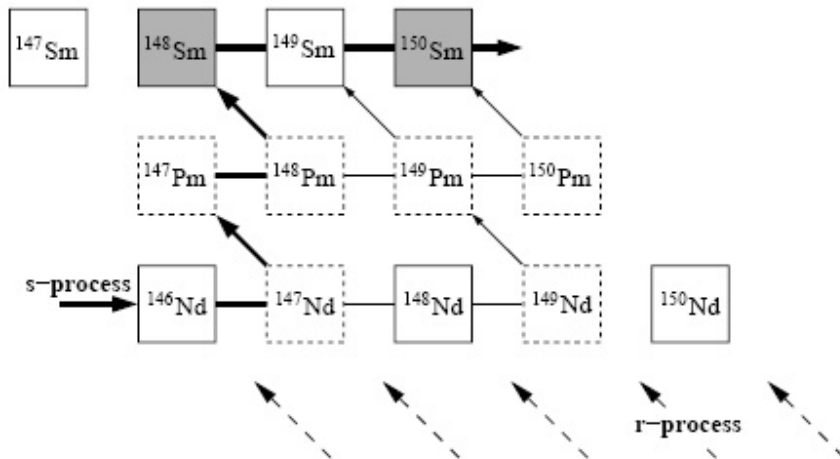


Figure 1.2: The *s*-process reaction path in the Nd-Pm-Sm region with the branchings at $A = 147, 148,$ and 149 . Note that ^{148}Sm and ^{150}Sm are shielded against *r*-process by the β -stability of ^{148}Nd and ^{150}Nd . Whenever ^{148}Sm or ^{150}Sm is found we know that the *s*-process is operating, and likewise for ^{148}Nd and ^{150}Nd which indicate an *r*-process contribution. Adapted from [14].

The main point of neutron capture nucleosynthesis is that one overcomes the coulomb barriers one mass unit at a time. For slow capture, β -decays will convert neutrons to protons inside the nuclei and allow for additional captures. However, this also means that the *s*-process will proceed close to the valley of stability and that it terminates at ^{209}Bi . When another neutron is captured on ^{209}Bi , subsequent β -decay will produce ^{210}Po . This nucleus decays on a short timescale by α emission into ^{206}Pb . The nuclei

heavier than bismuth found in Nature are therefore necessarily a result of the r -process. Here the neutron flux is very high and captures are faster than β -decay which means that one can produce very neutron-rich material (figure (1.3) illustrates the r -process path and the associated abundance peaks). When the flux drops below a certain critical value the r -process stops (this is referred to as the freeze-out). The progenitor distribution of neutron-rich nuclei will then decay back toward stability by β -decay. The produced peaks at neutron shells are slightly shifted compared to the s -process. The more neutron-rich progenitors at freeze-out will have lower charges when they decay back to stability (the left peaks in figure (1.1)). The r -process flow terminates when the nuclei get so heavy that fission becomes possible. If the end-point is reached with sufficient neutron supplies remaining, one can even have fission cycling where the fission fragments re-enter the capture process.

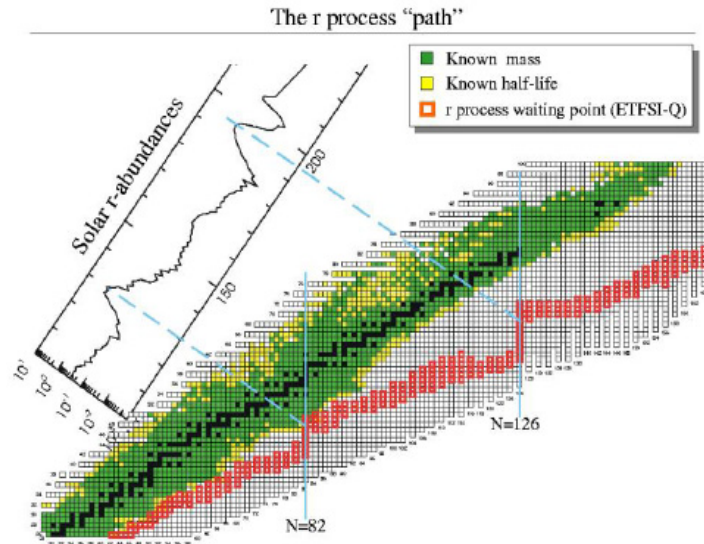


Figure 1.3: The figure shows a range of r -process paths. After decay to stability the abundance of the r -process progenitors produce the observed solar r -process abundance distribution. The r -process paths run generally through neutron-rich nuclei with experimentally unknown masses and half lives. Adapted from [15].

The mixing of material is another concern one has to consider with nucleosynthesis. The elements that are made in stars have to be ejected into the interstellar medium in the right amount. Galactic chemical evolution studies give us information about how much material of a given composition is needed to fit the final abundance pattern in our surroundings. Recent observations of abundance patterns in ultra-metal poor stars have, however, suggested that the r -process yields are quite robust and very close to solar

values for $A \geq 130$. These so-called halo stars are located at the out-skirts of our galaxy and are believed to be almost as old as the Milky Way itself. It is quite plausible that they contain material from only a few or ideally a single nearby Supernova event.² In figure (1.4) we show a plot of the measured abundances relative to those measured in the Sun. Striking agreement is immediate, supporting a robust r -process pattern for the heaviest nuclei (with deviations at lower masses that we will have more to say about in chapter (5)). Later we shall be particularly concerned with r -process nucleosynthesis and specifically the role played by fission, so we will omit a detailed discussion of the physical conditions for now.

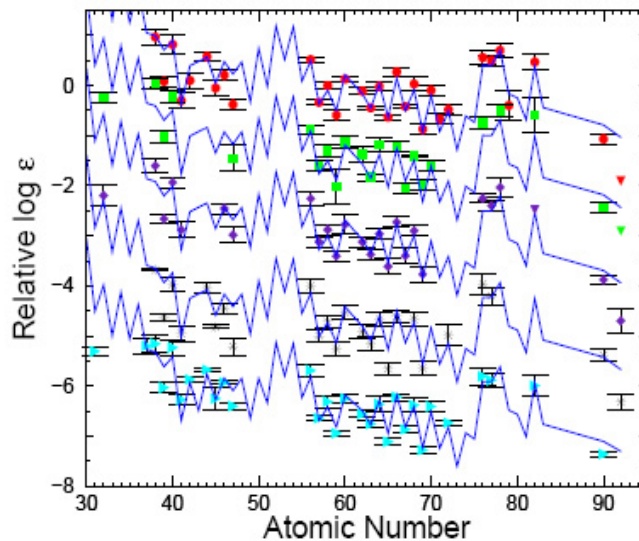


Figure 1.4: Relative abundances of measurements on ultra-metal poor stars relative to solar abundances for CS 22892-052 (red), HD 115444 (green), BD +17°3248 (violet), CS 31082-001 (black), and HD 221170 (cyan). The results for CS 22892-052 are to scale, whereas the others have been vertically shifted to fit within the plot. The blue curve showing the solar abundances has also been shifted to best fit the data for each individual star. Adapted from [10].

In closing this section we mention that s - and r -process nucleosynthesis are not solely responsible for the production of heavy nuclei. In nature we observe around 30 stable nuclei that are on the proton-rich side of stability. As such they cannot be produced through captures of neutrons. One often speaks of the p -process and rp -process (for photo dissociation and rapid pro-

²This belief is supported by the fact that Type II Supernovae have much shorter lifetimes than low-mass stars. One would therefore expect them to make a dominant contribution to the heavy element abundances at early galactic times. The extremely low abundances of iron in these stars point to a primary nucleosynthesis process, one where the heavy nuclei are formed from unprocessed nucleons and α 's.

ton capture) mechanisms. The astrophysical site of these processes remains largely unknown. Most suggestions assumes that they operate on seed nuclei coming from other kinds of nucleosynthesis. However, as we will discuss in detail later, we have recently found that proton-rich material can be produced in all core-collapse Supernovae through a primary process (one where the seeds are produced at the same site). It is intimately connected with the presence of neutrinos and has therefore been dubbed the νp -process [11]. Other groups have confirmed these findings [12] using other Supernova models, so the prediction seems robust. We have thus discovered a consistent way of producing proton-rich nuclei in generic Type II Supernova models. In addition, there are indications that the mechanism could also operate at other sites, such as gamma-ray bursts [13].

1.5 Angle of this Thesis Work

In this thesis we will attack the problems of stellar nucleosynthesis from the nuclear physics point of view. Weak interactions on nuclei are very important here and the angle of this work is to improve and expand the knowledge about some of these reactions. For the simulation of the innermost proton-rich ejecta in core-collapse Supernovae this involves calculation of neutrino and antineutrino captures on nuclei.

For r -process applications we will be concerned with weak reactions that can induce fission, such as neutrino captures and β -decays. This goal calls for accurate models of nuclear structure and a good description of the subsequent decay of the excited nucleus through various fission and particle evaporation channels.

Parallel to this work, we have tested our nuclear structure model by using it to calculate muon capture on nuclei. The weak interaction physics is practically the same for this process and, contrary to neutrino capture and β -decay in neutron-rich nuclei, there are plenty of experimental data available on muon capture. It is therefore a very nice way to check the consistency and predictive power of the model.

Chapter 2

Theoretical Nuclear Models

2.1 Weak Interactions

The story of the weak force is a long and rich one. We will be rather brief in our discussion but refer the interested reader to the excellent account of both history and formalism given in [17]. Shortly after Wolfgang Pauli had postulated the existence of the neutrino to account for hitherto unexplained features in the energetics of β -decays, Enrico Fermi proposed the first theoretical description of the process [16]. He used an analogy from electromagnetic theory where the interaction hamiltonian has the so-called current-current form. Lorentz symmetry dictates that only certain terms are allowed and the general form of the interaction hamiltonian density becomes

$$\mathcal{H}_{int} = \frac{G_F}{\sqrt{2}} \sum_i C_i \left(\bar{\psi}_p \hat{O}_i \psi_n \right) \left(\bar{\psi}_e \hat{O}_i \psi_\nu \right) + \text{h.c.}, \quad (2.1)$$

where $\psi_n, \psi_p, \psi_e, \psi_\nu$ are the Dirac wave functions of the nucleons and leptons participating in the β -decay, and G_F is the famous Fermi coupling constant ($1/\sqrt{2}$ is conventional). The \hat{O}_i 's are operators that ensure that the currents have the right transformation under the Lorentz group. These terms are scalar, pseudo scalar, tensor, vector, and axial vector respectively, or S, P, T, V, and A for short. The h.c. at the end stands for the addition of the hermitian conjugate term, so as to ensure that the total hamiltonian becomes an hermitian operator. If we assume CPT conservation¹ one can show that the constants C_i are real. It now took about twenty years before real progress was made again. In 1956 Lee and Yang made the groundbreaking observation that parity could be broken in weak decays [19]. The following year Wu *et al.* [20] confirmed this suggestion by examining β -decay

¹This refers to the combined operation of charge conjugation (exchange particles for antiparticles), time reversal, and parity. In the construction of field theories this symmetry is almost always assumed. Note, however, that CP is actually violated in nature, so the assumption of CPT means that time reversal must be broken.

on ^{60}Co . It became apparent that the weak interaction did not only violate parity but it did so in the maximal possible manner. For Dirac particles one can define a left- and right-handed component, roughly according to whether the spin is along or opposite the direction of propagation. It turned out that the weak force only couples to the left-handed component in β -decay. This was soon generalized by Feynmann and Gell-Mann, who proposed that all weakly interacting particles should couple left-handedly [21]. This also has the consequence that only vector and axial vector terms are allowed in equation (2.1), so it actually makes the interaction a little simpler. This is known as the V-A theory (vector minus axial vector). The next step was the advent of universality. This postulate states that the weak interaction is the same for all lepton families. Formally this amounts to the addition of further leptonic current for muon and tau with the same couplings C_i . Thus a truly general picture had emerged.

It was, however, clear that the weak interaction had some totally different properties than electromagnetic forces. Being mediated by the massless photon, electromagnetic interactions have infinite range. This is not so for the weak force, which is known to be extremely short ranged. A fact that could be understood if the carriers of the weak interaction are very massive particles. But this is a real challenge since one could not really use the lessons learned from the quantization of electrodynamics in the hugely successful theory QED. In the quantum field theories used to describe elementary phenomena there will always be infinities lurking. One can, however, get rid of these when using so-called gauge theories. Unfortunately this requires all mediator particles to be massless, so a gauge theory of the weak interactions seemed doomed from the start. The sixties saw a decade of intense investigation into this problem. This work finally succeeded with the invention of the unified electroweak theory for which Glashow, Salam and Weinberg received the Nobel Prize in 1979. By applying the so-called Higgs mechanism to a unified gauge theory of the weak and electromagnetic forces, they found that some mediators can indeed be massive. The theory also predicted neutral weak currents that were later discovered at CERN in 1974. The question of infinities in this new class of gauge theories was settled by t'Hooft in the early seventies. This earned him and his adviser, Martinus Veltman, the 1999 Nobel Prize.

Today the physics community has converged on the so-called Standard Model of particle physics. This includes the electroweak theory just described and a gauge theory of the strong interaction.² It has passed practically all experimental tests so far with flying colors. However, recent years have seen several new developments in the areas of neutrino physics and cos-

²Some people like to include gravitation as a spin two gauge theory along with the strong and electroweak parts. As the quantum theory of gravity still remains elusive we omit it here.

mology that overwhelmingly suggest that the Standard Model is inadequate and must be revised, expanded or replaced. Many in the physics community are also expecting to see evidence for supersymmetry when the next generation of particle accelerators starts taking data, hopefully sometime in late 2007.³ The final word has surely not been said and we are facing some exciting decades ahead for fundamental physics.

2.1.1 Weak Interactions in Nuclei

Since our goal is to describe neutrinos and leptons interacting with nuclei, we need to address the question of nuclear currents. The hamiltonian given in equation (2.1) contains a lepton and a nucleon current part. The leptonic part was already described above by the V-A theory and we will leave it at that for the moment. Since nucleons also feel the effect of the strong interaction, we cannot *a priori* expect it to have the same form. We have to go back to the principle of Lorentz invariance and work our way from there. The most general form that the nucleon current can have in momentum space is

$$\begin{aligned}
 J_i^\mu &= \bar{u}(p) \left[F_1 \gamma^\mu + \frac{i}{2M} F_2 \sigma^{\mu\nu} q_\nu + F_3 q^\mu \right. \\
 &\quad \left. + G_1 \gamma^\mu \gamma_5 + \frac{i}{2M} G_2 \sigma^{\mu\nu} q_\nu \gamma_5 + G_3 q^\mu \gamma_5 \right] \tau_i u(p'), \quad (2.2)
 \end{aligned}$$

where the nucleon is described by Dirac spinors $u(p)$ and $u(p')$ with momentum p and p' , M is the nucleon mass, and $q^\mu = p^\mu - p'^\mu$. The index i on the isospin operator τ_i is ± 1 for the charge-changing interactions we are concerned with. The constants in front of each term are called form factors and must necessarily be Lorentz scalars. They can therefore only depend on q^2 and are meant to describe the influence of the substructure of the nucleon on the weak processes in an effective way. We will now say a few words about how these are handled in our calculations.

The form factors F_1 and G_1 are the ones found in the leptonic V-A theory. However, here they are not merely ± 1 since the nucleon has strong forces. F_2 is a tensor-like term that is often called weak magnetism, referring to its electromagnetic counterpart. The term G_2 is called the induced pseudo scalar coupling and is attributed to the fact that the strong nuclear force is mediated by pions, which are pseudo scalar particles. The last two, F_3 and G_3 , are known as induced scalar and tensor couplings. It is possible to get some useful relations between the form factors by application of symmetry principles. Feynmann and Gell-mann did so by introducing the conserved vector current hypothesis [22]. An important consequence is that the form factors F_1 and F_2 can be taken directly from electron scattering.

³This paragraph was written in late 2006. At the time of revision of the manuscript, it seems more likely to be late 2008.

Furthermore since current conservation implies that the F_i terms must have vanishing divergence we have $F_3 = 0$. At the same time Weinberg found that since the strong interaction is invariant under CPT and isospin there can be no scalar or tensor terms in the current [23], leading to the conclusion $G_3 = 0$ and once more $F_3 = 0$. The pseudo scalar term G_2 can actually be related to the axial vector G_1 by the famous Goldberger-Treiman relation [24]. It states that

$$G_2(q^2) = \frac{2MG_1(q^2 = 0)}{q^2 + m_\pi^2} \quad (2.3)$$

where m_π is the pion mass. So we can get the pseudo scalar coupling from the axial vector one at zero momentum transfer.

As mentioned above, the form factors should take substructure into account through their dependence on q^2 . We will always use what is known as the dipole approximation for these functions [25]. This has the explicit form

$$F_i(q^2) = F_i(q^2 = 0) \left[\frac{1}{1 + \left(\frac{q^2}{m^2}\right)} \right]^2, \quad (2.4)$$

with a similar expression for the G_i 's. The mass m was taken to be $m = 843$ MeV for vector parts and $m = 1032$ MeV for axial vector parts. From electron scattering we get the vector couplings at $q^2 = 0$; $F_1(0) = 1.00$ and $F_2(0) = (\mu_p - \mu_n)/2M = 3.706/2M$, where μ_p and μ_n are the magnetic moments of the proton and neutron respectively. The axial vector form factor, G_1 , can be extracted from β -decay of the neutron, where a value of $G_1(0) = 1.26$ is found. However, as we shall discuss in more detail later there are renormalization effects in nuclear media to worry about. This phenomena is commonly referred to as in-medium quenching.

The weak processes that we would like to consider also require that we take the so-called Cabbibo mixing into account. In a 1963 paper [26], Cabbibo suggested that the hadron part of the weak current should be split into one that conserves strangeness (basically the number of strange quarks in a given reaction) and one that does not. In a more modern view involving quarks this means that we simply have a current that can change down to up and one that changes down to strange (and vice versa). To maintain unitarity this split is given by a 2D rotation on the quark wave function, so that the physical states are now

$$|d'\rangle = \cos \theta_c |d\rangle + \sin \theta_c |s\rangle \quad (2.5)$$

$$|s'\rangle = -\sin \theta_c |d\rangle + \cos \theta_c |s\rangle, \quad (2.6)$$

where θ_c is the Cabbibo angle. Experimentally it is found that $\sin \theta_c \approx 0.22$ and $\cos \theta_c \approx 0.98$. We will be concerned exclusive with reactions that take place within the first family of quarks. This gives a cosine factor and we

will be using an effective Fermi coupling constant given by $G = G_F \cos \theta_c$, where G_F is the value obtained from muon decay (using universality).

In closing this section we address the assumptions we make when constructing the nuclear current from the nuclear model that we introduce in section (2.2). We follow [18] and assume that the nuclear current can be expressed in second quantization as a one-body operator at the origin. Thus we have

$$J_i^\mu(0) = \sum_{p',s',t'} \sum_{p,s,t} \langle p', s', t' | J_i^\mu(0) | p, s, t \rangle a_{p',s',t'}^\dagger a_{p,s,t}, \quad (2.7)$$

where the sums are over all allowed momenta, spin and isospin projections. Since we are using a one-body density we are effectively neglecting any meson exchange currents, assuming that the many-body nuclear model we will employ takes care of such contributions. The matrix elements are from equation (2.2) and evaluated with free nucleon spinors. In reality the binding of the nucleons will modify these spinors, but as it is much less than the rest mass, we do not expect a big effect and we will neglect this. Through a series of reductions on the spinor expressions one can now make an expansion of the coordinate space currents in powers of the inverse nucleon mass [18]. This results in the following terms

$$\hat{\rho}_V^i(\vec{x}) = \sum_{j=1}^A G_E^i(j) \tau_i(j) \delta^{(3)}(\vec{x} - \vec{x}_j) \quad (2.8)$$

$$\hat{\vec{J}}_V^i(\vec{x}) = \sum_{j=1}^A \frac{G_E^i(j)}{2Mi} \tau_i(j) \left[\delta^{(3)}(\vec{x} - \vec{x}_j) \vec{\nabla}_j - \overleftarrow{\nabla}_j \delta^{(3)}(\vec{x} - \vec{x}_j) \right] \quad (2.9)$$

$$+ \vec{\nabla} \wedge \sum_{j=1}^A \frac{G_M^i(j)}{2M} \tau_i(j) \vec{\sigma}(j) \delta^{(3)}(\vec{x} - \vec{x}_j) \quad (2.10)$$

$$\begin{aligned} \hat{\rho}_A^i(\vec{x}) &= \frac{G_A^i}{2Mi} \sum_{j=1}^A \tau_i(j) \vec{\sigma} \cdot \left[\delta^{(3)}(\vec{x} - \vec{x}_j) \vec{\nabla}_j - \overleftarrow{\nabla}_j \delta^{(3)}(\vec{x} - \vec{x}_j) \right] \\ &+ \vec{\nabla} \cdot \sum_{j=1}^A \frac{m_\mu G_P^i(j)}{2M} \tau_i(j) \vec{\sigma}(j) \delta^{(3)}(\vec{x} - \vec{x}_j) \end{aligned} \quad (2.11)$$

$$\hat{\vec{J}}_A^i(\vec{x}) = \sum_{j=1}^A G_A^i(j) \tau_i(j) \vec{\sigma}(j) \delta^{(3)}(\vec{x} - \vec{x}_j), \quad (2.12)$$

where V is for vector current and A is for axial-vector current. Here we have introduced the Sachs form factors for the nucleon, $G_E(j)$ and $G_M(j)$ [27], which are different for protons and neutrons respectively. The axial vector coupling is denoted by G_A and the pseudo scalar is called G_P (evaluated at the relevant momentum transfer through equation (2.4)). These are the commonly used names and we will stick with them from now on. The index

i is again related to the isospin structure of the current and we maintain it on the couplings as they depend on isospin projection.

2.1.2 Cross Sections and Rates

We will now give basic formulas for the cross sections of neutrino and antineutrino scatterings and the rates for β -decays and charged lepton captures. First we need to make a very important assumption about the Hilbert space of nuclear states and that of the leptonic states. We assume that our nuclear model will always give us many-body states that have definite total angular momentum and parity. Furthermore, we assume that the leptonic part of the current-current interaction can be expanded in terms of functions of well-defined angular momenta and parity. Now we can use partial wave analysis and projection through the Wigner-Eckart theorem. This gives the following expression for the matrix element of the interaction when summed and averaged over initial and final nuclear angular momentum projections [18]

$$\begin{aligned}
 & \frac{1}{2J_i+1} \sum_{M_i} \sum_{M_f} |\langle f | H_{int} | i \rangle|^2 \\
 = & \frac{G^2}{2} \frac{4\pi}{2J_i+1} \left[\sum_{J=0}^{\infty} \{ (1 + \nu \cdot \beta) |\langle J_f || \mathcal{M}_J || J_i \rangle|^2 \right. \\
 & + [1 - \nu \cdot \beta + 2(\nu \cdot \mathbf{q})(\mathbf{q} \cdot \beta)] |\langle J_f || \mathcal{L}_J || J_i \rangle|^2 \\
 & - 2[\mathbf{q} \cdot (\nu + \beta)] \text{Re} \langle J_f || \mathcal{L}_J || J_i \rangle \langle J_f || \mathcal{M}_J || J_i \rangle^* \} \\
 & + \sum_{J=1}^{\infty} \{ [1 - (\nu \cdot \mathbf{q})(\mathbf{q} \cdot \beta)] [|\langle J_f || \mathcal{J}_J^{el} || J_i \rangle|^2 + |\langle J_f || \mathcal{J}_J^{mag} || J_i \rangle|^2] \\
 & - S 2[\mathbf{q} \cdot (\nu - \beta)] \text{Re} \langle J_f || \mathcal{J}_J^{el} || J_i \rangle \langle J_f || \mathcal{J}_J^{mag} || J_i \rangle^* \}, \quad (2.13)
 \end{aligned}$$

where all matrix elements are reduced by application of the Wigner-Eckart theorem [28]. J_i is the total angular momentum projection of the initial nuclear state. For neutrino and antineutrino scattering ν is the unit vector in the direction of the in-coming lepton and \mathbf{q} is the unit vector in the direction of the momentum transfer ($\mathbf{q} = \mathbf{k} - \nu$), whereas $\beta = |\mathbf{k}|/\varepsilon$ is the momentum to energy ratio of the out-going electron or positron. For charged lepton capture the roles are reversed giving $\mathbf{q} = \nu - \mathbf{k}$, and for β -decay we have both leptons in the final state so that $\mathbf{q} = \nu + \mathbf{k}$. The factor S is +1 for neutrino capture and β^- -decay, and -1 for antineutrino capture and

charged lepton capture. The multipole operators are defined by

$$\mathcal{M}_{JM}(\kappa) = \int d\vec{x} [j_J(\kappa x) Y_{JM}(\Omega_x)] J_0(\vec{x}) \quad (2.14)$$

$$\mathcal{L}_{JM}(\kappa) = \frac{i}{\kappa} \int d\vec{x} [\nabla(j_J(\kappa x) Y_{JM}(\Omega_x))] \cdot \vec{J}(\vec{x}) \quad (2.15)$$

$$\mathcal{J}_{JM}^{el}(\kappa) = \frac{1}{\kappa} \int d\vec{x} [\nabla \wedge (j_J(\kappa x) \mathcal{Y}_{JJ_1}^M)] \cdot \vec{J}(\vec{x}) \quad (2.16)$$

$$\mathcal{J}_{JM}^{mag}(\kappa) = \int d\vec{x} [j_J(\kappa x) \mathcal{Y}_{JJ_1}^M] \cdot \vec{J}(\vec{x}), \quad (2.17)$$

where $J^\mu = (J_0, \vec{J})$ is the four-current of the nucleus. The quantity κ is the magnitude of the three-momentum transfer at which the operators are to be evaluated. The other factor inside the integrals are from the multipole expansion of the leptonic current. Eqs. (2.14)-(2.17) are known as the Coulomb, Longitudinal, Transverse Electric, and Transverse Magnetic currents respectively. As mentioned, this expansion preserves good angular momentum and the integrals are thus projections onto partial waves of the nuclear current. This makes the operators so-called irreducible tensors and we can therefore manipulate them using the coupling techniques of angular momentum theory [28]. The parity assignments of our nuclear transition are determined by the orbital angular momenta of the different states in the matrix elements. We will comment on the meaning of this after we have introduced our nuclear structure model. For the moment we merely mention that we will use the notation J^π to indicate angular momentum J and parity π of nuclear states or transitions.

Neutrino and Antineutrino Capture

We now give the differential cross section for neutrino and antineutrino capture. The former changes a neutron to a proton in the nucleus and emits an electron and vice versa for the latter with positron emission instead. We will be working in the extreme relativistic limit where the out-going lepton

mass is neglected. In this case one finds

$$\begin{aligned}
 \left(\frac{d\sigma_{i \rightarrow f}}{d\Omega_l} \right)_{\nu, \bar{\nu}} &= \frac{G^2 \varepsilon^2}{2\pi^2} \frac{4\pi \cos^2(\Theta/2)}{2J_i + 1} F(Z \pm 1, \varepsilon_f) \left(\sum_{J=0}^{\infty} \sigma_{CL}^J + \sum_{J=1}^{\infty} \sigma_T^J \right) \\
 \sigma_{CL}^J &: = \left| \langle J_f \| \mathcal{M}_J(\kappa) + \frac{\omega}{\kappa} \mathcal{L}_J(\kappa) \| J_i \rangle \right|^2 \\
 \sigma_T^J &: = \left(-\frac{q^2}{2\kappa^2} + \tan^2(\Theta/2) \right) \times \\
 &\quad \left[\left| \langle J_f \| \mathcal{J}_J^{mag}(\kappa) \| J_i \rangle \right|^2 + \left| \langle J_f \| \mathcal{J}_J^{el}(\kappa) \| J_i \rangle \right|^2 \right] \\
 &\quad \mp \tan(\Theta/2) \sqrt{\frac{-q^2}{\kappa^2} + \tan^2(\Theta/2)} \times \\
 &\quad \left[2\Re \left| \langle J_f \| \mathcal{J}_J^{mag}(\kappa) \| J_i \rangle \right|^2 \left| \langle J_f \| \mathcal{J}_J^{el}(\kappa) \| J_i \rangle \right|^2 \right], \quad (2.18)
 \end{aligned}$$

where the minus (plus) is for neutrino (antineutrino) respectively. Θ denotes the angle between the leptons involved. The rest of the quantities are as in the previous section. The function $F(Z \pm 1, \varepsilon_f)$ is the so-called Fermi function, which is introduced to take the final-state interaction between lepton and daughter nucleus into account (see [29] and references therein). Since we will not be concerned with the direction of the out-going lepton, we shall always integrate the expression over all Θ to obtain the total capture cross section.

Muon Capture

The process of muon capture will be of great concern to us later as we use it as benchmark for the nuclear structure model. This is the capture of a negative muon on a proton in the nucleus, resulting in its conversion into a neutron and the emission of a muon neutrino. The nice feature of this process is the large rest mass of the muon: $m_\mu = 105.6$ MeV. This provides a lot of energy to be shared between neutrino and nucleus. However, since the neutrino is (almost) massless it carries away most of the energy. Typical captures still leave 15-25 MeV of energy for nuclear excitation. This means that the process can potentially excite giant resonance modes in the nucleus which are usually out of reach for β -decay and electron captures. Muon capture thus represents a valuable probe of these structures. Since the capture turns a proton into a neutron we also have full or partial blocking of the so-called allowed transitions (such as the Fermi and Gamow-Teller) in medium and heavy nuclei where neutrons always outnumber protons. This means that the process has to go by higher-order transitions, also called forbidden. We will say much more about these matters in chapter (3). For now we will merely give the capture rate formula usually employed in the literature.

The most common experimental starting point for total muon capture rate measurements is a muon located in the atomic 1s orbit, so we will be assuming this at all times. In the non-relativistic limit this gives us a very simple looking expression for the capture rate. We have

$$\begin{aligned} \omega_{fi} = & \frac{G^2 \nu^2}{2\pi} \frac{4\pi}{2J_i + 1} \left[\sum_{J=0}^{\infty} \left| \langle J_f \| \mathcal{M}'_J(\nu) - \mathcal{L}'_J(\nu) \| J_i \rangle \right|^2 \right. \\ & \left. + \sum_{J=1}^{\infty} \left| \langle J_f \| \mathcal{J}'^{mag}_J(\nu) - \mathcal{J}'^{el}_J(\nu) \| J_i \rangle \right|^2 \right] \times \mathcal{R}. \end{aligned} \quad (2.19)$$

Energy conservation gives us $\nu = m_\mu - \varepsilon_{orbit} + E_i^{nuc} - E_f^{nuc}$, where ε_{orbit} is the binding energy of the muon in the atomic 1s orbit. The operators are now primed to indicate that they have the 1s muon wave function included under the integral. As the 1s is spherically symmetric, this does not alter their tensor character. The factor \mathcal{R} comes from the nuclear recoil and is given by

$$\mathcal{R} = \left(1 + \frac{\nu}{M_{target}} \right)^{-1}. \quad (2.20)$$

Since we will always be interested in the total capture rate we have to sum the above expression over all possible nuclear states of excitation energy $E^* = m_\mu - \nu - \varepsilon_{orbit}$. The nucleus has a number of states for each given angular momentum J and parity. Naturally, we will truncate the sum at a reasonable J where convergence is achieved.

The above formula apply when we can treat the muon as non-relativistic. This is a good approximation for nuclei of low charge. However, for higher charges corrections from relativistic effects can be expected. To see this, let us estimate the muon orbital energy in the 1s state by using the simple hydrogen-like formula. The usual ground state energy is about 13.6 eV. This has to be scaled by the muon-to-electron mass ratio and the charge squared. So we get $2.8 \cdot Z^2$ keV. For a heavy nucleus like ^{208}Pb with $Z = 82$ this gives us 18.8 MeV, which is almost 20 percent of the muon rest mass. This estimate is actually a little too crude, since also the muon orbital radius will be smaller. It scales with inverse muon-to-electron mass ratio and with inverse charge, so it will be roughly $250 \cdot Z^{-1}$ fm. In ^{208}Pb it is about 3 fm, so well inside the nucleus which has a radius of roughly 7.2 fm. The effective charge that the muon sees in its 1s orbit is therefore smaller than 82 and the energy will thus be smaller than the estimate above. It is, however, clear that the investigation of relativistic effects in muon capture is warranted and this will be one of our main concerns in chapter (3).

β -Decay

The final weak process we will be concerned with is that of β -decay. As one of our goals is to use these β -decay rates in r -process simulations, we will

need to calculate β^- -decay (since the material is neutron-rich). The matrix element is that of equation (2.13) with $S = +1$. The phase-space factor is somewhat more complicated as we now have a three-body final state. This introduces the phase-space integral

$$f_0(Z, \omega) = \int_{m_e}^Q p_e E_e (\omega - E_e)^2 F(Z, E_e) dE_e, \quad (2.21)$$

where m_e , p_e , and E_e are mass, momentum, and energy of the electron and ω is the nuclear excitation energy. The upper limit on the integration is the process Q-value. The final state electron-nucleus interaction is taken into account by the Fermi function $F(Z, E_e)$, just as for neutrino captures. If we put this function to one, the integral can be done explicitly yielding a rather intricate expression. However, in the limit of large ω it goes like ω^5 , which is the famous Sargent's rule. This tells us that β -decay is very sensitive to the Q-value. To get a total β -decay rate we need to sum over all nuclear transitions with the matrix element squared from equation (2.13) multiplied by the phase integral above.

When calculating β -decay rates for large numbers of nuclei one often uses various approximations. Using only allowed Fermi (when energetically available) and Gamow-Teller transitions is quite common in the literature. In [30] a host of properties for a large set of nuclei, including β half life, were calculated in this approximation. The results are in good agreement with experiment where available, allowing us to have some faith in their predictive power in less well-known neutron-rich regions. The inclusion of forbidden transitions has been considered in various studies and will naturally reduce the lifetime as it simply introduces more channels to decay through. The effects are expected to be small as the forbidden strength is situated at higher energy. It can also have significant effects on β -delayed neutron emissions, especially around closed shells where it can reduce the emission probability [31]. However, for neutron-rich nuclei with large Q-values there can be significant contributions from forbidden transitions. We therefore take our β -strength from the method described in [169] which improves on [30] by including forbidden transitions and introducing smoothing in the strengths.

2.2 Nuclear Structure Modeling

The field of nuclear modeling has a long tradition. One of the first attempts was called the liquid-drop model and was conceived in analogy with insights from hydrophysics. One outcome was the famous semi-empirical mass formula of Bethe and Weizsäcker which is still very much in use today. It contains a number of terms each of which have their own special dependence on the mass, charge, and neutron number of the nucleus. The success

of this average description of the nuclear masses means that we use it as guidance for much more advanced models to make sure that they get these properties right. Advanced versions of the model are actually still used in studies of fission since the complexity of the process makes the application of more microscopic models very difficult.

Naturally, the various forms of the liquid-drop model can only be helpful in prediction of averaged properties of many-nucleon systems. A body of experimental evidence tells us that the individual nucleons act almost like independent particles. A single nucleon will feel the attraction from all the others on average, but as soon as another one comes too close they will scatter away due to a hardcore interaction at small distances. Experiments have shown that the mean free path is of order the size of the nucleus, so one does not expect the particles to come close very often. It is therefore reasonable to consider the nucleus as a system of particles that move around individually in the average field of all the others. This is embodied in the hugely successful independent particle model (IPM) of the nucleus for which Goeppert-Mayer and Jensen shared the 1963 Nobel Prize. Based on simple mean-field potentials analogous to those of atomic physics the model beautifully explains a host of properties. Perhaps most importantly it tells us why nuclei with certain numbers of protons or neutrons seem to exhibit stronger binding than their neighbors in the nuclear chart. Simple, yet physically realistic, assumptions on the parameters of the potential reproduced perfectly the so-called magic numbers of nucleons at the observed positions. A huge leap forward had been taken.

The next natural goal for nuclear physicists was to try to explain the appearance of such mean-field properties from basic knowledge of the nucleon-nucleon interaction. Atomic physicists had already considered this problem for the pure coulomb potential using the Hartree-Fock method. Unfortunately this turned out to be less simple to apply in nuclei. The nucleon-nucleon potential is very complicated and early results were not promising. Today we have a number of refined methods that give us much better agreement. No-core Shell Model, Green's function Monte Carlo, and hyperspherical expansion of the N-body Schrödinger equation are a few of the successful modern techniques used. However, some of these are extremely computationally intensive and only light or medium nuclei have been studied. So there is still plenty of work to be done in improving these methods.

The models mentioned above are typically used for prediction of ground-state properties. In applications where nuclear reactions are considered we also need to have an accurate description of the nuclear excitation spectra. This requires a model that can handle both single-particle excitations and also the very important coherent nuclear states where many particles conspire to create broad structures in the spectrum at higher energies that cannot be described by an IPM. The latter are often referred to as giant resonances. The nuclear structure model method of choice is a Large-Scale

shell model. The approach is to start from an IPM with a given number of nucleons and then diagonalize some residual interaction in a basis consisting of all possible arrangements of the particles in the IPM potential. With two- or even three-body interactions the number of configurations grows very fast, so the matrices are huge, restricting the method to light or medium systems. However, techniques using effective interactions and truncated model spaces with inert cores of non-interacting nucleons are becoming more advanced. With computers also gaining power, the future for large-scale modeling looks bright.

The goal of the work described in this thesis is to calculate weak interactions on a great number of nuclei, so shell model calculations are ruled out by memory constraints even in today's supercomputers. We need instead a fast method that can reproduce the giant resonances in the spectra as they turn out to be particularly important for our purposes. We therefore use the random phase approximation (RPA). This method starts from an IPM and then diagonalizes a residual interaction in a basis consisting of all configurations obtained by moving just one particle at a time. The basis is restricted to one particle-one hole excitations and is therefore much smaller than that used in large-scale shell model. This makes the method very fast for applications where particle-hole structures are sufficient.

Once we have our nuclear structure model that give us an excitation spectrum and probabilities to populate each state, we would like to consider subsequent decay of the excited daughter nucleus. This will be done under the assumption of the formation of a compound nucleus, a picture of nuclear decay first advocated by Niels Bohr in the late 1930ties. It assumes that the decay of the excited state is slow compared to the time it takes the nucleus to distribute the excitation energy among all the degrees of freedom that have quantum numbers satisfying all conservation laws. When this is achieved, the state of the nucleus is given by a statistical distribution, independent of the way the excited state was formed. Under these assumptions one can employ statistical decay models that use the nuclear density of states to find the widths of relevant decay channels. This naturally requires detailed knowledge of nuclear statistical properties over a wide range of energies so care must be taken that choices of masses, shell effects, pairing etc. are consistent. This will be discussed later when we introduce the statistical decay models that we have used.

2.2.1 Independent Particle Model

The first step in our nuclear structure modeling is to set up a reliable independent particle model to provide us with realistic single-particle energies and wave functions. As our goal is to calculate interactions for a range of nuclei that covers basically the whole nuclear chart, we need something universal with only a small amount of parameters needing adjustment for each

individual nucleus. Experiments have shown that the nuclear charge density resembles a Fermi-Dirac distribution quite well in medium and heavy nuclei. As the strong interaction of the nucleons is basically proportional to the number of nucleons this Fermi-Dirac form seems to be a good starting point for a mean-field potential description. More precisely one uses a potential of the form

$$V_{central}(r) = \frac{-V_0}{1 + \exp[\frac{r-R}{a}]}, \quad (2.22)$$

where R is the nuclear radius and a is called the surface diffuseness as it determines the thickness of the surface region. This is the Woods-Saxon potential (WS) [32]. It can reproduce some of the first magic nucleon numbers at 2, 8, and 20. Following Goeppert-Mayer and Jensen we can use this potential to reproduce also the higher magic numbers 28, 50, 82, 126, and 184 by including a phenomenological spin-orbit term. This is illustrated in figure (2.1) which is the original table from Goeppert-Mayer and Jensen.

The full potential that we will be using is of the form

$$V(r) = \frac{-V_0}{1 + \exp(\frac{r-R}{a})} - V_{SO}r_0^2 \frac{1}{r} \frac{\partial}{\partial r} \left(\frac{1}{1 + \exp(\frac{r-R}{a})} \right) (\vec{L} \cdot \vec{S}) + \frac{1 + \tau_3}{2} V_C(r), \quad (2.23)$$

where r_0 is a constant which involves the pion mass. The last term takes care of the coulomb repulsion for protons since the isospin factor will be one for protons and zero for neutrons. The actual form of the coulomb potential $V_C(r)$ is not critical and we will simply be assuming a homogeneously charged sphere.

Observe that the spin-orbit term contains the derivative of the central potential, which means that its main contribution comes from the nuclear surface. This is analogous to atomic physics where the term arises from the non-relativistic limit of the Dirac equation. In the nuclear case it can be shown to originate from so-called one-pion exchange forces. The quantities involved in the spin-orbit term can, however, be easily motivated from basic symmetry principles. It is an interaction between a spin and something else, so to get a scalar quantity in the hamiltonian that something has to be a pseudo vector like the spin vector. A nucleon moving close to the center of the nucleus has only one polar vector available, its momentum \vec{p} . At the surface where the density changes one can construct another vector, $\nabla\rho(r)$, and then take vector cross product of the two to get the desired pseudo vector. This was not possible in bulk since the density is roughly constant there; $\nabla\rho(r) = 0$. Since we already argued above that the density and potential should have similar forms, we can understand the spin-orbit structure above. However, notice that the spin-orbit force in a nucleus has the opposite sign to that in atomic physics. Therefore it lowers the state with $j = l + 1/2$ compared to $j = l - 1/2$ as can be seen in figure (2.1).

CHAPTER 2. THEORETICAL NUCLEAR MODELS

Table 1 -- Nuclear Shell Structure (from *Elementary Theory of Nuclear Shell Structure*, Maria Goeppert Mayer & J. Hans D. Jensen, John Wiley & Sons, Inc., New York, 1955.)

Angular Momentum ($\hbar\Omega/2\pi$)	Spin-Orbit Coupling ($1/2, 3/2, 5/2, 7/2, \dots$)	Number of Nucleons Shell	Total	Magic Number	
7	1j	1j 15/2	16	[184]	{184}
		3d 3/2	4	[168]	
6	4s	4s 1/2	2	[164]	
6	3d	2g 7/2	8	[162]	
		1i 11/2	12	[154]	
6	2g	3d 5/2	6	[142]	
		2g 9/2	10	[136]	
6	1i	1i 13/2	14	[126]	{126}
		3p 1/2	2	[112]	
5	3p	3p 3/2	4	[110]	
		2f 5/2	6	[106]	
5	2f	2f 7/2	8	[100]	
		1h 9/2	10	[92]	
5	1h	1h 11/2	12	[82]	{82}
4	3s	3s 1/2	2	[70]	
		2d 3/2	4	[68]	
4	2d	2d 5/2	6	[64]	
		1g 7/2	8	[58]	
4	1g	1g 9/2	10	[50]	{50}
		2p 1/2	2	[40]	{40}
3	2p	1f 5/2	6	[38]	
		2p 3/2	4	[32]	
3	1f	1f 7/2	8	[28]	{28}
		1d 3/2	4	[20]	{20}
2	2s	2s 1/2	2	[16]	
2	1d	1d 5/2	6	[14]	
		1p 1/2	2	[8]	{8}
1	1p	1p 3/2	4	[6]	
0	1s	1s 1/2	2	[2]	{2}

Figure 2.1: The independent particle model illustration table from the classical text of Goeppert Mayer and Jensen. Notice the assigned numbers on the far left. These are the harmonic oscillator shell numbers of the nuclear orbits.

We now go through the choice of parameters for the potential in eq. (2.23). For the nuclear radius we use the standard formula $R = r_0 \cdot A^{1/3}$. We have worked with $r_0 = 1.22$ fm, which is close to the value given in [32] and [33]. For protons the Coulomb potential should in principle use the charge radius instead. In [33] it was found that results based on the WS potential are not very sensitive to this parameter and we will simply use the nuclear radius in this term as well. There is another radius to be specified in the WS term that multiplies the spin-orbit operator. Again we have simply taken the nuclear radius as we have found our results to be insensitive to this parameter. For the diffuseness we use a value slightly below the recommendation of [33], working with $a = 0.53$ fm in all calculations. This value is probably better for lighter nuclei where the harmonic oscillator or square well potentials are good approximations. However, previous studies into isotope effects in total muon capture rates have shown that it requires large changes in a for any effects to be seen [34]. In that paper, $a = 1.00$ fm was used to obtain noticeable differences in the rates on very neutron-rich Sn isotopes compared to the muon capture rates with our standard value of $a = 0.53$. Based on this observation we have simply kept $a = 0.53$ fm in both central and spin-orbit terms. The magnitude of the spin-orbit interaction V_{SO} was set to 17.9 MeV in all calculations. This value was found by considering experimental numbers on medium mass nuclei. It agrees well with the value given in [33]. However, there are data suggesting that V_{SO} depends slightly on the asymmetry parameter $(N - Z)/A$. We have tested this in the case of muon capture and found that changes of a few MeV make little difference, presumably because the dependencies are taken care of by the derivative of the central potential. We therefore keep the same constant V_{SO} .

The numerical technique used to obtain the WS eigenvalues and eigenfunctions is truncation and diagonalization. The starting point is a basis consisting of the well-known eigenfunctions of the three-dimensional isotropic harmonic oscillator. We have used up to ten major shells to achieve good convergence. Notice that the coulomb part means that neutrons and protons have different potentials so we solve for these independently. A possible drawback of this method comes from the fact that all these functions are bound states from the beginning, and the solution for the WS potential will thus also always have exponential tails and all eigenvalues will be discrete. We will still get positive energy eigenvalues, but the corresponding eigenfunctions do not have the correct physical boundary conditions. Deep in the potential we expect the results to be quite accurate but for loosely bound states it is questionable. However, as we will see when we discuss muon capture in chapter (3) our simple model with only these discrete states works very well [35].

A final parameter that our model needs from the outside is something to fix the single-particle Fermi level. We need to have a good idea about the

energy of the orbit where the last proton and neutron is located. The energy of these levels depends on whether the process changes neutron to proton or vice versa. For muon and antineutrino capture the charge is decreased by one, so we change a proton in the mother nucleus into a neutron in the daughter. This means that proton orbits belong to the mother and neutron orbits belong to the daughter. A good approximation for the energy of the last proton level is therefore the proton separation energy S_p in the mother nucleus (A, Z) and for the neutron level it is the neutron separation energy S_n in the daughter $(A, Z - 1)$. The processes of neutrino capture and β -decay convert neutron to proton. We will thus fix the neutron orbits by S_n in the mother (A, Z) and the proton orbits by S_p in the daughter $(A, Z + 1)$. S_n and S_p were calculated based on the mass table of Möller, Nix, and Kratz [30].

2.2.2 Random Phase Approximation

To handle the nuclear excitation response we will use the random phase approximation. This is a well-established and computationally fast method. The basic idea is to try to obtain excited states of the nucleus by expanding these on a very simple basis of IPM wave functions. The basis consists of the so-called particle-hole states, which are IPM states where we allow the movement of one particle to some unoccupied orbit, leaving behind a hole in one of the lower orbits. The principles are thus very much in tune with the single-particle picture. However, the new element is the introduction of a residual interaction which acts between the particles around the Fermi level. We can diagonalize this interaction in the particle-hole basis and then hopefully get an accurate description of the excited states. This strategy is called the Tamm-Dancoff approximation (TDA) or simple particle-hole theory [36]. TDA has the problem that it does not satisfy important sum rules, which causes it to underestimate low-lying collective excitations [36]. What we can do better in this situation, is to take into account the effect of the residual interaction on the ground state itself, so that it is not simply the naive IPM state, but rather a superposition of particle-hole states (like the excited states in the TDA method). This procedure is called the random phase approximation (RPA). Originally it was introduced by Bohm and Pines [37] to describe plasma oscillations in electron gases. The term RPA referred to the neglect of modes with frequencies different from the collective field on the assumption that they would have arbitrary phases and thus cancel out on average. As we will see when we discuss the RPA equations below, the phases that are assumed to cancel in nuclear applications are those of fermion exchange correlations, allowing one to treat the corresponding operators as bosons. This also warrants the alternative name *quasi-boson approximation*.

We will always be working with discrete energy states (due to the bound

nature of the IPM states as introduced earlier). This is often called the simple RPA (SRPA). For loosely bound systems one should ideally include also continuum states in the equations, leading to the continuum RPA (CRPA). However, as was shown in [35], there is little difference between the two methods when calculating total muon capture rates for a broad range of nuclei. We therefore work strictly with the simpler SRPA model.

Basic RPA Equations

We start by looking at the TDA equations as a warm-up exercise. First we define creation operators for the TDA states, which are the following superpositions of particle-hole states

$$Q_{TDA,\nu}^\dagger = \sum_{m,i} X_{m,i}^\nu a_m^\dagger a_i, \quad (2.24)$$

where m labels unoccupied states and i labels occupied states. ν keeps track of the TDA solutions. The TDA vacuum is defined by the equation

$$Q_{TDA,\nu}|0\rangle_{TDA} = 0 \quad (2.25)$$

for all ν . Now we approximate the TDA vacuum by the IPM ground state, and using the so-called equations-of-motion method [36, 32]⁴, we get the following eigenvalue equation for the TDA solutions

$$\sum_{n,j} \{(\varepsilon_{m,i} \delta_{mn} \delta_{ij} + \bar{v}_{mj in})\} X_{n,j}^\nu = E_{TDA}^\nu X_{m,i}^\nu, \quad (2.26)$$

where $\varepsilon_{m,i}$ is the difference of particle and hole orbital energies, m, n refer to occupied, and i, j to unoccupied states. The residual particle-hole interaction is given by the following matrix element of IPM wave functions

$$\bar{v}_{mj in} = \langle mj|v|in\rangle - \langle mj|v|ni\rangle \quad (2.27)$$

which has a direct and an exchange part.

The RPA equations are produced by generalizing the operators for the TDA states above to also include terms that annihilate particle-hole pairs. The creation operators for the RPA states then take the general form

$$Q_{RPA,\nu}^\dagger = \sum_{m,i} X_{m,i}^\nu a_m^\dagger a_i - \sum_{m,i} Y_{m,i}^\nu a_i^\dagger a_m \quad (2.28)$$

⁴The method is inspired by the harmonic oscillator where the hamiltonian can be written as a product of annihilation and creation operators. Making such an ansatz for the nuclear hamiltonian and the using a variation of the operators Q_ν will give the TDA and RPA equations [36, 32].

with the same meaning of indices as above and a conventional minus sign between the two terms. Again we define the vacuum by

$$Q_{RPA,\nu}|0\rangle_{RPA} = 0 \quad (2.29)$$

for all ν . Going through exactly the same steps as for the TDA now gives us the RPA eigenvalue equations. Since there are now two sets of coefficients, X and Y , to be determined, the equations are most conveniently displayed in matrix form

$$\begin{pmatrix} A & B \\ B^* & A^* \end{pmatrix} \begin{pmatrix} X^\nu \\ Y^\nu \end{pmatrix} = \hbar E_{RPA}^\nu \begin{pmatrix} 1 & 0 \\ 0 & -1 \end{pmatrix} \begin{pmatrix} X^\nu \\ Y^\nu \end{pmatrix}, \quad (2.30)$$

where the dimension is twice the number of possible particle-hole pairs in the model space of IPM states. The matrix A is the same as for the TDA states

$$A_{minj} = \varepsilon_{m,i}\delta_{mn}\delta_{ij} + \bar{v}_{mjin}, \quad (2.31)$$

whereas that for B is

$$B_{minj} = \bar{v}_{mnij}. \quad (2.32)$$

The name *quasi-boson approximation* originates from the use of the IPM ground state instead of the RPA vacuum. When we take the commutator of different particle-hole pairs and make the replacement of the ground state we get

$${}_{RPA}\langle 0|[a_i^\dagger a_m, a_n^\dagger a_j]|0\rangle_{RPA} \approx {}_{IPM}\langle 0|[a_i^\dagger a_m, a_n^\dagger a_j]|0\rangle_{IPM} = \delta_{mm}\delta_{ij}. \quad (2.33)$$

We recognize that the approximation effectively means treating the particle-hole pair operators as bosons. This naturally violates the Pauli principle and this is where we need the contributions from the neglected fermionic commutator terms to be small or cancel due to random phases.

The real ground state of the many-body system can be built from the IPM with the addition of all n particle- n hole states by completeness. The new feature of the RPA over the TDA is that it also allows one to annihilate particle-hole pairs, so it includes correlations in the ground state. When we look at the equations we see that the TDA approximation is recovered if we set $Y_{m,i}^\nu = 0$. These coefficients are therefore a measure of the ground state correlations.

For the RPA to be a good approximation we need two conditions on the coefficients X and Y . The solutions should have many $X_{m,i}^\nu$ of the same order of magnitude, that is they should have a very collective character. This means that each particle-hole pair has a small probability of being excited and therefore the violation of the Pauli principle for individual pairs is not important. In addition, the $Y_{m,i}^\nu$ are also required to be small in magnitude, since otherwise the IPM ground state would be too far from the RPA ground

state and our approximation would break down. This can happen and is often referred to as the collapse of the ground state.

As mentioned above we treat protons and neutrons independently in the IPM. This means that we must also do so in the RPA equations. As described in the IPM section, the charge-changing processes of interest will change protons to neutrons and vice versa. We incorporate this into the RPA description by taking the particle-hole pairs so that they reflect the isospin direction of the process. If we are concerned with a process that changes neutron to proton then all particle states are neutrons and all hole states are protons and vice versa. We are thus working in a basis that consists of mixed particle species.

What we are ultimately interested in with our nuclear structure model is to be able to calculate transition matrix elements. For our purposes they are one-body operators between the ground state of the mother nucleus and excited states in the daughter. If we have an hermitian one-body transition operator T , then the RPA gives the following simple expression for the matrix element

$${}_{RPA}\langle 0|T|\nu\rangle_{RPA} = \sum_{m,i} T_{m,i} X_{m,i}^\nu + T_{m,i} Y_{m,i}^\nu, \quad (2.34)$$

where $T_{m,i} = \langle m|T|i\rangle$ is the matrix element of the operator with the relevant IPM states. Whereas the wave functions for the excited states are not very accurate, the RPA is known to do well in describing such transition elements.⁵ This is because such transitions elements depend not on the absolute wave functions but on their internal relationships. This is exactly the philosophy behind the equations-of-motion method that was used to derive the RPA equations above [36].

We have previously mentioned that we are interested in nuclear states of good total angular momentum. To achieve this in the RPA equations we have to switch to the coupled representation where the creation operators for particle-hole excitations carry good angular quantum numbers. The analogue of equation (2.28) in the coupled case is

$$Q_{RPA,\nu}^\dagger(JM) = \sum_{m,i} X_{m,i}^\nu A_{m,i}^\dagger(JM) - \sum_{m,i} Y_{m,i}^\nu (-1)^{j_m+j_i+M} A_{m,i}(JM). \quad (2.35)$$

The new creation and annihilation operators are constructed by using stan-

⁵This is in close analogy with standard perturbation theory where the energy corrections in lowest order are often very good and the wave functions are notoriously bad. The RPA can actually also be derived as the small amplitude limit of time-dependent Hartree-Fock theory (TDHF) so if we think of the transition operator as an external perturbation then the RPA is the lowest non-trivial approximation. From this point of view the RPA is called linear response theory.

standard coupling theory

$$A_{m,i}^\dagger(JM) = [a_m^\dagger a_i]^{JM} = \sum_{\mu_m, \mu_i} (-1)^{j_i + \mu_i} \langle j_m j_i J | \mu_m \mu_i M \rangle a_{j_m, \mu_m}^\dagger a_{j_i - \mu_i}, \quad (2.36)$$

where the indices on a^\dagger and a in the second equation are the angular quantum numbers of the particle and hole respectively. By using this expression for Q_{RPA}^\dagger we get good angular momentum J of all particle-hole pairs. The full RPA equations are thus split into separate eigenvalue problems for each value of J . We also split the equations into positive and negative parity. This is done by looking at the orbital angular momenta l_m and l_i of the particle-hole pairs. The parity is positive when $l_m + l_i$ is even and negative when the sum is odd.

Residual Interaction

To get realistic structure information from the RPA we need a good residual interaction. As explained above, we are working with a particle-hole RPA and we thus need an effective force between particles and holes to calculate the \bar{v}_{minj} terms in equations (2.31) and (2.32). The most pleasant way of doing this is to use a self-consistent RPA where the residual interaction is obtained from the same potential that produces the single-particle orbits. In such an approach one thus starts from a realistic nucleon-nucleon interaction and performs a Hartree-Fock calculation to get the IPM states. In addition, one gets an expression for the interaction between particle-hole states that can be used in the RPA. When this interaction is used, we also have nice stability properties of the solutions that are only approximate with phenomenological forces. However, this kind of self-consistent method is computationally quite expensive and many studies simply use phenomenological IPM potentials and residual interactions. Since the results of the latter are not dramatically different from self-consistent treatments we will take the phenomenological path.

The residual interaction we use is of the so-called Landau-Migdal type. This kind of force was originally considered by Landau in connection with finite Fermi systems [39] and later applied to nuclei by Migdal [40]. The force originates from an expansion in momentum space, and since we want to describe the excitations of the nucleus, and not ground state properties such as saturation, we take only the lowest order in p^2 [32]. This is a constant in momentum space and we thus have a delta function in coordinate space which is easy to work with in matrix elements. However, as is known the nucleon-nucleon interaction depends very much on both spin and isospin so these quantities must be included in the interaction. The interaction must be a scalar in all coordinates and one can therefore write down the following

general expression for the Landau-Migdal force

$$V(\vec{r}_1, \vec{r}_2) = C_0 \delta(\vec{r}_1 = \vec{r}_2) (f + f' \vec{\tau}_1 \cdot \vec{\tau}_2 + g \vec{\sigma}_1 \cdot \vec{\sigma}_2 + g' \vec{\tau}_1 \cdot \vec{\tau}_2 \vec{\sigma}_1 \cdot \vec{\sigma}_2). \quad (2.37)$$

The force should act differently inside the nucleus as opposed to outside. This is taken into account by making the parameters f and f' density dependent through the relation

$$f = f^{ext} + (f^{int} - f^{ext}) \frac{1}{1 + \exp[(r - R)/a]}, \quad (2.38)$$

where the nuclear radius R and diffuseness a are simply those of from the IPM model described above.

The values of the coupling constants in eq. (2.37) were taken from [41] with the modifications of [42]. These were adjusted to the isobaric analogue resonances in ^{48}Ca and ^{208}Pb . The explicit values are given in Table 2.1.

C_0	f^{int}	f^{ext}	f'^{int}	f'^{ext}	g	g'
300	0.20	-2.45	0.90	1.50	0.55	0.70

Table 2.1: Coupling constants used in the Landau-Migdal residual interaction. The unit of C_0 is MeV fm^3 whereas the rest of the values are dimensionless.

In recent applications of the Landau-Migdal residual interaction the coupling constants used are slightly different from those given in Table 2.1. In our discussion on muon capture in chapter (3) we will address this issue. The total capture rates are almost insensitivity to variations in all parameters except g' . As we will discuss later, the value of g' is most likely higher in heavy nuclei than that given in the table. However, the different values of g' result in roughly 10% changes in the capture rates. As we do not expect our evaluations of neutrino cross sections to have this level of accurate, we use the parameterization of table (2.1) in all neutrino calculations.

Partial Occupancy

The standard RPA equations assume that the ground-state nucleus has a closed-shell structure. All single-particle orbits below the Fermi level are completely occupied. This is a rather restrictive condition and allows one to treat only a limited number of nuclei. To treat nuclei with open shells one can instead use the so-called quasi-particle RPA (QRPA) method. This procedure starts from an IPM that includes both mean-field contributions and pairing (see f.x. [36] or [32]). The latter effect is known to be particular important for open shell nuclei. However, this also requires a more involved residual interaction that captures the effective force between the

quasi-particles (superpositions of particle and hole). In order to avoid this more complicated QRPA model, we instead use a weighting procedure on the interaction matrix elements of our standard RPA model. This was first done in [44] and shown to give accurate results for weak processes in ^{12}C . The modification to the residual interaction matrix element is a simple multiplication

$$\langle mi|V_{res}|m'i'\rangle \rightarrow n_i n_{i'} \langle mi|V_{res}|m'i'\rangle, \quad (2.39)$$

where n_i and $n_{i'}$ are the occupancy fractions of the two hole orbits. We thus weight the matrix elements by the degree to which they contribute according to an IPM ground state. This procedure requires that partially occupied orbits are included among both particle and hole states.

After the introduction of partial occupancies there is a natural next step in improving our model. The occupancies that resemble a full QRPA the most should be those that can be obtained from solving the BCS pairing problem. This depends on the single-particle level energies and the pairing gap parameter Δ . The equation for the partial occupancy of a level with index k is

$$v_k^2 = \frac{1}{2} \left(1 - \frac{\varepsilon_k - \mu}{\sqrt{\Delta^2 + (\varepsilon_k - \mu)^2}} \right), \quad (2.40)$$

where ε_k is the single-particle energy and μ is the chemical potential. We have the condition

$$N = \sum_k v_k^2 (2j_k + 1), \quad (2.41)$$

where N is the number of protons or neutrons depending on the species considered. One can solve this equation iteratively for the chemical potential and thus obtain all the v_k 's. The pairing gap Δ can be obtained from the masses of neighboring odd-even nuclei [33]. If these masses are not known, it is customary to use the expression $\Delta \approx 12/\sqrt{A}$ MeV with A the mass number.

As we will see when presenting our muon capture results, this approximate implementation of BCS occupancies works quite well. It helps cure some overly rigid shell effects that are present in the RPA and not in the experimental data by smoothing the closures. The absolute magnitude of the BCS corrections are, however, small and we have therefore used IPM partial occupancies in all neutrino and antineutrino calculations.

Sum Rules and Quenching

In nuclear structure models one often resorts to so-called sum rules to check the consistency of calculations. Sum rules are an extremely handy tool when trying to estimate whether a model of collective excitations is realistic or not. As the reactions we are concerned with are very dependent on the position and magnitude of collective phenomena, or giant resonances as they are

also called, we now discuss the relevant sum rules that guide our structure modeling.

A prominent example is the Thomas-Reiche-Kuhn (TKR) sum rule. It governs the dipole operator which is well-known in lowest-order electromagnetic transitions. The total cross section for dipole excitations can be written as a sum over all excited states as

$$\sigma_{total} = \frac{4\pi^2 e^2}{\hbar c} \sum_{\nu} (E_{\nu} - E_0) |\langle \nu | D | 0 \rangle|^2 = \frac{4\pi^2 e^2}{\hbar c} S_1(D), \quad (2.42)$$

where E_{ν} and E_0 are the energies of the excited state and ground state respectively and D is the dipole operator. The quantity $S_1(D)$ is called the energy-weighted strength. For a nucleus like ^{16}O it turns out that 50% of the strength is located in a broad resonance just above 20 MeV and in heavy nuclei this state can exhaust almost all of the strength given by the sum rule [32]. This state is well described in the famous Goldhaber-Teller model [45] which attributes the state to a coherent excitation of particle-hole pairs. It is therefore no wonder that the RPA does very well in describing such collective vibrations as it is based on exactly this assumption for the excited nuclear states. Not surprisingly, it can be shown that the RPA fulfills the energy-weighted sum rule exactly [32].

In the case of weak interactions we need to include isospin in the sum rules. This brings us to the famous Ikeda sum rule [46]. Consider the quantity

$$ISR = S_+ - S_- = \sum_f |\langle f | \hat{q}_{JM}^{\dagger} \tau_+ | i \rangle|^2 - \sum_f |\langle f | \hat{q}_{JM} \tau_- | i \rangle|^2, \quad (2.43)$$

where $|i\rangle$ is the ground state and the sum is over all final states f of the nucleus. The operators \hat{q}_{JM} are assumed to be irreducible tensor operators of rank J and projection M . τ_{\pm} are the usual step operators of isospin. The general Ikeda sum rule states that

$$ISR = (2J + 1)(N - Z) \quad (2.44)$$

where J is the angular momentum of the operator \hat{q}_{JM} above and N, Z are the neutron and proton numbers respectively. The factor $(2J + 1)$ comes from use of the Wigner-Eckart theorem.

The *ISR* basically arises from the assumption that isospin is conserved in the nucleus as we will now show. To avoid the complications of angular momentum coupling, we will take \hat{q}_{JM} to be the identity operator. This is a scalar so we have $(J, M) = (0, 0)$. In this case the sum rule follows from

the simple calculation

$$\begin{aligned}
 ISR(J=0) &= S_-^F - S_+^F \\
 &= \sum_f |\langle f|\tau_-|i\rangle|^2 - \sum_f |\langle f|\tau_+|i\rangle|^2 \\
 &= \sum_f \langle f|\tau_-|i\rangle \langle f|\tau_-|i\rangle^* - \sum_f \langle f|\tau_+|i\rangle \langle f|\tau_+|i\rangle^* \\
 &= \sum_f \langle f|\tau_-|i\rangle \langle i|\tau_+|f\rangle - \sum_f \langle f|\tau_+|i\rangle \langle i|\tau_-|f\rangle \\
 &= \langle i|\tau_+ \left(\sum_f |f\rangle \langle f| \right) \tau_-|i\rangle - \langle i|\tau_- \left(\sum_f |f\rangle \langle f| \right) \tau_+|i\rangle \\
 &= \langle i|[\tau_+, \tau_-]|i\rangle = \langle i|2\tau_3|i\rangle \\
 &= N - Z,
 \end{aligned} \tag{2.45}$$

where we have used $(\tau_\pm)^\dagger = \tau_\mp$ and the completeness of the sum over final states $\sum_f |f\rangle \langle f| = 1$. The quantities S_\pm are called the (Fermi) β -strengths. As promised, the *ISR* follows directly from the commutation relations for the isospin operator. The pure isospin operator is also called the Fermi operator and subsequently the rule is also known as the Fermi sum rule, explaining the superscript F on the strengths S_\pm . Equally important is the so-called Gamow-Teller (GT) sum rule, which is associated to the GT operator $\vec{\sigma}\tau_\pm$. It states that

$$ISR(J=1) = S_-^{GT} - S_+^{GT} = 3(N - Z). \tag{2.46}$$

It is the subject of much discussion since its fulfillment in low-energy reactions is not quite clear. We will have more to say about this issue below.

First we want to prove that the RPA actually fulfills the Ikeda sum rule. Again we will only show this for the Fermi transition as it avoids considerations of angular coupling. We start by writing down the Ikeda sum, remembering that this time it should run over the RPA solutions.

Using equation (2.34) we have

$$ISR(J=0)^{RPA} = \sum_{\nu} |\langle \nu | \tau_- | 0 \rangle|^2 - \sum_{\nu} |\langle \nu | \tau_+ | 0 \rangle|^2 \quad (2.47)$$

$$= \sum_{\nu} \left| \sum_{m,i} (X_{m,i}^{\nu} T_{m,i}^{-} + Y_{m,i}^{\nu} T_{i,m}^{-}) \right|^2 \quad (2.48)$$

$$- \sum_{\nu} \left| \sum_{m,i} (X_{m,i}^{\nu} T_{m,i}^{+} + Y_{m,i}^{\nu} T_{i,m}^{+}) \right|^2 \quad (2.49)$$

$$= \sum_{\nu} \left[\sum_{m,i} (|X_{m,i}^{\nu}|^2 |T_{m,i}^{-}|^2 + |Y_{m,i}^{\nu}|^2 |T_{i,m}^{-}|^2) \right] \quad (2.50)$$

$$+ 2\text{Re} \sum_{m,i,m',i'} X_{m,i}^{\nu*} T_{m,i}^{-*} Y_{m',i'}^{\nu} T_{i',m'}^{-} \quad (2.51)$$

$$- \sum_{\nu} \left[\sum_{m,i} (|X_{m,i}^{\nu}|^2 |T_{m,i}^{+}|^2 + |Y_{m,i}^{\nu}|^2 |T_{i,m}^{+}|^2) \right] \quad (2.52)$$

$$+ 2\text{Re} \sum_{m,i,m',i'} X_{m,i}^{\nu*} T_{m,i}^{+*} Y_{m',i'}^{\nu} T_{i',m'}^{+}, \quad (2.53)$$

where $T_{m,i}^{\pm} = \langle m | \tau_{\pm} | i \rangle$ and $|0\rangle$ is the self-consistent IPM ground state (from which the residual interaction comes). To proceed further we now change the order of summation and use the closure and orthogonality relation for the RPA solutions [32]

$$\sum_{\nu} (X_{m,i}^{\nu} X_{m',i'}^{\nu} - Y_{m,i}^{\nu} Y_{m',i'}^{\nu}) = \delta_{m,m'} \delta_{i,i'} \quad (2.54)$$

$$\sum_{\nu} (X_{m,i}^{\nu} Y_{m',i'}^{\nu} - Y_{m,i}^{\nu} X_{m',i'}^{\nu}) = 0. \quad (2.55)$$

Using these properties and the fact that $\langle m | \tau_{\pm} | i \rangle^* = \langle i | \tau_{\mp} | m \rangle$ we arrive at

$$ISR(J=0)^{RPA} = \sum_{m,i} \left(|T_{m,i}^{-}|^2 - |T_{m,i}^{+}|^2 \right). \quad (2.56)$$

In the first term we have an operator τ_- that turns neutrons into protons. When summing its squared amplitude over all protons m we get the occupation of neutrons in the i th orbit.⁶ An analogous argument gives us the proton occupation in the second term. We thus have

$$ISR(J=0)^{RPA} = \sum_i (2j_i + 1) n_i - \sum_m (2j_m + 1) n_m, \quad (2.57)$$

where i refers to neutrons and m refers to protons and n are the relevant occupations fraction of the orbits. We have explicitly multiplied by the

⁶Here we are assuming isospin symmetry of single-particle orbits so that proton and neutron model spaces are exactly the same. We thus neglect the Coulomb part of the WS potential in equation (2.23).

number of angular momentum projections $(2j + 1)$. Performing the sums will give us the promised result $ISR(J = 0)^{RPA} = N - Z$.

There is a very nice way in which the transition governed by the Fermi operator can be used to improve the model space. Under the assumption of isospin symmetry, the transition, which changes a neutron to a proton or vice versa, should be at zero excitation energy in the daughter and have strength $|N - Z|$. In real nuclei Coulomb interactions will break this isospin degeneracy. However, the value of this breaking can be accurately estimate by considering the change in charge of parent and daughter. The energy of this so-called isobaric analogue state (IAS) can thus be accurately described by the simple formula [47]

$$E_{IAS} \approx \Delta M_{nuc} \mp \Delta M_{np} \pm \frac{6}{5} \frac{Z\alpha\hbar c}{R_{nuc}}, \quad (2.58)$$

where ΔM_{nuc} is the mass difference of parent and daughter (Q-value of the process) and $\Delta M_{np} = 1.2934$ MeV is the neutron-proton mass difference. The last term is the change in Coulomb energy one obtains from the semi-empirical mass formula by changing the charge by one unit. The radius R_{nuc} is the charge radius. In [47] a good approximation for this was found to be $R_{nuc} \approx 1.12A^{1/3} + 0.78$ fm and we will be using this relation here. The upper signs in eq. (2.58) apply to neutrino capture and β -decay on $N > Z$ nuclei, whereas the lower ones are for antineutrino and muon capture on $Z > N$ nuclei. In all other cases (neutrino capture and β -decay on $Z \geq N$ nuclei etc.) the IAS state does not exist as the Fermi transition is blocked. We will use this estimated IAS energy to improve our model by fitting the single-particle energies so that this state (which is the dominant $J = 0^+$ contribution) is at the position given by eq. (2.58).

In principle the above considerations apply only to self-consistent versions of the RPA. However, if we use a phenomenological IPM model of the ground state and a good effective residual interaction we should expect our results to closely match the sum rules. We have previously calculated the strengths in representative nuclei across the chart and compared the GT sum rule with our model predictions [48]. It was found that the model exhausts over 95% of the sum rule.

As mentioned above there are complications with the GT sum rule at low energy. Measurements clearly show that it is reduced in the nuclear environment at low energy [49]. As the GT operator contains the nucleon spin it is connected to the coupling constant g_A discussed in section (2.1.1). The reduction is therefore referred to as the in-medium quenching of the axial-vector coupling. Two reasons for this fact have been suggested. One is sub nuclear degrees of freedom, as for example the nucleon Δ resonance. The idea is that these high energy states of the nucleon should interfere with the normal nucleon state to push the GT strength to higher energies. The second possible explanation is also an interference effect that pushes strength

upwards, although this time it comes from mixing with configurations in higher single-particle shells. Recent measurements of the GT sum rule show that one can account for over 90% of the strength by going up to excitation energies of around 90 MeV, thus favoring the configuration mixing scenario [50, 51]. The problem with the RPA approach is that it fulfills the GT sum rule exactly even though the GT transition contributions only reside at low energy. We need to compensate this fact by introducing a reduction factor for the GT transitions. We will use the value $(0.8)^2 = 0.64$ [52] which has become standard.

The GT operator has the structure $\vec{\sigma}\tau_{\pm}$. It can therefore connect states only to their spin-orbit partners. For example, if we have a $1f_{7/2}$ proton (neutron) then the GT operator can convert it into a $1f_{7/2}$ or $1f_{5/2}$ neutron (proton). These states reside at low energy and the GT strength is thus located here. The experimental information about the GT operator discussed above clearly indicate that the entire strength is not found at low energy. To remedy the situation we therefore introduce a reduction factor.

We must, however, be careful to apply this quench only when the GT operator actually contributes. In the RPA there are correlations in the ground-state that can promote particle-hole pairs into higher $1\hbar\omega$, $2\hbar\omega$ etc. shells.⁷ The GT operator can connect these correlations to spin-orbit partners when the latter are not blocked.

The multipole operators of eqs. (2.14)-(2.17) depend explicitly on the momentum transfer q and only in the limit $q \rightarrow 0$ will the 0^+ and 1^+ responses reduce to the Fermi and GT operators [27]. Strictly speaking, the considerations above apply only in this limit. At finite q other operators are present that can connect to states in different shells (with structure like $r^2\sigma\tau$). These states reside at higher energies and should not be quenched. For very low-energy processes like β -decay this is only a small effect since the momentum transfer is usually negligible. However, for neutrino and antineutrino reactions at Supernova energies and for muon capture, q can become sizable.

For muon capture we will use quenching only in a restricted cases (discussed in more detail in chapter (3)). Neutrino reactions and β -decay on most stable and all neutron-rich nuclei will have no blocking of the GT transition. Noting that the higher energy states contribute relatively little, we have used quenching on all 1^+ states for simplicity. Antineutrino processes are more delicate since correlations can introduce GT contributions as mentioned above. This will, however, only be relevant for low mass nuclei close to stability and we therefore use quenching in these cases exclusively.

⁷The nomenclature $n\hbar\omega$ refers to excitations that involve states that are n shells away from the initial configuration. Here one is referring to the level that the states would occupy in a harmonic oscillator IPM (see figure (2.1)). The strong nuclear spin-orbit splitting, however, causes the shells to overlap and mix parity in heavy nuclei. Opposite parity states coming down from above are referred to as intruder states.

There have been some investigations into the question of whether other operators may also be quenched in the nuclear medium (see the short review in [53]). There is clear evidence for quenching of the so-called M1 transition [53] which is a common participant in electromagnetic processes on nuclei. The associated operator is directly connected to the GT operator, so M1 transitions can also shed light on weak interactions. The evidence for quenching in multipoles other than GT and M1 are, however, not yet conclusive. In light of this we will not apply quenching to any other transition operators. Our muon capture rates presented in chapter (3) also suggest that the RPA nuclear model needs no quenching beyond that of the GT strength.

2.2.3 Reduction of Transition Operators

Now that we have an IPM model and the RPA solutions, the next step is to evaluate the nuclear weak transition operators with respect to these states. According to equation (2.34) we have to calculate single-particle matrix elements between particle and hole states, multiply by the amplitudes from the RPA solutions, and sum over particle-hole pairs.

When we wrote down the weak interaction operators in section (2.1) we insisted on good angular momenta. We therefore have transition matrix elements of the principal form

$$\langle J_f M_f | \hat{A}_{JM} | J_i M_i \rangle, \quad (2.59)$$

where $J_i M_i$ and $J_f M_f$ are total angular momentum and projection of the initial and final state respectively and \hat{A}_{JM} is an operator that carries angular momentum J and projection M . This expression can be reduced by the Wigner-Eckart theorem [28] to give

$$\langle J_f M_f | \hat{A}_{JM} | J_i M_i \rangle = (-1)^{J_f - M_f} \begin{pmatrix} J_f & J & J_i \\ -M_f & M & M_i \end{pmatrix} \langle J_f || \hat{A}_J || J_i \rangle, \quad (2.60)$$

where the last quantity carrying double bars is independent of the projection quantum numbers. This reduced matrix element is what enters in equation (2.13) and it is what we have to calculate. We are interested in evaluating transition operators between the parent ground state and all excited states in the daughter. The particle-hole elements needed can therefore be written as

$$\langle 0 || \hat{A}_J || [ph]_J \rangle = \langle p || \hat{A}_J || h \rangle, \quad (2.61)$$

where $[ph]_J$ is a particle-hole pair coupled to angular momentum J . Here we make the assumption that the ground state $|0\rangle$ always has $J^\pi = 0^+$ (we will discuss this restriction below). Since we assumed one-body currents in equation (2.7), the second equality follows from second quantization manipulations with the condition that p and h carry individual quantum numbers, j_p and j_h , that couple to J .

The reduced single-particle matrix elements can now be written out in full detail with all quantum numbers displayed

$$\langle (l_p 1/2) j_p || \hat{A}_J || (l_h 1/2) j_h \rangle, \quad (2.62)$$

where the orbital angular momentum, l , and spin, s , couples to total angular momentum j . The operator \hat{A}_J will in general contain parts that act on the spatial coordinates and others that act on the spin. There are beautiful, yet complicated, techniques available for dealing with such quantities [28]. Here we will summarize the results of such manipulations for the case of neutrino and antineutrino capture. The expressions for muon capture are similar, except that one needs to multiply by the muon wave function. As we will discuss in great detail in chapter (3), this is a trivial result for non-relativistic muons, whereas for relativistic muons additional operators are needed.

Vector Currents

The vector currents have three independent terms. The Coulomb vector part yields

$$\begin{aligned} \langle (l_p \frac{1}{2}) j_p || \mathcal{M}_J^V(\kappa) || (l_h \frac{1}{2}) j_h \rangle &= (-1)^{j_h + J - 1/2} \frac{[j_p][j_h][J]}{\sqrt{4\pi}} \begin{pmatrix} j_p & j_h & J \\ 1/2 & -1/2 & 0 \end{pmatrix} \\ &\times \int dr r^2 j_J(\kappa r) f_p^*(r) f_h(r), \end{aligned} \quad (2.63)$$

where $f(r)$ are the relevant single-particle wave functions of the nuclear WS potential. The longitudinal current can be obtained from the Coulomb part since we are assuming that the vector part of the current is conserved (chapter. (2.1)). Using CVC and the continuity equation one gets [18]

$$\langle i || \mathcal{L}_J || f \rangle = \frac{\omega}{\kappa} \langle i || \mathcal{M}_J || f \rangle, \quad (2.64)$$

where ω is the time component of the four-momentum transfer. The transverse vector parts of the current is

$$\begin{aligned}
 & \langle (l_p \frac{1}{2}) j_p || \mathcal{J}_J^{el,V}(\kappa) || (l_h \frac{1}{2}) j_h \rangle \\
 &= (-1)^{j_h+J-1/2} \frac{1}{2M} \frac{[j_p][j_h][J]}{\sqrt{4\pi}} \begin{pmatrix} j_p & j_h & J \\ 1/2 & -1/2 & 0 \end{pmatrix} \\
 & \times \frac{1}{\kappa} \int dr r^2 j_J(\kappa r) f_p^*(r) f_h(r) \left\{ \sqrt{J(J+1)} \frac{f_p^*(r) f_h'(r) - f_p'^*(r) f_h(r)}{r} \right. \\
 & \left. + \frac{l_p(l_p+1) - l_h(l_h+1)}{\sqrt{J(J+1)}} (f_p^*(r) f_h(r))' \right\} \\
 & + (-1)^{l_p} \frac{\kappa}{2M} \frac{[j_p][j_h][J]}{\sqrt{4\pi}} \begin{pmatrix} j_p & j_h & J \\ 1/2 & 1/2 & -1 \end{pmatrix} \\
 & \times \int dr r^2 j_J(\kappa r) f_p^*(r) f_h(r) \tag{2.65}
 \end{aligned}$$

$$\begin{aligned}
 & \langle (l_p \frac{1}{2}) j_p || \mathcal{J}_J^{mag,V}(\kappa) || (l_h \frac{1}{2}) j_h \rangle \\
 &= (-1)^{j_h+J-1/2} \frac{1}{2Mi} \frac{[j_p][j_h][J]}{\sqrt{4\pi}} \begin{pmatrix} j_p & j_h & J \\ 1/2 & -1/2 & 0 \end{pmatrix} \\
 & \times \int dr r^2 j_J(\kappa r) \frac{f_p^*(r) f_h(r)}{r} \left[\frac{(\chi_p + \chi_h)(\chi_p + \chi_h + 1) - J(J+1)}{\sqrt{J(J+1)}} \right] \\
 & + (-1)^{j_h+J-1/2} \frac{1}{2Mi} \frac{[j_p][j_h][J]}{\sqrt{4\pi}} \begin{pmatrix} j_p & j_h & J \\ 1/2 & -1/2 & 0 \end{pmatrix} \\
 & \times \int dr r^2 j_J(\kappa r) \\
 & \left\{ \frac{\sqrt{J(J+1)}}{r} + \frac{\chi_p + \chi_h}{\sqrt{J(J+1)}} \left(\frac{d}{dr} + \frac{1}{r} \right) \right\} f_p^*(r) f_h(r). \tag{2.66}
 \end{aligned}$$

Axial-vector Currents

The axial vector current is not conserved due to the finite pion mass.⁸, so there is no continuity to reduce the number of independent terms. The four terms are, however, somewhat less complicated than the vector ones. They

⁸The axial vector current is conserved in the limit where the pion mass goes to zero. The breaking of this symmetry is at the level of the pion to nucleon mass ratio which is a little over 10%. One therefore often uses the term Partially Conserved Axial Current (PCAC).

are

$$\begin{aligned}
 & \langle (l_p \frac{1}{2}) j_p || \mathcal{M}_J^A(\kappa) || (l_h \frac{1}{2}) j_h \rangle \\
 &= (-1)^{j_h + J + 1/2} \frac{1}{2Mi} \frac{[j_p][j_h][J]}{\sqrt{4\pi}} \begin{pmatrix} j_p & j_h & J \\ 1/2 & -1/2 & 0 \end{pmatrix} \\
 & \times \int dr r^2 j_J(\kappa r) \left\{ f_p^*(r) f_h'(r) - f_p'^*(r) f_h(r) + (\chi_h - \chi_p) \frac{f_p^*(r) f_h(r)}{r} \right\}
 \end{aligned} \tag{2.67}$$

$$\begin{aligned}
 & \langle (l_p \frac{1}{2}) j_p || \mathcal{L}_J^A(\kappa) || (l_h \frac{1}{2}) j_h \rangle \\
 &= (-1)^{j_h + J - 1/2} \frac{i}{\kappa} \frac{[j_p][j_h][J]}{\sqrt{4\pi}} \begin{pmatrix} j_p & j_h & J \\ 1/2 & -1/2 & 0 \end{pmatrix} \\
 & \times \int dr r^2 j_J(\kappa r) \left\{ (\chi_p + \chi_h) \frac{f_p^*(r) f_h(r)}{r} + \left(\frac{d}{dr} + \frac{1}{r} \right) f_p^*(r) f_h(r) \right\}
 \end{aligned} \tag{2.68}$$

$$\begin{aligned}
 & \langle (l_p \frac{1}{2}) j_p || \mathcal{J}_J^{el,A}(\kappa) || (l_h \frac{1}{2}) j_h \rangle \\
 &= (-1)^{j_h + J - 1/2} \frac{1}{i\kappa} \frac{[j_p][j_h][J]}{\sqrt{4\pi}} \begin{pmatrix} j_p & j_h & J \\ 1/2 & -1/2 & 0 \end{pmatrix} \\
 & \times \int dr r^2 j_J(\kappa r) \left\{ \frac{\sqrt{J(J+1)}}{r} + \frac{\chi_p + \chi_h}{\sqrt{J(J+1)}} \left(\frac{d}{dr} + \frac{1}{r} \right) \right\} f_p^*(r) f_h(r)
 \end{aligned} \tag{2.69}$$

$$\begin{aligned}
 & \langle (l_p \frac{1}{2}) j_p || \mathcal{J}_J^{mag,A}(\kappa) || (l_h \frac{1}{2}) j_h \rangle \\
 &= (-1)^{l_p} \frac{[j_p][j_h][J]}{\sqrt{4\pi}} \begin{pmatrix} j_p & j_h & J \\ 1/2 & 1/2 & -1 \end{pmatrix} \times \int dr r^2 j_J(\kappa r) f_p^*(r) f_h(r).
 \end{aligned} \tag{2.70}$$

We have stressed previously that we group the nuclear states in both angular momentum and parity. This is a huge advantage since the current terms can be classified according to parity as well. As usual, the total parity of a given matrix element is found by combining the parity of all quantities involved. These are the leptonic factor of angular momentum J in the multipole operators, the nuclear current operators given in section (2.1.1), and the parities of particle and hole wave functions. To determine the combined parity one needs to decouple the spin and orbital angular momenta and look at the orbital part. This can be done with standard coupling techniques. The result is that the vector Coulomb, longitudinal and transverse electric matrix elements are of natural parity, meaning that $l_p + l_h + J$ must be even. The transverse magnetic is unnatural, i.e. $l_p + l_h + J$ has to be odd (this is analogous to E and M type transition in electromagnetic interactions). For the axial vector terms it is the other way around. As with the implementation of good angular momentum, parity provides a nice reduction in the numerical calculation of nuclear structure.

2.2.4 Ground State and Model Space Considerations

We have mentioned that one of our basic assumptions on the ground state is that it has zero angular momentum and positive parity. However, for the neutrino reactions we would also like to calculate cross sections in even-odd and odd-odd systems. As we will see later, these reactions are dominated by giant resonances (such as the GT and spin-dipole resonances) in the region around 10-15 MeV and above. Classically inspired arguments about oscillations in finite quantum system show that sum rules and energies should be smooth as a function of nucleon number [54]. This has been confirmed by observation of resonance strengths and energies across the nuclear chart [32]. This smoothness is further supported by detailed large-scale shell model calculations of even-odd and odd-odd medium mass nuclei [55]. In our RPA model we can handle such nuclei by simply adjusting the occupation numbers described in section (2.2.2). We also observe that energy and strength of giant resonances behave in a smooth manner as a function of mass number A . We therefore have reason to believe that the RPA will also do well in odd systems where the ground-state is not $J = 0^+$. In muon capture we have also calculated the rates for experimentally known nuclei that are not even-even. The general trend of the results follow the experimental data, although we cannot reproduce the fine structure that exists in the strengths functions of nuclei with unpaired protons or neutrons. For neutrino reactions on nuclei there is very little experimental information available. Our cross sections show the expected smoothness with mass number and this fact alone will be our justification for using the structure model in odd-even and odd-odd nuclei as well.

Another concern is the size of the model space. As we would like to consider nuclei ranging from light to very heavy, we need a sensible overall approach. In some heavy nuclei one might be able to truncate some of the tightest bound single-particle states. However, initial calculations on ^{208}Pb showed that correlations were lost and muon capture rates were overestimated as a result. As the computational effort is not reduced much by this truncation we have simply chosen to always keep all single-particle states below the Fermi level. The question of valence space above the Fermi level is connected to convergence. One needs to include enough states so that the results change by less than some tolerance level when more states are added. The actual number differs for light and heavy nuclei. To illustrate this we have calculated muon capture rates in some test cases with different model space truncations.⁹

In table (2.2) we show the truncation test results for ^{40}Ca . The number of states ranges from the extreme case of only one valence orbit to 39. Since

⁹The residual interaction used is not quite the same as the one we will work with in chapter (3) and the magnitudes of the rates will therefore differ somewhat from the final results that we will compare to experiment.

^{40}Ca has 6 filled orbits in the IPM ground state this amounts to inclusion of 45 single-particle states (all oscillator shells up to and including $8\hbar\omega$). As we can see, the results are practically converged at the 1% level when 19 states are included on either side of the Fermi level for both species. It is also seen that there is smaller variation on the proton side than on the neutron side. This is of course expected as muon capture turns a proton into a neutron. Table 2.3 shows the variation of capture rates in ^{208}Pb . Here we have 16 proton and 22 neutron orbits fully occupied in the IPM ground state and we go up to $9\hbar\omega$ model space. We see a little more sensitivity in this heavy nucleus as expected. However, we still have less than 2% change from 29/23 ($8\hbar\omega$) to 36/30 ($9\hbar\omega$) in the rate.

p/n	1/39	9/39	19/39	29/39	39/39
Rate	2.997	2.316	2.289	2.285	2.284
p/n	39/29	39/19	39/9	39/1	19/19
Rate	2.288	2.242	1.986	0.665	2.251

Table 2.2: Test of different model space truncations for muon capture on ^{40}Ca . The first and third rows give the number of single-particle states above the Fermi level for protons/neutrons. The second and fourth rows give the total muon capture rate in 10^6 s^{-1} .

Our model space truncation tests show that convergence to within a few percent can be achieved with proton and neutron single-particle orbits up to and including the $8\hbar\omega$ shell. Since this space is also computationally fast for all the nuclei, we use this space in all structure calculations. One might worry somewhat that in going to $A = 300$ for r -process applications we could exhaust our neutron model space. However, for that purpose we will only compute neutrino captures. This is most sensitive to the proton hole states and we should be safe in this case also.

p/n	1/23	9/23	19/23	29/23	36/23
Rate	24.69	17.87	15.31	14.66	14.51
p/n	36/30	29/30	29/18	29/13	29/1
Rate	14.50	14.65	14.41	13.81	1.366

Table 2.3: Same as Table 2.2 for ^{208}Pb .

2.2.5 Excitation Spectra Examples

To illustrate the discussion in the previous sections we now present two examples of strength distributions calculated with the RPA model. One is for negatively charged lepton capture on ^{48}Ni and the other is for neutrino

capture on ^{208}Pb . The former nucleus is an example of a doubly-magic $Z > N$ nuclei. It lies beyond the proton drip line and is particle unstable. The latter is the standard example of a heavy nucleus. The magic neutron and proton numbers in both nuclei lead us to expect an accurate RPA results, even without the use of partial occupancies. Notice that the direction of the processes we consider are $\Delta T_z = 1$ for $Z > N$ and $\Delta T_z = -1$ for $N > Z$, leaving the GT and Fermi transitions unblocked so that we should see the major part of the strength in these reactions.

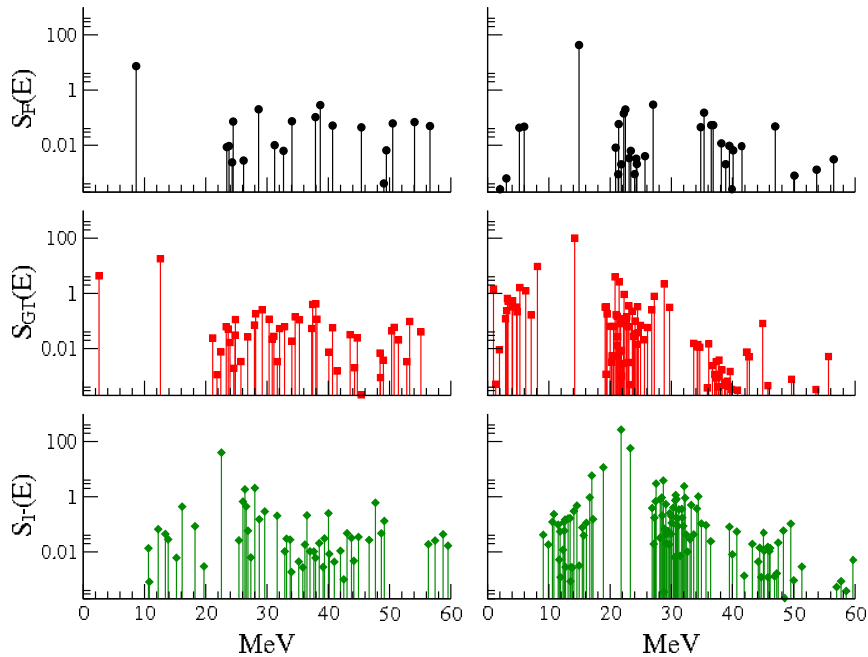


Figure 2.2: Strength distributions as a function of energy (in MeV) for ^{48}Ni (left) and ^{208}Pb (right). The top part gives the 0^+ (Fermi) strength, the middle gives the 1^+ (GT) strength, and the bottom shows the $J = 1^-$ multipole strength.

In figure (2.2) we present the strength distributions for the 0^+ (upper part, denoted S_F) and the 1^+ response (middle part, denoted S_{GT}).¹⁰ These were calculated at non-zero momentum transfer so the sum rules discussed in section (2.2.2) are in principal modified. However, we still find them to be fulfilled to better than 1%, indicating that the modifications are small in these examples. In the lower part of the figure we give the strength for the 1^- forbidden transition (mainly the spin-dipole term: $\vec{r} \wedge \vec{\sigma}$). The

¹⁰The figures give the discrete states calculated in the RPA. A real experiment would of course produce a smooth distribution due to finite resolution.

gaps that are seen in the distributions are due to the shell structure around magic numbers and the magnitude can thus be inferred directly from the single-particle orbit energies. ^{208}Pb is seen to have smaller gaps, which is expected since the density of single-particle levels grows with particle number and energy.

The largest contribution to the 0^+ strength is of course the IAS state from the Fermi transition, the position being given by the formula in eq. (2.58). The main contribution to the 1^+ strength has an energy that is roughly equal to that of the IAS state (as argued in [47]). However, the largest 1^+ contributions are split into multiple states. The $\vec{\sigma}$ operator can connect to both spin-orbit partners for any orbital angular momentum (in the single-particle language). The division of the GT response is therefore a consequence of the spin-orbit splitting in the IPM potential. This is particularly clear in ^{48}Ni where the magic structure leads to clean contributions from proton in $1f_{7/2}$ to neutron in $1f_{7/2}$ or $1f_{5/2}$, giving the two distinct peaks at low energy. The case of ^{208}Pb is more complicated since a scatter of states appears at low energy. This is caused by the many states in the $5\hbar\omega$ shell that the GT operator can connect to. Notice that the splitting of the two main peaks is larger in ^{48}Ni as expected from its larger spin-orbit splitting compared to ^{208}Pb [33]. We will see the importance of the main 0^+ (Fermi) and 1^+ (GT) contributions later when we discuss neutrino capture on uranium isotopes.

The 1^- response in the lower part of figure (2.2) has the large contributions residing at higher energies. This is explained by the parity change induced by the 1^- operator, meaning that it connects to states that are located at least $1\hbar\omega$ above in the oscillator picture. However, when we consider muon capture on $N \sim Z$ nuclei in chapter (3) the Fermi and GT transitions will be blocked in many cases and the 1^- becomes the dominant multipole. The phase space will of course be diminished by the higher energy of the 1^- resonance and the absolute capture rate from these states is therefore smaller.

The high-energy region of the responses have many small contributions closely spaced and the structure of this part is largely similar for the three transitions. These states represent 0^+ and 1^+ transitions to higher oscillator shells and are not induced by the purely inter shell Fermi or GT operators (1^- will connect to higher shell and intruder states as mentioned above). These are the states mentioned in the quenching discussion above that we do not wish to use any reduction on.

2.2.6 Neutrino and Antineutrino Cross Section Comparison

As we have already mentioned several times, the evaluation of the neutrino and antineutrino capture cross sections on nuclei requires a good description of the giant resonance responses. In particular, the GT operator will yield

a significant contribution if it is not blocked in the daughter nucleus. We discussed above the intrinsic problem of quenching of the GT response in the RPA model and this issue is a genuine concern in calculating neutrino capture processes. In chapter (3) we will discuss muon capture and one conclusion from this work is that the RPA model does well with all responses except for GT transitions. In view of this fact we now make a comparison to a hybrid model that isolates the problem.

For this purpose, we consider the work of Toivanen et al. [56]. They use a model similar to the one we use for all responses except the GT transition which was obtained from large-scale shell-model calculations. In table (2.4) we compare our RPA results (left side) with those of [56] (right side) for iron nuclei with different mass numbers and neutrino spectral temperatures (see section (2.4.3)). The two top panels give neutrino capture cross sections, whereas the two at the bottom give the same for antineutrino captures.

A/T	2.8	3.5	4	5	6.4	8	10	2.75	3.5	4	5	6.4	8	10
52	1	2	5	12	35	85	197	0	1	3	9	30	82	197
53	1	3	6	16	45	108	248	1	3	6	18	52	128	288
54	2	4	8	20	54	126	279	1	5	9	24	67	157	343
55	3	7	12	29	72	159	336	3	8	14	34	88	198	418
56	4	10	17	38	91	192	392	4	11	19	45	111	240	491
57	6	14	24	53	122	251	500	6	15	24	56	134	285	573
58	7	18	29	64	144	288	561	6	17	28	64	155	327	653
59	9	22	35	75	167	330	638	10	23	38	82	188	384	749
60	11	25	40	84	183	359	684	11	27	44	94	211	426	820
A/T	2.8	3.5	4	5	6.4	8	10	2.75	3.5	4	5	6.4	8	10
52	5	8	11	19	35	64	115	3	7	10	20	42	81	153
53	1	3	4	9	20	41	81	2	5	7	13	28	55	105
54	1	3	5	9	20	40	78	2	4	6	12	26	53	104
55	2	3	5	10	21	41	80	2	3	5	11	25	52	102
56	1	2	3	7	15	32	65	1	2	4	9	21	44	88
57	1	2	3	6	15	30	61	1	2	3	6	16	34	71
58	1	1	2	5	12	26	54	0	1	2	6	15	33	69
59	1	1	2	5	11	24	50	0	1	2	4	12	26	57
60	0	1	1	3	8	18	39	0	1	2	5	12	28	60

Table 2.4: Comparison of our RPA cross sections (left side) with those of [56] (right side) for iron nuclei as a function of mass number A and neutrino temperature T . The top panel shows neutrino capture and the bottom one shows antineutrino capture. All cross sections are in units of 10^{-42} cm^2 .

Looking at the table we find quite good agreement between our method and the more involved hybrid model. There is a tendency for the pure RPA method to underestimate the cross sections for higher neutrino temperatures (higher average energies). One would tend to trust more in the hybrid model results as large-scale shell-model calculations are very successful in the description of nuclear properties. However, since experimental data on neutrino-nucleus reactions are extremely sparse, the jury is still out. The reasonable agreement of the two methods does still support the reliability of the fast RPA structure model in studies with many nuclei.

2.3 Nuclear Decay Model

The structure model describes how the weak interaction processes excite the nucleus and change its charge. The neutrinos we are bombarding the nuclei with have average energies of more than 10 MeV and the β -decays that we will consider take place in nuclei with large neutron excess and therefore large Q-values. The states that we are exciting are therefore most often situated above particle thresholds, or even above the fission barrier in the daughter nucleus. The subsequent decay will thus have enhanced probability of particle emission or of breaking into fragments by fission. We need a model that can describe such processes.

The nuclear decay model we will employ starts from the so-called compound nucleus picture. Here it is assumed that the nucleus reaches statistical equilibrium before it decays. More precisely this means that the excitation energy is shared among all nuclear states that have the right quantum numbers (energy, angular momentum, parity etc.) with equal probability. The process of equilibration is assumed to take place independently of how the compound state was formed (this is often called the Bohr independence hypothesis). This allows us to simply multiply our cross sections or rates from the structure model by the branching ratios of different decay channels to obtain the final result. The cross section for a nuclear reaction that enters through channel α and decays through channel β is thus given by

$$\sigma_{\alpha,\beta} = \sigma_{CN}(\alpha) \frac{\Gamma_{\beta}}{\Gamma_{tot}}, \quad (2.71)$$

where $\sigma_{CN}(\alpha)$ is the cross section for the formation of the compound nuclear state α , Γ_{β} is the decay width through channel β and Γ_{tot} is the total decay width of all allowed channels (for β -decay one merely changes cross sections to rates). The ratio $\Gamma_{\beta}/\Gamma_{tot}$ is therefore a channel probability and it is the quantity that we need to calculate within our statistical decay model.

At energies slightly above particle thresholds the cross section as a function of energy tends to be dominated by individual resonances that are usually described by Breit-Wigner theory [57]. However, as the energy goes up there are more and more states available¹¹ in the nucleus and therefore the resonances start to overlap. The peaks start to merge and become broad features instead, in analogue to what happens if one varies the energy resolution of a cross section measurement. In this situation one may use either the Weisskopf-Ewing theory or the more advanced Hauser-Feshbach theory. They are both built on the principle of detailed balance which relates processes to their inverse. The key to a successful model of this sort is a good description of the nuclear density of states, the binding energies, and the barriers.

¹¹To a good approximation, the nuclear density of states scales as $\exp(\sqrt{E})$ at higher energies and the number of states therefore grows tremendously with energy [33].

2.3.1 Particle Decay Rates and Fission

We will be using the Weisskopf-Ewing theory [58] for the decay rates. This approach does not take angular momentum changes into account. This is done in the more advanced Hauser-Feshbach theory. However, we will be concerned with r -process relevant nuclei that are very neutron-rich so that essentially only neutron emission and fission contribute, and at low angular momenta these particular decay modes have little dependence on angular momentum. Since the neutrino and β -decay reactions populate states with low J , we will simply ignore the dependence on J and use the Weisskopf-Ewing theory henceforth. The expression for the decay width of a particle evaporation channel a is given by

$$\Gamma_a(E_i) = \frac{2J_a + 1}{\rho_p(E_i)} \frac{m_a}{\pi^2 \hbar^2} \int_0^{E_i - S_a} \sigma_a(\varepsilon_a) \rho_d(E_f) (\varepsilon_a - B_a) dE_f, \quad (2.72)$$

where ρ_p and ρ_d are the density of states in the parent and daughter nucleus respectively and σ_a is the cross section for the inverse process. The initial energy, E_i , is the compound nucleus excitation energy, S_a is the binding energy of the evaporated particle, and B_a is the barrier in case of charged particle evaporation. The integration variable E_f is related to the emitted particle energy, ε_a , through $\varepsilon_a = E_i - S_a - E_f$.

As it stands, this formula contains complicated quantities and we need to introduce some sensible approximations to make it tractable for calculations in many different nuclei. To reduce the integral in the width to a simpler form we will use the expression given in [59]. The width formula then becomes

$$\Gamma_a(E_i) = \frac{2J_a + 1}{\rho_p(E_i)} \frac{2m_a R^2}{\pi \hbar^2} T_d^2 \rho_d(E_i - S_a - B_a), \quad (2.73)$$

where T_d is the nuclear temperature in the daughter, defined as the inverse logarithmic derivative of the density of states with respect to energy at the maximum excitation energy in the daughter. R is the nuclear radius, coming from the inverse cross section which is approximated by the geometrical one (using the simple radius formula $R = 1.4A^{1/3}$ fm). To obtain the width from this expression we need a solid handle on the density of states in parent and daughter. We will discuss our choice of this quantity below.

In our r -process considerations we will be particularly concerned with fission. We therefore need a model where this channel is taken into account. The fission decay width will be handled by the transition-state method of Bohr and Wheeler [60]. Using an approximation similar to the one of the previous section we get [59]

$$\Gamma_{fis}^{BW}(E_i) = \frac{T_f}{2\pi \rho_p(E_i)} \rho_d(E_i - B_f), \quad (2.74)$$

where T_f is the nuclear temperature in the fissioning parent and B_f is the fission barrier. The barrier is a central quantity and we will discuss it in detail below. In low energy fission there are some known corrections to this formula. These can be included by multiplication of an enhancement factor that we get from [61].

Here we should make a cautionary statement. The transition-state model as given above does not describe the full dynamics of the fission process. In fact, the actual mechanism behind the fragmentation of the nucleus is surely in the dynamical exchange of energy between excitation degrees of freedom and those of deformation, eventually leading to break-up because of large distortions in the nuclear shape. The process is one of dissipation of energy between different degrees of freedom. Such problems are notoriously difficult but good progress was made in [62] where new analytic approximations were given for the time-dependence of the fission width that the dissipation causes. However, at low energies the effects are very small and the pure transition-state model works very well. For this reason we will use the expression in eq. (2.74) in all our calculations.

Nuclear Binding Energies

The nuclear binding energy is used in virtually all quantities that enter our width calculations. It is therefore pivotal to have a consistent nuclear mass compilation. There are quite a few of these on the market, some of which are actual tables and some that give analytical formulas from fits. Most of our calculation will be performed using the finite range liquid-drop (FRDM) model of Möller and Nix [63]. They include corrections for pairing and shells, so that all derived quantities will in principle have these features built in (see however the discussion of fission barriers below). However, to test the uncertainties of our predictions we have also done calculations with masses coming from the Thomas-Fermi model of Myers and Swiatecki [64] that uses the ground-state shell corrections and pairing energies from [65]. We will leave the discussion of the particulars of each table and specifically their differences until we encounter them when we present our r -process results in chapter (6).

Nuclear Density of States

As mentioned above the nuclear density of states is very important for the determination of decay widths. We will be using the following general expression

$$\rho(E) = K \frac{1}{a^{1/4} E^{5/4}} \exp\left(2\sqrt{aE}\right), \quad (2.75)$$

where K is a numerical constant and a is the so-called level density parameter. In general ρ will also depend on angular momentum and parity, but

in the Weisskopf-Ewing model we neglect this. The level density parameter is known to depend on both nuclear deformation and energy. To incorporate these effects we use the description of Ignatyuk *et al.* [66, 67]. This is based on phenomenology and fits to known experimental data and have been proven very robust [68]. We also employ a phenomenological collective enhancement factor that multiplies the state density [69]. In deformed nuclei this factor arises because of rotational bands, whereas for spherical nuclei it is the vibrational states that enhance the density. The theoretical derivation of such an enhancement factor was given in [70].

Fission Barriers

The question of fission barriers has always been a complicated one. Measurements are difficult and have only been performed in a limit number of nuclei, all of which lie close to the line of β -stability. Calculations involving nuclei that are far off this line, as is required for r -process applications, have to rely on semi-empirical or purely theoretical estimates of the barriers. This modeling is, however, also very complicated as it consists of determining the minima of nuclear potential energy surfaces which are multidimensional. As a result, two different barrier compilations can often differ by significant amounts. Realizing this difficulty, we will work with three different choices for the barriers as an attempt to estimate these uncertainties.

The first one is that of Sierk [71]. It is based on an early version of the FRDM model of Möller and Nix and has the advantage that it allows a good analytical fit. These barriers will be used in conjunction with Möller and Nix ground-state shell corrections from [65]. The second compilation is the Thomas-Fermi calculations of Myers and Swiatecki [64] that also use the ground-state shell corrections from [65]. The third choice is the recent Extended Thomas-Fermi Strutinsky Integral (ETFSI) method barriers of Mamdouh *et al.* [72]. This last calculation predicts barriers that rise very steeply at the magic neutron shell around $N = 184$ which is an important concern in r -process studies, particularly related to the question of the maximum mass reached in the process. The ETFSI barriers are several MeV above the two other compilations in most heavy neutron-rich isotopes so they could drastically change the endpoint. However, a recent study of the consistency of different mass compilations have cast some doubt on the ETFSI numbers. In [73] the experimental saddle-point masses ¹² and fission barriers were compared to the predictions of several compilations. This work

¹²The saddle-point is the boundary point of the nuclear potential where the meta-stable ground-state region is separated from the unstable fission region in deformation space. Beyond this point the system will gain energy by splitting into two (or more) fragments. This is merely an easily visualizable 1D definition. In real multi-dimensional potential landscapes matters are more complicated. However, the basic picture of the saddle-point as a boundary of different regions of stability remains.

showed that there are some inconsistencies in the ETFSI predictions, and also in the Howard and Möller barriers [74] that were used in a number of previous studies of the influence of fission on r -process nucleosynthesis. The barriers of Sierk, and Myers and Swiatecki did not have these inconsistencies.

2.3.2 Fission Fragments

In the fission process one is of course also interested in the mass and charge of the fragments. The theoretical modeling of this issue is another very complicated consideration of potential energy surfaces and phase space flows. The experimental information is rather sparse and detailed theoretical models that try to reproduce the fragment yields are often only applicable in a small region of the nuclear chart. The computational efforts involved in such theoretical descriptions also limit their use. To get a decent handle on the fragments of many different nuclei it therefore seems reasonable to try a semi-empirical approach. The goals would be to incorporate as much basic physics of the process as needed and to fit the remaining parameters to the available experimental data.

In figure 2.3 we show experimental information on low energy fission distributions for selected nuclei. As is seen in the insets on the figure, there can be subtle changes in the structure of the fragment distributions. In particular, one sees changes in structure from single- to double- and triple-hump as the mass is increased. Even more intricate is the fact that the actinides have smooth changes across isotopic chains, whereas the heavier Fermium isotopes show abrupt changes from double- to single-hump distribution. Any semi-empirical model that attempts to describe a large number of fissioning system has to take these effects into account.

A very successful implementation of such an approach is that of Benlliure *et al.* [77]. It applies the statistical model to the concept of fission channels. The fragments are determined by the density of states above the potential energy surface near the outer saddle-point. This density of states includes the same pairing, shell and collective effects that were mentioned earlier. The model assumes that the potential at the saddle-point can be written in terms of neutron number only. Effects of charge polarization in the fragments are taken into account later at the scission point.¹³ The excitation energy of the fragments is also calculated at scission, based on the deformation energy and excitation of the fissioning compound nucleus.

¹³Naively one would perhaps just assume that the charge distribution would follow that of the neutrons according to the simple rule $Z_{frag} = N_{frag} \frac{Z_{parent}}{N_{parent}}$. However, deviations from this expectation are well-known from experiment. This is known as charge polarization. Assuming that this degree of freedom equilibrates much faster than the saddle-to-scission time (scission being the point where the two fragments split) it is determined at the scission point. The actual implementation uses a combination of experimental information and theoretical considerations (see [76] and references therein for details).

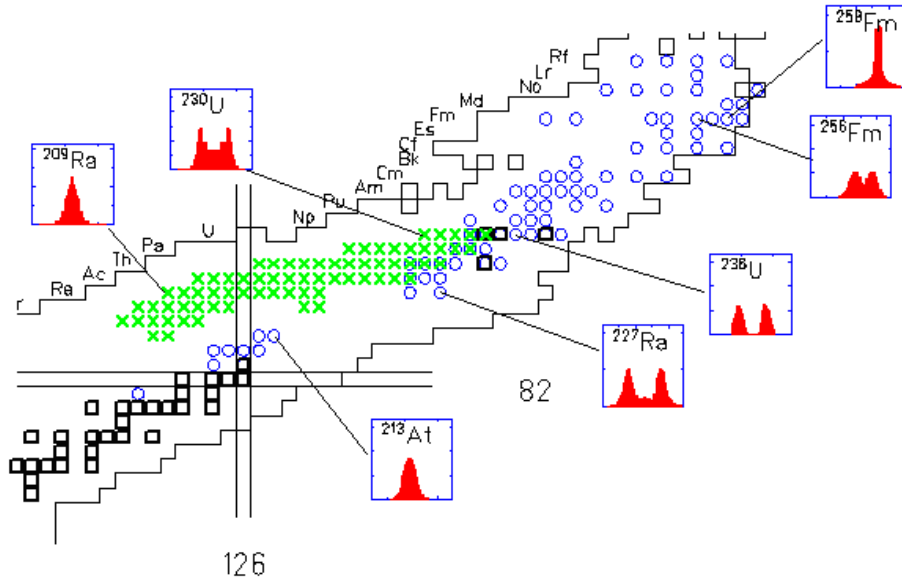


Figure 2.3: Available experimental data on mass and charge distribution of low-energy fission fragments. Green crosses indicate that charge distributions have been measured in electro-magnetic induced fission, whereas blue circles are nuclei where mass distributions have been measured in particle-induced fission (more details can be found in [75]). The small insets show measured mass or charge distributions for some interesting cases.

The nuclear potential at the saddle-point is chosen so as to reproduce known experimental features. It consists of a mass symmetric part, which is basically just a parabola (symmetric about $(N_{\text{compound}} - N_{\text{emitted}})/2$, where N_{emitted} is the number of particles emitted before fission). The known mass asymmetries in the fragments distributions at $N = 82$ and $N \approx 88$ (a magic number at non-zero deformation) are taken into account by introducing correction terms that lower the potential at these points to favor such fragments. The model thus incorporates three components in the determination of the fragments. As we are concerned with fission in very neutron-rich nuclear material, the inclusion of neutron shells is an essential feature.

In general, one would of course expect the symmetric component to become more pronounced as the excitation energy is raised, and pairing and shell effects are washed out. However, as the compound nucleus is created by weak processes with strengths that peak at rather low energies (below 20 MeV) it is essential to consider low-energy features in the fragment yields. R -process fission studies conducted in the past have almost exclusively assumed a symmetric fragment distribution. However, as we will show, this prescription is most likely too simplistic for progenitor nuclei on the r -process path

and for the nuclei that decay back toward stability after the r -process freezes out.

2.3.3 The Dynamical Code ABLA

In the previous sections we have described how we will calculate the decay width and, in the case of fission, how the fragment distribution is determined. To get a probability distribution for the different decay channels we will be using a dynamical code called ABLA [78, 77]. It is based on the Monte Carlo principle wherein a random number is used to determine the outcome of the compound nuclear decay. More concretely, a probability distribution is constructed based on the widths of all available channels and then a random number is used to determine which channel the nucleus decays into. This of course means that one needs thousands of runs for each nucleus and at all relevant excitation energies. The parameters that go into the model have to be easy to compute to maximize the runtime speed. This criterion is met by all quantities described above. Of course a Monte Carlo approach also provides motivation for using the simplest semi-empirical parametrization that incorporate the essential physics we want to describe.

One great feature of the ABLA code is that it follows the compound decay all the way to the ground state. This means that the daughter of any decay will again be subject to further decays at the relevant excitation energy (given by energy conservation between parent, daughter, and emitted particles or fragments). When fission is the outcome the code will even consider particles that are evaporated from the fragments. This turns out to be very important for neutron-rich nuclei as we will see later. The decay chain is eventually stopped when the available excitation energy goes below all particle thresholds. By running this process many times over we thus get probabilities for emission of particles, and for pre- and post-fission emission of particles.

The fragment distribution are determined by a subroutine called PROFI that runs a separate Monte Carlo evaluation. Whenever a fission event is the outcome of the main routine, PROFI will give two fragments sampled from the yields distribution described above. These fragments are then fed back to the main ABLA routine and allowed to individually decay to their ground state, possibly through further particle evaporations. In figure 2.4 we show a comparison of ABLA calculations and experimental data for fragment charge distributions in actinide nuclei. As can be seen the overall agreement is very good in the observed region.

At our hands we have a robust code that has been thoroughly tested against experimental data on heavy nuclei and which incorporates essential features that are expected to matter in neutron-rich nuclear material. It provides us with fission and particle emission probabilities and also fragment distributions. We therefore have confidence that ABLA can provide us with

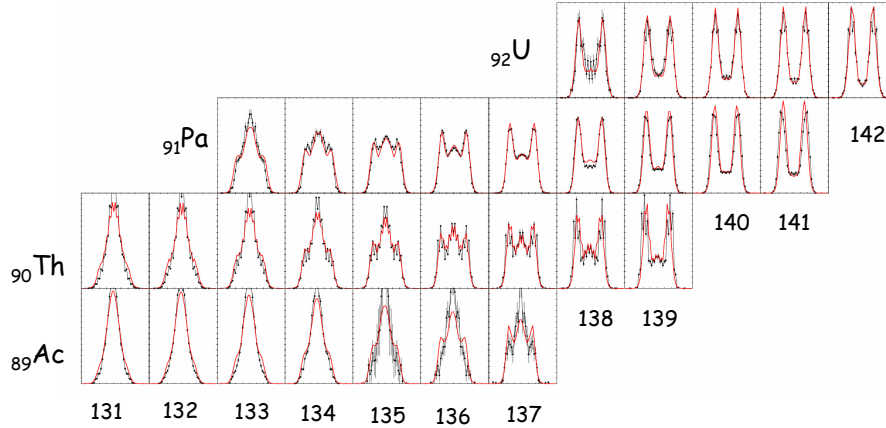


Figure 2.4: Comparison of measurements (black dots) and ABLA calculations (red line) of charge distributions in fission fragments from electromagnetically induced fission on several actinide nuclei in the range ^{220}Ac to ^{234}U shown on a nuclear chart. The distributions are all in the range $Z = 24$ to $Z = 65$. Experimental data from [75].

valuable information for use in r -process modeling.

2.4 Unified Nuclear Model

We have now described the nuclear structure and the statistical decay model to be used. Many essential features of how these two models are combined have already been introduced in earlier sections. In this section we will recap the combination for clarity and also comment on various concerns this procedure introduces.

In figure 2.5 we present the schematics of the model. The first step is modeling the nuclear structure of the initial nucleus that is subjected to (anti)neutrino capture or β -decay. For this we need a good handle on the resonances in the 10-20 MeV region in the daughter and also a reasonable description of low-lying states. For this we have chosen the RPA method as previously described. This method grants us a distribution of cross sections or rates for population of the excited states in the daughter nucleus as

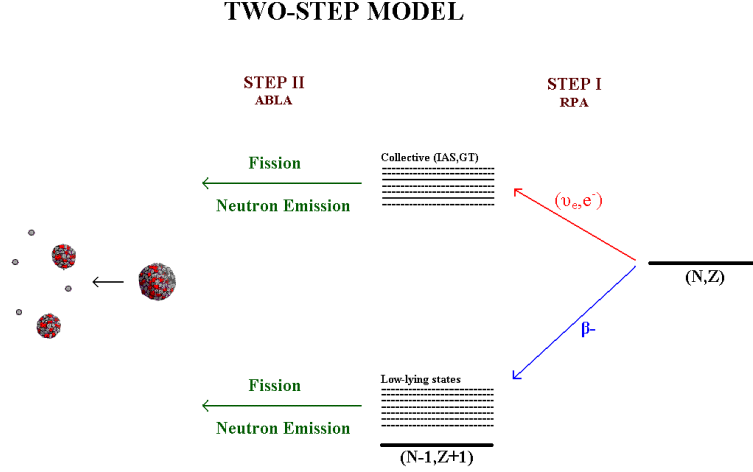


Figure 2.5: Schematic picture of the two-step model of weak interaction excitation followed by statistical decay through fission or particle evaporation.

indicate on figure 2.5. The decay of these daughter states is then governed by a statistical decay model, ABLA, as discussed in the last section.

Since we have assumed independence of the two steps, we can now easily get the total rates or cross sections for different channels by multiplying the outcomes of the two methods. To give an example of this procedure, consider a decay channel a (we will mainly be concerned with neutron emission and fission) that we wish to know the total cross section or rate for. This is given by the expression

$$\sigma_a(E_\nu) = \sum_i p_a(E_i) \cdot \sigma_i(E_\nu), \quad (2.76)$$

where E_i is the excitation energy of the i 'th nuclear state, p_a is the (energy dependent) decay probability into channel a , and σ_i is the cross section for excitation of the i 'th daughter state. E_ν is the initial neutrino or antineutrino energy. The formula for β -decay is similar

$$\lambda_a = \sum_i p_a(E_i) \cdot \lambda(E_i) \quad (2.77)$$

with the E_i ranging from zero to the Q-value for the particular nucleus.

The ABLA model allows the decaying nuclei to emit particles both before and after a fission event. In principle we therefore have very detailed

information about the fission decay channel. However, since this all takes place on the strong interaction timescale there is no point in keeping track of the emissions relative to the moment of fission. We therefore simply sum these emissions and sum the total number of particles emitted when a nucleus undergoes fission.

One of our main concerns is r -process nucleosynthesis, particularly the end-point of this process and the influence of fission. The nuclei that we will be considering are therefore mostly heavy and neutron-rich. Therefore our main decay channels are neutron emission (due to low separation energies) and fission for nuclei with high charge (which often have low fission barriers).

As mentioned in the section on ABLA, the code provides us with distributions for the fragments from fissioning nuclei. These distributions are constructed by taking all fission events, binning the fragment masses and charges, and then dividing by the total number of runs for the given nuclei. The yield is simply

$$Y_1(A_1, Z_1) = \frac{N(A_1, Z_1)}{N_{tot}}, \quad (2.78)$$

where $N(A_1, Z_1)$ is the number of fragments of mass A_1 and charge Z_1 and N_{tot} is the total number of Monte Carlo runs. To get the distribution for mass or charge alone one simply uses standard probability theory and sums over the superfluous variable. Generally, the yields depend on energy and this can be explicitly seen when we compare neutrino-induced processes at different energies in chapter (5).

2.4.1 Energy Mesh

At this point we need to address a technical issue concerning the calculation of decay probabilities using the statistical model. Since it takes the excitation energy of the compound nucleus as input, we have to think about the energies at which we employ this model. Obviously we would ideally take all states and their corresponding energies given to us by the nuclear excitation structure model and run the decay model with these data. However, since these spectra typically contain hundreds of states scattered below about 60-70 MeV with only little prior knowledge about their distribution and strength, this approach would be extremely time-consuming. It is thus clear that a binning of energies must be used in order to achieve our goal of calculating many nuclei in a reasonable time frame.

In the present work we have employed the simplest possibility available; the equally spaced energy mesh. This entails calculating the decay probabilities for each nucleus on a 1 MeV mesh up to the highest energy nuclear state. The potential trouble with this choice is concerned with situations where a particular channel is opening up. At such a point the probability changes rather rapidly and the equal mesh can become inadequate. In particular, if one uses a model where analytic formulas and experimental

information on the nuclear levels is combined (like the SMOKER code [79]) then one would have to be more careful with the energy mesh. However, the ABLA code uses analytic formulae and theoretical mass tables so this should be less of a concern. The 1 MeV mesh size was chosen based on tests performed in selected nuclei demonstrating that a decrease in the mesh size did not change the results noticeably.

The nuclear structure model also gives the angular momentum and parity of the excited states in the daughter, as was discussed in earlier sections. This can be incorporated in statistical models through a method like Hauser-Feshbach (used in the SMOKER code [79]). As mentioned, the ABLA code employs the simpler Weisskopf-Ewing theory, which does not take these quantum numbers into account. However, the fission barriers used in ABLA are still angular momentum dependent, so we have kept the angular momentum information in the combination process. The reactions we consider in this thesis typically induce excitations with angular momenta $J \leq 4$. This turns out to be very low on the scale of changes in the J -dependent barriers and letting all state be $J = 0$ turned out to have virtually no effect on the final results. However, the implementation was made J -dependent from the very beginning and since it did not prolong the calculations noticeably it was kept in the code. With respect to parity we simply summed over both values for each J and ignored it in the statistical model. Initial investigation into the changes occurring when parity is taken into account have recently been reported in [80].

2.4.2 Monte Carlo and Statistics

As we have previously discussed, the ABLA code uses Monte Carlo techniques to calculate the decay probabilities. Naturally this means that there is an intrinsic theoretical uncertainty in the calculation. Ideally one has to make sure that the decay probabilities are converged by varying the number of runs for each nuclei, excitation energy etc. Of course this is unfeasible for the present calculations of thousand of nuclei, so an efficient binning is again called for.

Initially we have checked the convergence for selected nuclei and excitation energies. The general picture that emerged suggested that little was gained in a change from 10000 to 100000 runs. However, below 10000 there was some fluctuations in the results. Running the codes with 10000 Monte Carlo runs for each bin and each nuclei would then seem ideal. Unfortunately, a quick estimate showed that this would simply take too long. At this point we can use the fact that our daughter excitation spectrum represent a distribution. To optimize statistics we thus take into account the percentage of the cross section or the rate that resides in each energy bin. Making the number of Monte Carlo runs energy dependent in this fashion ensures that the important giant resonance states have the best statistics.

This seems to be the best approach available when one does not have much prior information on the spectral distribution in the decaying nucleus.

2.4.3 Neutrino Spectra and Folding

The formula for the partial cross sections for different decay channels given above depends on the energy of the incoming neutrino or antineutrino. In the stellar environment that we are concerned with in this thesis these particles have certain distributions in energy. Our results are generally functions of the neutrino energy and ideally one would like to include the full energy dependent cross sections into stellar models. However, for simplicity we will mostly present total cross sections that are folded with an appropriate neutrino energy distribution to be discussed below.

The theoretical and experimental situation concerning the details of these distribution is incredibly rich. This is due to the fact that Supernovae release such an immense amount of energy in the form of neutrinos. The inferences from these spectra therefore hold great promise to reveal details about the nature of this stellar event. Since photons cannot escape the inner parts of this site, neutrinos are actually our only way to obtain this information. In the light of this, it is not surprising that many researchers work on the imprints of various mechanisms on these spectra and that part of the argument for constructing large neutrino detectors is the prospect of a galactic Supernova in the near future (estimates show that there should be a little over one event per century). We will not attempt to survey this vast field, but merely state the details needed for our scenario, commenting on some recent investigations into neutrino oscillations that could have a direct influence on some of the nucleosynthesis results.

We will be working under the assumption that the neutrino spectrum can be accurately described by a standard Fermi-Dirac energy distribution

$$f(E, T, \mu) = N \left[1 + \exp \left(\frac{E - \mu}{T} \right) \right]^{-1}, \quad (2.79)$$

where E is the neutrino energy, T is the temperature, and μ the chemical potential of the neutrino species in question. N is a normalization factor that we determine below. When addressing the neutrino spectra we will always use units where all these quantities are measured in MeV. In order to get the total cross section for a channel a we must fold the energy-dependent quantities of eq. (2.76) with this distribution. This yields

$$\sigma_a^{tot}(T, \mu) = \int_0^\infty \sigma(E_\nu)_a f(E_\nu, T, \mu) E^2 dE. \quad (2.80)$$

To get the total cross section over all channels we simply sum these partial cross sections over all a . The upper limit on the neutrino energy is taken

to be infinity. This is a good approximation since $f(E_\nu, T, \mu)$ falls off much faster than $\sigma(E_\nu)$ with energy. However, in actual calculations we need some reasonable cut-off on the integral. As we typically have very little strength in excited states with energies above about 50 MeV we have used a cut-off value of 60 MeV on the neutrino energy, using an equally spaced 1 MeV mesh in all nuclei.¹⁴ To test this choice we have tried going to 100 MeV and found practically no changes in the results.

The fragment distributions also need to take the Fermi-Dirac profile into account when considering neutrino-induced fission events. As mentioned, the fragment yields are energy dependent so we also have to fold these with the neutrino distribution. To get the mass or charge distributions we simply sum the distributions at each neutrino energy, weight by the Fermi-Dirac factor and then renormalize. The procedure for fission events induced by β -decays is very similar, only with weighting given by the energy-dependent partial rate contributions.

The core-collapse Supernova event is perhaps the only place in the Universe where it actually matters that neutrinos are fundamentally fermions. Due to the excessive densities and subsequent neutrino trapping before bounce, they become degenerate in the inner core and have non-zero chemical potential. However, after bounce they diffuse out and are essentially free streaming from beyond a radius known as the neutrino sphere. Simulations show that the expected spectra are not quite Fermi-Dirac but of a more narrow shape [81, 82]. Having the detailed energy-dependent cross sections would of course principally enable simulation groups to take the exact spectra into account in simulations of neutrino-induced composition changes. Such an approach is extremely computationally intensive and only very recently have some groups started to incorporate these. In many cases the stellar evolution model that gives the neutrino spectra are run independently of the codes that calculate the subsequent neutrino reactions on the outer layers of the collapsing star. However, quite accurate fits to the spectra from detailed evolution codes still display an approximate Fermi-Dirac shape with some effective average neutrino energy. We will therefore work under this assumption throughout.

The above observations have led many subsequent studies to give the average energy for the various neutrino species in terms of the thermal Fermi-Dirac distribution. The average energy of a Fermi-Dirac distributed neutrino is easily connected to the temperature parameter T , which is the variable usually given in nucleosynthesis studies where neutrinos are relevant. We remark that zero chemical potential is most often quite accurate for the spectra and we will assume this from now on.¹⁵ To get the relation between

¹⁴This is of course a combined effect of transition matrix elements and phase space. The latter grows quadratically with neutrino energy. The exponential fall-off of the Fermi-Dirac is, however, strong enough to suppress this effect.

¹⁵Simulations of neutrino transport often show that the high-energy tail of the distri-

$\langle E \rangle$ and T , we first need to normalize f . Integrating over all energies with a phase space factor of $E^2 dE$ (since the neutrinos we consider here are ultra relativistic) gives

$$\int_0^\infty f(E, T) E^2 dE = T^3 \int_0^\infty \frac{x^2}{1 + \exp(x)} dx. \quad (2.81)$$

The integral cannot be done analytically, but numerical integration gives 1.803. The normalization factor for the distributions is thus $0.5546/T^3$. To get the average energy we must calculate

$$\langle E \rangle = \int_0^\infty f(E, T) E^3 dE = \frac{0.5546}{T^3} \int_0^\infty \frac{x^3}{1 + \exp(x)} dx. \quad (2.82)$$

This integral is also found when calculating the energy of a photon gas and has the analytical value $7\pi^4/120$. Upon insertion one gets

$$\langle E \rangle = 3.15 T. \quad (2.83)$$

We thus see that a factor magically close to π connects energy and temperature. This relation allows us to talk about the neutrino temperature and the average neutrino energy interchangeably.

When addressing the energy or temperature of the out-going neutrinos we have to be very specific about which species we are talking about. The typical temperature of electron neutrinos and antineutrinos are generally not the same. This feature originates from the fact that the place of last interaction (the neutrino sphere) is located at a different radius for the two kinds. Since the material in the proton-neutron star is neutron-rich, there will be more ν_e on neutron reactions than $\bar{\nu}_e$ on proton. The antineutrinos will thus decouple at a smaller radius than the neutrinos. Smaller radius means higher matter temperature and the antineutrinos will therefore have a higher average energy when they stream out. For the μ and τ species the argument is similar, except that these only have neutral current interactions (the charged current cannot contribute due to the large masses of the 2nd and 3rd family leptons). The cross section is generally about 1/6 smaller for neutral current and we thus have decoupling at an even smaller radius than the electron neutrino species.

The typical value for the temperatures of the different species have varied over the years. There has been a tendency for the temperatures to go down slightly as the simulation models become more advanced. Also the energy splitting of different species have become smaller. Some recent values from comparisons of different supernova models [83, 84] are

$$T_{\nu_\mu} \sim T_{\bar{\nu}_\mu} \sim T_{\nu_\tau} \sim T_{\bar{\nu}_\tau} \sim 8 \text{ MeV} \quad (2.84)$$

$$T_{\bar{\nu}_e} \sim 4.5 \text{ MeV} \quad (2.85)$$

$$T_{\nu_e} \sim 3.5 \text{ MeV}. \quad (2.86)$$

bution is weaker than a $\mu = 0$ Fermi-Dirac distribution. This can be effectively taken into account by using non-zero chemical potentials.

The hierarchy discussed above is apparent.¹⁶ The energies given here are for those neutrinos that emerge from the cooling phase of the protoneutron star as it equilibrates by releasing excess energy. This process lasts for a period of about 10-20 seconds, during which each species has about equal luminosities. This is not so for earlier stages of the collapse. In particular, around the time of core bounce and shock formation where fluctuations in both luminosity and average energy are seen. This will be of some concern to us when we discuss the inner-most ejecta but we will postpone the details until then.

In our studies of r -process nucleosynthesis, we can safely work with the numbers quoted above as this process takes place some seconds after bounce. The r -process is of course connected to an environment with many free neutrons and neutron-rich nuclei. We therefore only need to take electron neutrinos into account. We will almost exclusively work with one fixed temperature of $T = 4$ MeV, a value that is widely used in previous literature (see for instance [82]). The average energy for this neutrino temperature is about 12 MeV. This is a rather high energy in nuclear excitation terms and we thus expect to populate the giant resonances discussed in previous sections even for low Q -values. For heavy, neutron-rich nuclei these states are located at somewhat higher energies of 15 MeV and above, but the considerable tail of the Fermi-Dirac distribution and high Q -values still allow population. So we are well within a window of energy where potentially interesting effects of neutrino capture on nuclei can occur.

2.4.4 Anisotropy and Exotica

In this section we will briefly address some of the current topics of great interest in Supernova neutrino research. Earlier we have discussed the failure of realistic 1D models to produce consistent Supernova explosions. The progress in 2D and 3D simulation codes has now shown that a likely factor in getting successful explosions is convective features that are not present in the spherically symmetric models (see section (1.3)). Such convection would overturn the layers in the star and results in more efficient neutrino energy transport. Furthermore, the higher-dimensional models show generic anisotropies in the dynamics. These effects help explode the star, but they could also be influential in r -process nucleosynthesis in the hot wind above the protoneutron star.

The increased energy transport and deposition brought on by convection would mean shorter dynamical timescales for the r -process and also help get the large entropies that are needed to get a high neutron-to-seed ratio. This can be modeled in an effective way by increasing the neutrino luminosities

¹⁶A recent study by Keil *et al.* [85] finds the values 5.5 MeV, 5 MeV, and 4 MeV (with respect to the order of neutrino species introduced above), indicating that the hierarchy is perhaps less pronounced.

by some factor. One such study was reported in [86] where it was shown to yield consistent r -process nucleosynthesis of the third peak at $A \sim 195$. The need for multi-D simulations with full transport is once again underlined. These issues should thus be kept in mind later when we explore timescale and entropy dependencies of our r -process nucleosynthesis calculations in more detail.

Recently the question of neutrino oscillations was finally settled. The initial findings by John Bahcall and Raymond Davis in their ground-breaking Homestake experiment have been confirmed: Neutrinos undergo flavor oscillations as they propagate through spacetime. The modern large-scale experiments have now given us very detailed information on these oscillations in terms of the mixing angles and the mass squared differences of the various species. It is thus not surprising that several studies have looked at how these facts could influence neutrinos in core-collapse Supernovae.

The effect that some people have looked at is the oscillation of the μ and τ species into electron neutrino and antineutrinos. The larger average energies would then be transferred to a species that can interact with the surrounding material. This energy boost would enhance cross sections and lead to a stronger energy deposition, possibly helping the explosion of the star. One early study did find a positive effect on the explosion from this scenario [87]. The underlying supernova model used in that work is, however, controversial in that it produces explosion in 1D that cannot be reproduced by other studies. The key fact was to have the characteristic length of oscillation smaller than the gain radius (beyond which neutrinos do not heat the material). Other studies showed that this length was bigger than the gain radius, providing no help. The parameters needed for the mechanism to work are now known to be inconsistent with experimental bounds on neutrino properties.

Other studies consider the so-called Mikheyev-Smirnov-Wolfenstein effect for resonant oscillations. This effect occurs due to the interaction with the density of electrons in the stellar environment. Some of the first studies showed the effect occurring in Supernova [88]. These parameters were also found to be at odds with experimental bounds.

More recently there has been a number of investigations into the effects of neutrino flavor conversion on nucleosynthesis. The light-element synthesis that takes place in the outer shells of the star could possibly reside at radii of roughly the oscillation length and be influenced. Such a study was carried out in [89] where possible ways to constrain neutrino properties by measuring light-element abundance ratios was suggested.

For the r -process there could also be an effect if neutrino conversion takes place. In particular, the effect of so-called active-sterile neutrino oscillations have been considered. This is connected to the desire of some particle physics models to add heavy and very weakly interacting neutrino species (called sterile) to the Standard Model in order to address certain un-

natural quantities, like the apparent smallness of observed neutrino masses. However, for Supernova applications one needs the sterile neutrinos to be light, something which the LSND experiment suggests could exist.¹⁷ Using these light steriles, a consistent r -process nucleosynthesis in the neutrino wind above the protoneutron star was found in a large portion of parameter space [90, 91].

The possible influence of neutrino conversion through various oscillation scenarios discussed above is something that we will comment on later in calculations of r -process relevant nuclei. The higher neutrino temperatures that would be a result of these mechanisms will of course enhance the cross sections due to simple phase space considerations. We do not expect the probabilities for neutron emission and fission to change drastically, but there could be an effect from the fact that fission fragment distributions are energy-dependent. The larger average neutrino energies could therefore have an influence on the redistribution of material when fission becomes important for the heaviest nuclei at the r -process end-point.

¹⁷There is considerable controversy surrounding this experiment as it seems to get different results from all other experiments that can obtain the same quantities. The follow-up experiment at Fermilab called MiniBooNE is therefore closely watched and have published their first results just recently [92]. The initial conclusion goes against the LSND results and supports the three light active neutrino species solution.

Chapter 3

Muon Capture

3.1 Introduction

We have already mentioned muon capture as a reaction suited for testing nuclear structure models. As discussed above, the main reasons are the relatively large amount of energy available for daughter excitation and the large body of experimental data across the nuclear chart. The study of this semi-leptonic process has a long history and some excellent review articles exist by now. Early classics are Mukhopadhyay [94] and Walecka [18], whereas a recent comprehensive review with many experimental details is that of Measday [93].

In typical muon capture experiments on not too light nuclei one produces a beam of muons and stop them in a target of the nuclei one would like to measure the capture rate on. This requires a trigger telling you when a muon is incident on the target and another trigger to tell you that it was actually stopped. The former task one can handle with a suitable scintillator. The stop process is indicated by the emission of gamma rays when the muon cascades down from its initial capture orbit, which has a high Bohr number, to the ground state $1s$ atomic orbital. This process is electromagnetic and therefore very fast compared to the nuclear capture governed by the weak interaction. When a stopped muon is detected, one then starts a timer and waits for some characteristic signal in the spectrum of the daughter nucleus. In practice, one looks for a gamma ray coming from deexcitation which will also occur on a short timescale compared to the capture process. The trick is therefore to prepare a good target from the relevant nucleus and to have a good knowledge of the daughter nucleus spectrum for tagging the capture process. The experimental techniques for measuring the capture rate have been greatly refined over the years and we now have accuracy of a few percent in most stable nuclei, excellent data for comparison to theoretical models.

Through the years, there has been a number of theoretical investigations

devoted to global methods for calculating muon capture rates. Papers using a self-consistent Hartree-Fock random phase approximation scheme similar to the present work have been around for a number of years [95, 96]. Those studies found good agreement with experiment, however, only for a limited selection of nuclei. Capture rates for a broad range of nuclei were also given in [97]. That study was focused on radiative corrections to the process and the total capture rates were a by-product which overestimated the experimental data. There are also a number of investigations using the simple local Fermi gas model [98, 99, 100], where good agreement with measurements for a selection of light, medium and heavy nuclei was found.

To our knowledge, there was not a fully comprehensive calculation of the capture rates in existence that covered the entire nuclear chart. The goal was therefore to perform such a global evaluation of the total capture rates. This would constitute a test of our understanding of the nuclear response in the energy window favored by the process. As we have already pointed out earlier, the capture is dominated by giant resonances at energies up to about 30 MeV. More generally, it provides a test of our ability to treat semi-leptonic weak charged-current reactions at momentum transfer q of order the muon mass $m_\mu = 105.6$ MeV. Having a good handle on the muon process would give us the needed confidence to proceed with neutrino-nucleus reactions at similar energetics and momentum transfers, an area where very little experimental information is presently available.

3.1.1 Previous Studies

Before we venture into the results obtained during the thesis work we will briefly discuss the status of our particular model for use in muon capture as of 2003. The work reported here extends the investigations by Kolbe *et al.* [101, 35]. The first of these papers was concerned with the capture rate in ^{12}C , ^{16}O and ^{40}Ca . Here the continuum RPA was used, an extension over the simple RPA described earlier that takes continuum states into account. Some adjustment to the residual interaction was needed to get agreement with other observables in carbon and oxygen, but the final results compared well with data. Capture rates on a selection of heavier nuclei were considered in the second paper [35]. Apart from an overestimation of the rate in ^{208}Pb , good agreement was again found. This latter paper also showed that one gets almost identical results when using the standard RPA (SRPA) over the computationally expensive continuum version. We thus use the former in all calculations presented below. This SRPA approach was already used to study nuclear structure effects along isotope chains in Calcium [104] and in Nickel and Tin isotopes [34]. These calculations also show good agreement with the sparse data on isotope effects that exists at the moment.

In figure (3.1) we show an evaluation of the total muon capture rates on all nuclei where data are available and on some heavy nuclei where no

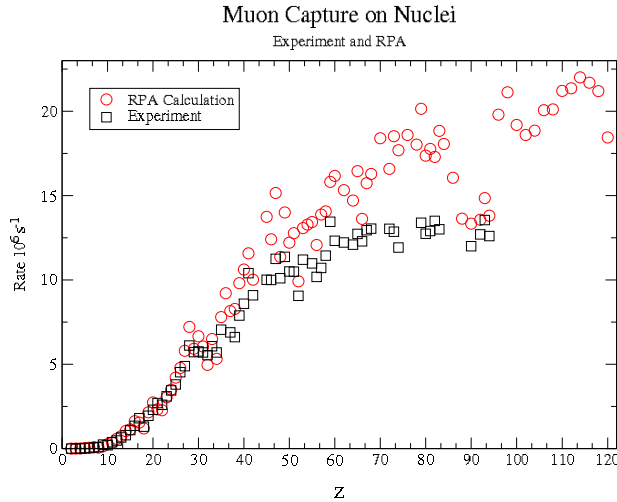


Figure 3.1: Total muon capture rates as a function of atomic number. Experimental data from [102].

measurements have been done. These rates were calculated with the SRPA similar to the work reported in [35, 104, 34]. The data are seen to give very good agreement for $Z \leq 40$. Above this point clear deviations are seen and also rather wild fluctuations. Some of these fluctuations could be caused by the inclusion of odd nuclei for which the SRPA is not expected to be very accurate due to the non-zero angular momentum ground-state. We also see that some large offsets are found around the magic charge numbers $Z = 20, 28, 50,$ and 82 . For $Z = 82$ the dip after the magic nucleus is so pronounced that it brings the calculation very close to the experimental numbers. This region is known to be deformed so this should merely be seen as accidental. However, we do note that the experimental data also show a dip-like structure at the magic numbers so this is a satisfactory behavior of our model.

The deviations around magic numbers indicate that our model has the right shell closure, but that it tends to overestimate the effects. We have tried to counter this by using BCS partial occupancies as discussed in section (2.2.2). Using this smoothed distribution on the single-particle level spectrum is likely to make the structure more soft and possibly yield rates that are closer to experiment.

When considering the region of large Z a large systematic deviation from the experimental numbers is present. We have chosen to continue the calculations show in figure (3.1) beyond $Z = 94$ to see the trend after the decrease at $Z = 82$ to confirm our initial suspicions that the deviations grow

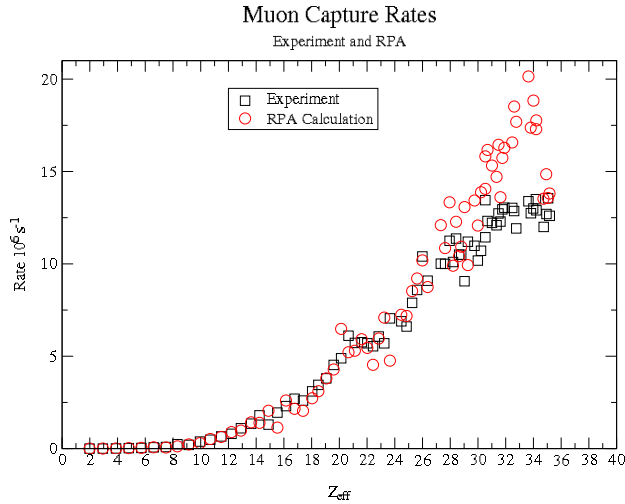


Figure 3.2: As figure (3.1) but as a function of the effective charge (Z_{eff} also from [102]).

with charge. These trends for large Z nuclei led us to suspect that there could be relativistic effects that were not taken properly into account. As we have estimated previously, the muon orbital energy grows with Z^2 and can become a significant fraction of its rest mass in heavy nuclei. However, its orbit radius goes as Z^{-1} so one should use an effective quantity that measures the charge inside the muon orbit. The effective charge, Z_{eff} , includes this finite size effect and are tabulated for the (mostly) stable nuclei we are concerned with here (we have used the values given in [102] which cites [103] as the original reference). In figure (3.2) we show the rates as a function of Z_{eff} . This plots confirms that the heaviest nuclei with large Z cause trouble for the current calculations. The closer spacing of data points at high Z_{eff} is also of interest. It tells us why the general trend in total capture rates shown in figure (3.1) tends to flatten out. Little is gained from adding protons to heavy nuclei since the core is at saturation and the muon effective sees only the inner particles.

The main part of our work on muon capture has been devoted to this relativistic effect, which will constitute the bulk of this chapter. After working through these modifications, we will comment on other important issues that we have attacked along the way. In particular, the issue of quenching of the GT response and the related discussion of the spin-isospin response and the parameters of the residual interaction. We round of this chapter with a presentation and discussion of our results for the capture rate on all measured nuclei.

3.2 The Relativistic Muon

When we presented the capture rate formula for muon capture in section (2.1.2), we commented that the muon atomic $1s$ wave function was a mere factor in the nuclear multipole operators [18]. However, this can be done only under the assumption that the muon is essentially non-relativistic so that its Dirac 4-spinor can be reduced to a radial function times a simple 2-spinor for the muon spin. The radial function can then be found by solving a Schrödinger equation with a potential given by the nuclear charge distribution, which we will also assume is of the standard Woods-Saxon form (using the same parameters that went into the calculation of the nuclear single-particle wave functions). For low charges one can use just the constant value of the wave function at $r = 0$, occasionally multiplied by a reduction factor for finite-size effect [18].

As a first step toward improving this wave function, we have hitherto worked with a radial wave function that came from an actual numerical solution of the full Dirac equation in the nuclear proton potential. As we discuss in appendix (A.3), this gives us two radial solutions; a large and a small component (referring to the non-relativistic limit). However, only the large component (that gives the Schrödinger solution in the low-momentum limit) was used in the rate calculation. As the muon binding energy grows with Z , the small component is expected to become increasingly important. We would therefore like to incorporate it into the muon capture rate formula.

When attempting this, one is immediately faced with a severe problem. In appendix (A.3) one sees that the large (g) and small (f) components do not have the same orbital angular momentum. This can be traced back to the fact that the Dirac equation does not separately conserve this quantity, only when the spin is added do we get conservation of total angular momentum. For g we know that we must have $l = 0$ since in the low-momentum limit it must represent the $1s$ orbit. Since g and f components must differ by one unit of orbital angular momentum (appendix (A.3)), this forces f to have $l = 1$. This is very bad news since it means that the strategy of multiplying the nuclear multipole operators by f will destroy their character as tensor under rotations.

One could start in full generality and consider capture from an arbitrary atomic state into some nuclear states of good angular momenta. Then one would re-couple the muon wave function with the multipole operators and let them act in the nuclear Hilbert space. Such derivations were carried out in an older paper by Morita and Fujii [105]. There are, however, a number of difficulties in the adaption of these results. The paper is written prior to the advent of the Standard Model of particle physics. At that time, the pure left-handedness of the neutrino was not an accepted fact.¹ This means that

¹Ironically, the recent discovery of neutrino oscillations and mass have yet again started

the out-going neutrino will produce contributions in wave function factors that are hard to disentangle when comparing to a more modern treatment like that of Walecka [18]. The conventions at that time are also less transparent. In particular, the classification of states into allowed, forbidden, 1st forbidden etc. takes a lot of work to translate into the multipole expansion that we work with. Upon careful consideration, we therefore decided to derive the expressions from scratch in the modern language.

3.2.1 The Leptonic Current

The leptonic part of the current has the standard V-A form

$$l^\mu \equiv \bar{\psi} [\gamma^\mu (1 - \gamma_5)] \phi, \quad (3.1)$$

where ψ is the neutrino and ϕ is the muon wave function respectively. The term $(1 - \gamma_5)$ is the projection operator onto the left-handed component which we need for weak interactions.

The muon wave function comes from the Dirac equation for spherical potentials as given in appendix (A.3). Here we will only be concerned with the capture from the $1s$ atomic orbit so we immediately specialize the wave function to that particular case. The total angular momentum is $j = 1/2$ and this yields the expression

$$\phi_{1/2m} = \begin{pmatrix} ig(r)\Omega_{1/20m}(\hat{r}) \\ -f(r)\Omega_{1/21m}(\hat{r}) \end{pmatrix}, \quad (3.2)$$

where $g(r)$ and $f(r)$ are the large and small components respectively. The angular functions have the explicit forms

$$\Omega_{1/2,0,m} = Y_{0,0}(\hat{r})\chi_{\text{sgn}(m)} \quad (3.3)$$

$$\Omega_{1/2,1,m} = -\sqrt{\frac{3/2-m}{3}}Y_{1,m-1/2}(\hat{r})\chi_+ + \sqrt{\frac{3/2+m}{3}}Y_{1,m+1/2}(\hat{r})\chi_-, \quad (3.4)$$

where χ_\pm are the two-spinor with spin up (+) and down (-). Here we can explicitly see the appearance of $l = 1$ terms in the spherical harmonics that multiply $f(r)$ and complicate things.

Since the neutrino is not influenced by the interaction of the nucleus it will have a simple plane wave form. It still has to obey the Dirac equation for fermions and as such there is a 4-spinor factor to consider. The contents of this 4-spinor is dictated by the fact that we assume a purely left-handed Standard Model neutrino. This entails a spin that is opposite to the three-momentum. The solution of the Dirac equation with these restrictions can

serious discussions about right-handed neutrino components.

be found in [106]. If we take the momentum \vec{p} along the positive z-axis we get

$$\psi = N \begin{pmatrix} \chi_- \\ -\chi_- \end{pmatrix} \exp(i\vec{p} \cdot \vec{x}), \quad (3.5)$$

where χ_- are the usual spin down Pauli two-spinors and N is a normalization constant (given in appendix (A.1)).

We now have to calculate the leptonic current l^μ with these wave functions. To keep good tensor properties, we use the standard spherical basis vectors, taking $\vec{e}_0 = \hat{z}$ (appendix (A.2)). The neutrino plane wave has a factor $\exp(i\vec{p} \cdot \vec{x})$. With the choice of coordinates one has $\vec{p} = k_f \hat{z} = \vec{q}$ since the neutrino moves in the positive z-axis direction. Therefore $\exp(i\vec{p} \cdot \vec{x}) = \exp(i\vec{q} \cdot \vec{x})$. The reason for using the vector \vec{q} is to keep with standard conventions for denoting the three-momentum transfer. In our case the muon has a localized wave function and thus no well-defined three-momentum. From conservation of momentum we therefore conclude that the transferred momentum is equal to that of the out-going neutrino.

The time component of the lepton current becomes

$$\begin{aligned} l_0 &= \bar{\psi} \gamma_0 (1 - \gamma_5) \phi \\ &= \psi^\dagger \gamma_0^2 (1 - \gamma_5) \phi \\ &= \psi^\dagger (1 - \gamma_5) \phi \\ &= ((1 - \gamma_5) \psi)^\dagger \phi \\ &= 2\psi^\dagger \phi, \end{aligned} \quad (3.6)$$

where we have used the fact that the neutrino wave function is left-handed and thus an eigenfunction of $(1 - \gamma_5)$. Now we insert the explicit spinor wave functions given earlier to get

$$\begin{aligned} l_0 &= 2N^* \exp(-i\vec{q} \cdot \vec{x}) \begin{pmatrix} \chi_-^\dagger & -\chi_-^\dagger \end{pmatrix} \begin{pmatrix} ig(r)\Omega_{1/2,0,m} \\ -f(r)\Omega_{1/2,1,m} \end{pmatrix} \\ &= 2N^* \exp(-i\vec{q} \cdot \vec{x}) \left\{ ig(r)\chi_-^\dagger \Omega_{1/2,0,m} + f(r)\chi_-^\dagger \Omega_{1/2,1,m} \right\} \\ &= 2N^* \exp(-i\vec{q} \cdot \vec{x}) \left\{ ig(r)Y_{0,0}\delta_{m,-1/2} + f(r)\sqrt{\frac{3/2+m}{3}}Y_{1,m+1/2} \right\}. \end{aligned} \quad (3.7)$$

Similarly we get the third component of the lepton current $\mu = 3$ ($\lambda = 0$ in

terms of the spherical basis components)

$$\begin{aligned}
 l^3 &= \bar{\psi}\gamma^3(1-\gamma_5)\phi \\
 &= \psi^\dagger\gamma_0\gamma^3(1-\gamma_5)\phi \\
 &= \psi^\dagger\begin{pmatrix} 0 & \sigma_z \\ \sigma_z & 0 \end{pmatrix}(1-\gamma_5)\phi \\
 &= \left(\begin{pmatrix} 0 & \sigma_z \\ \sigma_z & 0 \end{pmatrix}\psi\right)^\dagger(1-\gamma_5)\phi \\
 &= (\sigma_z\gamma_5\psi)^\dagger(1-\gamma_5)\phi \\
 &= -(\sigma_z\psi)^\dagger(1-\gamma_5)\phi \\
 &= (\psi)^\dagger(1-\gamma_5)\phi \\
 &= 2\psi^\dagger\phi \\
 &= l_0,
 \end{aligned} \tag{3.8}$$

where σ_z is always implicitly multiplied by the 4x4 identity. Here we have used

$$\sigma_z\begin{pmatrix} \chi_- \\ -\chi_- \end{pmatrix} = \begin{pmatrix} \sigma_z\chi_- \\ -\sigma_z\chi_- \end{pmatrix} = -\begin{pmatrix} \chi_- \\ -\chi_- \end{pmatrix} \tag{3.9}$$

since the Pauli two-spinors are eigenstates of σ_z . This equality actually follows straight from current conservation at the lepton vertex, since in momentum space we have (for massless particles with $E = p$)

$$q_\mu l^\mu = q_0 l_0 - \vec{q} \cdot \vec{l} = q_0 l_0 - q l^3 \quad \Rightarrow \quad l_0 = l^3. \tag{3.10}$$

The $\lambda = +1$ spherical component of the lepton current is

$$\begin{aligned}
 l^{\lambda=+1} &= \bar{\psi}\left(-\frac{1}{\sqrt{2}}(\gamma^1 + i\gamma^2)\right)(1-\gamma_5)\phi \\
 &= -\sqrt{2}\psi^\dagger\begin{pmatrix} 0 & \sigma_+ \\ \sigma_+ & 0 \end{pmatrix}(1-\gamma_5)\phi \\
 &= -\sqrt{2}\left(\begin{pmatrix} 0 & \sigma_- \\ \sigma_- & 0 \end{pmatrix}\psi\right)^\dagger(1-\gamma_5)\phi \\
 &= 0,
 \end{aligned} \tag{3.11}$$

$$\tag{3.12}$$

where we use the fact that $\sigma_-\chi_- = 0$. We see that one spherical component vanishes which is not surprising since we have an explicitly left/right-handed symmetry breaking current. The other spherical components is non-zero and

can be evaluated in the same way as above to give

$$\begin{aligned}
 l^{\lambda=-1} &= \bar{\psi}(\frac{1}{\sqrt{2}}(\gamma^1 - i\gamma^2))(1 - \gamma_5)\phi \\
 &= \sqrt{2}\psi^\dagger \begin{pmatrix} 0 & \sigma_- \\ \sigma_- & 0 \end{pmatrix} (1 - \gamma_5)\phi \\
 &= \sqrt{2}\left(\begin{pmatrix} 0 & \sigma_+ \\ \sigma_+ & 0 \end{pmatrix}\psi\right)^\dagger(1 - \gamma_5)\phi \\
 &= \sqrt{2}N^* \exp(-i\vec{q}\cdot\vec{x})\left(\begin{pmatrix} 0 & \sigma_+ \\ \sigma_+ & 0 \end{pmatrix}\begin{pmatrix} \chi_- \\ -\chi_- \end{pmatrix}\right)^\dagger(1 - \gamma_5)\phi \\
 &= \sqrt{2}N^* \exp(-i\vec{q}\cdot\vec{x})\begin{pmatrix} -\chi_+ \\ \chi_+ \end{pmatrix}^\dagger(1 - \gamma_5)\phi \\
 &= \sqrt{2}N^* \exp(-i\vec{q}\cdot\vec{x})\left((1 - \gamma_5)\begin{pmatrix} -\chi_+ \\ \chi_+ \end{pmatrix}\right)^\dagger\phi \\
 &= \sqrt{2}N^* \exp(-i\vec{q}\cdot\vec{x})\begin{pmatrix} -2\chi_+ \\ 2\chi_+ \end{pmatrix}^\dagger\phi \\
 &= -2\sqrt{2}N^* \exp(-i\vec{q}\cdot\vec{x})\begin{pmatrix} \chi_+ \\ -\chi_+ \end{pmatrix}^\dagger\phi \\
 &= -2\sqrt{2}N^* \exp(-i\vec{q}\cdot\vec{x})\begin{pmatrix} \chi_+^\dagger & -\chi_+^\dagger \end{pmatrix}\begin{pmatrix} ig(r)\Omega_{1/2,0,m} \\ -f(r)\Omega_{1/2,1,m} \end{pmatrix} \\
 &= -2\sqrt{2}N^* \exp(-i\vec{q}\cdot\vec{x})\{ig(r)Y_{0,0}\delta_{m,1/2} - \\
 &\quad f(r)\sqrt{\frac{3/2-m}{3}}Y_{1,m-1/2}\}. \tag{3.13}
 \end{aligned}$$

We now have the components of the leptonic current in place. These have to be inserted into the interaction hamiltonian

$$H_{int} = \frac{G}{\sqrt{2}} \int d^3\vec{x} j_\mu^{lep} J_{nuc}^\mu = \frac{G}{\sqrt{2}} \int d^3\vec{x} (j_0 J^0 - \vec{j} \cdot \vec{J}). \tag{3.14}$$

Formally we must take the inner product of this field hamiltonian between the final and initial states which live in the tensor product of nuclear and lepton Hilbert spaces. This we write as

$$\langle f|H|i\rangle = \frac{G}{\sqrt{2}} \int d^3\vec{x} (l^0(\vec{x})J^0(\vec{x})_{fi} - \vec{l}(\vec{x}) \cdot \vec{J}(\vec{x})_{fi}), \tag{3.15}$$

where

$$J^\mu(\vec{x})_{fi} \equiv \langle f_{nucleus}|J^\mu|i_{nucleus}\rangle \tag{3.16}$$

is the nuclear current part, which we get from the nuclear structure model described in chapter (2). We were careful to make sure that the nuclear states have good total angular momentum and in order not to spoil this property we must be careful when combining the nuclear and lepton parts.

3.2.2 The Non-Relativistic Limit

Before we derive the full expression including large and small muon wave function components, we digress to make a sensible consistency check of the method used. We need to make sure that the formalism introduced above gives the correct limit when we set $f(r) = 0$. For convenience (and easy of comparison to the formalism in [18]) we first make a slight redefinition of the currents to exclude the plane wave exponential factors from the neutrino wave. Thus

$$\begin{aligned}
 l_0 &\rightarrow l_0 \exp(-i\vec{q} \cdot \vec{x})g(r)Y_{0,0} \Rightarrow l_0 = 2N^*i\delta_{m,-1/2} \\
 l^3 &\rightarrow l^3 \exp(-i\vec{q} \cdot \vec{x})g(r)Y_{0,0} \Rightarrow l^3 = 2N^*i\delta_{m,-1/2} \\
 l^{\pm 1} &= 0 \\
 l^{-1} &\rightarrow l^{-1} \exp(-i\vec{q} \cdot \vec{x})g(r)Y_{0,0} \Rightarrow l^{-1} = -2\sqrt{2}N^*i\delta_{0,1/2}, \quad (3.17)
 \end{aligned}$$

where $l^{\pm 1}$ are the spherical $\lambda = \pm 1$ components. Now we use the partial wave expansion of the plane wave (appendix (A.2)) in the interaction hamiltonian to get

$$\begin{aligned}
 \text{H} &= \frac{G}{\sqrt{2}} \int d^3\vec{x} \exp(-i\vec{q} \cdot \vec{x})g(r)Y_{0,0} \{l_0 J_0 - l^3 \vec{e}_0 \cdot \vec{J} \\
 &\quad + \sum_{\lambda=\pm 1} l^\lambda \vec{e}_{-\lambda} \cdot \vec{J}\} \\
 &= \frac{G}{\sqrt{2}} \int d^3\vec{x} g(r)Y_{0,0} \{l_0 J_0 \sum_{J=0}^{\infty} \sqrt{4\pi} [J] (-i)^J j_J(\kappa x) Y_{J,0} \\
 &\quad - l^3 \frac{i}{\kappa} \sum_{J=0}^{\infty} \sqrt{4\pi} [J] \nabla (j_J(\kappa x) Y_{J,0}) \cdot \vec{J} \\
 &\quad + \sum_{\lambda=\pm 1} l^\lambda \sum_{J=1}^{\infty} \sqrt{2\pi} [J] (-i)^J [\lambda j_J(\kappa x) \vec{\mathcal{Y}}_{J,J,1}^{-\lambda} + \frac{1}{\kappa} \nabla \wedge (j_J(\kappa x) \vec{\mathcal{Y}}_{J,J,1}^{-\lambda})]\} \\
 &= \frac{G}{\sqrt{2}} \left[\sum_{J=0}^{\infty} \sqrt{4\pi} [J] (-i)^J \left\{ \mathcal{M}'_{J,0} l_0 - \mathcal{L}'_{J,0} l^3 \right\} \right. \\
 &\quad \left. + \sum_{\lambda=\pm 1} l^\lambda \sum_{J=1}^{\infty} \sqrt{2\pi} [J] (-i)^J \left\{ \lambda \mathcal{J}'_{J,-1}{}^{mag} + \mathcal{J}'_{J,-1}{}^{el} \right\} \right], \quad (3.18)
 \end{aligned}$$

where the multipole operators are those defined in equations (2.14), (2.15), (2.16), and (2.17). The prime indicates that they are multiplied by $g(r)Y_{00}$ (which causes no problem with the tensor characters).

The assumption of well-defined angular momenta for the nuclear states allows the use of the Wigner-Eckart theorem [28] to reduce the matrix elements through

$$\langle J_f M_f | \mathcal{T}_{J,M} | J_i M_i \rangle = (-1)^{J_f - M_f} \begin{pmatrix} J_f & J & J_i \\ -M_f & M & M_i \end{pmatrix} \langle J_f || \mathcal{T}_J || J_i \rangle. \quad (3.19)$$

To get the rate one needs the matrix element squared. Assuming an unpolarized nucleus, we must average over M_i and sum over M_f . For this we use the orthogonality relation for the 3-j symbols in the form

$$\sum_{M_i, M_f} \begin{pmatrix} J_f & J & J_i \\ -M_f & M & M_i \end{pmatrix} \begin{pmatrix} J_f & J' & J_i \\ -M_f & M' & M_i \end{pmatrix} = \frac{1}{2J+1} \delta_{J, J'} \delta_{M, M'}. \quad (3.20)$$

Using this we get the squared matrix element (there is no interference between the two sums as they have different values of M)

$$\begin{aligned} \frac{1}{2J_i+1} \sum_{M_i, M_f} |\langle f | \mathbf{H} | i \rangle|^2 &= \frac{1}{2J_i+1} \frac{G^2}{2} [4\pi |l_0|^2 \sum_{J=0}^{\infty} \left| \langle J_f || \mathcal{M}'_J - \mathcal{L}'_J || J_i \rangle \right|^2 \\ &+ \sum_{\lambda=\pm 1} l^\lambda (l^\lambda)^* \sum_{J=1}^{\infty} \left| \langle J_f || \lambda \mathcal{J}'^{mag} + \mathcal{J}'^{el} || J_i \rangle \right|^2]. \end{aligned} \quad (3.21)$$

At this point we can use the following identity for the spherical components

$$\sum_{\lambda=\pm 1} l^\lambda (l^\lambda)^* |a + \lambda b|^2 = (\vec{l} \cdot (\vec{l})^* - l^3 (l^3)^*) (|a|^2 + |b|^2) - i(\vec{l} \wedge (\vec{l})^*)_3 2\text{Re}(a^* b), \quad (3.22)$$

where a and b are any complex numbers (this is easily shown by using the definition the spherical basis given in appendix (A.2)). We thus need the cartesian components of \vec{l} to use the formula. Since $\lambda = +1$ vanishes, the transformation is easily done. The result is

$$l_0 = l^3 = l^z = 2N^* i \delta_{m, -1/2} \quad l^x = -2N^* i \delta_{m, 1/2} \quad l^y = i l^x = 2N^* \delta_{m, 1/2}. \quad (3.23)$$

The quantities we need above are therefore

$$\vec{l} \cdot (\vec{l})^* - l^3 (l^3)^* = 8|N|^2 \delta_{m, 1/2} \quad (3.24)$$

$$(\vec{l} \wedge (\vec{l})^*)_3 = l^x (l^y)^* - l^y (l^x)^* = -8i|N|^2 \delta_{m, 1/2}. \quad (3.25)$$

Inserting this in the matrix element of eq. (3.21) gives

$$\sum_{\lambda=\pm 1} l^\lambda (l^\lambda)^* |a + \lambda b|^2 = 8|N|^2 \delta_{m, 1/2} |a - b|^2. \quad (3.26)$$

Using this in the summed matrix element squared gives

$$\begin{aligned} \frac{1}{2J_i+1} \sum_{M_i, M_f} |\langle f | \mathbf{H} | i \rangle|^2 &= \\ \frac{1}{2J_i+1} 8\pi |N|^2 G^2 [\delta_{m, -1/2} \sum_{J=0}^{\infty} \left| \langle J_f || \mathcal{M}'_J - \mathcal{L}'_J || J_i \rangle \right|^2 \\ + \delta_{m, 1/2} \sum_{J=1}^{\infty} \left| \langle J_f || \mathcal{J}'^{el} - \mathcal{J}'^{mag} || J_i \rangle \right|^2]. \end{aligned} \quad (3.27)$$

When averaged over muon spin states $m = \pm 1/2$ (assuming an unpolarized muon) this gives (with suitable normalization and phase space) the non-relativistic rate formula given in equation (2.19). So the formalism is consistent with previous work using only the large component of the muon wave function.

3.2.3 The Relativistic Rate Formula

We now proceed to derive the full relativistic muon capture rate formula with large and small components included. The interaction hamiltonian has the general form

$$\begin{aligned}
 H &= \frac{G}{\sqrt{2}} \int d^3\vec{x} \{ l_0 J_0 - l^3 \vec{e}_0 \cdot \vec{J} \\
 &\quad + \sum_{\lambda=\pm 1} l^\lambda \vec{e}_{-\lambda} \cdot \vec{J} \} \\
 &= \frac{G}{\sqrt{2}} \int d^3\vec{x} \{ l_0 J_0 - l^3 \vec{e}_0 \cdot \vec{J} \\
 &\quad + l^{-1} \vec{e}_1 \cdot \vec{J} \}, \tag{3.28}
 \end{aligned}$$

since the $\lambda = +1$ components was zero. We now want to consider the contributions from the leptonic part term by term.

The Time Component l_0

From the general expression given earlier we have

$$l_0 = 2N^* \exp(-i\vec{q} \cdot \vec{x}) \left\{ ig(r) Y_{0,0} \delta_{m,-1/2} + f(r) \sqrt{\frac{3/2+m}{3}} Y_{1,m+1/2} \right\}. \tag{3.29}$$

We insert the multipole expansion of the plane wave and obtain

$$\begin{aligned}
 \int d^3\vec{x} l_0 J_0 &= 2N^* \int d^3\vec{x} \sum_{J=0}^{\infty} \sqrt{4\pi[J]} (-i)^J j_J(\kappa x) Y_{J,0} \\
 &\quad \times \left\{ ig(r) Y_{0,0} \delta_{m,-1/2} + f(r) \sqrt{\frac{3/2+m}{3}} Y_{1,m+1/2} \right\} J_0 \\
 &= 2N^* \sum_{J=0}^{\infty} \sqrt{4\pi[J]} (-i)^J \{ i \delta_{m,-1/2} \int d^3\vec{x} g(r) Y_{0,0} j_J(\kappa x) Y_{J,0} J_0 \\
 &\quad + \sqrt{\frac{3/2+m}{3}} \int d^3\vec{x} f(r) j_J(\kappa x) Y_{J,0} Y_{1,m+1/2} J_0 \}. \tag{3.30}
 \end{aligned}$$

The first term is just the old \mathcal{M}' term, whereas the second does not have good tensor character as it stands. To remedy this we use a product formula

for spherical harmonics to reduce it to a sum of harmonics. The formula is

$$Y_{l_1, m_1} Y_{l_2, m_2} = \sum_k \frac{[l_1][l_2]}{\sqrt{4\pi}[k]} \langle l_1 l_2 k | 0 0 0 \rangle \langle l_1 l_2 k | m_1 m_2 m_1 + m_2 \rangle Y_{k, m_1 + m_2}, \quad (3.31)$$

where k is restricted by the usual triangle rule for l_1, l_2 , and k . Consider now the second term in eq. (3.30) above. Here one has $l_1 = J$ and $l_2 = 1$, and one would naively assume the sum over k to be restricted to $k = J - 1, J, J + 1$. The Clebsch-Gordan $\langle l_1 l_2 k | 0 0 0 \rangle$, however, restricts this by the condition that $J + 1 + k$ must be even. So only $k = J - 1$ and $J + 1$ are allowed. To simplify our expression we define the following quantities

$$\mathcal{M}'_{J, M} = \int d^3 \vec{x} g(r) Y_{0,0} j_J(\kappa x) Y_{J, M} J_0 \quad (3.32)$$

$$\alpha(\rho, J, m) = \sqrt{\frac{3/2+m}{3}} \sqrt{\frac{3}{4\pi}} \frac{[J]}{[\rho]} \langle J 1 \rho | 0 0 0 \rangle \langle J 1 \rho | 0 m + \frac{1}{2} m + \frac{1}{2} \rangle \quad (3.33)$$

$$\mathcal{T}_1(\rho, J, \mu) = \int d^3 \vec{x} f(r) j_J(\kappa x) Y_{\rho, \mu} J_0, \quad (3.34)$$

where the first is simply the coulomb multipole with the large component. The new tensor containing $f(r)$ has the indicated tensor character (ρ, μ) . Remember that the constant α has a dependence on the muon spin projection m . With these definitions and the expansion of the spherical harmonics we get

$$\begin{aligned} \int d^3 \vec{x} l_0 J_0 &= 2N^* \sum_{J=0}^{\infty} \sqrt{4\pi}[J] (-i)^J \{ i \delta_{m, -1/2} \mathcal{M}'_{J,0} \\ &\quad + \alpha(J-1, J, m + \frac{1}{2}) \mathcal{T}_1(J-1, J, m + \frac{1}{2}) \\ &\quad + \alpha(J+1, J, m + \frac{1}{2}) \mathcal{T}_1(J+1, J, m + \frac{1}{2}) \} \end{aligned} \quad (3.35)$$

for the time component (where it is understood that if any of the first two arguments in α and \mathcal{T}_1 are negative the term is zero). We thus see that this term adds another two tensors to the general matrix element.

The Third Component l^3

The third component of the current ($\lambda = 0$ component in spherical notation) is more complicated since it contains a derivative that we have to expand and re-couple. As we have previously seen, the leptonic current is the same as that of the time component

$$l^3 = 2N^* \exp(-i\vec{q} \cdot \vec{x}) \left\{ i g(r) Y_{0,0} \delta_{m, -1/2} + f(r) \sqrt{\frac{3/2+m}{3}} Y_{1, m+1/2} \right\}. \quad (3.36)$$

Using the multipole expansion of the exponential factor one gets

$$\begin{aligned}
 \int d^3\vec{x} l^3 \vec{e}_0 \cdot \vec{J} &= 2N^* \int d^3\vec{x} \frac{i}{\kappa} \sum_{J=0}^{\infty} \sqrt{4\pi} [J] (-i)^J \nabla (j_J(\kappa x) Y_{J,0}) \cdot \vec{J} \\
 &\quad \times \left\{ ig(r) Y_{0,0} \delta_{m,-1/2} + f(r) \sqrt{\frac{3/2+m}{3}} Y_{1,m+1/2} \right\} \\
 &= 2N^* \sum_{J=0}^{\infty} \sqrt{4\pi} [J] (-i)^J \{ i \delta_{m,-1/2} \int d^3\vec{x} g(r) Y_{0,0} \nabla (j_J(\kappa x) Y_{J,0}) \cdot \vec{J} \\
 &\quad + \sqrt{\frac{3/2+m}{3}} \int d^3\vec{x} f(r) \nabla (j_J(\kappa x) Y_{J,0}) Y_{1,m+1/2} \cdot \vec{J} \}. \quad (3.37)
 \end{aligned}$$

The last term with $f(r)$ is again not a good tensor. To remedy this we expand the gradient using the identity (appendix (A.2))

$$\nabla_{\rho} (j_J(\rho) Y_{J,M}(\Omega_{\rho})) = \sqrt{\frac{J+1}{2J+1}} j_{J+1}(\rho) \vec{\mathcal{Y}}_{J,J+1,1}^M + \sqrt{\frac{J}{2J+1}} j_{J-1}(\rho) \vec{\mathcal{Y}}_{J,J-1,1}^M.$$

This turns the problem into a reduction of the product $Y_{1,\mu} \vec{\mathcal{Y}}_{\rho,\gamma,1}^M$. Using the definition of the vector spherical harmonic one has

$$Y_{1,\mu} \vec{\mathcal{Y}}_{J,L,1}^M = \sum_m \langle L J 1 | m M - m M \rangle Y_{L,m} Y_{1,\mu} \vec{e}_{M-m}.$$

First we reduce the product of spherical harmonics by using

$$Y_{1,\mu} Y_{L,m} = \sum_{\rho} \sqrt{\frac{3}{4\pi} \frac{[L]}{[\rho]}} \langle 1 L \rho | 0 0 0 \rangle \langle 1 L \rho | \mu m \mu + m \rangle Y_{\rho,\mu+m}.$$

Now we want to relate the product $\vec{e}_{\lambda} Y_{l,m}$ to the vector spherical harmonic by using inversion of the Clebsch-Gordan coefficients (appendix (A.2))

$$\vec{e}_{\lambda} Y_{l,m} = \sum_{\gamma} \langle l 1 \gamma | m \lambda m + \lambda \rangle \vec{\mathcal{Y}}_{\gamma,l,1}^{m+\lambda},$$

where the sum over γ is restricted to $\gamma = l-1, l, l+1$. Inserting these formulae gives

$$\begin{aligned}
 Y_{1,\mu} \vec{\mathcal{Y}}_{J,L,1}^M &= \sum_{\rho,\gamma,m} \sqrt{\frac{3}{4\pi} \frac{[L]}{[\rho]}} \langle 1 L \rho | 0 0 0 \rangle \langle 1 L \rho | \mu m \mu + m \rangle \\
 &\quad \times \langle L 1 J | m M - m M \rangle \langle \rho 1 \gamma | \mu + m M - m M + \mu \rangle \vec{\mathcal{Y}}_{\gamma,\rho,1}^{M+\mu}.
 \end{aligned}$$

We can reduce the expression by using the following relation between the Clebsch-Gordan coefficients and the Racah W symbols (which can be found in [107] or [28])

$$\begin{aligned}
 &\sum_m \langle 1 L \rho | \mu m \mu + m \rangle \langle \rho 1 \gamma | \mu + m M - m M + \mu \rangle \langle L 1 J | m M - m M \rangle \\
 &= [J][\rho] W(1 L \gamma 1; \rho J) \langle 1 J \gamma | \mu M M + \mu \rangle.
 \end{aligned}$$

When inserting this we finally have the formula for the product

$$\begin{aligned}
 Y_{1,\mu} \vec{\mathcal{Y}}_{J,L,1}^M &= \sum_{\rho,\gamma} \sqrt{\frac{3}{4\pi}} [J][L] W(1 L \gamma 1; \rho J) \langle 1 J \gamma | \mu M M + \mu \rangle \\
 &\quad \times \langle 1 L \rho | 000 \rangle \vec{\mathcal{Y}}_{\gamma,\rho,1}^{M+\mu}.
 \end{aligned} \tag{3.38}$$

The presence of the W coefficient gives us four triangle relations; $\Delta(1 L \gamma)$, $\Delta(1 \rho J)$, $\Delta(1 L J)$ and $\Delta(1 \rho \gamma)$, which restrict the sum over ρ and γ for given J and L . The last Clebsch-Gordan gives us the triangle $\Delta(1 L \rho)$, so that $L + 1 + \rho$ must be even.

We now expand the $f(r)$ term to get

$$\begin{aligned}
 &\int d^3 \vec{x} \frac{i}{\kappa} \sum_{J=0}^{\infty} \sqrt{4\pi} [J] (-i)^J f(r) \sqrt{\frac{3/2+m}{3}} Y_{1,m+1/2} \\
 &\quad \times \kappa \left\{ \sqrt{\frac{J+1}{2J+1}} j_{J+1}(\rho) \vec{\mathcal{Y}}_{J,J+1,1}^0 + \sqrt{\frac{J}{2J+1}} j_{J-1}(\rho) \vec{\mathcal{Y}}_{J,J-1,1}^0 \right\} \\
 &= i \sum_{J=0}^{\infty} \sqrt{4\pi} (-i)^J \sqrt{\frac{3/2+m}{3}} \{ \\
 &\quad \sqrt{\frac{J+1}{2J+1}} \int d^3 \vec{x} f(r) j_{J+1}(\kappa x) Y_{1,m+1/2} \vec{\mathcal{Y}}_{J,J+1,1}^0 + \\
 &\quad \sqrt{\frac{J}{2J+1}} \int d^3 \vec{x} f(r) j_{J-1}(\kappa x) Y_{1,m+1/2} \vec{\mathcal{Y}}_{J,J-1,1}^0 \},
 \end{aligned} \tag{3.39}$$

where the factor of κ in the numerator comes from the fact that the Bessel functions depend on $\rho = \kappa x$, which gives $\frac{d\rho}{dx} = \kappa$. We now insert the reduction formula derived above in the first term and get

$$\begin{aligned}
 &\sqrt{\frac{3/2+m}{3}} \sqrt{\frac{J+1}{2J+1}} \int d^3 \vec{x} f(r) j_{J+1}(\kappa x) \sum_{\rho,\gamma} \sqrt{\frac{3}{4\pi}} [J][J+1] \\
 &\quad \times W(1 J + 1 \gamma 1; \rho J) \langle 1 J \gamma | m + \frac{1}{2} 0 m + \frac{1}{2} \rangle \langle 1 J + 1 \rho | 000 \rangle \vec{\mathcal{Y}}_{\gamma,\rho,1}^{m+1/2}.
 \end{aligned}$$

The last Clebsch-Gordan restricts $\rho + J + 2$ to an even integer. Thus $\rho = J, J + 2$ are the only allowed values. γ is obtained by coupling ρ and 1, so naively $\gamma = \rho - 1, \rho, \rho + 1$. However, we have a triangle $\Delta(1 J + 1 \gamma)$ from W , which does not allow $J - 1$. Similarly for $\rho = J + 2$ the value $J + 3$ is not allowed. Lastly we also have $\Delta(1 J \gamma)$ from W , so that $\gamma = J + 2$ is ruled out. We therefore have three allowed combinations in the sum: $(\rho = J, \gamma = J - 1)$, $(\rho = J, \gamma = J)$, and $(\rho = J + 2, \gamma = J + 1)$, with the rule that whenever ρ or γ is negative the term vanishes. The second term

in equation (3.39) can be treated analogously to yield

$$\begin{aligned} & \sqrt{\frac{3/2+m}{3}} \sqrt{\frac{J}{2J+1}} \int d^3 \vec{x} f(r) j_{J-1}(\kappa x) \sum_{\rho, \gamma} \sqrt{\frac{3}{4\pi}} [J][J-1] \\ & \times W(1 J - 1 \gamma 1; \rho J) \langle 1 J \gamma | m + \frac{1}{2} 0 m + \frac{1}{2} \rangle \langle 1 J - 1 \rho | 000 \rangle \vec{\mathcal{Y}}_{\gamma, \rho, 1}^{m+1/2}. \end{aligned}$$

Repeating the analysis of allowed terms as done above we get the following contributions to the sum: $(\rho = J - 2, \gamma = J - 1)$, $(\rho = J, \gamma = J - 1)$, and $(\rho = J, \gamma = J)$.

We now define the following convenient quantities

$$\mathcal{L}'_{J,M} = \frac{i}{\kappa} \int d^3 \vec{x} g(r) Y_{0,0} \nabla (j_J(\kappa x) Y_{J,M}) J_0 \quad (3.40)$$

$$\begin{aligned} \beta_+(\gamma, \rho, m) &= \sqrt{\frac{3/2+m}{3}} \sqrt{\frac{3}{4\pi}} \sqrt{J+1} [J+1] \langle 1 J + 1 \rho | 000 \rangle \\ &\times \langle 1 J \gamma | m + \frac{1}{2} 0 m + \frac{1}{2} \rangle W(1 J + 1 \gamma 1; \rho J) \quad (3.41) \end{aligned}$$

$$\mathcal{T}_2(\gamma, \rho, \mu) = \int d^3 \vec{x} f(r) j_{J+1}(\kappa x) \vec{\mathcal{Y}}_{\gamma, \rho, 1}^\mu \cdot \vec{J} \quad (3.42)$$

$$\begin{aligned} \beta_-(\gamma, \rho, m) &= \sqrt{\frac{3/2+m}{3}} \sqrt{\frac{3}{4\pi}} \sqrt{J} [J-1] \langle 1 J - 1 \rho | 000 \rangle \\ &\times \langle 1 J \gamma | m + \frac{1}{2} 0 m + \frac{1}{2} \rangle W(1 J - 1 \gamma 1; \rho J) \quad (3.43) \end{aligned}$$

$$\mathcal{T}_3(\gamma, \rho, \mu) = \int d^3 \vec{x} f(r) j_{J-1}(\kappa x) \vec{\mathcal{Y}}_{\gamma, \rho, 1}^\mu \cdot \vec{J}, \quad (3.44)$$

where the two tensors $\mathcal{T}_2, \mathcal{T}_3$ have character (γ, μ) . Using these definitions we can write the contribution from the third component as

$$\begin{aligned} & \int d^3 \vec{x} l^3 \vec{e}_0 \cdot \vec{J} = 2N^* \sum_{J=0}^{\infty} \sqrt{4\pi} [J] (-i)^J i \{ \delta_{m, -1/2} \mathcal{L}'_{J,0} \\ & + \beta_+(J, J, m) \mathcal{T}_2(J, J, m + \frac{1}{2}) \\ & + \beta_+(J + 1, J, m) \mathcal{T}_2(J + 1, J, m + \frac{1}{2}) \\ & + \beta_+(J + 1, J + 2, m) \mathcal{T}_2(J + 1, J + 2, m + \frac{1}{2}) \\ & + \beta_-(J - 1, J - 2, m) \mathcal{T}_3(J - 1, J - 2, m + \frac{1}{2}) \\ & + \beta_-(J - 1, J, m) \mathcal{T}_3(J - 1, J, m + \frac{1}{2}) \\ & + \beta_-(J, J, m) \mathcal{T}_3(J, J, m + \frac{1}{2}) \}, \quad (3.45) \end{aligned}$$

where it is understood that for a term to give a non-zero contribution the first two arguments must be non-negative.

The $\lambda = -1$ Component

The leptonic part of this component has the form

$$l^{\lambda=-1} = -2\sqrt{2}N^* \exp(-i\vec{q} \cdot \vec{x}) \{ ig(r) Y_{0,0} \delta_{m, 1/2} - f(r) \sqrt{\frac{3/2-m}{3}} Y_{1, m-1/2} \}. \quad (3.46)$$

Inserting the multipole expansion of the plane wave yields

$$\begin{aligned}
 \int d^3\vec{x} l^{-1} \vec{e}_1 \cdot \vec{J} &= -2N^* \int d^3\vec{x} \sum_{J=1}^{\infty} \sqrt{4\pi} [J] (-i)^J [-j_J(\kappa x) \vec{\mathcal{Y}}_{J,J,1}^1 \\
 &\quad + \frac{1}{\kappa} \nabla \wedge (j_J(\kappa x) \vec{\mathcal{Y}}_{J,J,1}^1)] \cdot \vec{J} \\
 &\quad \times \left\{ ig(r) Y_{0,0} \delta_{m,1/2} - f(r) \sqrt{\frac{3/2-m}{3}} Y_{1,m-1/2} \right\} \\
 &= -2N^* \sum_{J=1}^{\infty} \sqrt{4\pi} [J] (-i)^J \{ i \delta_{m,1/2} \int d^3\vec{x} g(r) Y_{0,0} \\
 &\quad \times [-j_J(\kappa x) \vec{\mathcal{Y}}_{J,J,1}^1 + \frac{1}{\kappa} \nabla \wedge (j_J(\kappa x) \vec{\mathcal{Y}}_{J,J,1}^1)] \\
 &\quad + \sqrt{\frac{3/2-m}{3}} \int d^3\vec{x} f(r) j_J(\kappa x) \vec{\mathcal{Y}}_{J,J,1}^1 Y_{1,m-1/2} \\
 &\quad - \sqrt{\frac{3/2-m}{3}} \int d^3\vec{x} f(r) \nabla \wedge (j_J(\kappa x) \vec{\mathcal{Y}}_{J,J,1}^1) Y_{1,m-1/2} \} \cdot \vec{J}.
 \end{aligned} \tag{3.47}$$

The first two terms are simply the transverse magnetic and electric multipole operators of eqs. (2.16) and (2.17) with the large component included

$$\mathcal{J}_{J,M}^{el} = \frac{1}{\kappa} \int d^3\vec{x} g(r) Y_{0,0} \nabla \wedge (j_J(\kappa x) \vec{\mathcal{Y}}_{J,J,1}^M) \cdot \vec{J} \tag{3.48}$$

$$\mathcal{J}_{J,M}^{mag} = \int d^3\vec{x} g(r) Y_{0,0} j_J(\kappa x) \vec{\mathcal{Y}}_{J,J,1}^M \cdot \vec{J}. \tag{3.49}$$

The first of the terms involving $f(r)$ can be handled using the same methods as for the third component above. Reduction of the product of vector spherical and spherical harmonic yields

$$\begin{aligned}
 &\sqrt{\frac{3/2-m}{3}} \int d^3\vec{x} f(r) j_J(\kappa x) \sum_{\rho,\gamma} \sqrt{\frac{3}{4\pi}} [J]^2 W(1 J \gamma 1; \rho J) \\
 &\quad \times \langle 1 J \gamma | m - \frac{1}{2} \ 1 \ m + \frac{1}{2} \rangle \langle 1 J \rho | 000 \rangle \vec{\mathcal{Y}}_{\gamma,\rho,1}^{m+1/2}.
 \end{aligned}$$

Since $\rho + J + 1$ must be even only $\rho = J - 1, J + 1$ are allowed. The triangle relations coming from the W coefficient give the conditions $\gamma = J - 1, J, J + 1$ and $\gamma = \rho - 1, \rho, \rho + 1$. Taking all this into account restricts the sum to the following terms: $(\rho = J - 1, \gamma = J - 1)$, $(\rho = J - 1, \gamma = J)$, $(\rho = J + 1, \gamma = J)$, and $(\rho = J + 1, \gamma = J + 1)$. Defining the quantities

$$\delta(\gamma, \rho, m) = \sqrt{\frac{3/2-m}{3}} \sqrt{\frac{3}{4\pi}} [J]^2 \langle 1 J \rho | 000 \rangle \tag{3.50}$$

$$\times \langle 1 J \gamma | m - \frac{1}{2} \ 1 \ m + \frac{1}{2} \rangle W(1 J \gamma 1; \rho J) \tag{3.51}$$

$$\mathcal{T}_4(\gamma, \rho, \mu) = \int d^3\vec{x} f(r) j_J(\kappa x) \vec{\mathcal{Y}}_{\gamma,\rho,1}^\mu \cdot \vec{J}, \tag{3.52}$$

the allowed terms become

$$\begin{aligned}
 & \delta(J-1, J-1, m) \mathcal{T}_4(J-1, J-1, m + \frac{1}{2}) \\
 & \delta(J, J-1, m) \mathcal{T}_4(J, J-1, m + \frac{1}{2}) \\
 & \delta(J, J+1, m) \mathcal{T}_4(J, J+1, m + \frac{1}{2}) \\
 & \delta(J+1, J+1, m) \mathcal{T}_4(J+1, J+1, m + \frac{1}{2}).
 \end{aligned}$$

For the second term containing $f(r)$ we need to expand the cross product by using the identity given in appendix (A.2). Multiplying by $\frac{1}{\kappa}$ and remembering that the differentiation gives a factor κ , we arrive at

$$\begin{aligned}
 \frac{1}{\kappa} \nabla \wedge \left(j_J(\kappa x) \vec{\mathcal{Y}}_{J,J,1}^M \right) &= -i \sqrt{\frac{J}{2J+1}} j_{J+1}(\kappa x) \vec{\mathcal{Y}}_{J,J+1,1}^M \\
 &+ i \sqrt{\frac{J+1}{2J+1}} j_{J-1}(\kappa x) \vec{\mathcal{Y}}_{J,J-1,1}^M.
 \end{aligned}$$

The analysis of these terms can be carried out in complete analogy to the previous ones so we skip the details. It is convenient to define some final quantities before giving the general expression for this part of the current. We introduce

$$\begin{aligned}
 \eta_+(\gamma, \rho, m) &= \sqrt{\frac{3/2-m}{3}} \sqrt{\frac{3}{4\pi}} \sqrt{J} [J+1] \langle 1 J+1 \rho | 000 \rangle \\
 &\times \langle 1 J \gamma | m - \frac{1}{2} 1 m + \frac{1}{2} \rangle W(1 J+1 \gamma 1; \rho J) \quad (3.53)
 \end{aligned}$$

$$\begin{aligned}
 \eta_-(\gamma, \rho, m) &= \sqrt{\frac{3/2-m}{3}} \sqrt{\frac{3}{4\pi}} \sqrt{J+1} [J-1] \langle 1 J-1 \rho | 000 \rangle \\
 &\times \langle 1 J \gamma | m - \frac{1}{2} 1 m + \frac{1}{2} \rangle W(1 J-1 \gamma 1; \rho J). \quad (3.54)
 \end{aligned}$$

There is no need to define new tensors at this point as the ones that arise here are simply \mathcal{T}_2 and \mathcal{T}_3 introduced above. Putting everything together we end up with the following rather lengthy expression for the $\lambda = -1$ spherical

component of the current

$$\begin{aligned}
 \int d^3\vec{x} l^{-1} \vec{e}_1 \cdot \vec{J} &= 2N^* \sum_{J=1}^{\infty} \sqrt{4\pi} [J] (-i)^J \{ i\delta_{m,1/2} \{ \mathcal{J}'_{J,1}{}^{el} - \mathcal{J}'_{J,1}{}^{mag} \} \\
 &\quad -\delta(J-1, J-1, m) \mathcal{T}_4(J-1, J-1, m + \frac{1}{2}) \\
 &\quad -\delta(J, J-1, m) \mathcal{T}_4(J, J-1, m + \frac{1}{2}) \\
 &\quad -\delta(J, J+1, m) \mathcal{T}_4(J, J+1, m + \frac{1}{2}) \\
 &\quad -\delta(J+1, J+1, m) \mathcal{T}_4(J+1, J+1, m + \frac{1}{2}) \\
 &\quad +i\eta_+(J, J, m) \mathcal{T}_2(J, J, m + \frac{1}{2}) \\
 &\quad +i\eta_+(J+1, J, m) \mathcal{T}_2(J+1, J, m + \frac{1}{2}) \\
 &\quad +i\eta_+(J+1, J+2, m) \mathcal{T}_2(J+1, J+2, m + \frac{1}{2}) \\
 &\quad -i\eta_-(J-1, J, m) \mathcal{T}_3(J-1, J, m + \frac{1}{2}) \\
 &\quad -i\eta_-(J, J, m) \mathcal{T}_3(J, J, m + \frac{1}{2}) \\
 &\quad -i\eta_-(J-1, J-2, m) \mathcal{T}_3(J-1, J-2, m + \frac{1}{2}) \}.
 \end{aligned} \tag{3.55}$$

The Full Interaction Hamiltonian

We now summarize the derivation by giving the full relativistic hamiltonian. It has the lengthy expression

$$\begin{aligned}
 H &= \frac{G}{\sqrt{2}} \int d^3\vec{x} \{ l_0 J_0 - l^3 \vec{e}_0 \cdot \vec{J} + l^{-1} \vec{e}_1 \cdot \vec{J} \} \\
 &= \frac{2GN^*}{\sqrt{2}} \left[\sum_{J=0}^{\infty} \sqrt{4\pi}[J] (-i)^J \{ i\delta_{m,-1/2} \{ \mathcal{M}'_{J,0} - \mathcal{L}'_{J,0} \} \right. \\
 &\quad + \alpha (J-1, J, m + \frac{1}{2}) \mathcal{T}_1 (J-1, J, m + \frac{1}{2}) \\
 &\quad + \alpha (J+1, J, m + \frac{1}{2}) \mathcal{T}_1 (J+1, J, m + \frac{1}{2}) \\
 &\quad - i\beta_+ (J, J, m) \mathcal{T}_2 (J, J, m + \frac{1}{2}) \\
 &\quad - i\beta_+ (J+1, J, m) \mathcal{T}_2 (J+1, J, m + \frac{1}{2}) \\
 &\quad - i\beta_+ (J+1, J+2, m) \mathcal{T}_2 (J+1, J+2, m + \frac{1}{2}) \\
 &\quad - i\beta_- (J-1, J-2, m) \mathcal{T}_3 (J-1, J-2, m + \frac{1}{2}) \\
 &\quad - i\beta_- (J-1, J, m) \mathcal{T}_3 (J-1, J, m + \frac{1}{2}) \\
 &\quad \left. - i\beta_- (J, J, m) \mathcal{T}_3 (J, J, m + \frac{1}{2}) \right\} \\
 &\quad + \sum_{J=1}^{\infty} \sqrt{4\pi}[J] (-i)^J \{ i\delta_{m,1/2} \{ \mathcal{J}'_{J,1}{}^{el} - \mathcal{J}'_{J,1}{}^{mag} \} \\
 &\quad - \delta (J-1, J-1, m) \mathcal{T}_4 (J-1, J-1, m + \frac{1}{2}) \\
 &\quad - \delta (J, J-1, m) \mathcal{T}_4 (J, J-1, m + \frac{1}{2}) \\
 &\quad - \delta (J, J+1, m) \mathcal{T}_4 (J, J+1, m + \frac{1}{2}) \\
 &\quad - \delta (J+1, J+1, m) \mathcal{T}_4 (J+1, J+1, m + \frac{1}{2}) \\
 &\quad + i\eta_+ (J, J, m) \mathcal{T}_2 (J, J, m + \frac{1}{2}) \\
 &\quad + i\eta_+ (J+1, J, m) \mathcal{T}_2 (J+1, J, m + \frac{1}{2}) \\
 &\quad + i\eta_+ (J+1, J+2, m) \mathcal{T}_2 (J+1, J+2, m + \frac{1}{2}) \\
 &\quad - i\eta_- (J-1, J, m) \mathcal{T}_3 (J-1, J, m + \frac{1}{2}) \\
 &\quad - i\eta_- (J, J, m) \mathcal{T}_3 (J, J, m + \frac{1}{2}) \\
 &\quad \left. - i\eta_- (J-1, J-2, m) \mathcal{T}_3 (J-1, J-2, m + \frac{1}{2}) \right\}. \tag{3.56}
 \end{aligned}$$

This hamiltonian is truly a horrible piece of formalism! In order to reduce it to something that is more convenient when trying to group the terms, we

now make another round of definitions.

$$\mathcal{X}^1(J, 0) = i\delta_{m,-1/2} \left\{ \mathcal{M}'_{J,0} - \mathcal{L}'_{J,0} \right\} \quad (3.57)$$

$$\begin{aligned} \mathcal{X}^2(J-1, m + \tfrac{1}{2}) &= \alpha(J-1, J, m + \tfrac{1}{2}) \mathcal{T}_1(J-1, J, m + \tfrac{1}{2}) \\ &\quad - i\beta_-(J-1, J-2, m) \mathcal{T}_3(J-1, J-2, m + \tfrac{1}{2}) \\ &\quad - i\beta_-(J-1, J, m) \mathcal{T}_3(J-1, J, m + \tfrac{1}{2}) \end{aligned} \quad (3.58)$$

$$\begin{aligned} \mathcal{X}^3(J, m + \tfrac{1}{2}) &= -i\beta_+(J, J, m) \mathcal{T}_2(J, J, m + \tfrac{1}{2}) \\ &\quad - i\beta_-(J, J, m) \mathcal{T}_3(J, J, m + \tfrac{1}{2}) \end{aligned} \quad (3.59)$$

$$\begin{aligned} \mathcal{X}^4(J+1, m + \tfrac{1}{2}) &= \alpha(J+1, J, m + \tfrac{1}{2}) \mathcal{T}_1(J+1, J, m + \tfrac{1}{2}) \\ &\quad - i\beta_+(J+1, J, m) \mathcal{T}_2(J+1, J, m + \tfrac{1}{2}) \\ &\quad - i\beta_+(J+1, J+2, m) \mathcal{T}_2(J+1, J+2, m + \tfrac{1}{2}) \end{aligned} \quad (3.60)$$

$$\mathcal{Z}^1(J, 1) = i\delta_{m,1/2} \left\{ \mathcal{J}'_{J,1}{}^{el} - \mathcal{J}'_{J,1}{}^{mag} \right\} \quad (3.61)$$

$$\begin{aligned} \mathcal{Z}^2(J-1, m + \tfrac{1}{2}) &= -\delta(J-1, J-1, m) \mathcal{T}_4(J-1, J-1, m + \tfrac{1}{2}) \\ &\quad - i\eta_-(J-1, J, m) \mathcal{T}_3(J-1, J, m + \tfrac{1}{2}) \\ &\quad - i\eta_-(J-1, J-2, m) \mathcal{T}_3(J-1, J-2, m + \tfrac{1}{2}) \end{aligned} \quad (3.62)$$

$$\begin{aligned} \mathcal{Z}^3(J, m + \tfrac{1}{2}) &= -\delta(J, J-1, m) \mathcal{T}_4(J, J-1, m + \tfrac{1}{2}) \\ &\quad - \delta(J, J+1, m) \mathcal{T}_4(J, J+1, m + \tfrac{1}{2}) \\ &\quad - i\eta_-(J, J, m) \mathcal{T}_3(J, J, m + \tfrac{1}{2}) \end{aligned} \quad (3.63)$$

$$\begin{aligned} \mathcal{Z}^4(J+1, m + \tfrac{1}{2}) &= -\delta(J+1, J+1, m) \mathcal{T}_4(J+1, J+1, m + \tfrac{1}{2}) \\ &\quad + i\eta_+(J+1, J, m) \mathcal{T}_2(J+1, J, m + \tfrac{1}{2}) \\ &\quad + i\eta_+(J+1, J+2, m) \mathcal{T}_2(J+1, J+2, m + \tfrac{1}{2}). \end{aligned} \quad (3.64)$$

These terms have the advantage that they have the tensor character (J, M) indicated in the parenthesis. One must, however, remember that the constants in these expressions depend explicitly on m . The above quantities can now be inserted into the hamiltonian. However, each of these is non-zero only when the angular momentum is non-negative. To ease the application of the Wigner-Eckart theorem in squaring the matrix element, it is advantageous to change the bounds on the sums over angular momenta. This yields

the following more compact hamiltonian

$$\begin{aligned}
 H &= \frac{2GN^*}{\sqrt{2}} \left[\sum_{J=0}^{\infty} \sqrt{4\pi}[J](-i)^J \{ \mathcal{X}^1(J, 0) + \mathcal{X}^3(J, m + \frac{1}{2}) \} \right. \\
 &+ \sum_{J=0}^{\infty} \sqrt{4\pi}[J](-i)^J \{ \mathcal{X}^4(J + 1, m + \frac{1}{2}) \} \\
 &+ \sum_{J=1}^{\infty} \sqrt{4\pi}[J](-i)^J (\mathcal{X}^2(J - 1, m + \frac{1}{2}) + \mathcal{Z}^2(J - 1, m + \frac{1}{2}) \\
 &\left. + \mathcal{Z}^1(J, 1) + \mathcal{Z}^3(J, m + \frac{1}{2}) + \mathcal{Z}^4(J + 1, m + \frac{1}{2}) \right). \quad (3.65)
 \end{aligned}$$

We now shift the sums so that all tensors have angular momentum J to make it simpler to calculate the interference terms when squaring. This yields

$$\begin{aligned}
 H &= \frac{2GN^*}{\sqrt{2}} \left[\sum_{J=0}^{\infty} \sqrt{4\pi}[J](-i)^J \{ \mathcal{X}^1(J, 0) + \mathcal{X}^3(J, m + \frac{1}{2}) \} \right. \\
 &+ \sum_{J=1}^{\infty} \sqrt{4\pi}[J - 1](-i)^J i \mathcal{X}^4(J, m + \frac{1}{2}) \\
 &+ \sum_{J=1}^{\infty} \sqrt{4\pi}[J](-i)^J \{ \mathcal{Z}^3(J, m + \frac{1}{2}) + \mathcal{Z}^1(J, 1) \} \\
 &+ \sum_{J=0}^{\infty} \sqrt{4\pi}[J + 1](-i)^J (-i) \{ \mathcal{X}^2(J, m + \frac{1}{2}) + \mathcal{Z}^2(J, m + \frac{1}{2}) \} \\
 &\left. + \sum_{J=2}^{\infty} \sqrt{4\pi}[J - 1](-i)^J i \mathcal{Z}^4(J, m + \frac{1}{2}) \right). \quad (3.66)
 \end{aligned}$$

The Matrix Element

We need to find the matrix element with the nuclear states of good angular momentum and use the Wigner-Eckart theorem to get reduced matrix elements. For simplicity we introduce the notations

$$a_J^M = (-1)^{J_f - M_f} \begin{pmatrix} J_f & J & J_i \\ -M_f & M & M_i \end{pmatrix} \quad (3.67)$$

$$|\mathcal{T}_J| = \langle J_f || \mathcal{T}_J || J_i \rangle. \quad (3.68)$$

The completeness relation for the 3-j symbols is then given by

$$\sum_{M_i, M_f} (a_J^M)^* a_J^{M'} = \frac{1}{2J+1} \delta_{M, M'} \delta_{J, J'} = [J]^{-2} \delta_{M, M'} \delta_{J, J'}. \quad (3.69)$$

Using these notations, the matrix element becomes (with $\mu = m + \frac{1}{2}$)

$$\begin{aligned}
 \langle f | \mathbf{H} | i \rangle &= \frac{2\text{GN}^*}{\sqrt{2}} \left[\sum_{J=0}^{\infty} \sqrt{4\pi} [J] (-i)^J \{ a_J^0 | \mathcal{X}_J^1 | + a_J^\mu | \mathcal{X}_J^3 | \} \right. \\
 &+ \sum_{J=1}^{\infty} \sqrt{4\pi} [J-1] (-i)^{J-1} a_J^\mu | \mathcal{X}_J^4 | \\
 &+ \sum_{J=1}^{\infty} \sqrt{4\pi} [J] (-i)^J \{ a_J^1 | \mathcal{Z}_J^1 | + a_J^\mu | \mathcal{Z}_J^3 | \} \\
 &+ \sum_{J=0}^{\infty} \sqrt{4\pi} [J+1] (-i)^{J+1} \{ a_J^\mu | \mathcal{X}_J^2 | + a_J^\mu | \mathcal{Z}_J^2 | \} \\
 &\left. + \sum_{J=2}^{\infty} \sqrt{4\pi} [J-1] (-i)^{J-1} a_J^\mu | \mathcal{Z}_J^4 | \right]. \tag{3.70}
 \end{aligned}$$

We assumed an unpolarized nucleus and thus have to average over initial projection quantum numbers for both nucleus and muon. We also have to sum over final states since we assume that no polarization is measured in the final state. The quantity we are interested in is thus

$$\frac{1}{2} \sum_{\mu=0,1} \frac{1}{2J_i + 1} \sum_{M_i, M_f} |\langle f | \mathbf{H} | i \rangle|^2. \tag{3.71}$$

We notice that for ($m = -\frac{1}{2} \Leftrightarrow \mu = 0$) we only have interference terms between \mathcal{X}^1 and all the $f(r)$ terms ($\mathcal{X}^i, \mathcal{Z}^i, i \geq 2$). For ($m = \frac{1}{2} \Leftrightarrow \mu = 1$) it is only \mathcal{Z}^1 that has these interference terms. Another way to see this is to notice that the definitions of these leading multipole operators \mathcal{X}^1 and \mathcal{Z}^1 involve $\delta_{m, \pm 1/2}$.

First we find the terms that contribute for ($m = -1/2 \Leftrightarrow \mu = 0$). There are a couple of direct terms (same sum in eq. (3.70))

$$\sum_{J=0}^{\infty} |\mathcal{X}_J^1|^2 + 2\text{Re} \sum_{J=0}^{\infty} |\mathcal{X}_J^1|^* |\mathcal{X}_J^3|. \tag{3.72}$$

The other terms give expressions like

$$\begin{aligned}
 &2\text{Re} \sum_{J=0}^{\infty} \sum_{J'=1}^{\infty} [J][J'-1] (i)^J (-i)^{J'-1} |\mathcal{X}_J^1|^* |\mathcal{X}_{J'}^4| \sum_{M_i, M_f} (a_J^0)^* a_{J'}^0 \\
 &= 2\text{Re} \sum_{J=1}^{\infty} \frac{[J-1]}{[J]} i |\mathcal{X}_J^1|^* |\mathcal{X}_J^4|. \tag{3.73}
 \end{aligned}$$

The case with $m = 1/2, \mu = 1$ is analogous. Using these techniques we can now write down our final expression for the total matrix element in terms

of reduced matrix elements of the various tensor operators. The result is

$$\begin{aligned}
 & \frac{1}{2} \sum_{\mu=0,1} \frac{1}{2J_i+1} \sum_{M_i, M_f} |\langle f | \mathbf{H} | i \rangle|^2 = \frac{4\pi G^2 |N|^2}{2J_i+1} \left[\sum_{J=0}^{\infty} |\mathcal{X}_J^1|^2 + \sum_{J=1}^{\infty} |\mathcal{Z}_J^1|^2 \right. \\
 & + 2\text{Re} \left\{ \sum_{J=0}^{\infty} |\mathcal{X}_J^1|^* |\mathcal{X}_J^3| + \sum_{J=0}^{\infty} \frac{[J+1]}{[J]} (-i) |\mathcal{X}_J^1|^* (|\mathcal{X}_J^2| + |\mathcal{Z}_J^2|) \right. \\
 & + \sum_{J=1}^{\infty} \left(\frac{[J-1]}{[J]} i |\mathcal{X}_J^1|^* |\mathcal{X}_J^4| + |\mathcal{X}_J^1|^* |\mathcal{Z}_J^3| + |\mathcal{Z}_J^1|^* (|\mathcal{X}_J^3| + |\mathcal{Z}_J^3|) \right) \\
 & + \sum_{J=2}^{\infty} \frac{[J-1]}{[J]} i (|\mathcal{X}_J^1|^* + |\mathcal{Z}_J^1|^*) |\mathcal{Z}_J^4| \\
 & + \sum_{J=1}^{\infty} \frac{[J+1]}{[J]} (-i) |\mathcal{Z}_J^1|^* (|\mathcal{X}_J^2| + |\mathcal{Z}_J^2|) + \sum_{J=1}^{\infty} \frac{[J-1]}{[J]} i |\mathcal{Z}_J^1|^* |\mathcal{X}_J^4| \left. \right\} \\
 & + \sum_{\mu=0,1} \left[\sum_{J=0}^{\infty} \left(\frac{[J+1]^2}{[J]^2} \{ |\mathcal{X}_J^2|^2 + |\mathcal{Z}_J^2|^2 \} + |\mathcal{X}_J^3|^2 + |\mathcal{Z}_J^3|^2 \right) \right. \\
 & + \sum_{J=1}^{\infty} \frac{[J-1]^2}{[J]^2} |\mathcal{X}_J^4|^2 + \sum_{J=2}^{\infty} \frac{[J-1]^2}{[J]^2} |\mathcal{Z}_J^4|^2 \\
 & + \sum_{\mu=0,1} 2\text{Re} \left\{ \sum_{J=1}^{\infty} \frac{[J-1][J+1]}{[J]^2} (-i)^2 |\mathcal{X}_J^4|^* [|\mathcal{X}_J^2| + |\mathcal{Z}_J^2|] \right. \\
 & + \sum_{J=2}^{\infty} \left[\frac{[J-1]^2}{[J]^2} |\mathcal{X}_J^4|^* |\mathcal{Z}_J^4| + \frac{[J-1][J+1]}{[J]^2} (i)^2 |\mathcal{Z}_J^4|^* (|\mathcal{X}_J^2| + |\mathcal{Z}_J^2|) \right] \\
 & + \sum_{J=1}^{\infty} \left[\frac{[J-1]}{[J]} i |\mathcal{X}_J^3|^* |\mathcal{X}_J^4| + |\mathcal{X}_J^3|^* |\mathcal{Z}_J^3| \right] \\
 & + \sum_{J=2}^{\infty} \frac{[J-1]}{[J]} i [|\mathcal{X}_J^3|^* |\mathcal{Z}_J^4| + |\mathcal{Z}_J^3|^* |\mathcal{Z}_J^4|] \\
 & + \sum_{J=1}^{\infty} \left[\frac{[J-1]}{[J]} i |\mathcal{Z}_J^3|^* |\mathcal{X}_J^4| + \frac{[J+1]}{[J]} (-i) |\mathcal{Z}_J^3|^* (|\mathcal{X}_J^2| + |\mathcal{Z}_J^2|) \right] \\
 & \left. + \sum_{J=0}^{\infty} \frac{[J+1]}{[J]} (-i) |\mathcal{X}_J^3|^* [|\mathcal{X}_J^2| + |\mathcal{Z}_J^2|] \right\}. \tag{3.74}
 \end{aligned}$$

The first two terms are those that contain only the large component $g(r)$. The next block are the interference terms of multipoles with $g(r)$ and $f(r)$ respectively. After that we have the terms with only $f(r)$. There are both direct and interference terms coming from the latter, since they are present for both values of μ . We must remember that the constants that we have defined through this derivation depend explicitly on m or $\mu = m + 1/2$. In the first block of interference terms we can get the value of μ by looking

at whether the term multiplies an \mathcal{X}^1 or a \mathcal{Z}^1 factor. The former is only present for $\mu = 0$, whereas the latter exists only for $\mu = 1$. For the other terms we have simply kept the sum over μ .

Evaluation of the Tensor Terms

To arrive at the expression for the matrix element given above, we introduced four new tensors in addition to the four that we gave in eqs. (2.14), (2.15), (2.16), and (2.17). They were defined by

$$\mathcal{T}_1(\rho, J, \mu) = \int d^3\vec{x} f(r) j_J(\kappa x) Y_{\rho, \mu} J_0 \quad (3.75)$$

$$\mathcal{T}_2(\gamma, \rho, \mu) = \int d^3\vec{x} f(r) j_{J+1}(\kappa x) \vec{\mathcal{Y}}_{\gamma, \rho, 1}^\mu \cdot \vec{J} \quad (3.76)$$

$$\mathcal{T}_3(\gamma, \rho, \mu) = \int d^3\vec{x} f(r) j_{J-1}(\kappa x) \vec{\mathcal{Y}}_{\gamma, \rho, 1}^\mu \cdot \vec{J} \quad (3.77)$$

$$\mathcal{T}_4(\gamma, \rho, \mu) = \int d^3\vec{x} f(r) j_J(\kappa x) \vec{\mathcal{Y}}_{\gamma, \rho, 1}^\mu \cdot \vec{J}. \quad (3.78)$$

Notice that the tensors have a dependence on the angular momentum J on their spherical Bessel components coming from the multipole expansion of the neutrino plane wave.

To implement these new terms in our nuclear model we need to insert the nuclear current operators and reduce the expressions to single-particle matrix elements, in the same fashion as for the neutrino capture operators in section (2.2.3). The procedure becomes more involved due to the presence of the muon wave function and the fact that the order of the spherical Bessels are different in the new tensor (as mentioned above). It is, however, a principally straightforward exercise in coupling and recoupling of tensor products along the lines of Edmonds [28].

3.3 Quenching of Multipoles

We showed in section (2.2.2) that the RPA model fulfills the sum rules for the important cases of Fermi and GT transitions. Previous works on muon capture using the RPA have suggested that no quenching is needed on the nuclear axial-vector coupling G_A [101, 35]. As we have stressed several times, the response is dominated by giant resonances at energies of around and above 15 MeV (decreasing with mass and charge numbers), so we do not expect to be very sensitive to low energy strength. In addition, the GT operators will contribute very little in heavier nuclei due to Pauli blocking of the states that the GT can connect to, so again we should not be too sensitive to quenching of this operator.

For lighter nuclei there can be contributions at low energy from the GT operator and in order not to overestimate these we use quenching here. In

particular, we have reduced the low energy (up to 15 MeV) part of the 1^+ multipole (which is virtually only GT contributions) by the common factor $(0.8)^2 = 0.64$ which is the recommended value [108]. This procedure has been used for all nuclei with N or Z less than 40.

In principle, our calculations here can also tell us about quenching in other multipoles. We have found that no such quenching was needed in order to get a good reproduction of the experimental data on muon capture. This leads us to conclude that inclusive semi-leptonic processes with momentum transfer of order $q \sim m_\mu$ can be described accurately with the unquenched strengths of operators other than GT. Higher multipoles generally have their resonances at higher energies so we can conclude that our model works quite well for weak interactions on nuclei in a wide energy range. We thus feel confident that it can also be used for neutrino processes in the same range of energy, including the ones that come from Supernovae that will be our concern in subsequent chapters.

3.4 The Residual Interaction

A final detail that we have to address before presenting the results, is concerned with the parameters of the residual interaction. In section (2.2.2) we have presented the typical parameters of the Landau-Migdal force that we use as residual interaction. Since muon capture in most stable nuclei suffers severe Pauli blocking effects, it is dominated by forbidden transitions (higher order spin-isospin operators) and the most important parameter is therefore the spin-isospin coupling g' . We will therefore only discuss g' in connection with muon capture, keeping the rest of the parameters fixed at the values given earlier.²

In the older recommendations of Rinker and Speth [41] the value $g' = 0.7$ is given. This was found to be quite good for reproducing the data in light nuclei such as ^{12}C and ^{16}O [101]. However, the calculations with $g' = 0.7$ shown in figure (3.1) have obvious problems for heavier nuclei as discussed earlier. Considering the fact that the spin-isospin term is repulsive for the dominant $T = 1$ and $S = 1$ term in muon capture on heavy nuclei (the 1^+ multipole), a larger g' pushes strength to higher energies and thus reduces the rate. So we are in a situation where we seem to need different parameters for light and heavy nuclei.

Fortunately, the recent review [43] cites a recommended value in heavy nuclei of $g' = 0.96$. So we have an indication that there could be a mass dependence of the coupling. For simplicity (and lack of a better, more consistent option), we introduce the following simple interpolation formula

$$g' = c_1 + c_2 A^{1/3}. \quad (3.79)$$

²We have made several investigations into the dependence of the capture rate on the other parameters and have found very little sensitivity.

The constants c_1 and c_2 are fitted so that $g' = 0.74$ in ^{16}O and $g' = 0.96$ in ^{208}Pb . We now have a mild dependence on nuclear mass in the axial coupling constant, which introduces about 10% changes in the rate as compared to the fixed value $g' = 0.7$ for all nuclei.

3.5 Results and Discussion

Having discussed all the particular features needed to specify and improve our model for describing muon capture, we are now ready to present the results of the new rate calculations. We will only be presenting rates for even-even nuclei since these are (principally) the cases where the model is applicable. Including odd-even and odd-odd could introduce deviations due to the $J \neq 0$ ground-state and we therefore exclude these nuclei to make the comparison more transparent (we note that the general trends of the data are reproduced for these cases as well).

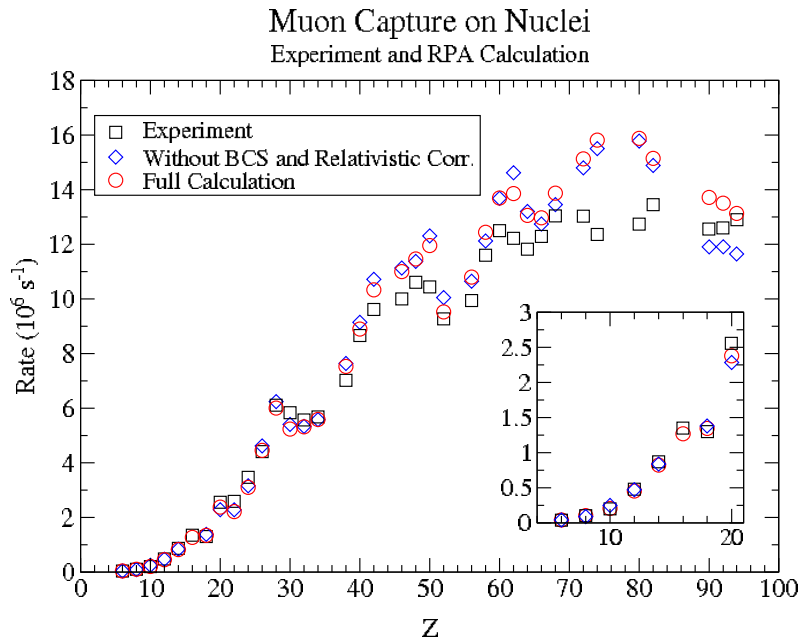


Figure 3.3: Comparison between the measured total muon capture rates [102] denoted by squares \square , the calculated rates with all corrections (empty circles \circ), and the calculated rates without the BCS and relativistic corrections (diamonds \diamond). The insert, in larger scale, shows the same results for light nuclei. When the measurements are for the natural abundance of a given element, the calculation represent the corresponding combination of the individual isotopes.

In figure (3.3) the total capture rates as a function of charge for all

measured even-even nuclei is shown. We see that the overall agreement is now quite good. In particular, the new results represent a vast improvement over the results of our old model shown in figure (3.1). The region around $Z = 74$ and $Z = 80$ is the exception to the overall good agreement, a point that we will comment on below. With these exceptions in mind we have obtained agreement with the data to 15% or better in all nuclei. This we display graphically in figure (3.4) where we plot the ratio of the new RPA calculations to the experimental values.

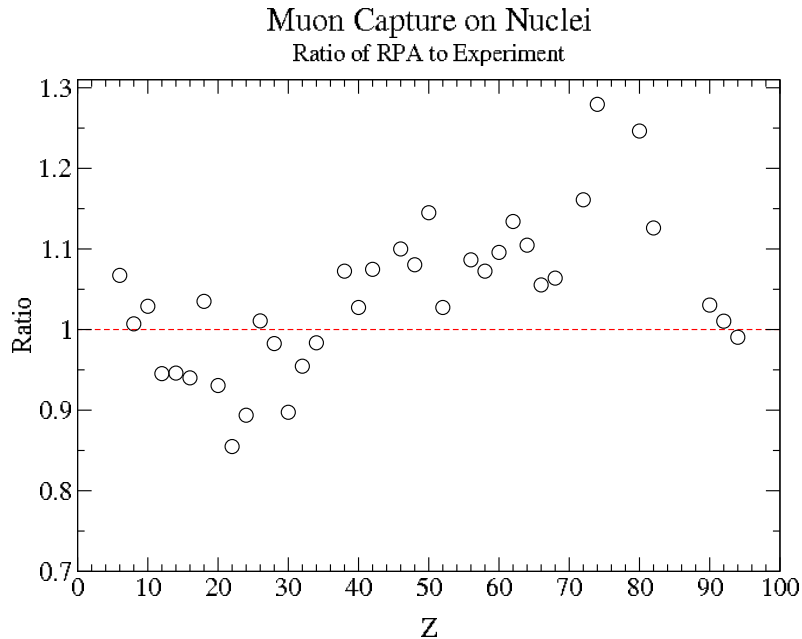


Figure 3.4: Ratios of the calculated and measured total muon capture rates versus the atomic number.

The rates have also been given without the BCS occupancies and with no relativistic corrections to the muon wave function. Inspecting figure (3.3) we see that the differences to the full calculation is small, justifying the previous work [101, 35, 34]. However, the corrections from BCS and the full muon wave function generally tend to improve the overall agreement with data. We note that we have a very good reproduction of the distinct dips in the rate at magic numbers $Z = 20$ and 28 . At $Z = 50$ we see the same thing, although we overshoot the experimental data somewhat. At the $N = 82$ shell closure (coming in above $Z = 60$) we also overestimate the rates, a trend that continues into the region between $Z = 72$ and 80 , and to a lesser extent also for the doubly-magic nucleus ^{208}Pb . Here it must be remembered that some nuclei in the region below ^{208}Pb are deformed. This

means that the single-particle structure is certainly different from the one of our spherical mean-field model. We should therefore not expect perfect agreement. When looking at the heaviest nuclei where the rate is known experimentally, Th, U, and Pu, we find much better agreement. This is, however, likely a consequence of the dips beyond magic shell closure that we also saw at lower Z (an effect that was also noted in [111], see in particular Fig. 3 of that reference).

As we have noted above, we have used the unquenched axial-vector coupling constant for all states, except for the low-energy 1^+ contributions, the region where the Gamow-Teller transition is found. For light- and medium-mass nuclei the dominant multipole is the spin-dipole 1^- operator (and to a lesser extent also the quadrupole-like 2^+ multipole). Our results thus indicate that no quench is needed for these operators. However, for heavier nuclei like ^{208}Pb and beyond we get significant contributions from the 1^+ transition. The neutron excess of these nuclei completely block the pure GT operator and the 1^+ in this case corresponds to a transition across two major oscillator shells, a $2\hbar\omega$ mode. The relatively good agreement with data thus supports absence of quenching for such modes.

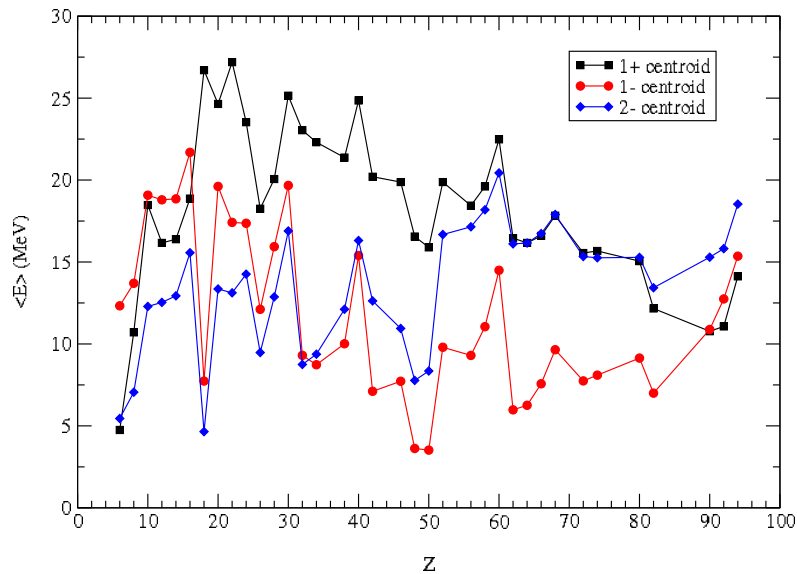


Figure 3.5: Centroids for 1^+ (black squares), 1^- (red circles), and 2^- (blue tilted squares) multipole responses as a function of the charge Z . The centroids are calculated from $\langle E \rangle = \sum_f \lambda_f E_f / \lambda_{tot}$, where the sum is over all states f that contribute to the particular multipole, λ_f is the partial rate of the state f , and E_f is the energy of this state in the daughter. λ_{tot} is the total rate for the multipole.

To further elaborate on the discussion of multipole contributions, we show centroids of some important operators in figure (3.5). For the 1^+ we clearly see the trends referred to earlier; it starts out at low energy for light nuclei (where the GT gives contributions), then resides at high energy for medium-mass (where GT is blocked and $2\hbar\omega$ are high in the spectrum) and finally starts moving downwards for heavy nuclei. Meanwhile, we see that the two forbidden transitions shown, 1^- and 2^- , have lower energy centroids except for the heaviest region. The figure also nicely illustrates the shell structures found in our calculations. We clearly see the dips around the same positions as seen in the total rates.

In table (3.1) we give the results for all nuclei that were calculated in the new study. The table has both natural elements and the values for all isotopes that contribute significantly to the natural abundance. An important issue for nuclear structure models is to be able to reproduce trends in the rate that are observed as a function of neutron number for fixed charge. Such effects are taken into account by the well-known Primakoff scaling law that gives the rate as a function of $(N - Z)$ [114]. In the table we have included three isotope chains (Ca, Cr and Ni) where the rates are known experimentally in the individual isotopes. Here one clearly sees the isotope dependence of the rate as the increase of N blocks final states. This is well reproduced by our model, as was also concluded in [34, 104].

In figure (3.6) we compare the results of our calculations for all nuclei given in table (3.1) to the Primakoff scaling rule

$$\Lambda(A, Z) = Z_{eff}^4 X_1 \left[1 - X_2 \frac{A - Z}{2A} \right] \quad (3.80)$$

where X_1 is the capture rate in hydrogen (reduced by the neutrino phase space), and X_2 parametrizes Pauli blocking. We have used the values $X_1 = 170 \text{ s}^{-1}$ and $X_2 = 3.125$ from [102]. To isolate the actual structure effects, we have plotted the reduced rates in figure (3.6), which have been divided by Z_{eff}^4 (Z_{eff} from [102]). Looking at the figure, we see good agreement between our calculations and the Primakoff rule for all nuclei except some of those with $(A - Z)/2A = 0.25$. The latter deviations are for the lightest nuclei where we do not expect perfect agreement. We thus conclude that our method can handle isotopic features for many nuclei across the nuclear chart.

3.6 Concluding Remarks

We have found above that our simple RPA calculations reproduce the muon capture rate for virtually all measured nuclei with an accuracy of 15% or better. We also reproduce structure effects of shell closures when considering the rate as a function of charge and mass numbers. No indication

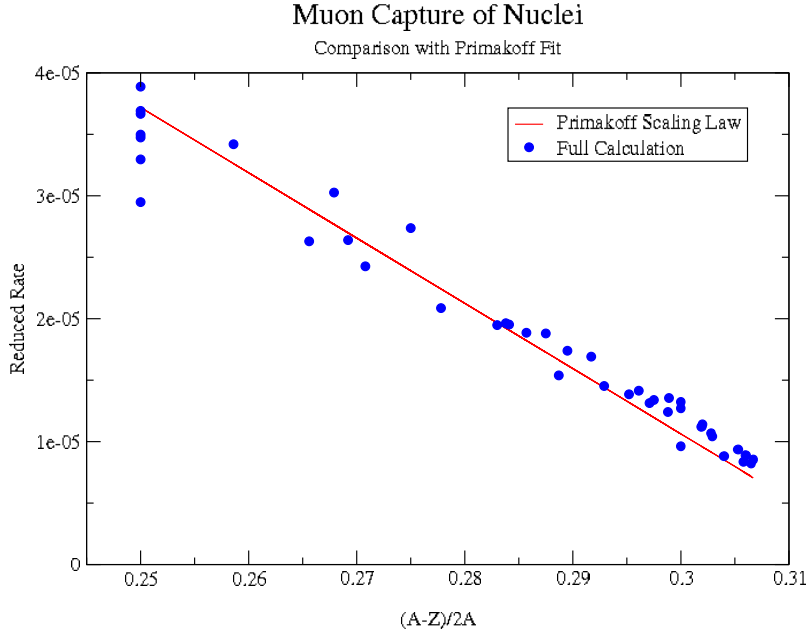


Figure 3.6: Comparison of the calculated muon capture rates with the Primakoff scaling rule given in eq. (3.80).

of quenching of nuclear response was found, apart from $0\hbar\omega$ 1^+ transitions at low energy associated with the spin-isospin GT operator. In order to describe the rate for a great number of nuclei, we have included both smearing of the Fermi level through BCS-like single-particle occupation and also the full Dirac wave function for the muon. We found the effects of both to be small, yet still enough to make a noticeable improvement on the overall agreement between experiment and calculation.

Our study of muon capture across the nuclear chart thus leaves us with confidence that the model handles semi-leptonic weak processes on nuclei with similar momentum transfers accurately. As the neutrino and antineutrino capture reactions have similar energetics, we expect that our model will also work to within the same accuracy for those processes.

Nuc	exp	calc	Nuc	exp	calc	Nuc	exp	calc
¹² C	0.039	0.042	¹⁶ O	0.103	0.104	¹⁸ O	0.088	0.089
²⁰ Ne	0.204	0.206	²⁴ Mg	0.484	0.454	²⁸ Si	0.871	0.823
³² S	1.352	1.269	⁴⁰ Ar	1.355	1.345	⁴⁰ Ca	2.557	2.379
⁴⁴ Ca	1.793	1.946	⁴⁸ Ca	1.214 ¹	1.455	⁴⁸ Ti	2.590	2.214
<i>nat</i> Cr	3.472	3.101	⁵⁰ Cr	3.825	3.451	⁵² Cr	3.452	3.085
⁵⁴ Cr	3.057	3.024	⁵⁶ Fe	4.411	4.457	<i>nat</i> Ni	5.932	6.004
⁵⁸ Ni	6.110	6.230	⁶⁰ Ni	5.560	5.563	⁶² Ni	4.720	4.939
<i>nat</i> Zn	5.834	5.235	⁶⁴ Zn		5.735	⁶⁶ Zn		4.976
⁶⁸ Zn		4.328	<i>nat</i> Ge	5.569	5.317	⁷⁰ Ge		5.948
⁷² Ge		5.311	⁷⁴ Ge		4.970	<i>nat</i> Se	5.681	5.588
⁷⁸ Se		6.023	⁸⁰ Se		5.485	⁸² Se		5.024
<i>nat</i> Sr	7.020	7.529	⁸⁶ Sr		8.225	⁸⁸ Sr	6.610	7.445
<i>nat</i> Zr	8.660	8.897	⁹⁰ Zr		8.974	⁹² Zr		9.254
⁹⁴ Zr		8.317	<i>nat</i> Mo	9.614	10.33	⁹² Mo		10.80
⁹⁴ Mo		11.01	⁹⁶ Mo		10.04	⁹⁸ Mo		9.153
<i>nat</i> Pd	10.00	11.00	¹⁰⁴ Pd		12.71	¹⁰⁶ Pd		11.44
¹⁰⁸ Pd		10.44	¹¹⁰ Pd		9.607	<i>nat</i> Cd	10.61	11.46
¹¹⁰ Cd		12.58	¹¹² Cd		11.51	¹¹⁴ Cd		11.21
¹¹⁶ Cd		10.44	<i>nat</i> Sn	10.44	11.95	¹¹⁶ Sn		13.08
¹¹⁸ Sn		12.35	¹²⁰ Sn		11.64	¹²² Sn		10.82
¹²⁴ Sn		10.15	<i>nat</i> Te	9.270	9.523	¹²⁶ Te		10.20
¹²⁸ Te		9.639	¹³⁰ Te		9.043	<i>nat</i> Ba	9.940	10.80
¹³⁶ Ba		11.45	¹³⁸ Ba		10.73	<i>nat</i> Ce	11.60	12.44
¹⁴⁰ Ce		12.38	¹⁴² Ce		12.95	<i>nat</i> Nd	12.50	13.70
¹⁴² Nd		13.67	¹⁴⁴ Nd		14.12	¹⁴⁶ Nd		13.15
<i>nat</i> Sm	12.22	13.86	¹⁴⁸ Sm		15.01	¹⁵² Sm		13.23
¹⁵⁴ Sm		12.08	<i>nat</i> Gd	11.82	13.06	¹⁵⁶ Gd		14.15
¹⁵⁸ Gd		13.06	¹⁶⁰ Gd		12.03	<i>nat</i> Dy	12.29	12.97
¹⁶² Dy		13.45	¹⁶⁴ Dy		12.54	<i>nat</i> Er	13.04	13.87
¹⁶⁶ Er		14.46	¹⁶⁸ Er		13.51	¹⁷⁰ Er		13.22
<i>nat</i> Hf	13.03	15.13	¹⁷⁸ Hf		15.44	¹⁸⁰ Hf		14.89
<i>nat</i> W	12.36	15.81	¹⁸² W		16.37	¹⁸⁴ W		15.79
¹⁸⁶ W		15.32	<i>nat</i> Hg	12.74	15.88	¹⁹⁸ Hg		17.17
²⁰⁰ Hg		16.29	²⁰² Hg		15.43	²⁰⁴ Hg		14.58
<i>nat</i> Pb	13.45	15.15	²⁰⁶ Pb		15.54	²⁰⁸ Pb		14.97
²³² Th	12.56	13.71	²³⁴ U	13.79	14.89	²³⁶ U	13.09 ²	14.17
²³⁸ U	12.57 ²	13.51	²⁴² Pu	12.90	13.13	²⁴⁴ Pu	12.40 ³	12.70

Table 3.1: Calculated rates for natural elements and for the important individual isotopes. All rates are in the form $xx \times 10^6 \text{ s}^{-1}$. If the natural abundance has more than 90% of a given isotope then the Nuc column gives this particular isotope and the calculation is done for this nucleus only. Whenever a nucleus has the superscript *nat* the calculation is a weighted combination of all isotopes contributing more than 10% to the natural abundance. An empty experiment box means that the given isotope has not been measured. Natural abundance measurements appear in the box next to the most abundant isotope. Experimental data are from [102], where the original sources may be found. ¹ is taken from [112], ² is from [111], and ³ is from [113].

Chapter 4

Neutrinos and Proton-Rich Ejecta

4.1 Introduction

In nature one finds small abundances of proton-rich (p) nuclei.¹ They are generally believed to be produced by a photo dissociation process (called the p -process) and the conditions for such reactions to take place and produce the right abundances was already discussed in the classical nucleosynthesis work of B²FH [6] and Cameron [7]. The site of this process is thought to be the hot Supernova environment. However, while heavy p nuclei are accounted for by photo disintegration of preexisting heavy elements (produced in neutron capture processes), the lighter ones are under produced in previous studies [115, 116, 117]. The p -process has therefore been shrouded by mystery throughout the 50 years that have elapsed since the foundational work of B²FH.

There is strong evidence from galactic chemical evolution studies that light elements are produced in primary processes [118, 119, 120]. This means that the environment must simultaneously produce the seed nuclei on which to capture neutrons or protons. This is true for the r -process, whereas the s -process that produces the heavy nuclei around stability is secondary. For p nuclei the mechanism is largely unknown but there are indications that suggest primary Supernova birth for these as well [121]. The same indication comes about from measurements of hyper-metal-poor stars in the Milky Way [122] (as discussed in chapter (1)).

Meanwhile, a number of recent Supernova simulation studies have found that the ejected matter from the innermost regions around the mass cut is proton-rich during the early stage of the explosion [123, 124, 125]. The proton densities and temperatures in this matter are in line with the suggestions of B²FH and it therefore seems a viable candidate for p -process

¹These nuclei lie above the line of β -stability in the nuclear chart.

nucleosynthesis. As we will discuss below, neutrinos have a decisive influence on both the proton-richness and the subsequent nucleosynthesis of the innermost supernova ejecta. This is not surprising since the material sits close to the protoneutron star and the flux of neutrinos is large. Our main concern is the influence of these neutrinos on the composition of these inner layers of matter. As we will see, this environment holds promise toward a consistent production of light p nuclei in a collaborative effort of neutrinos and protons that we have termed 'the νp -process'.

4.2 Neutrino Reactions on Matter

As mentioned, the innermost ejecta that we want to study are subject to large neutrino fluxes. We thus need to consider their effect on the material. The important quantity of concern to us is the electron fraction Y_e introduced in chapter (1). It is determined by the interplay of the weak interactions in the material, mainly through the reactions



We thus see that dominant neutrino/positron capture can drive the material proton-rich, whereas neutrino emission and electron capture will drive it neutron-rich. The balance between these reactions can be quite complicated in realistic models and the subsequent evolution equations must be solved numerically for the relevant environment given by the hydrodynamical stellar model. We will briefly touch upon this in the next section.

It is worth discussing a few aspects of the physics governing Y_e and particularly the conditions for proton-richness of the material (this is discussed in some detail in [129], building on the classic study by Bruenn [130]). The relevant variables are the electron chemical potential μ_e , the neutron-proton mass difference $M_{np} = 1.293$ MeV, and the neutrino energy. In dense environments, the electron gas is squeezed to degeneracy with large μ_e and favorable conditions for electron capture on nucleons and nuclei. However, as the star explodes, matter is diluted and μ_e drops. The neutrino and antineutrino energies dominate over both μ_e and M_{pn} and under these conditions the evolution of Y_e is given by [131]

$$\frac{dY_e}{dt} \approx \lambda_{\nu_e n} - Y_e(\lambda_{\nu_e n} + \lambda_{\bar{\nu}_e p}), \quad (4.3)$$

where the λ 's are the rates for the processes in subscript. In weak equilibrium we have

$$\frac{dY_e}{dt} = 0 \Rightarrow (Y_e)_{eq} = \frac{\lambda_{\nu_e n}}{\lambda_{\nu_e n} + \lambda_{\bar{\nu}_e p}}. \quad (4.4)$$

This ratio can be expressed in terms of the average neutrino energies, luminosities and M_{pn} as given by eq. (77) of [131]. Under the assumption of similar neutrino and antineutrino luminosities, one can proceed to show that the material will be proton-rich in weak equilibrium when the following inequality is satisfied [129]

$$4M_{pn} > (\langle E_{\bar{\nu}_e} \rangle - \langle E_{\nu_e} \rangle), \quad (4.5)$$

where the energies on the right-hand side are the averages over the neutrino spectra.

This inequality is thus the indicator as to when the material will be proton-rich. However, we note that these are all equilibrium considerations and the ejecta will generally not reach this state before the weak reactions that determine Y_e freeze out. The true value of Y_e will evolve toward the equilibrium value given above for the local conditions of the matter (density, temperature, reaction timescale etc.). The full simulation results given in [129] show that this evolution toward equilibrium will yield proton-rich matter for the innermost layers, yielding a good candidate site for p -process nucleosynthesis.

4.3 Hydrodynamical Simulation

The hydrodynamical calculations that have been performed are based on spherically symmetric simulations with neutrino Boltzmann transport that include effects of general relativity. The details are technical and we refer the reader to [129] and the relevant references therein. The progenitor star model had a main sequence mass of $20 M_{\odot}$ [132]. However, as we have already discussed in section (1.3), this sort of core-collapse simulation does not produce explosions. We therefore have to introduce some artificial mechanism to force a successful explosion and subsequent ejection of the stellar envelope.

The expected sensitivity of the matter composition in the innermost ejecta to the actual explosion mechanism is a major concern. Previously, people have employed artificial thermal bombs (raising the temperature at a given radius) or pistons (pushing the matter layers) to explode the models. The observational knowledge of the total explosion energy gives us a handle on the input needed and such techniques have been used to model the outer layers. These methods will not give the mass cut consistently from the simulation and this must be determined from other conditions. Clearly, these kinds of forced explosions are not good for innermost ejecta.

The technique used to explode the models here is scaling. The first (model A) method multiplies the neutral current neutrino scattering cross sections by a factor between 0.1 and 0.7. This will decrease the neutrino opacity in the protoneutron star and thus allow more diffusion out of the

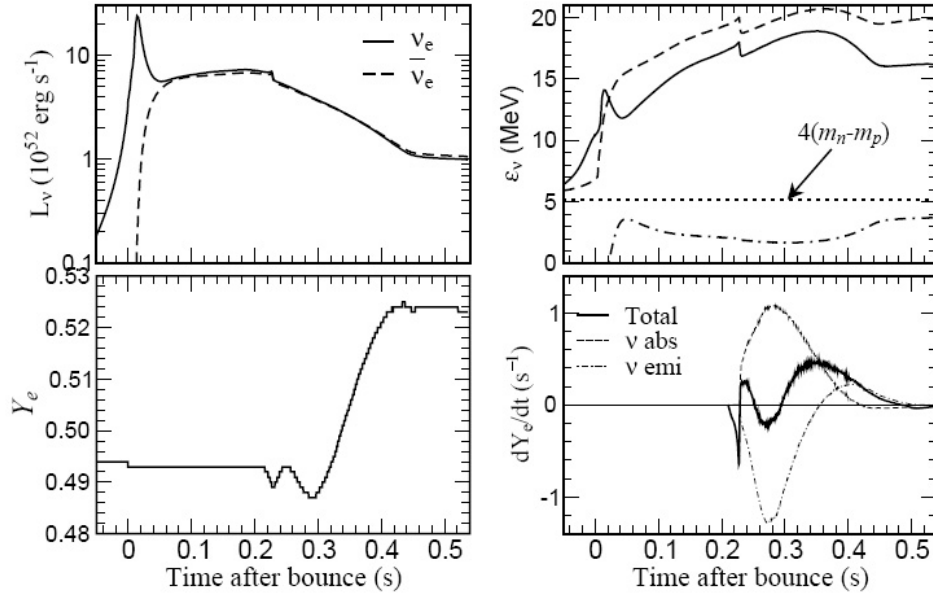


Figure 4.1: Time evolution after core bounce of an ejected layer at $0.005 M_{\odot}$ outside of the mass cut from a $20 M_{\odot}$ supernova progenitor. Top left: Luminosity of neutrinos and antineutrinos. Bottom right: Electron fraction Y_e . Top left: Average neutrino and antineutrino energies $\epsilon_{\nu} = \langle E_{\nu}^2 \rangle / \langle E_{\nu} \rangle$ (thick solid and dashed lines). The difference in average neutrino energy, $(\epsilon_{\bar{\nu}} - \epsilon_{\nu})$ (thick dot-dashed line) and four times the mass difference between neutron and protons (thin dashed line) are shown in the lower part. Bottom right: Individual weak interaction contributions leading to $Y_e > 0.5$. The individual contributions from neutrino/antineutrino captures and electron/positron captures are a factor ten larger than the total resulting dY_e/dt . Adapted from [129].

high density region. This will in turn boost the luminosity in the heating region (where the material receives the needed kinetic energy to escape the gravitational field). This is expected to represent effects of convection in the proton-neutron star region below. The second method (model B) puts a scaling factor larger than one on the rates for the reactions given in eqs. (4.1) and (4.2) in the heating region. This reduces the neutrino heating timescale and is done to mimic possible convective overturn in these highly unstable layers.

The important point about both methods above is that they will not influence the equilibrium temperature and Y_e . For model A this is trivial since nothing is changed in the heating region except the neutrino luminosities, whereas for model B we have an equal factor on all weak reactions that change Y_e . We therefore expect the value of Y_e to reflect the results of a more involved multi-D model producing explosions. Another nice feature of these artificial explosion mechanisms is the fact that the mass cut emerges

from the model automatically and we do not need any external conditions to determine where the innermost ejecta are located.

In figure (4.1) we show the time evolution of various quantities that we have discussed above as a function of time after core bounce. The figure corresponds to a layer that is $0.005 M_{\odot}$ outside the mass cut. The initial peak seen in the neutrino luminosity just after bounce comes from electron captures on the protons that the shock produces by dissolving nuclei (before the shock arrives, the protons are inside neutron-rich nuclei with large electron capture thresholds that suppress this reaction). The initial Y_e of the layer is a result of the progenitor model which has mainly iron group nuclei in these regions (see the bottom left in figure (4.1)). The neutrons in these nuclei are protected from the $n + \nu_e$ reaction relative to free nucleons so there is little effect from the initial luminosities (antineutrino captures are suppressed by nuclear structure Pauli blocking effects). Y_e is therefore set by these iron group nuclei which have a value slightly below $1/2$.

The shock front passes the mass zone just after 0.2 s, dissociating the nuclei and lowering the density. The small bumps in Y_e just after the shock are a result of the complicated interplay of the reactions in eqs. (4.1) and (4.2) as a function of density and temperature. However, ultimately the decrease of the chemical potential μ_e leads to more neutrino absorption than emission, thus driving Y_e above $1/2$. In the top right portion of figure (4.1) the neutrino and antineutrino energies are shown and compared to $4M_{pn}$ which was the indicator of proton-richness introduced above. We clearly see that the energy difference (thick dot-dashed line) is always below $4M_{pn}$.

The proton-rich innermost ejecta are found for models A and B [129]. However, the extend of this $Y_e > 1/2$ region (and the location of the mass cut itself) varies with the values of the rate reduction/enhancement factors. When considering regions from the mass cut and out to $0.1 M_{\odot}$ the average Y_e is still close to the progenitor value. The strong convective instability of the region does make it likely that mixing will occur on a short timescale and we expect Y_e to remain high on average (this is also discussed in [133]).

4.4 Network and Neutrinos

The effect of neutrinos on nucleosynthesis of light and medium mass elements in the supernova mantle was first introduced in [126, 127] and considered in great detail by Woosley *et al.* [128]. Since then a great number of studies have considered the effects of neutrinos on various nucleosynthesis processes. The core-collapse environment that we are concerned with is one of primary production of light and medium mass elements and we therefore need to consider a great number of nuclei in our network and all their relevant interactions.

As discussed in [129], the nucleosynthesis of the material was calculated

with a network consisting of nucleus-nucleus and nucleus-nucleon reactions on all relevant nuclei up to and including $Z = 50$. The standard weak interaction rates (electron/positron captures and β^\pm -decays) were likewise included up to mass $A = 65$. All these rates are temperature and density dependent.

Element	Mass Range (ν capture)	Mass Range ($\bar{\nu}$ capture)
n	1	1
H	1	1
He	6	6
Li	7–9	7–9
Be	8–12	8–12
B	10–14	10–14
C	11–18	11–18
N	13–21	13–21
O	14–22	14–22
F	16–26	16–26
Ne	18–29	17–29
Na	20–32	19–22
Mg	21–35	21–35
Al	22–37	22–37
Si	24–39	23–39
P	26–42	25–42
S	28–42	27–42
Cl	30–42	29–42
Ar	32–44	31–44
K	34–48	33–48
Ca	36–50	35–50
Sc	38–52	37–52
Ti	40–54	39–54
V	42–56	41–56
Cr	44–58	43–58
Mn	45–62	45–62
Fe	48–64	46–64
Co	50–66	49–66
Ni	52–68	51–68
Cu	54–70	53–70
Zn	56–74	55–74
Ga	58–78	57–78
Ge	60–78	59–78
Se	67–84	66–84
Br	69–86	68–86
Kr	71–92	70–92
Rb	73–92	72–92
Sr	77–80	74–80

Table 4.1: Nuclei for which neutrino and anti-neutrino captures are included. The mass range given indicates for each element the nucleus with the lowest mass number and the nucleus with the highest mass number.

The final set of reactions that we need to describe changes of Y_e is of

course neutrino and antineutrino captures. In table (4.1) we give all nuclei for which these rates were included in the network. These range from Hydrogen and neutrons up to ^{120}Sn . The range of masses chosen for each Z is from the proton drip line to stability, including also a few mass units toward the neutron drip line. Since we are concerned with proton-rich matter this seems a sensible choice.

The neutrino and antineutrino capture cross sections were calculated for several values of the neutrino spectral temperature between 2.8 and 10 MeV. Through eq. (2.83), this converts into average neutrino energies between 8.8 and 31.5 MeV. By using interpolation between these values we describe the cross sections consistently for all relevant average energies. We can thus use the detailed neutrino energy information under the assumption of a Fermi-Dirac spectrum.

We should mention that neutrino scattering events were not included since they do not change Y_e . They can, however, change composition by spallation events during deexcitation. This will be implemented in future work.

4.5 νp -process Nucleosynthesis

The nucleosynthesis was followed with all the reactions mentioned above included for the inner, proton-rich layers (defined by the condition $Y_e > 1/2$) where we expect free protons to exist. This layer had different thickness for models A and B, and for the different parameters. However, the abundance yields turn out very similar (see [129]). We therefore focus on the model B07 as in [134] (referring to a factor of 7 on the rates of the reactions in eqs. (4.1) and (4.2)).

In figure (4.2) we show the abundance evolution as a function of time after bounce. The solid lines are with neutrino interactions in the network, whereas the dashed ones are without. We clearly see a large effect on Y_e and the neutron abundance. The curve for ^{56}Ni is an indicator as to the time when nuclei start to form. We note that the inclusion of neutrino reactions on nuclei has practically no effect on Y_e .

The enhanced potential for nucleosynthesis of this environment comes from the increased neutron abundance produced by antineutrino captures on the proton-rich material. Capture on protons and nuclei occur on timescales that are short (a few seconds) at the nuclear production radius of roughly 1000 km (much shorter than the β -decay lifetimes of nuclei like ^{56}Ni and ^{64}Ge). For neutrinos this is a different story since there is a threshold for capture on the proton-rich side of stability. The larger abundance of protons in the material thus leads us to a situation where antineutrino captures on protons produce a significant abundance of free neutrons. These neutrons do not suffer from small binding energies that would otherwise inhibit the

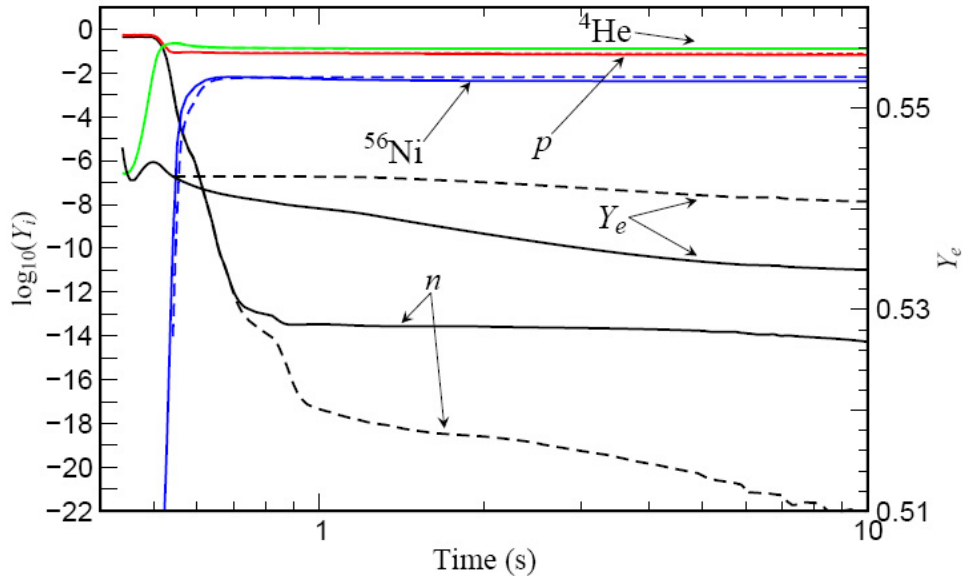


Figure 4.2: Evolution of the abundance of neutrons, protons, α -particles, and ${}^{56}\text{Ni}$ in a nucleosynthesis trajectory resulting from model B07 of reference [129]. The abundance, Y , is defined as the number of nuclei of the species i present divided by the total number of nucleons which is conserved during the calculation. The solid (dashed) lines display the nucleosynthesis results which include (omit) neutrino and antineutrino absorption interactions after nuclei are formed. The abscissa measures the time since the onset of the supernova explosion.

nucleosynthesis process.

The abundances that we get from the calculation are shown as filled circles in figure (4.3). The open circles show the same calculation with no neutrinos included for comparison. The results are given relative to solar abundances. We immediately see a striking difference for $A > 64$ when we include the neutrinos. This feature has been traced to a novel mechanism that allows one to overcome waiting points that arise due to β lifetimes and Coulomb barriers. The abundances for the heavier nuclei are up to 10^5 times larger than the solar values in figure (4.3). This is compensated by the small amount of material with $Y_e > 1/2$ in the model. Since this amount is around $10^{-5} M_\odot$ the solar abundances can be produced if all the proton-rich material is ejected by the explosion.

The synthesis of elements with $A > 64$ was obtained in proton-rich ejecta in previous studies also [136]. However, those studies required entropies per baryon of $s \approx 150 - 170 k_B$ which is roughly a factor of three above the estimates for core-collapse events [133, 129].² The scenario presented here

²The entropy variable can seem counterintuitive when discussing nucleosynthesis. Some clarifications of this issue can be found in appendix (C).

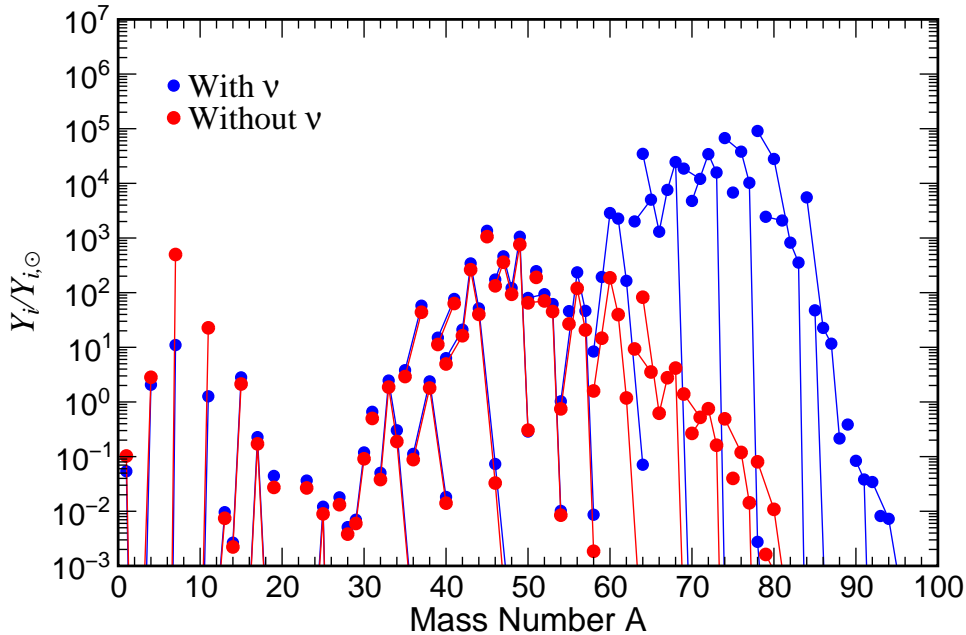


Figure 4.3: Abundances for model B07 relative to solar abundances [135]. Two different calculations are shown: with neutrino-induced reactions in the network (filled circles) and without neutrino-induced reactions in the network (open circles).

is therefore much more realistic and in fact expected to be generic as we will discuss at the end of this chapter.

The key waiting point that one has to get across in order to get appreciable nucleosynthesis of $A > 64$ nuclei is ^{64}Ge . The (p, γ) reaction is suppressed by the negative proton separation energy of ^{65}As . Furthermore, ^{64}Ge has a β lifetime of about 64 s, much longer than the expansion timescale of order 10 s so β -decay will also be too slow. In the presence of free neutrons one can, however, bypass this by the (n, p) reaction which has a lifetime of about 0.25 s at the relevant temperature ($2 \cdot 10^9$ K), shorter than the dynamical timescale. One can therefore produce ^{64}Ga which can capture further protons. This allows the flow to continue until the next α nucleus, ^{68}Se , and then the story repeats.³ This novel process has been dubbed the νp process [134]. As one can see in figure (4.3) the flow of matter stops just below $A = 100$. Here one reaches the region of ^{100}Sn where α -decay ends the flow (analogous to the cycle at ^{210}Po in the s -process discussed in chapter (1)). A similar flow termination cycle was found around $^{106-108}\text{Te}$ by Schatz *et al.* [137] for the rp -process.

³One would perhaps also expect neutrinos and antineutrino captures to play a role in breaching these waiting points. Simple estimates show, however, that the lifetime against capture for nuclei like ^{64}Ge is of the order of several seconds. Thus the (n, p) reaction will still be dominant.

We note that when $Y_e < 1/2$ as in r -process nucleosynthesis the scenario does not take place. Neutrino capture on neutrons will produce protons that combine with remaining neutrons into α 's and light nuclei which will not capture on heavy nuclei due to large barriers. This means that one cannot enhance the r -process by including neutrinos in the reactions (the production of too many seed nuclei through neutrino capture on neutrons is also devastating. This will be addressed again in the next chapter). One could, however, imagine effects of neutrinos on the endpoint of the r -process. The latter will be explored in the next chapter.

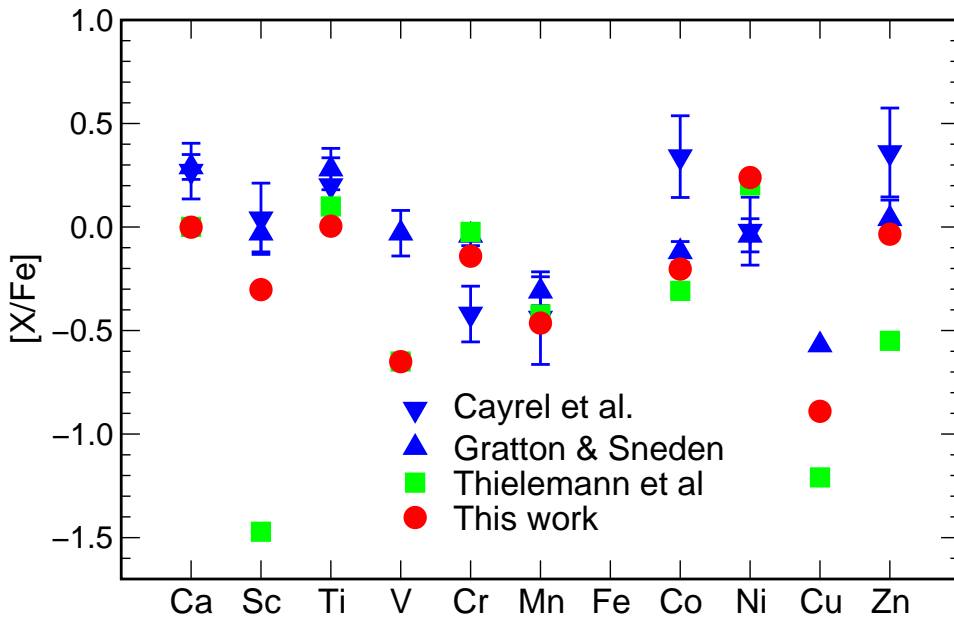


Figure 4.4: Comparison of elemental overabundance in the mass range Ca to Zn for different calculations. The triangles with error bars represent observational data. The triangles facing upwards [139] originate from an analysis of stars with $-2.7 < [\text{Fe}/\text{H}] < -0.8$. The triangles facing downwards [140] are data for a sample of extremely metal poor stars ($-4.1 < [\text{Fe}/\text{H}] < -2.7$). The circles are abundances of this work combined with the work of TNH96 to obtain the same amount of Fe-group elements. The squares show the pure abundances of the previous reference.

For the $A < 64$ nuclei there seems to be little difference in the abundances on figure (4.3) with and without neutrinos. To make a real comparison one would have to carry out a full calculation for all the iron group layers above the mass cut. For lack of such a study, the current data for the innermost ejecta were combined with the results of [138] for the outer layers. We skip the abundance plots (given in [129]) and show instead the comparison with measurements of some ultra-metal poor stars. In figure (4.4) we show element overabundances⁴ compared to both [138] (squares) and the combined

⁴The overabundances are defined as the element ratio normalized to the same ratio in

results just described (circles). Note particularly the improved agreement for the very rare ^{45}Sc . This is the only isotope of Sc that exists in nature and the production of it has not been previously understood.

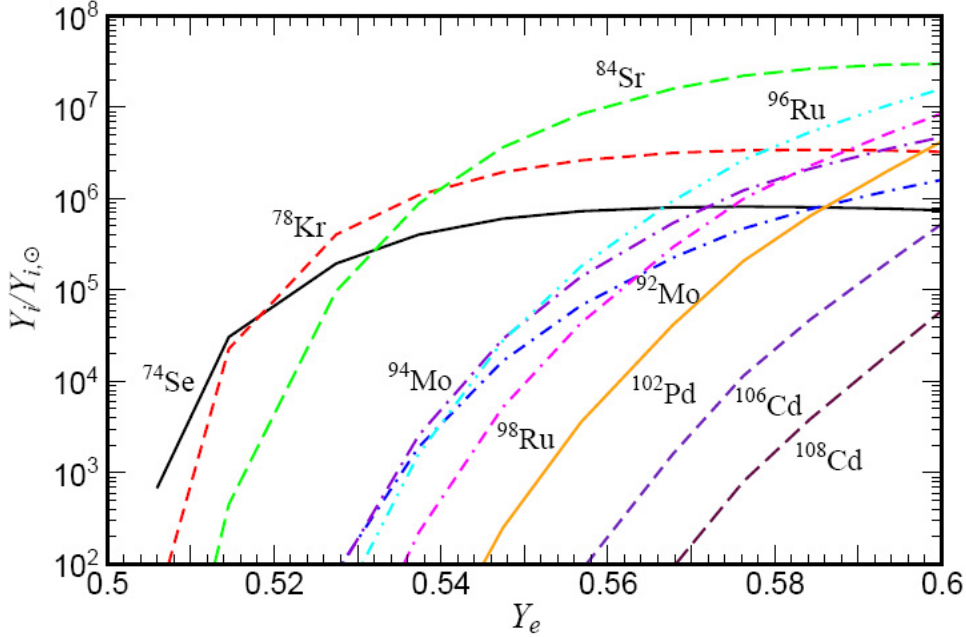


Figure 4.5: Light p -nuclei abundances in comparison to solar abundances as a function of Y_e . The Y_e values given are the ones obtained at a temperature of 3 GK that corresponds to the moment when nuclei are just formed and the νp -process starts to act.

The nucleosynthesis of some of the rare light p nuclei are expected to be very sensitive to the Y_e value. To explore the dependence of the νp -process to variations in Y_e , an adiabatic parametric study was performed along the lines of [136, 141]. However, contrary to those references, a realistic entropy per baryon of $s = 50 k_B$ was used. Different Y_e 's were obtained by varying the neutrino and antineutrino spectral temperatures. In figure (4.5) the results of such a procedure for $0.5 < Y_e < 0.6$ are shown. We see that the abundances of the $A > 64$ nuclei are very sensitive to Y_e . Particularly, the abundances of the nuclei $^{92,94}\text{Mo}$ and $^{96,98}\text{Ru}$ are seen to raise for large Y_e . The origin of these nuclei is currently considered unknown, but the present results give us hope that they could be consistently produced in the innermost ejecta of core-collapse Supernova through the νp process. Similar results were obtained by [12]. The sensitive question about the nuclear mass dependence of production of these p nuclei is also discussed in [12] where it is stressed that some of the important masses are not experimentally known.

the Sun.

In closing we summarize the facts that lead us to believe that the νp -process described here is actually a generic feature of Type II Supernova. Recent core-collapse models that start from different progenitor models and employ 1D and 2D simulations of transport all indicate that proton-richness is a feature of the innermost ejecta [123, 124, 125, 133, 129]. There is also little doubt that these layers will be subject to intense neutrino fluxes from the proton-neutron star region below. This latter fact has already prompted studies in the past that found evidence for p nuclei production in such intense neutrino fluxes [47, 142]. One could still worry about whether fallback could prevent the nuclei from getting out into the interstellar medium but, as discussed in [143], mixing before fallback will always lead to some ejection also for the innermost layers. We therefore believe that the process will operate in all core-collapse Supernova. The sensitivity to the actual explosion mechanism could mean that the yields will be very dependent on stellar mass, rotation, magnetic fields etc. This is not a bad thing, since it might help to explain diversities found in observations of enriched stars. It will be interesting to see the process operating in a nucleosynthesis calculation of the full ejecta and likewise to see how it will influence galactic chemical evolution studies.

Chapter 5

Neutrinos and the r -process

5.1 r -process Nucleosynthesis

The synthesis of heavy elements in the r -process and the nuclear reactions that are involved in this process will be our main focus for the remainder of the thesis. We therefore provide a brief overview of some central features needed for this discussion. As was mentioned in the introduction, the r -process produces elements through neutron captures on a timescale much faster than the β -decay lifetime of the extremely neutron-rich nuclei involved. We thus need an astrophysical environment with extreme neutron fluxes. The site for the r -process is not easy to point out and there is not yet full consensus on this issue. However, there is a site connected to core-collapse Supernovae that has been favored by many authors for a number of years, and it will be our reference scenario. We will discuss it in more detail below, but first we briefly summarize some general features of the r -process.

5.1.1 General Conditions

The r -process is responsible for producing about half of the elements heavier than iron that we find in the solar system, and it is (presumably) the sole production event for nuclei heavier than ^{209}Bi . The classical process is assumed to take place in an equilibrium between the (n, γ) and (γ, n) reactions, both of which are assumed much faster than β -decays. The Saha equation for the equilibrium abundances now gives us a relation for the ratio of abundances

$$\frac{Y(Z, A + 1)}{Y(Z, A)} \propto \rho_n \exp\left(\frac{S_n(Z, A + 1)}{T}\right), \quad (5.1)$$

where ρ_n is the neutron number density and T is the temperature of the material. The process therefore occurs in nuclei that have the same neutron separation energy S_n , the value of which is typically 2-3 MeV (depending

on the neutron density and the temperature). Assuming a steady flow, we also have β equilibrium

$$\lambda_\beta(Z-1)Y(Z-1) = \lambda_\beta(Z)Y(Z), \quad (5.2)$$

where $Y(Z) = \sum_A Y(Z, A)$ is the total yield of a particular element and $\lambda_\beta(Z) = \sum_A \lambda_\beta(Z, A)Y(Z, A)/Y(Z)$ is the β -weighted abundances. We thus see that the total yields are inversely proportional to the total rates, or proportional to the lifetime. For given Z there is usually one or two nuclei that have the S_n to be on the *r*-process path. These are the waiting point nuclei, since the process has to wait for their β -decay to proceed further up the nuclear chart. This, in turn, means that nuclei with magic numbers have high yields due to the small S_n and long β lifetimes (these peaks can be clearly seen in figure (1.3)).

The discussion above shows us that two key ingredients needed to model the process are ρ_n and T . Through various constraints (including the very important fact that the process needs to reproduce the solar abundances when *s*-process elements are subtracted) one finds that neutron densities of $10^{22} - 10^{24} \text{ cm}^{-3}$ and temperatures of about 10^9 K ($\sim 100 \text{ keV}$) are needed. Considering that the actinides have to be produced, we can estimate the duration of the process by summing all the β lifetimes of the waiting point nuclei up to mass $A \sim 240$. This tells us that the *r*-process lasts for about 1-2 s. This way of viewing the process is called classical *r*-process. Later we will be concerned with presumably more realistic dynamical models where the conditions change with time. The process eventually stops at the very heavy nuclei since the fission channel opens up. We will have more to say about this end-point issue in the next chapter.

The process terminates when ρ_n drops significantly below the values given above, referred to as the freeze-out. In stellar ejecta the point and time at which this happens is determined by the outflow velocity (through the radial dependence of the neutron flux). After freeze-out one needs to follow the nuclei as they β -decay back to stability and give the final nucleosynthesis results. During this period there can still be neutrons released that induce further fission reactions. This will also be addressed in the subsequent chapter.

The density, temperature, and duration given above indicate that explosive conditions are required. The observations of metal-poor star indicate that the process is likely primary and we therefore have good reason to believe that it could be connected to core-collapse Supernovae.

5.1.2 The Neutrino-driven Wind

As mentioned, the site of the *r*-process is still not fully agreed upon. An early suggestion was the He-shell which is also the site of the *s*-process. This could, however, not produce the neutron fluxes needed. Later suggestions

include neutron-star mergers, Supernova fallback, magnetic winds and accretion disks. The currently favored site is a neutrino-driven wind that is thought to occur above the mass cut of core-collapse Supernovae. This latter scenario is the one that we will assume and we therefore proceed to give further details of this environment.

Some of the first papers to emphasize the potential for *r*-process nucleosynthesis in the hot neutrino-driven wind above the protoneutron star were those of Woosley and Hoffmann [144] and Meyer *et al.* [145]. The region lies just behind the stalled shock front from the core bounce and is exposed to huge neutrino fluxes that come from cooling of the accreting protoneutron star below. This raises the temperature and the entropy of the material in a low density region called the 'hot bubble'. The entropy typically goes up to several hundreds per baryon and the temperature is around 10^{10} K. This hot bubble scenario occurs about 1-20 s after the bounce, so later than the νp -process of the previous chapter.

In figure (5.1) we show a schematic cartoon of the process to help guide the discussion. The high temperature means that charged particle reactions can build up nuclei (through the so-called α -process) that can act as seeds for the free neutrons to capture on. For this process to reach the actinides we need a neutron-to-seed ratio of roughly 100 (assuming that the charged particle reactions will build seed up to $A \sim 100$). This would require $n/p \sim 7 - 8$ ($Y_e \sim 0.1$) under normal circumstances. However, the extremely high entropy that one finds in the hot bubble can allow a high neutron-to-seed ratio even in moderately neutron-rich material with $Y_e > 0.4$ (see appendix (C)).

The moderate neutron-richness of the material can be produced in core-collapse supernova since (as we have already seen in the model discussed in the previous chapter) the antineutrino energy is generally higher than the neutrino energy. During the cooling phase one expects equal luminosities in all species and this will tend to drive the material to $Y_e < 1/2$. There is a danger with the neutrinos since they can capture on neutrons to produce protons that recombine into α s and thus lower the neutron-to-seed ratio [47]. This can be avoided by a very fast expansion as discussed in [146]. Another very attractive feature of this particular site is that it provides roughly $10^{-4}M_{\odot}$ per core-collapse Supernova event. This is the right amount when one considers the event rate in our galaxy, the total amount of observed material coming from *r*-process, and the galaxy lifetime and mass [144, 145].

In our discussion of the neutrino-driven wind it should be clear that one needs rather specialized conditions to make the *r*-process work in this environment. This is of course the reason for the continued uncertainty about the site that still exists (see for example the recent review in [9]). In the *r*-process studies, that we will present in the next chapter, questions related to site are put aside by simply parameterizing the conditions of the nuclear material that undergoes nucleosynthesis (we will give more detail

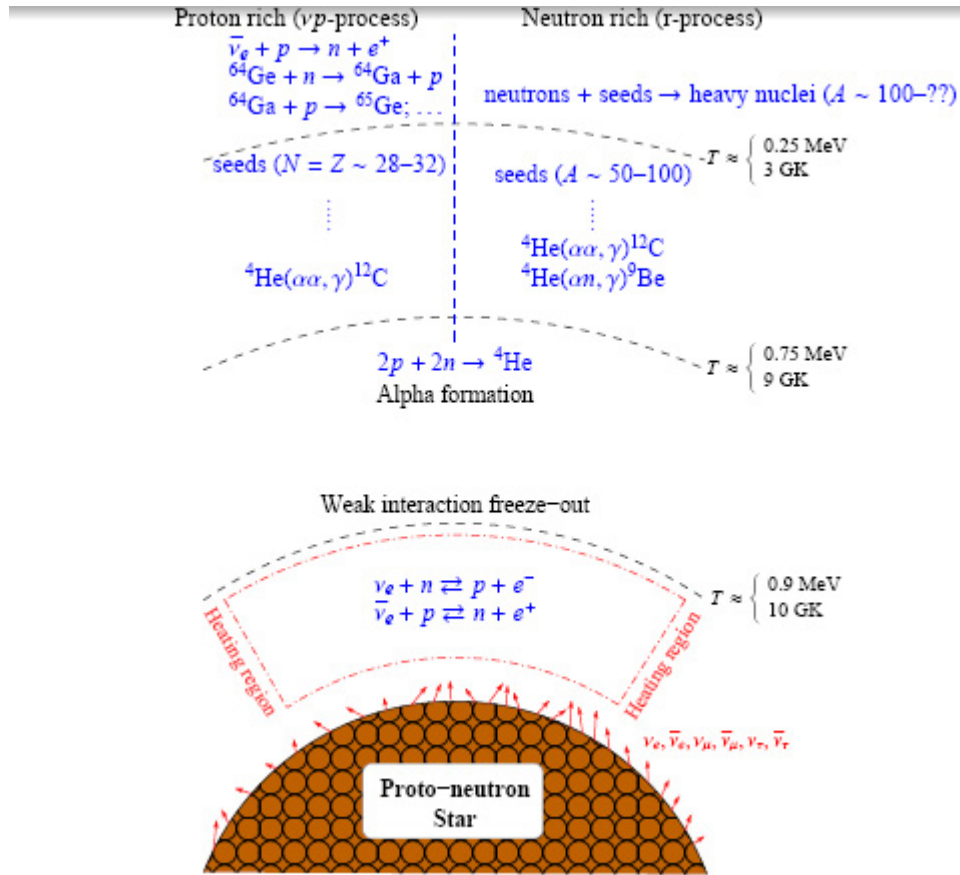


Figure 5.1: The figure shows the outflow and the nucleosynthesis stages leading up to the νp -process discussed in chapter (4) (left-hand side) and the r -process (right-hand side). Shown are some relevant reactions and temperatures at which they operate. Weak interaction freeze-out is the point at which Y_e is determined. During alpha formation large neutrino fluxes can hinder the r -process from producing the heaviest nuclei (see section (6.4.4)). Figure courtesy of Gabriel Martínez-Pinedo.

about the conditional variables in the next chapter). This enables us to ignore the site to a certain extent and consider parameter studies that could point to generic features of the process.

Finally we mention that one can actually make a strong argument for the Supernova site based on the way neutrinos transmute the material after freeze-out [148, 149]. Knowing the r -process abundance pattern and the reaction cross sections with good accuracy allows one to subtract the effects of neutrinos from a model calculation and compare to measurements. One then finds that several interesting isotopes around $N = 50$ and $N = 82$ are very likely a result of neutrino interactions during and after the r -process. This is referred to as neutrino post processing. It produces a shift of the

abundance peaks to the left since the reactions spallate neutrons from the synthesized nuclei. During the r -process there will also be an effect on the waiting points since neutrino capture can aid β -decays in bridging these and move the matter flow upward (still allowing for the observed peaks around magic numbers). These neutrino effects can therefore be used to constrain the neutrino flux, dynamical time scale, and freeze-out radii. In [148, 149] these considerations were found to favor the core-collapse Supernova site.

5.2 UMP Stars and Neutrino-induced Fission

As we have already discussed in chapter (1), recent advances in observations of elemental abundances in ultra-metal poor (UMP) stars provide us with detailed information about the heavy nuclei that the r -process is believed to be responsible for. We showed abundance pattern for several UMP stars in figure (1.4) and pointed out the astonishing agreement with solar values. In figure (5.2) we show the UMP star CS 22892-052 pattern in more detail, including the measurement of lighter nuclei with $Z < 50$ (or $A < 130$). The agreement with the scaled solar abundances (solid line) is seen to be worse, particularly for the nuclei Rh, Pd, Ag, and Cd. One is therefore prompted to study how the r -process scenario described above can accommodate such variations.

In early studies of fission dynamics in the r -process it has been found that fission cycling can occur [152]. This means that matter that undergoes fission during the process produces fragments that continue to capture neutrons and move upwards along the flow. Under certain conditions this can effectively create a cycle for the involved nuclei. This effect was seen in several studies [153, 154], and in particular one found a robust abundance pattern for $A > 130$ [155]. Naively, the regular abundance pattern found for $A > 130$ in UMP stars can now be explained by an r -process with a neutron-to-seed ratio large enough for fission cycling and the lower mass elements could be attributed to an appropriately smaller neutron-to-seed ratio (or an incredibly effective s -process component in early generation stars) [156]. But, as shown by Qian [156, 9], the assumption of a robust cycling producing $A > 130$ nuclei contradicts observations in the UMP stars CS 31082-001. So it seems that another mechanism must be operating.

This led Qian [156] to suggest that, assuming the nucleosynthesis took place in an environment of intense neutrino fluxes, a process with fission but no fission cycling could explain the observations. The proposal uses neutrino reactions as a way of getting the progenitor r -process nuclei to fission after freeze-out. Qian's scenario starts from a freeze-out distribution covering $190 < A < 320$ so a large neutron-to-seed ratio would be needed but without fission cycling. Recent fission barrier calculations for neutron-rich nuclei that are generally higher than previous calculations seem to support

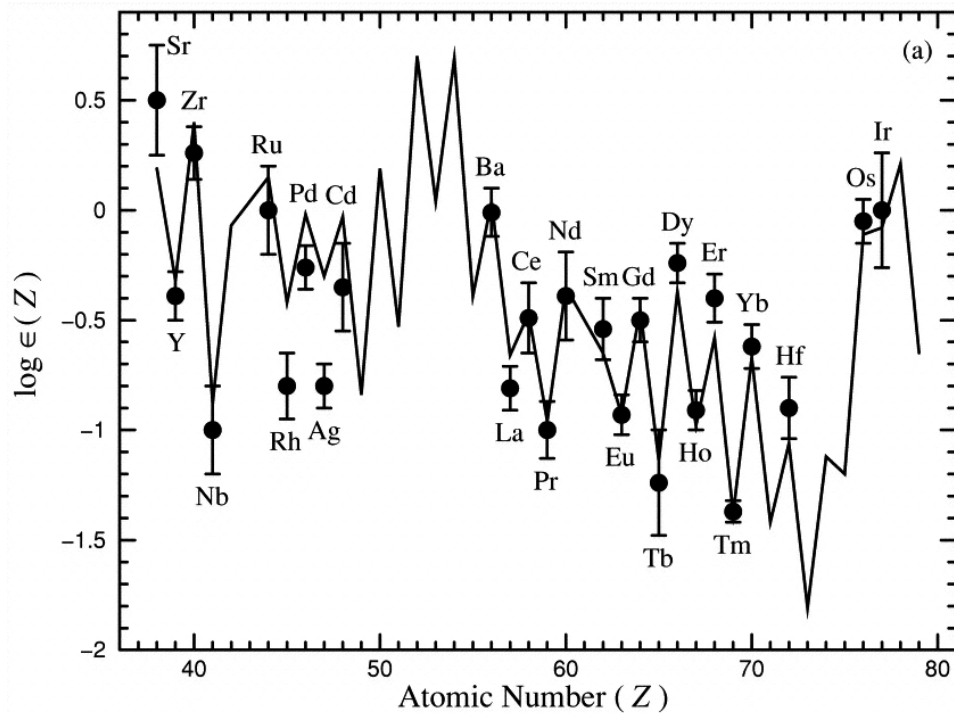


Figure 5.2: Measured abundances of neutron capture elements in CS 22892-052 (*filled circles*; data from [150]) compared to solar r -process pattern (solid line), translated to fit the Eu data. Solar pattern is obtained by subtraction of model-based s -process from the solar values [151].

the absence of cycling due to a pile up of matter at high mass [72] (we will return to this point in the next chapter). Spontaneous fission is assumed to occur for all nuclei with $260 < A < 320$ and for some of those in the range $230 < A < 260$. The highly energetic neutrinos are then supposed to cause an enhancement of fission for $230 < A < 260$ and perhaps even for $190 < A < 230$.

The fragments from the fission events in Qian's proposal are then supposed to fall in the interval $86 < A < 109$ with enhanced structures at $A \sim 90$ (from fission of the $A \sim 195$ peak) and $A \sim 132$ (from the fission of $230 < A < 320$ which will likely have a fragment in the doubly magic ^{132}Sn region). Qian goes on to estimate the ratio of fission yields $86 < A < 190$ to surviving nuclei in the range $190 < A < 260$ under these assumptions and finds that around 40% of the $190 < A < 260$ nuclei must fission to accommodate the data from CS 22892-052 and about 20% for CS 31082-001. This difference can potentially be explained by varying the amount of neutrino-induced interactions on the nuclei after freeze-out. The neutrino flux from cooling is expected to last about 20 s [157] so there is plenty of time for neutrino reactions after freeze-out (during the r -process neutrino

captures are severely limited for the $A \sim 195$ peak to be produced [47]). The number of neutrino-induced fission events will vary with the neutrino luminosity and time scale of cooling and differences in these variables could then explain the observations. The needed level of neutrino reactions is also consistent with the previously discussed post processing [148, 149].

After the freeze-out the material will start to β -decay back toward the value of stability. Therefore the charge will increase and this influences the fission probability of a given nucleus.¹ One could therefore hope that numerous β -decays will increase the probability for neutrino reactions to cause fission. However, this must happen when the neutrino flux is appreciable during the first 20 s after core bounce. Using the β lifetimes of [30], Qian estimates that Z can increase about 8 units within the first 10 seconds for $190 < A < 260$. So for the above scenario to work one needs neutrino-induced fission to become significant during these eight steps. We will return to this when we present our detailed calculations of the neutrino cross sections below.

5.3 Neutrino-induced Fission on r -process Nuclei

The suggestions of Qian described above clearly requires detailed calculations of the neutrino-induced fission reaction both on the r -process path and on the decay back to stability. The first calculations along these lines was presented recently in Kolbe *et al.* [158]. That study considered the neutrino capture cross sections of selected isotopes with $Z = 84 - 92$ for the fission and neutron emission channels (the dominant ones for neutron-rich matter). However, [158] used a model where only the first decay of the deexcitation in the daughter was considered, meaning that potential fission events after neutron emission(s) were not taken into account. The neutrinos have energies that are high enough for the latter processes to contribute. The calculations of [158] were also unable to give information about the fission yield distributions. These facts made it difficult to evaluate the potential of Qian's proposal.

The desire to remedy the above situation was part of the motivation that led to us to develop the nuclear model presented in section (2.4). The first application of it was therefore naturally the calculation of cross sections and fragment distributions for charged current neutrino-induced fission on r -process relevant nuclei [159]. Note that this process starts with a neutrino capture (ν, e^-) which means that the decaying daughter nucleus has charge $Z_{\text{parent}} + 1$. The rest of this chapter will be devoted to the discussion of our results and how they influence the Qian scenario. However, for a full comparison one needs to put the nuclear data obtained into a detailed nu-

¹From the surface to coulomb term one can estimate that the fission probability scales with Z^2/A .

cleosynthesis network calculation. This will be the focus of the next chapter in which we will see the influence of neutrinos on the fission dynamics of the r -process.

5.3.1 Initial Uranium Calculations

The first calculations we did were for neutrino-induced processes on uranium isotopes from $A = 238$ to $A = 302$. In figure (5.3) we show the cross sections as a function of neutrino energy. Shown are the total, partial fission, and partial neutron emission results (the latter defined as events where the nucleus survives fission but might emit one or more neutrons during deexcitation). Other reaction channels, like proton or α emissions, are negligible for virtually all nuclei considered. The range of neutrino energies in figure (5.3) covers the entire interval of interest for the reference spectral temperature $T = 4$ MeV.

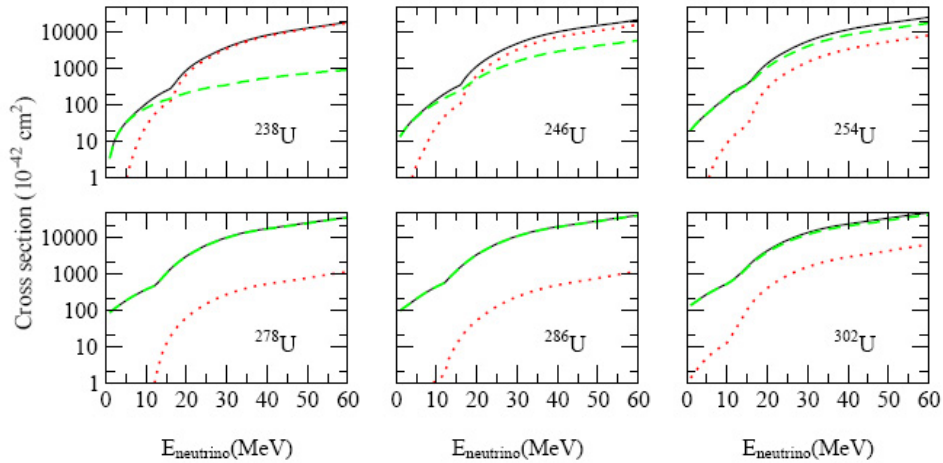


Figure 5.3: Total (solid) and partial fission (dotted) and neutron evaporation (dashed) cross sections (in 10^{-42}cm^2) for neutrino-induced (ν_e, e^-) reactions on uranium isotopes as function of neutrino energy.

In the figure we can clearly see a strong increase of the cross sections at neutrino energies of around $E_\nu \sim 17$ MeV. This is due to the IAS and GT resonances which open up at around these energies. Notice that the positions where these are located are decreasing slightly with mass number, which is mainly a result of the increasing reaction Q-value. The fission channel is seen to dominate in the first two isotopes for $E_\nu > 20$ MeV, whereas for the larger nuclei it is quite small. The latter is expected since S_n becomes very small for the heavier isotopes (see table (5.1)), causing the neutron emission mode to dominate.

A_{prog}	S_n	σ_{tot}	σ_{fiss}	σ_{evap}	σ_{tot} [158]	σ_{fiss} [158]
238	6.15	4.71(+02)	3.53(+02)	1.18(+02)	4.93(+02)	3.46(+02)
246	4.83	6.05(+02)	3.33(+02)	2.72(+02)	6.31(+02)	3.32(+02)
254	4.51	7.10(+02)	1.50(+02)	5.60(+02)	7.84(+02)	5.73(+02)
262	3.81	8.48(+02)	4.85(+01)	8.00(+02)	8.57(+02)	5.35(+02)
270	3.10	1.05(+03)	3.19(+01)	1.02(+03)	9.39(+02)	3.27(+02)
278	1.77	1.46(+03)	2.90(+01)	1.43(+03)		
286	1.58	1.64(+03)	2.57(+01)	1.61(+03)		
294	1.16	1.79(+03)	1.28(+02)	1.66(+03)		
302	0.57	2.06(+03)	1.85(+02)	1.88(+03)		

Table 5.1: Total and partial fission and neutron evaporation cross sections (in units of 10^{-42} cm²) for neutrino-induced (ν_e, e^-) reactions on uranium isotopes with mass numbers A_{prog} , adopting a Fermi-Dirac distribution with parameters $T = 4$ MeV and $\mu = 0$ appropriate for supernova ν_e neutrinos. The exponents are given in parentheses. S_n are from [30]. The last two columns give the total and the partial fission cross sections, as calculated in [158] using the fission barriers of [74].

The folded cross sections for the uranium isotopes are given in table (5.1). We have used a neutrino temperature of $T = 4$ MeV and chemical potential $\mu = 0$ which are the recommended values for Supernova neutrinos as discussed in section (2.4.3). Here we can clearly see that fission is only a dominant decay mode for the first two species as expected from the profiles of figure (5.3). The total cross section is seen to increase with mass number in an almost linear fashion. This is a result of the strengths of the Fermi and GT transitions which depend on $N - Z$ (section (2.2.2)). We can thus see that our earlier statements about the importance of these contributions were well-founded.

The results presented here differ from the earlier study in [158] where fission dominated below $A = 270$ as one can see in the last two columns of table (5.1). This was expected since those results were obtained with the barriers of Howard and Möller [74] which are quite low in that region compared to the Sierk barriers [71] used here. To investigate this expectation in detail, we did the calculation using the Howard and Möller barriers (with all other ABLA parameters unchanged) and found results similar to [158]. As another test we tried using the recent barriers of Mamdouh *et al.* [72] which are considerably higher for very neutron-rich nuclei compared to Howard and Möller. The results of this latter test came out roughly the same as those given above with the Sierk barriers.² Earlier investigations [160, 161, 162] have suggested that the larger barriers used here are the more realistic choice.

²These barrier studies are not self-consistent since only the fission barriers were varied. The masses, shell corrections etc. in the statistical code were not changed accordingly. As such we can only rely on this as essentially a barrier parameter study. In the next chapter we will explore how changes in mass tables, barriers etc. influence the r -process fission dynamics when done in a more consistent fashion.

At this point we wish to address the neutrino spectral temperature dependence of our results. In table (5.2) we therefore give the total cross sections for neutrino capture reaction on three of the uranium isotopes considered above. Also shown is the percentage of the total cross section that goes into the fission channel. The strong increase of the total cross sections is of course a result of the increasing average neutrino energy, leading to stronger excitation of the giant resonances and larger phase space factors. The nucleus ^{278}U is on the r -process path (to be discussed below) and one could therefore be interested in how the lifetime against neutrino capture varies with T . Using the formula given in appendix (B) we find a lifetime between 0.02 s ($T = 2.8$ MeV) and 0.006 s ($T = 10.0$ MeV), assuming a luminosity of 10^{51} erg/s and a radius of 100 km. The estimated β half life is 0.018 s [30]. We thus see that neutrinos can compete with β -decays for all temperatures considered, provided that the reactions occur at this rather small radius. However, the dependence on spectral temperature of these effects is obvious and must be taken into account in detailed simulations.

A_{prog}	$T = 2.8$	$T = 3.5$	$T = 4.0$	$T = 5.0$	$T = 8.0$	$T = 10.0$
238	1.55(+02)	3.11(+02)	4.71(+02)	8.91(+02)	2.34(+03)	3.00(+03)
	52	68	75	83	90	91
278	5.62(+02)	1.02(+03)	1.45(+03)	2.52(+03)	5.75(+03)	7.02(+03)
	1.2	1.7	2.0	2.3	2.7	2.8
302	8.24(+02)	1.46(+03)	2.06(+03)	3.51(+03)	7.83(+03)	9.51(+03)
	6.3	8.1	9.0	10	11	12

Table 5.2: Total cross section (in units of 10^{-42} cm 2) for neutrino-induced (ν_e, e^-) reactions on ^{238}U , ^{278}U , and ^{302}U for neutrino spectral temperatures between $T = 2.8$ and $T = 10.0$ MeV. The exponents are given in parentheses. The fission percentage ($\sigma_{\text{fission}}/\sigma_{\text{tot}}$) is given below each cross section.

When looking at the fission percentages in table (5.2) we confirm the discussion above with regards to the barriers. For ^{238}U fission becomes increasingly dominant with spectral temperature as the neutrino energy is essentially always above the barrier, whereas for the two heavier isotopes the contribution from fission is only slightly increasing with T . The latter two have high barriers and much lower S_n so the behavior is expected. We have also calculated the average number of neutrons emitted during the reactions. For ^{238}U one gets $\langle N \rangle_{\text{tot}} = 1.76$ at $T = 4$ and 2.83 at $T = 8$ MeV. In ^{278}U we found 3.15 and 5.13 and in ^{302}U it is 10.9 and 13.6 (for $T = 4$ and $T = 8$ MeV respectively). All numbers given represent the average over both fission and neutron emission channels. Again the changes with T are not dramatic. However, since the released neutrons can induce further reactions when captured on other nuclei one needs to take these effects into account.

The fission fragment yield for the uranium isotopes were also calculated and in figure (5.4) we show the results for the three selected isotopes of table (5.2). In the figure we give the fragment distributions for neutrino temper-

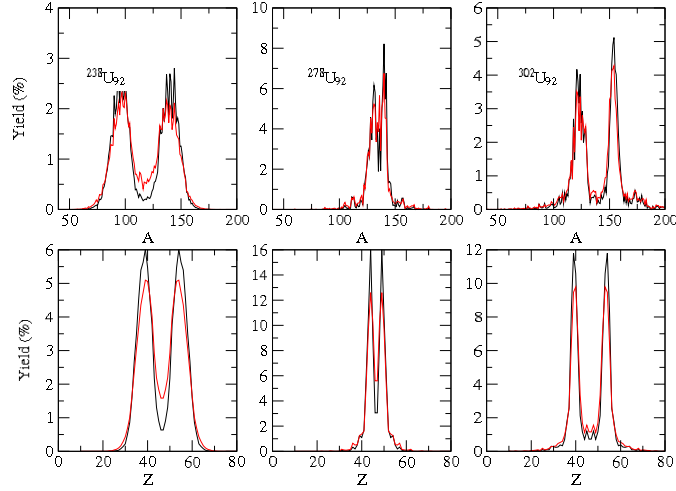


Figure 5.4: Mass (top) and charge (bottom) distributions (in percent) of fission fragments produced in (ν_e, e^-) reactions on ^{238}U , ^{278}U , and ^{302}U . The black curves show the distributions for neutrinos spectral temperature $T = 4$ MeV and the red curves show those with $T = 8$ MeV. Notice that we have varied the range on the yield axis to maximize visibility.

atures $T = 4$ (black curves) and $T = 8$ MeV (red curves). In ^{238}U (whose daughter is ^{238}Np) one sees the double-hump pattern (this is experimentally well-known in this actinide region [57]). There is a peak around $A \sim 138$ related to the neutron shell at $N = 82$ and one at the $A \sim 95$.³ The wiggles on the mass distributions are due to an expected odd-even staggering (see figure (2.4)). The corresponding charge distributions show peaks at $Z = 38$ and $Z = 54$ which means that the yields are neutron-rich and will likely undergo one or more β -decays toward stability. The heavier isotopes also show the double-hump structure with ^{278}U showing a clear attraction toward the doubly-magic region around ^{132}Sn . ^{302}U is a more complicated story, since we have to take into account that most fission events are accompanied by many released neutrons (between 25 and 30 for fission at excitation energies below 10 MeV). The high peak contains slightly more probability since this is where the symmetric mode lies. The position of the peak ($A \sim 155$) is connected to the presence of a neutron shell closure at $N \sim 88$ for deformed nuclei (as discussed in section (2.3.2)).

The fragment distributions are thus seen to be quite complicated as a function of mass number, going from the broad double-hump in ^{238}U , over

³Mass conservation dictates that the sum of fragments and emitted neutrons should equal the progenitor mass A . Since we only consider the fission and neutron emission channels we therefore have $A = A_{\text{frag1}} + A_{\text{frag2}} + N_{\text{emitted}}$.

the narrow hump in ^{278}U , and back to the broad one in ^{302}U (again remember that the fissioning daughter nucleus is Np). This reflects the interplay between symmetric and asymmetric fission modes. One would expect such effects to be less pronounced for higher average excitation energies in the fissioning nucleus. The red curves in figure (5.4) give the yield for spectral temperature $T = 8$ MeV, giving an average neutrino energy of about 25 MeV. We clearly see a tendency for increase of the symmetric mode in ^{238}U and for some odd-even effects to be washed out (as the pairing energy becomes less important). Although it is harder to see on the figure for the heavier nuclei, we find the same tendencies there also.

5.3.2 r -process Nuclei

The neutrino-induced reactions on nuclei along the r -process path was the next issue considered. The path was defined as the nuclei with $S_n \sim 2$ MeV according to the mass table [30], a value that is generally agreed upon in the literature [160]. In table (5.3) we present the results for $Z_{\text{prog}} = 90 - 108$ where neutrino-induced fission starts to be noticeable.

The cross sections are seen to be of order 10^{-39} cm². At luminosity 10^{51} erg/s and a radius of 100 km, this gives a half life against neutrino capture of about 0.02 s, only slightly longer than the β -decay half lives which range between 0.005 and 0.02 s according to [30]. The total cross sections is similar for lighter species along the r -process path and we note that heavy nuclei with $Z_{\text{prog}} > 82$ can therefore compete with β -decay during the r -process. Again we have to be cautious with these statements, as the radial dependence can diminish the effect if the reactions take place at larger radii (beyond $r = 500$ km we have $\tau_\nu > 0.5$ s). When looking at the partial cross sections for fission and neutron emission, we see that fission will be negligible for $Z_{\text{prog}} < 94$ and dominant for $Z_{\text{prog}} > 96$. This is around the region where the r -process is expected to terminate according to a recent study [163]. In the next chapter we present simulation results indicating that the termination could be at even higher charges. Neutrinos could therefore have a role in this termination if the process operates close to the neutron star (we will return to this point in the next chapter).

In the last two columns of figure (5.3) we give the average number of neutrons released in the fission and neutron evaporation channels. The lower Z_{prog} nuclei are dominated by evaporation and emit around 3 neutrons during the deexcitation. This is in agreement with earlier studies of neutrino-induced reactions on r -process nuclei [47, 149, 148, 164]. When fission is the dominant decay mode we see that many more neutrons are released on average ($\langle N \rangle > 10$). One might naively think that these neutrons could alter the flow during the r -process. However, since we have (n, γ) equilibrium they are not expected to be important. After the freeze-out, however, there could be effects that alter the final distributions from r -process nucleosynthesis.

A_{prog}	Z_{prog}	σ_{tot}	σ_{fiss}	σ_{evap}	N_{fiss}	N_{evap}
274	90	1.45(+03)	1.15(+01)	1.44(+03)	0.06	3.01
275	91	1.43(+03)	1.69(+01)	1.41(+03)	0.10	3.42
278	92	1.46(+03)	2.85(+01)	1.43(+03)	0.17	2.98
281	93	1.48(+03)	5.31(+01)	1.43(+03)	0.30	2.95
286	94	1.48(+03)	8.01(+01)	1.40(+03)	0.57	3.10
293	95	1.57(+03)	2.44(+02)	1.33(+03)	2.10	3.99
296	96	1.57(+03)	8.68(+02)	7.03(+02)	7.29	1.48
297	97	1.53(+03)	5.68(+02)	9.66(+02)	5.09	2.70
300	98	1.53(+03)	1.01(+03)	5.27(+02)	9.25	1.12
301	99	1.50(+03)	1.15(+03)	3.48(+02)	10.65	0.93
304	100	1.52(+03)	1.36(+03)	1.63(+02)	12.83	0.21
307	101	1.53(+03)	1.52(+03)	1.34(+01)	14.85	0.01
308	102	1.50(+03)	1.48(+03)	1.50(+01)	14.28	0.00
313	103	1.64(+03)	1.63(+03)	4.21(+00)	16.23	0.00
314	104	1.59(+03)	1.59(+03)	2.06(-01)	15.72	0.00
321	105	1.75(+03)	1.75(+03)	1.64(-01)	18.60	0.00
322	106	1.71(+03)	1.70(+03)	1.39(+00)	18.26	0.00
325	107	1.73(+03)	1.73(+03)	1.56(-01)	18.87	0.00
324	108	1.62(+03)	1.62(+03)	2.30(-02)	17.39	0.00

Table 5.3: Total and partial fission and neutron evaporation cross sections (in units of 10^{-42} cm²) for neutrino-induced (ν_e, e^-) reactions on nuclei along the r -process path identified by their mass and charge numbers A_{prog}, Z_{prog} , respectively. The exponents are given in parentheses. N_{fiss} and N_{evap} are the numbers of neutrons emitted during the fission process and by neutron evaporation, respectively. The results are calculated adopting a Fermi-Dirac distribution with parameters $T = 4$ MeV and $\mu = 0$ for the neutrino spectrum.

This will be addressed again below when we have considered the intermediate nuclei that lie between the path and stability.

The large number of emitted neutrons from neutrino-induced fission on the r -process path is also expected to occur for β -delayed fission of the heaviest nuclei. To estimate this effect we followed [163] and assumed an end-point for the process at $A_{prog} \sim 300$. On a nucleus like ^{300}No ($Z = 102$ and $S_n = 3.1$ MeV) we find $\langle N \rangle > 10.4$ from neutrino-induced fission. β -delayed fission would take place from the daughter of ^{300}No which is ^{300}Lr . Here the β -strength function is expected to peak at high energy (~ 10 MeV) [163]. We find that more than 10 neutrons are released at 8 MeV excitation energy in ^{300}Lr (where we predict a fission probability of about 90%). We will return to the calculation of β -delayed processes in the next chapter.

The fission fragment distributions for selected nuclei on the r -process path are shown in figure (5.5). They show the same pronounced double-

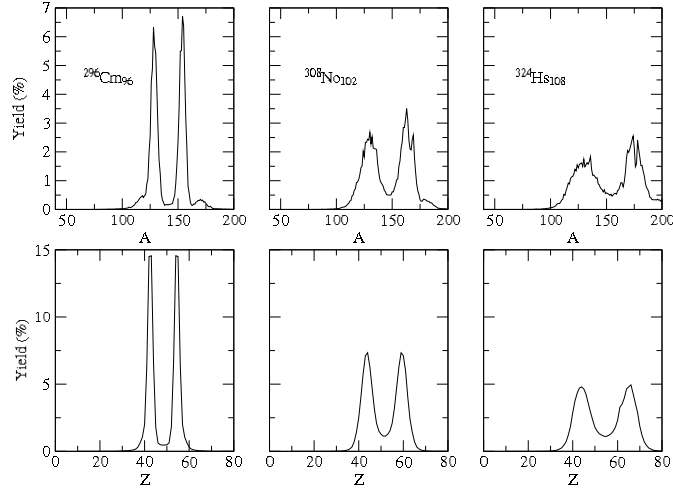


Figure 5.5: Mass (top) and charge (bottom) distributions (in percent) of fission fragments produced in (ν_e, e^-) reactions on some selected progenitor nuclei along the r -process path.

hump structure that was evident in the uranium isotopes. One peak is found at $A_{\text{low}} \sim 130$ and a second one at higher mass. This latter fragment is considerably below $A_{\text{prog}} - A_{\text{low}}$ due to the many neutrons released during the decay. Previous r -process simulations assumed symmetric fragments for simplicity [153] from both β - and neutron-induced fission events. The results presented here show that this is not the case for neutrino-induced reactions and that a more careful evaluation is needed. This is in accord with the conclusions of [165]. As we will see in the next chapter, our results strongly indicate that this conclusion is true for β - and neutron-induced fission as well.

In order to address Qian's scenario presented in section (5.2), we need to consider the nuclei as they decay toward stability. Therefore we will now present and discuss representative species in the mass ranges $A_{\text{prog}} = 200, 215, 230, 245, 260,$ and 275 with S_n that range from about 2 MeV on the r -process path to around 8 MeV at the line of stability. The results for these nuclei are presented in tables (5.4) and (5.5).

For progenitors with $A_{\text{prog}} \sim 200$ we see that fission is completely negligible. This is a result of the higher barriers relative to S_n (for all the barrier compilations mentioned). This is also the case for $A_{\text{prog}} \sim 215$, although fission does become competitive to neutron emission for $S_n > 6$ MeV. The nuclei with $Z_{\text{prog}} = 85 - 87$ are, however, α emitters with half lives of less than 1 ms. Therefore we do not expect neutrino-induced fission

A_{prog}	Z_{prog}	S_n	σ_{tot}	σ_{fiss}	σ_{evap}	N_{fiss}	N_{evap}
200	70	2.63	6.29(+02)	0.00(+00)	6.29(+02)	0.00	2.10
199	71	3.01	5.40(+02)	0.00(+00)	5.40(+02)	0.00	2.23
202	72	2.88	5.57(+02)	0.00(+00)	5.57(+02)	0.00	1.81
199	73	5.02	4.52(+02)	0.00(+00)	4.52(+02)	0.00	1.48
200	74	5.40	4.32(+02)	0.00(+00)	4.32(+02)	0.00	1.27
201	75	5.47	3.93(+02)	0.00(+00)	3.93(+02)	0.00	1.27
200	76	6.51	3.41(+02)	6.03(-09)	3.41(+02)	0.00	0.93
199	77	6.82	2.85(+02)	0.00(+00)	2.85(+02)	0.00	0.87
200	78	7.28	2.74(+02)	1.29(-09)	2.74(+02)	0.00	0.80
215	71	2.23	9.39(+02)	0.00(+00)	9.39(+02)	0.00	3.90
214	72	2.75	8.77(+02)	0.00(+00)	8.77(+02)	0.00	2.62
215	75	3.34	6.60(+02)	0.00(+00)	6.60(+02)	0.00	2.39
214	76	3.72	6.01(+02)	0.00(+00)	6.01(+02)	0.00	1.68
215	79	4.08	4.62(+02)	3.46(-05)	4.62(+02)	0.00	1.80
216	80	4.36	4.47(+02)	3.16(-04)	4.47(+02)	0.00	1.19
216	82	5.05	3.74(+02)	5.24(-02)	3.74(+02)	0.00	0.95
215	85	5.94	2.71(+02)	4.60(+01)	2.25(+02)	0.17	0.64
215	87	6.80	2.39(+02)	1.64(+02)	7.56(+01)	0.61	0.12
216	88	7.31	2.30(+02)	1.69(+02)	6.15(+01)	0.47	0.00
215	89	8.48	1.85(+02)	1.72(+02)	1.34(+01)	0.82	0.00
216	90	9.54	1.78(+02)	1.48(+02)	3.07(+01)	0.54	0.00
216	92	10.08	1.45(+02)	1.32(+02)	1.36(+01)	0.82	0.00
226	76	2.83	9.21(+02)	0.00(+00)	9.21(+02)	0.00	2.75
234	80	2.99	8.94(+02)	1.35(-02)	8.94(+02)	0.00	2.19
233	81	3.31	8.04(+02)	2.74(-03)	8.04(+02)	0.00	2.23
231	83	4.12	7.05(+02)	3.94(-02)	7.05(+02)	0.00	1.44
233	85	4.47	6.57(+02)	4.88(-01)	6.57(+02)	0.00	1.17
234	86	4.85	6.37(+02)	1.58(+00)	6.35(+02)	0.00	0.92
233	87	5.14	5.62(+02)	6.59(+00)	5.56(+02)	0.03	0.89
230	88	5.58	5.03(+02)	3.20(+01)	4.71(+02)	0.12	0.47
231	89	6.48	4.75(+02)	1.02(+02)	3.73(+02)	0.56	0.43
230	90	6.79	4.33(+02)	2.75(+02)	1.58(+02)	1.06	0.04
229	91	7.04	3.86(+02)	2.78(+02)	1.08(+02)	1.38	0.03
232	92	7.26	3.95(+02)	3.00(+02)	9.48(+01)	0.91	0.00
231	93	7.67	3.48(+02)	3.38(+02)	1.03(+01)	1.98	0.00

Table 5.4: Total and partial fission and neutron evaporation cross sections (in units of 10^{-42} cm²) for neutrino-induced (ν_e, e^-) reactions on r-process progenitors in the mass $A_{prog} \sim 200$ region, identified by their mass and charge number A_{prog}, Z_{prog} , respectively. The exponents are given in parentheses. N_{fiss} and N_{evap} are the numbers of neutrons emitted during the fission process and by neutron evaporation, respectively. The results are calculated adopting a Fermi-Dirac distribution with parameters $T = 4$ MeV and $\mu = 0$ for the neutrino spectrum. S_n is the neutron separation energy (in MeV) taken from [30].

A_{prog}	Z_{prog}	S_n	σ_{tot}	σ_{fiss}	σ_{evap}	N_{fiss}	N_{evap}
245	83	3.13	9.31(+02)	2.55(-02)	9.31(+02)	0.00	3.23
246	88	4.07	7.58(+02)	2.91(+00)	7.55(+02)	0.01	1.29
246	92	4.83	6.05(+02)	1.29(+02)	4.77(+02)	0.61	0.56
245	95	6.06	4.78(+02)	3.32(+02)	1.46(+02)	1.59	0.03
245	97	6.96	3.92(+02)	3.53(+02)	3.86(+01)	1.96	0.02
246	100	7.72	2.99(+02)	2.46(+02)	5.38(+01)	1.52	0.00
261	87	2.54	1.26(+03)	8.37(-01)	1.26(+03)	0.00	3.24
259	91	3.91	8.88(+02)	1.61(+02)	7.27(+02)	1.12	1.91
259	97	5.26	5.83(+02)	5.70(+02)	1.33(+01)	3.54	0.01
260	100	6.15	4.76(+02)	4.12(+02)	6.40(+01)	3.00	0.11
261	103	7.04	3.75(+02)	3.75(+02)	0.00(+00)	3.22	0.00
261	107	8.16	2.46(+02)	2.46(+02)	0.00(+00)	2.58	0.00
275	95	3.19	1.08(+03)	4.44(+02)	6.41(+02)	2.44	1.20
276	98	3.96	9.42(+02)	7.92(+02)	1.50(+02)	4.15	0.05
276	102	5.13	6.81(+02)	6.67(+02)	1.43(+01)	4.39	0.02
276	106	6.02	4.69(+02)	4.69(+02)	0.00(+00)	4.10	0.00
276	110	6.96	3.41(+02)	3.41(+02)	0.00(+00)	3.73	0.00
276	112	7.84	2.77(+02)	2.77(+02)	0.00(+00)	2.87	0.00

Table 5.5: The same as table (5.4), but for r -process progenitors in the mass $A_{prog} \sim 215$ region.

to compete. The only effect seems to be at stability where we have found asymmetric fragment distribution with one peak at $A_{high} \sim 150$ and one at $A_{low} \sim 215 - A_{high}$.

The nuclei in the mass range 230 also show fission to be a relevant decay mode only close to stability ($S_n > 5.5$ MeV). In figure (5.6) the fragment distributions from ^{230}Th , ^{229}Pa , and ^{232}U are shown. They have the double-hump structure with peaks at $A_{low} \sim 90$ and $A_{high} \sim 135$. This is in accord with the abundances in UMP stars and supports Qian's suggestion. The fission fragments shown in the figure also agree well with those measured in [75] where excitation energies of around 11 MeV were induced by electromagnetic interaction.⁴ This energy is close to the average neutrino energy of the $T = 4$ MeV Fermi-Dirac distribution (and the Q -values are small for the particular nuclei). We therefore have extra confidence in our results for these examples.

In table (5.5) we see that the importance of fission increases with mass number, becoming dominant for $S_n > 5$ MeV for $A \sim 245$ and $A \sim 260$

⁴These electromagnetic reactions have a close connection to neutral current weak interactions. Here we are considering charged current reactions and the comparison is therefore less obvious. However, in our two step model the initial state producing the daughter excitation is not important, only the energetics matters.

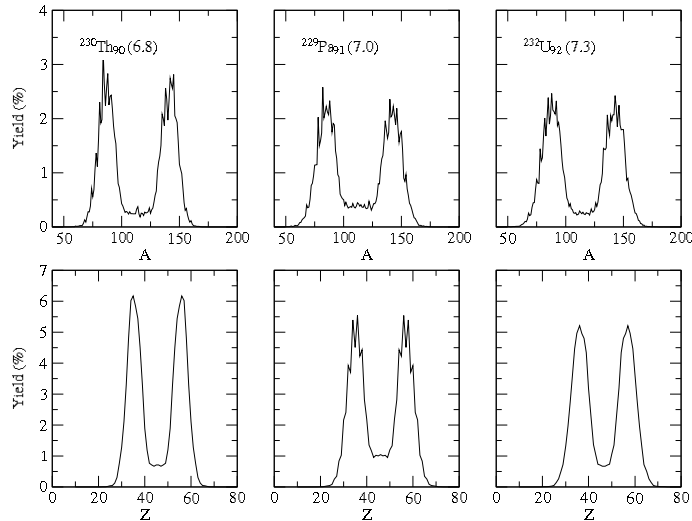


Figure 5.6: Mass (top) and charge (bottom) distributions (in percent) of fission fragments produced in (ν_e, e^-) reactions on some selected progenitor nuclei in mass range $A_{prog} \sim 230$. Number in parenthesis is the neutron separation energy (in MeV).

nuclei and for $S_n > 4$ MeV for $A \sim 275$. We note that these nuclei have β half lives that are longer than 1 s and one would expect the neutrino-induced reactions to be relevant out to radii of several 100 km. Figures (5.7), (5.8), and (5.9) show the fragment distributions for most of the nuclei given in table (5.5). The $A \sim 245$ mass range shows again the double-hump structure with peaks at $A_{high} \sim 140$ and $A_{low} \sim 100$. The $A \sim 260$ range shows a different behavior with ^{259}Pa having the two peaks while the others have broad distributions with little features. The $A \sim 275$ species have narrow symmetric distributions related to the $A = 132$ shell closure.

We see again the intricate competition between symmetric and asymmetric components as a function of mass and charge that was pointed out in section (2.3.2). The details of our predictions are subject to uncertainty due to the lack of experimental information on the fission process in very neutron-rich nuclei. We do, however, believe that our calculations show with clarity that complex fragment distributions can be expected from the influence of shell structure. We therefore re-iterate that simulations should include more detailed information about the fission fragments.

Finally we want to address the number of neutrons emitted during decay back to stability. The number is obviously smaller than on the r -process path since β -decays and β -delayed neutron emission increases S_n and the neutron excess. However, there will still be $\langle N \rangle \sim 2 - 4$ emitted from neutrino-

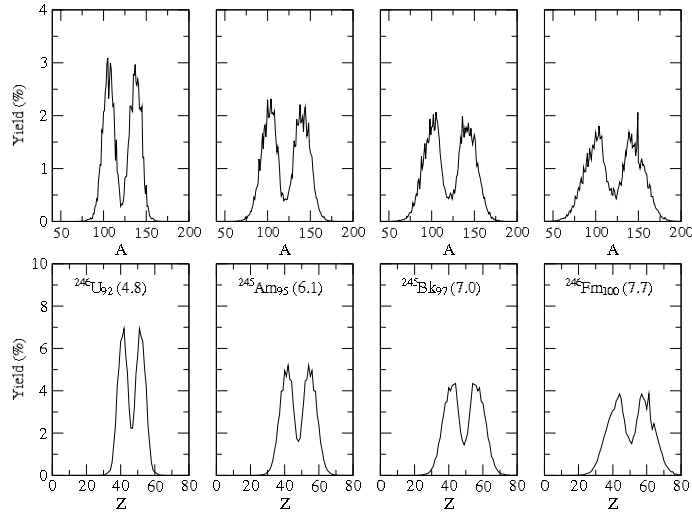


Figure 5.7: The same as figure (5.6 but for nuclei in the mass range $A_{\text{prog}} \sim 245$).

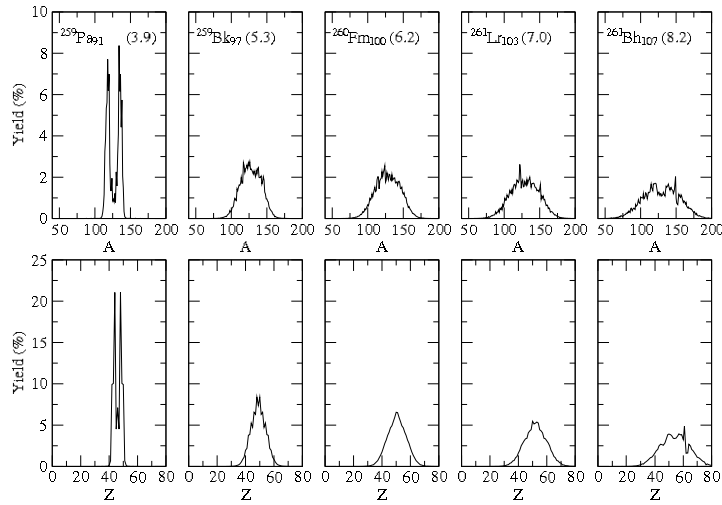


Figure 5.8: The same as figure (5.6 but for nuclei in the mass range $A_{\text{prog}} \sim 260$).

induced reactions and they could potentially capture on other nuclei and induce further reactions. This also needs to be taken into account in r -process simulations. We will explore these issues in the next chapter.

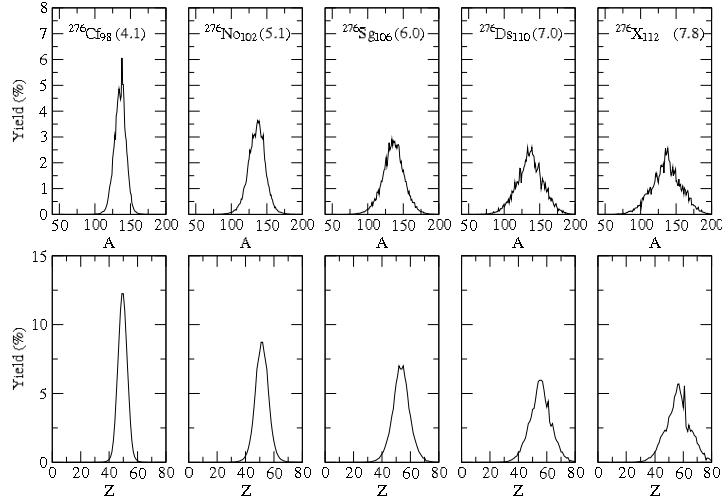


Figure 5.9: The same as figure (5.6 but for nuclei in the mass range $A_{\text{prog}} \sim 275$).

5.3.3 Preliminary Conclusions

The results presented above represent a significant improvement over previous studies by using (presumably) more realistic fission barriers and giving the detailed fragment distributions for the first time. Qian’s proposal seems to be supported by the fragment peaks from symmetric and asymmetric components that showed enhancement at $A \sim 90$ and $A \sim 135$. However, we find negligible neutrino-induced fission in the mass range $A_{\text{prog}} \sim 200 - 215$ and only for $Z > 92$ will fission become dominant. It therefore appears that the fission probability from neutrino-induced reactions are smaller than assumed by Qian (as was also concluded in [158]). As mentioned above, dynamical r -process simulations are needed to settle the issue in a proper manner. This will also require us to include β -delayed and neutron-induced processes for a consistent simulation.

The prospect of getting fission cycling from neutrino-induced fission also looks slim. The number of neutrons that come out from the reactions is simply not large enough ([158] estimates that between 70 and 100 neutrons per reaction is needed). As noted by Qian, one will have around eight β -decays in the first 10 s after bounce where neutrino fluxes are large. Looking back on our results for nuclei on the r -process path and those that are located between the path and stability, we see that it will be hard to reach nuclei with appreciable fission probabilities and many neutron emissions. For example, in mass range 275 where $Z_{\text{prog}} \sim 90 - 92$ on the path (table

(5.3)), we need the charge to increase by 8-10 units for fission to become dominant according to table (5.5). In agreement with [158], we find that fission cycling from neutrinos seems out of the question.

Chapter 6

Fission and the r -process

6.1 Introduction

The r -process relevant results discussed in the previous chapter gave a preliminary idea about the effects of fission. To make these considerations quantitative we need to implement the nuclear details into full network calculations. The heaviest elements in the r -process network can undergo fission through a number of reactions: neutron-induced, β -induced, neutrino-induced, and spontaneous fission. Having already discussed intensely the neutrino-induced channel, we still need to address the other processes in terms of rates, cross sections and fragment distributions. The network calculation that we have performed also includes the charged particle reactions that built up the seed nuclei, on which the excess neutrons are captured, from some initial distribution of nucleons and α -particles. The next section will therefore be devoted to the nuclear physics input that are employed.

6.2 Nuclear Physics Input

Apart from fission and neutrino reactions, the nuclear physics processes that are included in our calculations are basically inherited from the network of Freiburghaus *et al.* [155]. We have, however, used another selection of mass models. These are the Duflo-Zuker masses [166], the Möller, Nix, and Kratz FRDM masses [30], and the ETFSI-Q masses [167, 168]. The similarities and differences of these mass compilations will be discussed when we present our results in the next sections. The neutrino reactions included in the network for $A < 200$ and $Z < 70$ are an extension of those given in table (4.1) to cover the neutron-rich region also (although here no antineutrino reactions are considered as they are Pauli blocked). The neutrino-induced fission and neutron emission reactions described in the previous chapter are in the network for all nuclei with $Z = 70 - 120$ from stability to the neutron drip-line. We will now discuss the other fission channels in some detail and

then present and compare the fragment distribution used in the network for a selection of nuclei.

6.2.1 β -delayed Fission

To calculate the β -delayed processes on r -process relevant nuclei we need to consider fission and neutron emission channels. As we have discussed previously, this requires knowledge of the β -strength distribution in the nucleus that can be fed to the statistical model to yield the partial rates for the two reactions. In principle, we could use the RPA structure model to calculate the β -decay rates and then perform basically the same steps as for the neutrino-induced calculations. Given the large number of nuclei that we would like to include, this procedure would be prohibitively time-consuming. We therefore searched for an alternative. An obvious possibility was to initiate a collaboration with a group that had RPA or QRPA calculations of the relevant quantities at their disposal. This was harder than we had initially expected and we were prompted to use a crude method based on publicly available data.

The method that we have used is based on the FRDM model β -decay rates of Möller *et al.* [169]. This compilation gives both the rates and the emission probabilities for 0, 1, 2, and 3 neutrons. We have assumed that the branching ratios can be approximated by a distribution from zero to the Q-value that should reflect the emission probabilities of [169]. To elaborate on what this approximation entails we now give an example.

$T_{1/2}$	P_{0n}	P_{1n}	P_{2n}	P_{3n}	S_{1n}	S_{2n}	S_{3n}
0.02729	0.0553	0.2548	0.1583	0.5317	1.541	3.876	4.715

Table 6.1: β -decay details for ^{285}Am .

Consider the nucleus ^{285}Am which is located in the region where fission is expected. In table (6.1) we show the β halflife $T_{1/2}$ in seconds, the neutron emission probabilities P_{xn} , and the neutron separation energies S_{xn} in MeV. We can get the total decay rate by the simple relation $\lambda_{\text{tot}} = \ln(2)/T_{1/2}$, which we know to be the sum over all partial rates for all the individual nuclear states between zero and the Q-value of 10.309 MeV. The assumption we will make is that 5.53% of the rate lies between zero and S_{1n} , 25.48% between S_{1n} and S_{2n} , 15.83% between S_{2n} and S_{3n} , and the rest lies from S_{3n} up to the Q-value (all in the daughter nucleus). Within these intervals we now uniformly distribute the given percentages of the total decay rate and make an appropriate energy mesh on which to calculate the β -induced reactions using ABLA. The combination of the ABLA probabilities and fragment distributions with the rates then proceed exactly as described in section (2.4)

The β -induced fission probabilities calculated for a selection of Cf iso-

A	ABLA1 P_f	ABLA2 P_f	HM P_f	MS P_f	ETFSI P_f	FRDM $\langle N \rangle$	ABLA1 $\langle N \rangle_f$	ABLA1 $\langle N \rangle_e$
260	60	10	0	01	0	0	1.8	0
261	70	29	4	23	4	0	2.2	0
262	50	0	0	01	0	0	1.5	0
263	60	29	71	99	58	0	1.9	0
264	50	10	05	01	00	0	1.6	0
265	60	40	99	99	97	0	2.0	0
266	40	30	87	01	01	0	1.3	0
267	60	60	99	99	99	0	2.0	0
268	40	40	99	99	16	0	1.3	0
269	50	60	99	04	99	0	1.7	0
270	40	50	99	01	97	0	1.4	0
271	60	60	99	06	99	0	2.1	0
272	40	40	99	99	93	0	1.4	0
273	60	50	99	99	99	0	2.2	0
274	49	30	97	99	93	0	1.8	0
275	60	59	99	99	98	0.2	2.3	0
276	49	29	80	99	10	0.2	1.9	0
277	83	63	99	99	99	0.7	3.4	0.1
278	64	43	99	99	49	0.6	2.7	0.1
279	64	49	99	99	98	0.7	2.8	0.2
280	62	38	99	99	01	0.6	2.9	0.1
281	65	25	99	99	84	0.8	3.1	0.2
282	63	47	99	99	00	0.8	3.2	0.1
283	60	30	99	99	05	1.2	3.1	0.2
284	52	54	-	99	00	1.2	3.0	0.2
285	36	66	-	99	98	0.8	2.1	0.3
286	73	98	-	99	99	1.1	4.6	0.2
287	43	98	-	99	99	1.4	2.8	0.5
288	60	99	-	99	20	0.9	4.3	0.3

Table 6.2: Comparison of β -delayed fission probabilities (columns 2 through 6) and average neutrons emitted (columns 7 through 9) for Cf isotopes. Barriers used were from Sierk [71] (ABLA1), Howard and Möller [74] (HM), Myers and Swiatecki [170] (MS and ABLA2), and Mamdouh *et al.* [72] (ETFSI). The 7th column labelled FRDM gives the average number of neutrons emitted from the Möller *et al.* table [169] using the formula $\langle N \rangle = \sum_x x P(xn)$. $\langle N \rangle_f$ gives the average number of neutrons emitted from fission events, whereas $\langle N \rangle_e$ is from neutron emission events (both using ABLA1).

topes are presented in table (6.2) and compared to those given in table 2 of [163]. The column ABLA1 shows the calculation using the Sierk barriers [71] (FRDM mass model), whereas ABLA2 uses the Thomas-Fermi barriers and masses of [170]. We see that the two ABLA calculations yield rather similar numbers, and that the odd-even effects are smaller than for the MsSw and ETFSI barriers. The HM barriers give the highest fission probabilities which is expected since they are generally lower. Recalling the inconsistencies of the HM and ETFSI barriers discussed in section (2.3.1), we are more inclined to trust the MS barriers. It is therefore nice to see similar trends for ABLA2 and MS. However, our results are mostly below the other calculations and we find about equal probabilities for fission and neutron emission(s) in many cases. This tells us that the assumption used in many r -process studies of $P_{\text{fission}} = 1$ above $A \sim 245$ (see discussion and references in [163]) should be more carefully examined. We will address this question again below when we consider the importance of the different fission channels.

In the last columns of table (6.2) we give the average number of neutrons emitted according to a simple estimate from the Möller *et al.* table (see the table caption) and the number from fission and neutron evaporation events calculated with ABLA using FRDM masses and Sierk barriers (the sum of these two numbers gives the average for a β -induced reaction). We see that the FRDM estimate and the neutron evaporation in ABLA have similar trends with FRDM lying 0.5-1.0 neutrons above ABLA. However, if we sum both ABLA numbers we see that these are always larger. This is quite likely caused by the evaporation taking place in the fission fragments as they are generally closer to the drip-line than the parent nucleus. Since we do not have the number of neutrons emitted in fission events with the other methods, this comparison would seem unfair. We do, however, stress again that these effects should be put in the network as the neutrons released can induce further reactions (we will elaborate on this issue below).

6.2.2 Neutron-induced and Spontaneous Fission

Neutron-induced reactions could in principle be calculated with the ABLA code if one had the strength distribution for (n, γ) reactions on the nuclei (which is normally obtained from the inverse reaction through detailed balance). However, since this information was not accessible on a reasonable timescale, we had to find another solution. We did have the neutron-induced fission rates from [163] and therefore only the fragment distributions were needed. For that purpose one needs a sensible guess of the strength distribution. Here we employed the presumably simplest method one can think of. We assume that the entire strength is located at S_n in the $(A+1, Z)$ nucleus. This gave us an energy as input for ABLA. We further assumed zero angular momentum as this has little influence as discussed in section (2.4). In order to get the fragment distribution in this fashion, we are only interested in

the fission channel (neutron emission is basically the (γ, n) reaction which is already in the network). Therefore we forced ABLA to simulate fission events by putting all other channels to zero.

Spontaneous fission is also expected to have importance and we need to have a description of this as well. Here we have used the experimental value when available. For nuclei where there is no experimental information we use a formula obtained from a regression fit to the data (see [171] and references therein),

$$\log T_{\text{sf}} = 8.0B_f - 21.5, \quad (6.1)$$

where the half life is measured in seconds and the fission barrier B_f is in MeV. The barriers used in the formula are always those of MS [170]. There are of course several issues with this crude approach to the spontaneous fission half life. We will discuss some possible future improvements of this description in the next chapter.

The work on r -process nucleosynthesis in [171] also used an empirical formula for the fragment distributions. The expression used was

$$Y_{A_f, Z_f}(Z, A) \propto \exp(-(Z - Z_A)^2/c_Z) \times [\exp(-(A - A_L)^2/c_A) + \exp(-(A - A_H)^2/c_A)] \quad (6.2)$$

where c_Z and c_A are the widths, and Z_A , A_L , and A_H are specific functions of the mass A_f and charge Z_f of the fissioning nucleus. The formula is thus seen to contain a single gaussian for the charge and a two gaussian sum for the mass. While this is adequate in some regions (f.x. around uranium and thorium), we have repeatedly argued that this picture now appears too simplistic. In the next section we will show some specific examples that contrast the formula above with the results from ABLA. Despite these problems we will still employ eq. (6.2) for spontaneous fission yields.

6.2.3 Fragment Distributions

The fission fragment distributions for two examples of Am isotopes are shown in figures (6.1) and (6.2). The two were chosen since they play roles at different times during the r -process simulations that we will discuss below. As one can see, the ABLA yield from all processes are qualitatively very different. For all processes displayed we see a single-hump structure in ^{275}Am , whereas ^{287}Am shows a much more complicated pattern with four peaks for β - and neutron-induced fission, and a double-hump for neutrino-induced fission. This should be less surprising as we have already seen in section (2.3.2) that the profiles can change dramatically within an isotopic chain, and with excitation energy.

We see clearly that β - and neutron-induced yields are very similar. This fact is to be expected since the strength is located at roughly the same energies (around and below 5 MeV in both species). The number of neutrons

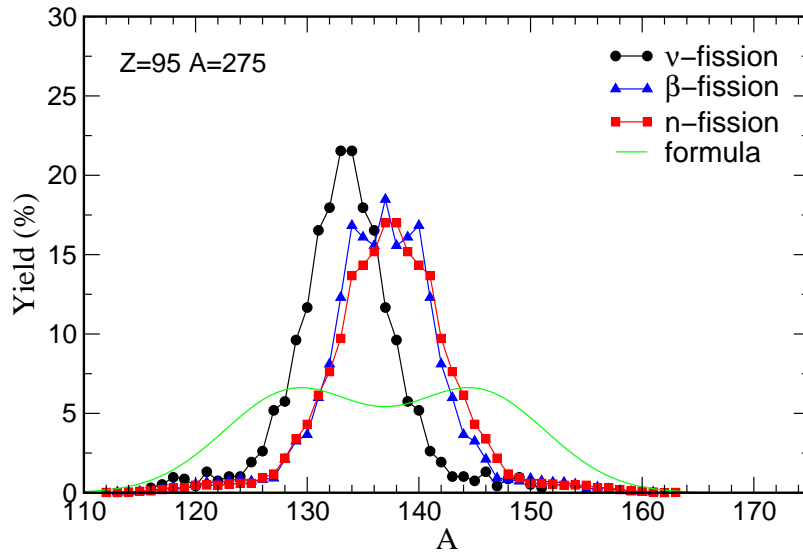


Figure 6.1: Fission fragment distribution yields from fission of the daughter ^{275}Am by the indicated processes. The green curve is the fit using the formula in eq. (6.2).

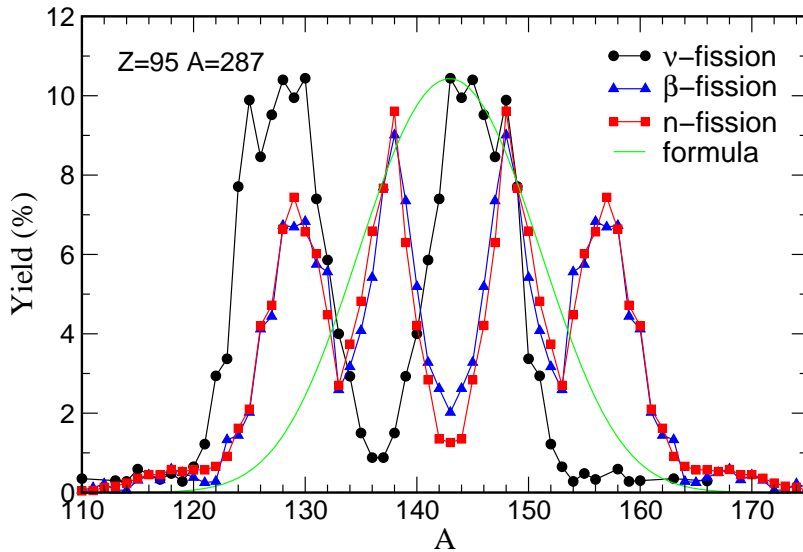


Figure 6.2: Same as figure (6.1 for ^{287}Am .)

released from these events are also similar and of order 5 in ^{275}Am and 10 in ^{287}Am . Neutrino-induced fission has its strength at higher energies and the symmetric mode is therefore likely to be more visible as in figure (6.1). The larger number of neutrons released from neutrinos could then explain the shift to lower mass of the peak. However, this is in contrast to figure (6.2) where a clear asymmetric yield is found (the shift could still be

explained from more neutrons released). Alternatively, it could be a result of the $A \sim 132$ doubly-magic fragment being dominant at higher energies. The other processes could then be showing the transition to the low energy region where a more complicated pattern emerges (from the influence of pairing, shell corrections, and possibly deformation).

The green curves in both figures give the fragment distributions according to the formula of eq. (6.2). These are clearly not like the results of ABLA for any of the other processes. It appears that they are actually opposite to the ABLA trends, being symmetric in the multiple-hump case of ^{287}Am and asymmetric for ^{275}Am . It would therefore be very interesting to treat spontaneous fission within the ABLA model to get a more consistent picture.

6.3 r -process Simulation Model

We now proceed to describe the essential details of the dynamical r -process simulation model that we have used. The physical situation that we are interested in is the hot neutrino-driven wind scenario discussed in chapter (5) and we therefore need a dynamical approach. The model used is basically a modified version of the one of Freiburghaus *et al.* [155] and our discussion will be close to the one given in that paper. In contrast to classical r -process simulations where one fixes the neutron density ρ_n , the temperature T , and the duration time τ_r , the dynamic approach allows these to vary while keeping the entropy S , the proton-to-neutron ratio Y_e , and the expansion timescale τ fixed. We are thus assuming adiabatically expanding matter where the variation of T is determined by the equation of state and the condition that ρr^3 is constant (r and ρ are the radius and density of the matter). For the equation of state we depart from [155] and use a more realistic choice [172].

The simulation will consider an initial distribution of neutron, proton, and α particle in NSE (see appendix (C)) for the specific Y_e (we will use $Y_e = 0.45$ throughout). At constant S , these combine into heavier nuclei (primarily Fe group) during the expansion with some α s and neutrons remaining. For high S there will be an α -rich freeze-out from charged particle reactions at lower temperatures that produces $A \sim 80 - 100$ nuclei. These can act as a seed distribution Y_{seed} for the remaining neutrons Y_n to capture on for r -process nucleosynthesis. The model is simply that of a homogeneously expanding volume $V(t)$ containing some fixed mass with an expansion timescale that is relevant to the Supernova problem and the neutrino-driven wind scenario. The latter of course implies a flux of neutrinos in the model. Here we will assume a standard luminosity ($L_\nu \sim 10^{51}$ erg s $^{-1}$, as argued in [149], see also section (5.1.2)) with an r^{-2} scaling and a spectral temperature of 4 MeV (suitably modified to account for the

red-shift effect of the protoneutron star).

During the adiabatic expansion we have the standard thermodynamic identity

$$T(t) = T_0 \left[\frac{V_0}{V(t)} \right]^{\gamma-1} \quad (6.3)$$

with adiabatic exponent γ and otherwise obvious notation. Since we are furthermore assuming a uniform expansion with constant velocity, we have for the radius $r(t) = r_0 + vt$ with v the expansion velocity. For the initial condition we follow [155] and assume $T_0 = 9 \times 10^9$ K, $r_0 = 130$ km, and $v = 4500$ km s⁻¹. Defining the expansion timescale by $T(\tau) = T_0/e$ we get $\tau = 50$ ms for the mentioned velocity (with $\gamma = 4/3$ since radiation dominates the entropy).

A change in the expansion timescale τ would have a direct effect on the very important quantity Y_n/Y_{seed} . This ratio was already discussed in section (5.1.2) where we argued that it needs to be 100 or more to account for heavy nuclei including the actinides. If τ becomes shorter (for larger expansion velocities) then one will actually increase Y_n/Y_{seed} . This is a consequence of the α particles having less time to break the 3α and αn bottlenecks, resulting in less heavy nuclei and more neutrons for them to capture. Turning this argument around we conclude that shorter timescales require smaller S to produce even the heaviest elements ([146] has an extensive discussion of these issues),

The advantage of this adiabatically expanding model over the classical r -process simulation should be clear when considering our preferred site. It takes the changes in the r -process path with T and the possible non-equilibrium of the (n, γ) reactions during freeze-out into account.

6.4 Results

We now present the results of the r -process fission studies. These have been carried out in a parametric way where we have varied the initial entropy to see the effects. We have also studied the influence of different mass models and found some very interesting features. The importance of the different fission channels will be addressed, also within different mass models. Lastly we will comment on some issues of consistency of theoretical inputs in this type of study.

6.4.1 The Region and Role of Fission

First we will discuss the region where fission takes place in the r -process. For this purpose we show a detailed contour plot of the fission barriers from the Thomas-Fermi model of [170] in figure (6.3). For all the mass models shown we clearly see the influence of the $N = 184$ shell closure. When the

r -process reaches charges $Z \sim 85 - 90$ the matter will accumulate at this magic number where large fission barriers are found. Fission can therefore only occur for nuclei that manage to pass this waiting-point. This depends on the strength of the shell gap of the particular mass model and also on the β half lives (we will explore this effect below). We see the weakest gap in the Duflo-Zuker masses, followed by FRDM, and with the ETFSI model showing the strongest gap. This results in slightly less fission for the ETFSI model compared to the other two (we will quantify this below).

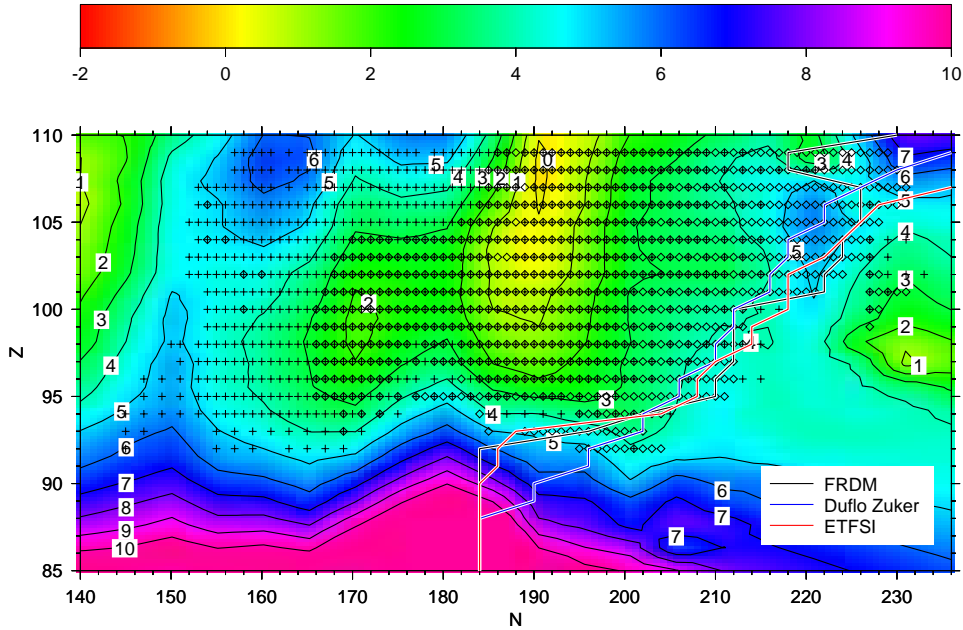


Figure 6.3: Region of the nuclear chart where fission takes place during the r -process. The contour lines represent the Thomas-Fermi fission barrier heights in MeV. Crosses show the nuclei for which neutron-induced fission dominates over (n, γ) (based on [163]). Diamonds show the nuclei for which the spontaneous fission or β -delayed fission operates in a time scale smaller than 1 second (the former based on [171], the latter based on the method of section (6.2.1)). The lines show the location for which negative neutron separation energies are found in different mass models (FRDM [30], ETFSI [167] and Duflo-Zuker [166]).

Once the matter reaches high enough Z to fission it will mainly occur through the neutron-induced channel, as we will discuss shortly. The event will generally release many neutrons (more than 10 on the r -process path and around 6 when fission happens after freeze-out). Most of these neutrons come from the fission fragments which will lie closer to the drip-line than the parent nucleus. These neutrons can then be recaptured by other, mainly heavy nuclei (since the cross sections are larger). We can therefore have a chain-reaction effect that fissions the heavy material on a timescale of a few seconds. This will also be the case after ρ_n drops and the r -process

effectively ends since the matter at $N = 184$ will β -decay toward 'stability' and produce further β -delayed neutrons. We note that these qualitative considerations are independent of the fission barriers (see for example [173] where a similar figure for the ETFSI barriers [72] is given).

The fragment distributions shown in figures (6.1) and (6.2) are very appropriate with respect to the discussion above as they are located in the two different places where fission can take place. ^{287}Am is encountered on the r -process path, whereas ^{275}Am is on the decay back to stability after freeze-out. It is therefore interesting to consider the very different yield profiles. For ^{287}Am the fragments at $A < 130$ and $A \sim 160$ could contribute to the low end of the $A \sim 130$ 2nd r -process peak and the small peak at $A \sim 160$ (expected to come from fission since the early work of [152]). In ^{275}Am we have two fragments in the high part of the $A \sim 130$ peak. We thus see that the heavier nuclei will give fragments that are lighter than the less neutron-rich ones. The endpoint of the r -process might therefore be important for the $A < 130$ region where the UMP measurements show interesting deviations from solar abundances.

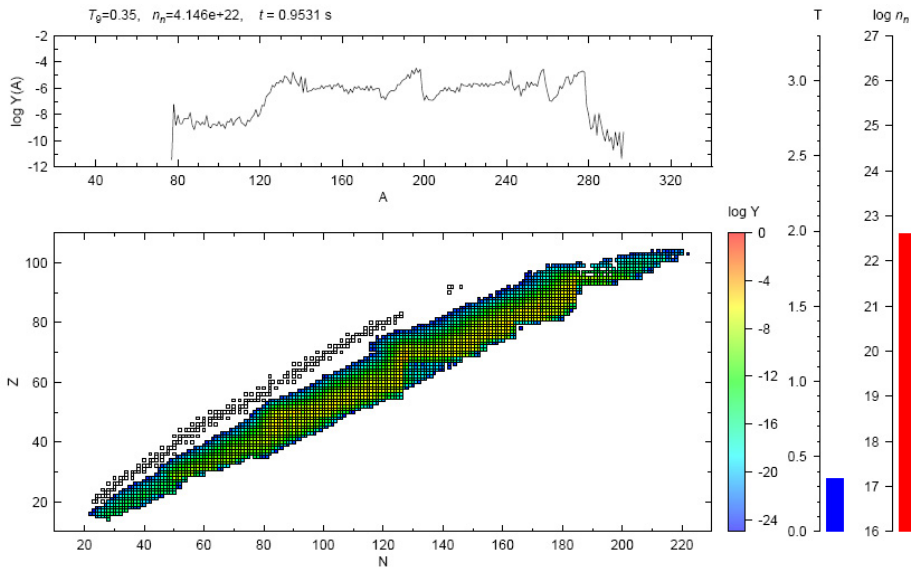


Figure 6.4: Abundance pattern of an r -process simulation after around 1 s. Upper panel shows the mass abundance profiles on a logarithmic scale. A contour plot of the relevant part of the nuclear chart is shown in the lower panel. The simulation used the FRDM masses [30] and had $S = 400$ ($Y_n/Y_{\text{seed}} = 186$).

In figure (6.4) we show a snapshot of a simulation using the FRDM mass model. The parameters are $S = 400$ or $Y_n/Y_{\text{seed}} = 186$. The distribution of nuclei is shown roughly one second after the simulation was begun (when the nuclei reach the fission region). From the contour color coding and the abundance pattern one clearly sees the shell closures at $N = 82$, 126 , and

184 (minor shells are also seen just below $N = 184$, see the FRDM part of figure (6.8)). As discussed above, we see the accumulation of matter happening at $N = 184$ for $Z \sim 90 - 95$ and also the matter that has climbed above the shell closure to $A \sim 285$. The endpoint of the r -process is seen to be around $A \sim 280$ (this turns out to be true for all the mass models used). The nuclei above $A \sim 200$ (except actinides) will of course decay, the heaviest ones doing so through fission to produce fragments in the range $A = 130 - 190$. This does, however, depend on the particular mass model used as we will discuss below.

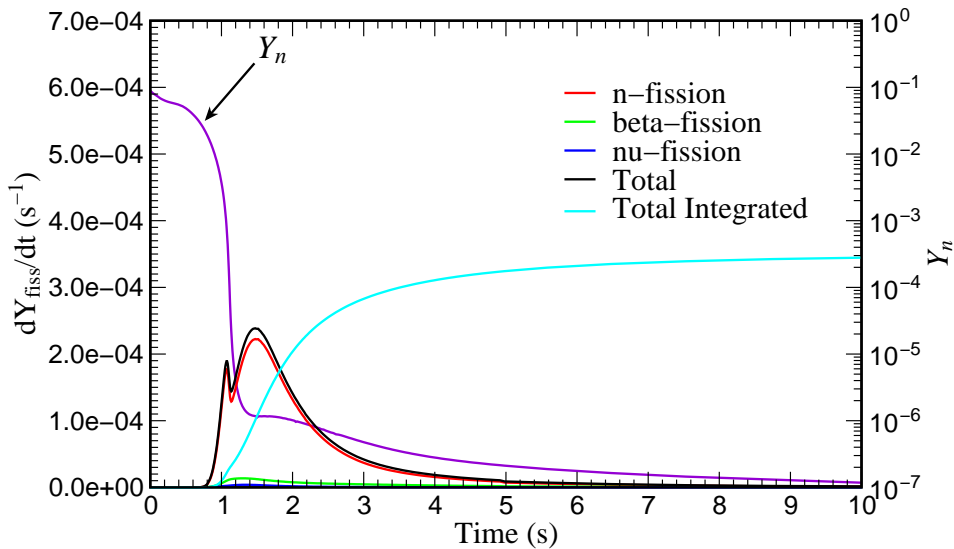


Figure 6.5: The influence of the different fission channels as a function of time. Shown are differential contributions $\frac{dY_{\text{fiss}}}{dt}$ (left axis) for neutron-induced (red), β -induced (green), neutrino-induced (dark blue), and total (black). The integrated total (light blue) and Y_n (purple) are also displayed (right axis). The simulation used the FRDM masses [30] and had $S = 400$ ($Y_n/Y_{\text{seed}} = 186$).

The timescale and periods of fission is illustrated in figure (6.5) where the abundance changes due to the various fission channels are plotted along with Y_n . The total is clearly seen to be dominated by neutron-induced fission with very little contribution from β -induced and virtually no neutrino-induced. This holds true for all mass models as one can see from table (6.3) which gives the relative contributions for different values of the entropy S . We see that the contributions of different fission channels are increasing with S and generally very similar for the different mass models (except for ETFSI-Q at $S = 350$, see below).

Figure (6.5) shows two characteristic periods. There is an initial phase (up to about 1 s) where fission takes place at and above the $N = 184$ peak as discussed above. After the neutron density drops the matter will start to β -decay back to stability and release neutrons that can induce further

$S = 350$ ($Y_n/Y_{\text{seed}} = 116$)	(n,fission)	β -induced	ν -induced	Total
ETFSI-Q	0	0	0	0
FRDM	10	1	0	11
Duflo-Zuker	10	1	0	11
$S = 400$ ($Y_n/Y_{\text{seed}} = 186$)	(n,fission)	β -induced	ν -induced	Total
ETFSI-Q	33	5	0	38
FRDM	36	3	0	39
Duflo-Zuker	36	3	0	39
$S = 500$ ($Y_n/Y_{\text{seed}} = 417$)	(n,fission)	β -induced	ν -induced	Total
ETFSI-Q	56	4	0	60
FRDM	58	5	0	63
Duflo-Zuker	58	5	0	63

Table 6.3: Percentages of different fission channel for different mass models and various entropies (or Y_n/Y_{seed}).

fission. This is seen as a 2-3 second period where neutron-induced fission is high and Y_n drops only slowly. This dominance of neutron-induced over β -induced and spontaneous fission is a consequence of its timescale during the first seconds of the simulation. Here the neutron density is around 10^{18} cm^{-3} and above which gives a lifetime for neutron capture of order a few ms, whereas the β -half lives are an order of magnitude larger. For spontaneous fission the simple formula in eq. (6.1) predicts that the barriers should be around 2 MeV or below to compete. According to figure (6.3) this would require $Z \gtrsim 97$ during the decay back to stability which seems unrealistic. These timescale considerations were also found to be independent of the barriers, although they can be quite dependent on the mass model used and particularly the β -decay properties.

6.4.2 The $N = 184$ Shell and Half lives

The discussion above made it clear that the $N = 184$ shell closure has a decisive role in the fission dynamics of the r -process in our simulations. Here we find the mentioned accumulation of matter occurring for all the mass models explored. The neutrons that are released from β -delayed neutron emission will start the fission chain reactions described in section (6.4.1). The lifetime against β -decay in the region is therefore important.

To elaborate on this dependence, we have performed calculations where the half lives are scaled to make them both longer and shorter than standard values. In figure (6.6) we show the results of these simulations. Evidently, the longer half lives have a major influence on the $A \sim 195$ peak and also on the actinide abundances. This is a result of the drop in neutron densities (down to around 10^{18} cm^{-3}) that happens while waiting for the β -decays. This produces a weak r -process or strong s -process peak that is shifted to the right. The severe depletion of the actinide region is also very unfortunate as this would change the U/Th cosmochronometers. For the reduced half

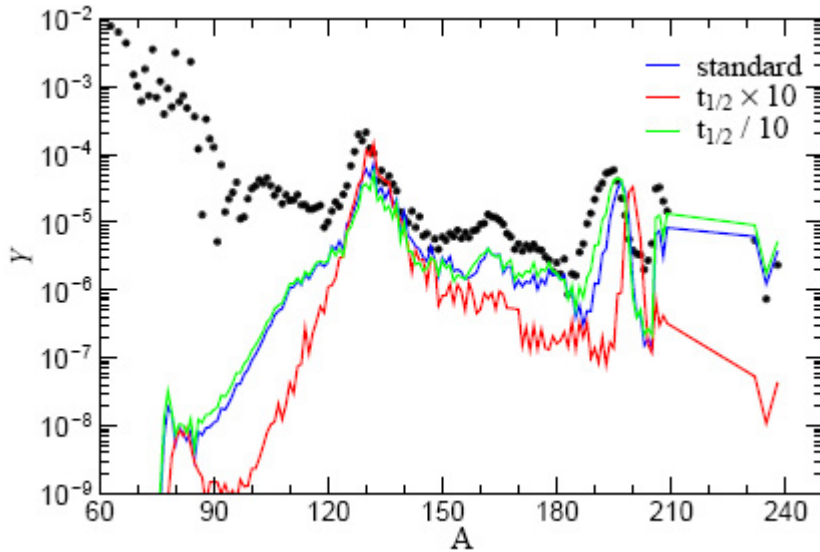


Figure 6.6: Abundance patterns for an FRDM simulation with $S = 400$. The blue curve shows the result with standard β half lives [30]. The red curve shows the results of multiplying the half lives by 10 and the green curve has half lives that are divided by a factor 10.

lives we see the opposite tendency with good agreement for actinides and a $A \sim 195$ peak that is closer to solar compared to that seen when using the standard FRDM decay rates [30].

There are good reasons to believe that the actual half lives could be shorter than the FRDM numbers in [30]. The more recent tables of [169] which include also forbidden transitions show shorter half lives in the $N = 184$ region of interest. Similar efforts to include forbidden transitions in the half lives within a QRPA model are reported in [174] and [175] where a shortening of the half lives by factors of 2-5 compared to those given in [169] is found. This points in the direction of the green curve of figure (6.6) and further investigation into this issue is under way.

6.4.3 The $N = 82$ Shell Closure

In this section we present results for the influence of the shell structure at lower neutron numbers. We have calculated the r -process abundances for the different mass models after 1.6 Gy when all decay toward stability has ceased (except for naturally occurring radioactivity). These results are shown in figure (6.7) as a function of entropy S . The profiles shown for FRDM and Duflo-Zuker masses are very similar, whereas that for ETFSI-Q clearly differs. This is related to the shell closures at $N = 126$ and (particularly) $N = 82$ which are quenched in ETFSI-Q. The other two have strong shell gaps also close to the drip-line. This can be clearly seen in figure

(6.8) where the r -process path at freeze-out is shown for the mass models. The conditions of figure (6.7) have almost no gap at $N = 82$ for the EFTSI-Q masses and the matter therefore passes right through. This means that most neutrons are stuck in heavy nuclei and cannot induce fission events.

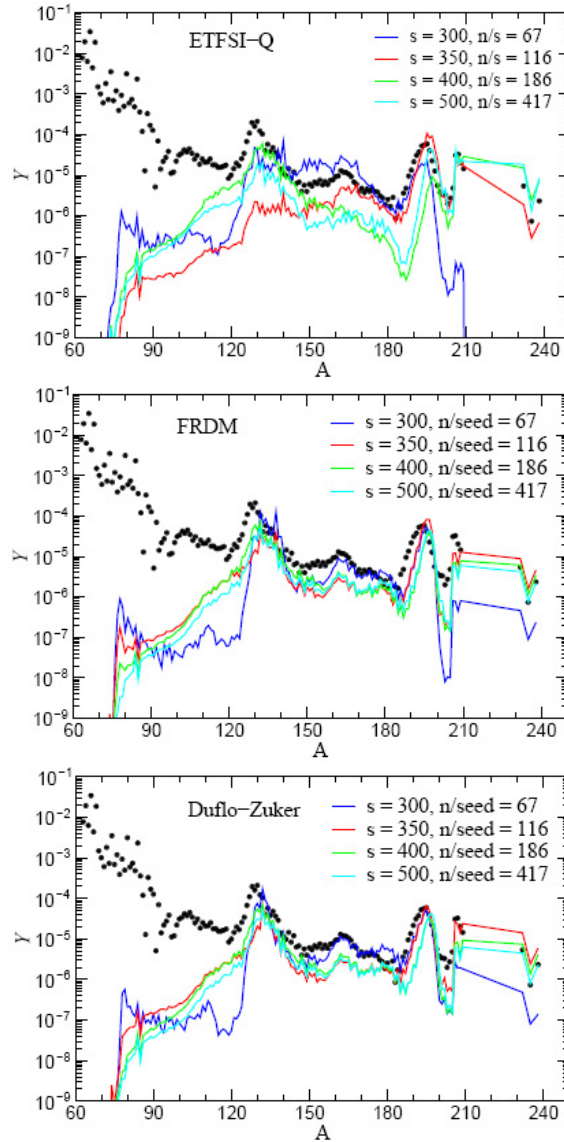


Figure 6.7: Final r -process abundances (after 1.6 Gy) obtained using different mass models (FRDM [30], EFTSI-Q [168] and Duflo-Zuker [166]). The solid circles correspond to a scaled solar r -process abundance distribution [176].

For the other mass tables there is some accumulation of matter at $N = 82$ and $N = 126$ and when this matter finally reaches the fission region there are still many neutrons around to induce fission and release even more neutrons

to allow a longer r -process. This, in turn, means that more matter will originate as fission fragments and explains why FRDM and Duflo-Zuker produces more matter with $A = 130 - 190$. We thus see that the shell structure at $N = 82$ plays a decisive role for the fission dynamics of the r -process. We also notice that the Duflo-Zuker results seem to be better for the $A \sim 195$ peak. In figure (6.8) we see a softer gap at $N = 184$ for this particular mass model, implying shorter β half lives. The peak being closer to solar for Duflo-Zuker is thus not surprising in light of the discussion on half lives above.

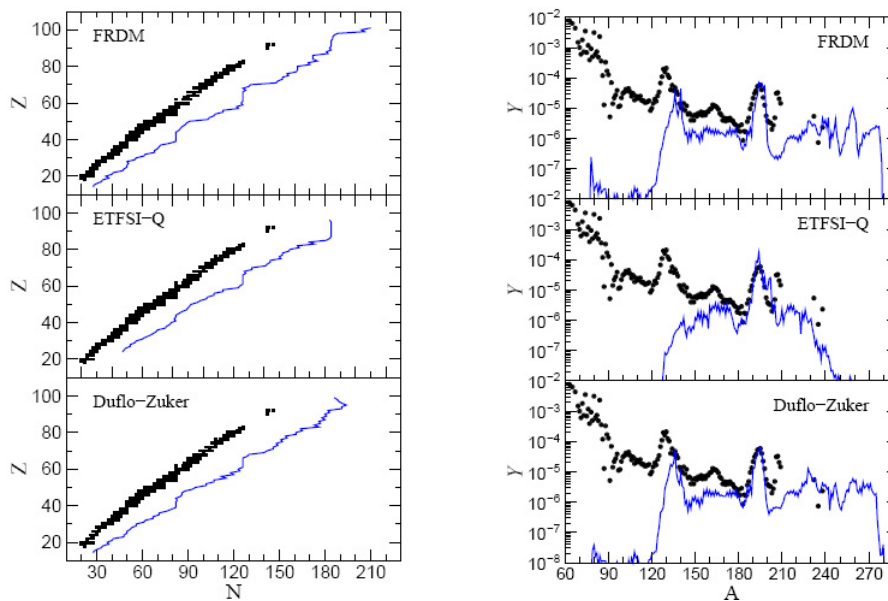


Figure 6.8: The left panel shows the r -process path at freeze-out for the calculation with $S = 350$ or $Y_n/Y_{\text{seed}} = 116$ for different mass models. The right panel shows the abundance distribution at freeze-out.

When we consider the FRDM and Duflo-Zuker results in figure (6.7) we see the abundances for $S = 350, 400,$ and 500 are quite similar. These are the values where Y_n/Y_{seed} is large enough for fission to be important (see table (6.3)) and shows a robustness of the predictions. Calculations based on mass models with strong shell gaps are thus seen to be less dependent on initial conditions once fission operates. This might explain observations of UMP stars where universal abundances are found for $A > 130$ as discussed in chapter (1) and section (5.2).

6.4.4 Fission and Neutrinos

In this section we briefly summarize our results on the influence of neutrino-induced fission in relation to the questions posed in the last chapter. The

clear conclusion from the results presented in this chapter is that fission through neutrinos does not appear to have any significant effect on the r -process under normal circumstances. One could of course imagine an astrophysical site with luminosities different from the standard one assumed for the neutrino-driven wind. To investigate this possibility, calculations with larger L_ν were carried out. In figure (6.9) we show the results with a factor of 5 and 10 on the neutrino fluency (which basically means multiplication of L_ν by the same factor). This figure clearly shows that such increases are not viable as they destroy the ability to produce heavy r -process nuclei (this is the α -effect discussed by [47] and [177]. See also figure (5.1)).

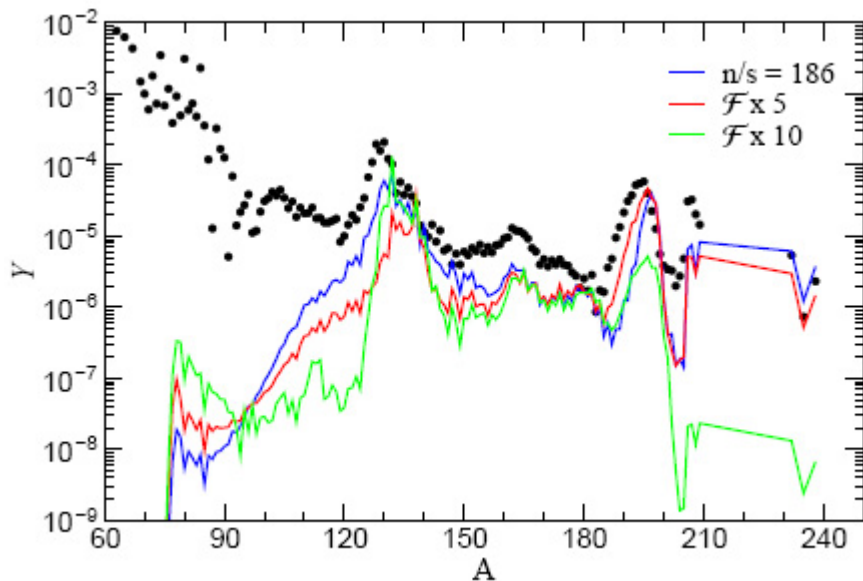


Figure 6.9: The effects of increasing the neutrino fluency for a simulation with the FRDM mass model and $S = 400$.

6.5 Nuclear Data Consistence

We have now discussed our results with respect to three different mass models. However, these were all obtained with the Thomas-Fermi fission barriers of [170]. This is of course not quite consistent. We do not expect that there will be major changes when considering other barriers also but further studies will have to be done. Unfortunately there are some mass tables that are not extended beyond $A \sim 300$ which is what one needs. While sorting out these difficulties one can still do parameter-like studies on the barriers by combining the mass models above with the various barrier compilations mentioned in this and the last chapter. Ultimately one would of course like to have all quantities including masses, β half lives, barriers, and fission

yields from a single model but this is still to come.

With respect to neutron-induced fission there is still the issue of the simple placement of the strength discussed in section (6.2.2). This can be improved by taking a realistic strength distribution and calculating the ABLA outcome as mentioned above. Such calculations are currently under way. Through an improvement of the treatment of low-energy barrier penetration one would also be able to calculate spontaneous fission yields with ABLA, although the half lives still need to be introduced from the outside.

6.6 Concluding Remarks

The studies of fission in the r -process clearly show that mass models are very important. In particular, our results show that the $N = 82$ shell determines the amount of fission taking place during the process. Mass models that have strong gaps at $N = 82$ turned out to have very robust abundance patterns once fission starts operating. The ETFSI-Q mass model therefore seems to have trouble in describing the influence of fission when compared to FRDM or Dufflo-Zuker. We get variations that cannot explain the observed robustness of the r -process for $A \geq 130$. The need for more experimental measurements of the masses in this region is therefore essential. This would also constrain theoretical models and provide a better basis for extrapolation into the unknown terrain where fission occurs during the r -process.

The discussion on the influence of β half lives at $N = 184$ showed that shorter half lives are one of the things needed to get a true r -process peak at $A \sim 195$. The need for shorter half lives to avoid accumulation of matter at $N = 184$ seems to be met by the most recent calculations as discussed above, but the theoretical models could benefit from stronger constraints coming from experiment.

We have addressed the issue of fission cycling at several points in the preceding chapters. The cycling time was estimated to be around 1.5 s in our calculation and since this is of the same order as the duration of the r -process we have no more than one cycle. We therefore expect no influence of cycling to stabilize the abundance pattern. However, the barriers at the $N = 184$ are still a concern in this respect. If they are low (and the β half lives are short) then fission cycling could perhaps take place.

The possibility of finding super heavy elements in r -process studies is another interesting issue. In some simulations we have found nuclei with masses up to $A \sim 320$. However, even if they are present after freeze-out, they will undergo fission during the β -decay back to stability and leave no trace amount. If the barriers were different one could potentially produce some super heavies that would be left over after an r -process. Investigating the barrier dependencies could possibly give clues to this intriguing subject.

Finally we mention that the r -process results presented above can also

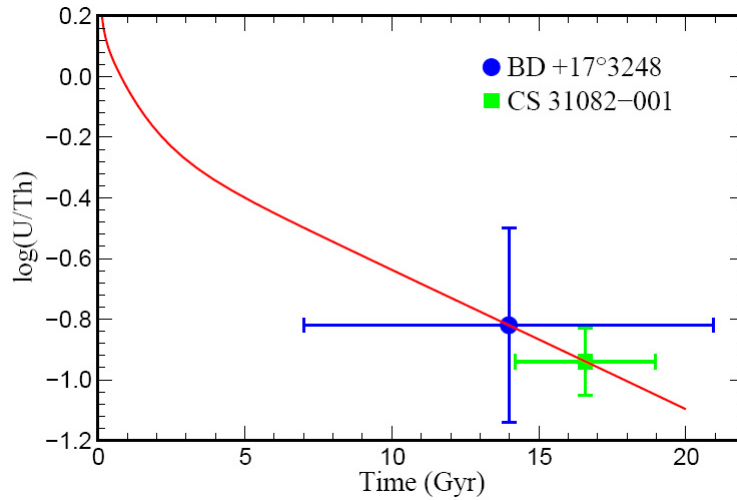


Figure 6.10: The logarithm of the Uranium to Thorium ratio as a function of time. The red curve shows the simulation result averaged over FRDM and Duflo-Zuker masses and over entropies $S = 350, 400,$ and 500 where fission contributes significantly. The measurement for CS 31082-001 is from [179] and that of BD +17°3248 is from [180].

be used to estimate the age of the oldest stars in the galaxy. This would then put limits on the age of the Milky way and the Universe in general. The recent detection of Th and U in metal-poor stars [178] means that one can make a more accurate age determination than using the traditional Th to Eu ratio since Th and U are produced through α -decays coming from the same mass region. As a simple test we can average the U/Th ratio over $S = 350, 400,$ and 500 for FRDM and Duflo-Zuker and compare to measured ratios. This is done in figure (6.10) where the ratio is plotted as a function of time. The agreement between the measured values and the simulation curve is striking, although the uncertainties are still quite large. As argued in [181], these prediction are very dependent on the inclusion of fission in the r -process network. In particular, [181] argues that spontaneous fission is especially important for cosmochronometry using the actinides. Improving the description of this channel in the manner outlined above is therefore a high priority.

Chapter 7

Summary and Outlook

In this thesis we have considered nuclear physics data that are needed for modeling of astrophysical environments. We were particularly concerned with excitation of nuclei through weak interactions and the subsequent decay through various channels. The deexcitation of daughter nuclei was treated within a statistical approach that included particle emissions and fission. For the latter reaction our model was also able to determine yield distributions of fission fragments via a Monte Carlo sampling technique. The calculated nuclear data were then implemented in astrophysical models and the effects of the new results were discussed.

The first major application treated was the inclusion of neutrino and antineutrino cross sections in early, proton-rich ejecta from core-collapse Supernovae. This environment is a good candidate for the production site of the rare proton-rich elements that are observed in nature. A very interesting new nucleosynthetic flow was discovered when fully including the neutrinos in the nuclear network. It is expected to be generic to proton-rich environments that are traversed by significant neutrino fluxes and was dubbed the νp -process. Through antineutrino on proton reactions the process makes neutrons that can overcome the Coulomb barriers and capture on nuclei to help build up proton-rich material with masses between $A = 64$ and $A \sim 100$.

Depending on the details of the process, it could likely explain the origin of the very rare isotopes $^{92,94}\text{Mo}$ and $^{96,98}\text{Ru}$ which is currently not generally understood. The νp -process is primary, meaning that it produces its own seeds (contrary to what happens in the well-known s -process). This is consistent with recent galactic chemical evolution studies [121] that suggest a primary Supernova origin for these proton-rich nuclei.

In a second application of neutrino reactions we considered the role of neutrino-induced fission reactions in r -process nucleosynthesis. A proposal by Qian [156] attempts to explain recent observations of abundances in very metal-poor stars by invoking a given amount of neutrino interaction in the

r -process that was responsible for the observed patterns. The suggestion was that neutrino-induced fission could produce enhanced structure in the abundances at $A \sim 130$ and $A \sim 90$. However, this requires a high neutrino-induced fission probability during the r -process and on the decay back to stability of the synthesized matter.

We carried out detailed calculations of neutrino-induced processes on nuclei along the r -process path and for representatives on the decay back to stability to evaluate this scenario. Using more realistic barriers than the earlier work of [158], we found that the probabilities are unfavorable. We did, however, find that the fragment yields could accommodate those needed in the proposal. Later investigations using dynamical r -process simulations confirmed our suspicions that neutrino-induced fission had virtually no effect (less than 1%). The present work therefore rules out the suggestion of Qian [156].

Finally, we considered the general role of fission in the r -process. For this purpose we calculated fragment distributions for all relevant nuclei from neutron-, β -, and neutrino-induced fission. Included was also spontaneous fission based on older work [171]. We found that fission takes place in the region around the $N = 184$ shell closure, independent of barriers and mass models used. The fission events were largely neutron-induced with a small contribution from β -induced fission.

The β half lives around this region were instrumental to get a good reproduction of the 3rd r -process peak at $A \sim 195$ (with shorter lifetimes giving results closer to the observed solar abundances). This was a result of the many neutrons that β -decays produce in neutron-rich nuclei with large Q -values. These could then initiate neutron-induced fission event that would also produce even more neutrons, resulting in a chain reaction mechanism. Longer half lives would then give neutrons off on a longer timescale, shifting the 3rd peak to the right (toward the s -process peak).

The r -process simulations were also found to be very sensitive to the strength of the $N = 82$ shell gap. The mass models that had a strong gap at $N = 82$ produced results that were largely independent of the initial condition whenever the fission region could be reached. For models with a quenching of the shell we found no such convergence. In particular, the EFTSI-Q model [168], which has almost no gap at the drip line, showed poor reproduction of the abundances compared to the FRDM [30] and Duflo-Zuker [166] mass models.

7.1 Outlook - Nuclear Physics

The theoretical nuclear physics that we have used in this thesis is continuously subject to revision. Mainly from new experimental data on nuclear properties that allow one to constrain parameters, but also from new insight

into pure nuclear theory. Throughout the preceding chapters we have already commented on the needed quantities our model requires and we will only briefly reiterate those that are most important.

The consistency of mass models, barriers etc. that was discussed in section (6.5) is a major concern in nucleosynthesis modeling. We would like to have one single nuclear framework within which all relevant numbers can be calculated. Unfortunately this does not exist at the moment. Therefore one has to be careful with combinations of different data compilations to ensure maximum compatibility. Alternatively, one can perform parameter studies with all the different models to check for obvious inconsistencies. The treatment of fission in the r -process is particularly complicated in this respect as the nuclear data need to extend to very high mass numbers. Studies on the influence of other mass models and barrier compilations are therefore being carried out at the moment.

We have emphasized the importance of β -decay around the magic numbers. To improve and compare our results for this process we need to consider other models for calculating the strength. This work is already in progress within a QRPA model [174, 175]. The QRPA results give shorter lifetimes around the $N = 184$ shell which is favorable for the r -process as discussed in section (6.4.2). To check the consistency of the simple RPA model used for the neutrino capture reactions, we have also calculated these processes within the QRPA. For the test cases considered thus far we see only small deviations between the two approaches. Additional work on β -decay could also help improve the crude approximation used in section (6.2.1) by providing the strength distributions. However, due to the rather small influence of β -induced fission in our simulations we do not expect significant changes in the results from such improvements.

In order to describe spontaneous and neutron-induced fission in a more consistent way we also need some improvement in the ABLA code. In particular, low-energy barrier penetration must be taken fully into account. The neutron capture strength and the lifetime against spontaneous fission could then be taken from a calculation based on the same masses used in ABLA. The combined results would then give a more consistent picture of these fission channels.

Another very important feature that one would like to incorporate into the ABLA method is the quenching of shell closures in the fragment calculations. The softening of shell gaps was only taken into account in the mass models and the fragments therefore still follow the standard gaps. Including the quenching will most likely also change the fragments and thus the r -process abundances.

A reaction that we have only briefly touched upon is neutrino-induced particle spallation in light nuclei. In the earliest epoch of the Supernova explosion there could be considerable effects from inelastic neutrino and antineutrino scattering on light and medium mass nuclei. The subsequent

deexcitation can have high probability for particle emissions and could therefore influence the nuclear distribution of the material. To consistently include this effect one would also need to calculate the neutral-current reactions. These processes can be induced by the other neutrino flavors which can have higher average energies. This could then compensate the smaller coupling compared to charged currents (which are roughly a factor of 6 larger). It would be interesting to include these in nucleosynthesis studies like those discussed in chapter (4) for the νp -process.

7.2 Outlook - Nuclear Astrophysics

The νp -process for production of $A < 100$ proton-rich elements discussed in chapter (4) is believed to be generic. However, to test this belief more work is needed. First of all it would be nice to see a full nucleosynthesis calculation including the entire iron group as in [138] with all neutrino reactions included, and with the different explosion models described in chapter (4). Such calculations are currently in progress.

It would be very interesting to investigate whether the νp -process and the r -process could operate in the same neutrino-wind simulation. The synthesis of light proton-rich nuclei in the wind was discussed already in the work of Fuller and Meyer [47] and also Hoffman *et al.* [146]. However, no r -process was found. In the recent work of Wanajo [182] there are indications of both proton-rich nuclei and r -process matter being synthesized in the same wind (although a rather large neutron star mass of $2M_{\odot}$ seems to be required).

There are several indications that there are at least two r -process components needed to reproduce observations [183]. There seems to be different mechanism needed to produce the nuclei above $A \sim 120$ and those below this region. A recent study by Kratz *et al.* [184] indicates that this can be attributed to different values of the neutron density. They found that values in the range $10^{20} - 10^{23} \text{ cm}^{-3}$ produce the nuclei with $A = 80 - 100$, whereas the heavier nuclei needed larger densities to be made. An overall good agreement with the solar abundances could be achieved with an appropriate superposition of densities up to 10^{28} cm^{-3} [184]. The same kind of superposition studies was also done in Freiburghaus *et al.* [155] where abundances from different entropies were combined. The physical origin of such superpositions could be variations in initial conditions from convection, rotation or even magnetic fields at the astrophysical production site. It would be very interesting to try similar superpositions with fission included in the r -process network.

In order to really test which features of our astrophysical results are truly generic we would like to collaborate with other groups in order to implement the nuclear data into different simulation models. Hopefully this will give similar results of course. Work in this direction is already in progress.

The potential effects of our results on galactic chemical evolution studies is yet another very interesting direction to explore. The recent findings of Travaglio *et al.* [185] suggests a light element primary process that operates very early in the Galaxy and is independent of the r -process. The νp -process could very well be a good candidate for this mechanism. The assumption that all core-collapse events will have a νp -process could be tested by calculating the yields for different progenitor star masses and implementing these in chemical evolution models.

The subject of stellar nucleosynthesis has an intrinsic statistical nature. Many stars of vastly different masses and from various epochs of the Universe contribute to the patterns we observe. The future directions of research mentioned above are of course dependent on the continued expansion and refinement of the observational data. A larger number of observed stars would also allow us to infer something about the frequency of stellar events. Improvements in resolution and in the number of isotopes that can be detected would also be a great help to modelers, particularly in the popular field of cosmochronometry. We need more high quality abundance measurements on interesting stellar objects to work out the details of the grand picture of nucleosynthesis in our Universe.

Appendix A

Formalism and Conventions

A.1 Units and Definitions

Natural units where $c = \hbar = 1$ are used. In some equations where Boltzmann's constant enters we will also set $k_B = 1$. The four-vectors used are given by $A^\mu = (A^0, \vec{A})$. The metric is diagonal with positive time-component. It is thus equal to its own inverse and has the explicit form

$$g_{\mu\nu} = g^{\mu\nu} = \text{Diag}(1, -1, -1, -1). \quad (\text{A.1})$$

The inner-product of two four-vectors is thus: $A^\mu B_\mu = A^0 B^0 - \vec{A} \cdot \vec{B} = A^0 B^0 - \sum_{i=1}^3 A^i B^i$. One also has $A_0 = A^0$ and $A^i = -A_i$.

We use the Dirac matrices

$$\beta = \begin{pmatrix} 1 & 0 \\ 0 & -1 \end{pmatrix} \quad \vec{\alpha} = \begin{pmatrix} 0 & \vec{\sigma} \\ \vec{\sigma} & 0 \end{pmatrix} \quad (\text{A.2})$$

and the gamma matrices in the so-called Dirac representation

$$\gamma^0 = \beta = \begin{pmatrix} 1 & 0 \\ 0 & -1 \end{pmatrix} \quad \vec{\gamma} = \beta \vec{\alpha} = \begin{pmatrix} 0 & \vec{\sigma} \\ -\vec{\sigma} & 0 \end{pmatrix} \quad (\text{A.3})$$

$$\gamma^5 = \gamma_5 = i\gamma^0\gamma^1\gamma^2\gamma^3 = \begin{pmatrix} 0 & 1 \\ 1 & 0 \end{pmatrix}. \quad (\text{A.4})$$

For the 4x4 spin matrix we leave out the factor of $\frac{1}{2}$

$$\vec{\Sigma} = \begin{pmatrix} \vec{\sigma} & 0 \\ 0 & \vec{\sigma} \end{pmatrix} \quad (\text{A.5})$$

so that helicity $\vec{\Sigma} \cdot \hat{p}$ can have the values ± 1 . The metric is used to raise and lower gamma matrix indices, so that

$$\gamma_\mu = g_{\mu\nu} \gamma^\nu. \quad (\text{A.6})$$

This means that $\gamma^0 = \gamma_0$ and $\gamma^i = -\gamma_i, i = 1, 2, 3$.

We assume that the neutrino is a massless spin-half Dirac particle. In this setup it is well-known that the spinor can be chosen as an eigenfunction of both the helicity $\vec{\Sigma} \cdot \hat{\mathbf{p}}$ and chirality γ_5 [186]. Furthermore, for positive energy solutions (needed in the muon capture processes of chapter (3)) the eigenvalues of helicity and chirality are the same. For a neutrino moving along the positive z-axis, the two possible solution are

$$\psi = N \begin{pmatrix} \chi_+ \\ \chi_+ \end{pmatrix} \exp(i\vec{p} \cdot \vec{x}) \quad (\text{A.7})$$

for positive helicity and chirality and

$$\psi = N \begin{pmatrix} \chi_- \\ -\chi_- \end{pmatrix} \exp(i\vec{p} \cdot \vec{x}) \quad (\text{A.8})$$

for negative. Here χ_{\pm} are the usual Pauli two-spinors and N is a normalization constant which is given by $N^{-2} = (2\pi)^3 2\varepsilon$, where ε is the neutrino energy. We employ the normal Standard Model assumption and take the neutrino to be purely left-handed which is the same as negative helicity.

The isospin formalism used has basis elements for neutron (n) and proton (p) given by

$$|n\rangle = \begin{pmatrix} 1 \\ 0 \end{pmatrix}, \quad |p\rangle = \begin{pmatrix} 0 \\ 1 \end{pmatrix}. \quad (\text{A.9})$$

The $SU(2)$ isospin group that acts on these vectors have generators denoted by $\vec{\tau} = (\tau_1, \tau_2, \tau_3) = \frac{1}{2}\vec{\sigma}$. These are of course identical to the usual Pauli matrices as indicated and the introduction of a different notation is to avoid any confusion with normal angular momentum. We see that neutrons have isospin projection (τ_3 eigenvalue) 1/2 and protons have projection -1/2.

For a nucleus with A nucleons we define the total isospin in the obvious fashion

$$\hat{\mathbf{T}} = \sum_{i=1}^A \vec{\tau}_i. \quad (\text{A.10})$$

As for standard angular momentum coupling, the projections merely add and we have

$$\hat{\mathbf{T}}_3 = \frac{1}{2}(N - Z), \quad (\text{A.11})$$

where N is the number of neutrons and Z is the number of protons. This is the important relation needed for the derivation of sum rules in eq. (2.45).

A.2 Angular Momentum Coupling and Spherical Functions

The angular momentum conventions used are basically those of Edmonds [28]. However, the Clebsch-Gordan coefficients are written with total angu-

lar momentum first and then projection after the separator in the following fashion

$$\langle J_1 J_2 J | J_{1z} J_{2z} J_z \rangle, \quad (\text{A.12})$$

where we are coupling J_1 and J_2 to total angular momentum J . The projections are self-explanatory. The Wigner 3J symbols and the Racah W symbols are defined as in [28].

We use the triangle notation $\Delta(J_1 J_2 J)$, which is one if J_1 and J_2 can reach J when stepping from $J_1 + J_2$ down to $|J_1 - J_2|$ in unit steps and zero otherwise.

The standard square-root factors in angular coupling are defined as $[J] = \sqrt{2J+1}$. We have also used the notation $\chi_i = (l_i - j_i)(2j_i + 1)$, where i can be a particle or hole index, l_i is the orbital angular momentum of i , and j_i is the total angular momentum of i .

The vector spherical harmonics are defined by

$$\mathcal{Y}_{J,l,1}^M = \sum_{\mu\lambda} \langle l1J | \mu\lambda M \rangle Y_{l\mu} \vec{e}_\lambda, \quad (\text{A.13})$$

where $Y_{l\mu}$ are the usual spherical harmonic with angular momentum l and projection μ . These function satisfies a number of divergence and curl properties that may be found in [28, 18]. The most important relation needed in chapter (3) is the inversion relation

$$Y_{l\mu} \vec{e}_\lambda = \sum_{JM} \langle l1J | \mu\lambda M \rangle \mathcal{Y}_{J,l,1}^M, \quad (\text{A.14})$$

which is obtained by using the unitarity properties of the Clebsch-Gordan coefficients.

The multipole expansion used is given in Walecka appendix B [18]. Introduce $\vec{e}_z = \vec{\kappa}/|\vec{\kappa}|$ and take the two other basis vectors of 3-space so that $\{\vec{e}_x, \vec{e}_y, \vec{e}_z\}$ forms a right-handed orthonormal basis. Then introduce the spherical basis vectors

$$\vec{e}_0 = \vec{e}_z \quad , \quad \vec{e}_{\pm 1} = \mp \frac{1}{\sqrt{2}} (\vec{e}_x \pm i\vec{e}_y). \quad (\text{A.15})$$

These spherical components satisfies the identities

$$(\vec{e}_\lambda)^\dagger = (-1)^\lambda \vec{e}_{-\lambda} \quad , \quad (\vec{e}_\lambda)^\dagger \cdot \vec{e}_{\lambda'} = \delta_{\lambda,\lambda'}. \quad (\text{A.16})$$

Then the partial wave expansion of the plane wave is given by

$$\exp(i\vec{\kappa} \cdot \vec{x}) = \sum_{J=0}^{\infty} \sqrt{4\pi} [J] i^J j_J(\kappa x) Y_{J,0}(\Omega_x). \quad (\text{A.17})$$

Here the $j_J(\kappa x)$ is the spherical Bessel function of order J and $Y_{J,M}(\Omega_x)$ is the spherical harmonic of order J and projection M . We have introduced

APPENDIX A. FORMALISM AND CONVENTIONS

the notation $|\vec{\kappa}| = \kappa$, $|\vec{x}| = x$ and $[J] = \sqrt{2J+1}$. The product of the spherical basis components and the partial wave expansion is now given by the expressions

$$\vec{e}_\lambda \exp(i\vec{\kappa} \cdot \vec{x}) = -\frac{i}{\kappa} \sum_{J=0}^{\infty} \sqrt{4\pi}[J] i^J \nabla (j_J(\kappa x) Y_{J,0}(\Omega_x)) \quad (\text{A.18})$$

for $\lambda = 0$ and

$$\vec{e}_\lambda \exp(i\vec{\kappa} \cdot \vec{x}) = -\sum_{J=1}^{\infty} \sqrt{2\pi}[J] i^J \left[\lambda j_J(\kappa x) \mathcal{Y}_{J,J,1}^\lambda + \frac{1}{\kappa} \nabla \wedge (j_J(\kappa x) \mathcal{Y}_{J,J,1}^\lambda) \right] \quad (\text{A.19})$$

for $\lambda = \pm 1$. Here $\mathcal{Y}_{J,L,1}^M$ is the vector spherical harmonic. This represents the coupling of spherical harmonic $Y_{L,m}$ and the spherical basis vectors, which have intrinsic angular momentum $(1, \lambda)$, to total angular momentum (J, M) . Now we will need also the conjugate relations to get the plane wave of the opposite sign. For the plane wave alone we have

$$\exp(-i\kappa \cdot \vec{x}) = \sum_{J=0}^{\infty} \sqrt{4\pi}[J] (-i)^J j_J(\kappa x) Y_{J,0}(\Omega_x). \quad (\text{A.20})$$

This follows easily from the fact that the Bessel is real and spherical harmonics $(J, 0)$ are proportional to the Legendre polynomial of order J , which is also real. For the product of plane wave and spherical basis components we get

$$\vec{e}_\lambda \exp(-i\vec{\kappa} \cdot \vec{x}) = \frac{i}{\kappa} \sum_{J=0}^{\infty} \sqrt{4\pi}[J] (-i)^J \nabla (j_J(\kappa x) Y_{J,0}(\Omega_x)) \quad (\text{A.21})$$

for $\lambda = 0$ and

$$\vec{e}_{-\lambda} \exp(-i\vec{\kappa} \cdot \vec{x}) = \sum_{J=1}^{\infty} \sqrt{2\pi}[J] (-i)^J \left[\lambda j_J(\kappa x) \mathcal{Y}_{J,J,1}^{-\lambda} + \frac{1}{\kappa} \nabla \wedge (j_J(\kappa x) \mathcal{Y}_{J,J,1}^{-\lambda}) \right] \quad (\text{A.22})$$

for $\lambda = \pm 1$. Here we have used $(\vec{e}_\lambda)^\dagger = (-1)^\lambda \vec{e}_{-\lambda}$ and the following identity for the vector spherical harmonics

$$(\mathcal{Y}_{J,l,1}^M)^\dagger = (-1)^{l+1-J+M} \mathcal{Y}_{J,l,1}^{-M} \quad (\text{A.23})$$

and the expressions

$$\nabla_\rho (j_J(\rho) Y_{J,M}(\Omega_\rho)) = \sqrt{\frac{J+1}{2J+1}} j_{J+1}(\rho) \vec{\mathcal{Y}}_{J,J+1,1}^M + \sqrt{\frac{J}{2J+1}} j_{J-1}(\rho) \vec{\mathcal{Y}}_{J,J-1,1}^M \quad (\text{A.24})$$

$$\begin{aligned} \frac{1}{\kappa} \nabla \wedge (j_J(\kappa x) \vec{\mathcal{Y}}_{J,J,1}^M) &= -i \sqrt{\frac{J}{2J+1}} j_{J+1}(\kappa x) \vec{\mathcal{Y}}_{J,J+1,1}^M \\ &+ i \sqrt{\frac{J+1}{2J+1}} j_{J-1}(\kappa x) \vec{\mathcal{Y}}_{J,J-1,1}^M. \end{aligned} \quad (\text{A.25})$$

A.3 Spherical Dirac Equation

We assume that the potential origination from the nucleus is spherically symmetric and minimally coupled. Separation of the Dirac equation in spherical coordinates may therefore be performed (see example 9.3 of [186]). This yields the following wave function

$$\phi_{jm} = \begin{pmatrix} ig(r)\Omega_{jlm}(\hat{r}) \\ -f(r)\Omega_{jl'm}(\hat{r}) \end{pmatrix}, \quad (\text{A.26})$$

where $|l - l'| = 1$ since the two components have opposite parity [186]. The radial functions fulfill the following equations

$$\frac{d}{dr} \begin{pmatrix} g \\ f \end{pmatrix} = \begin{pmatrix} -\frac{1+\kappa}{r} & E + m - V(r) \\ -E + m + V(r) & -\frac{1-\kappa}{r} \end{pmatrix} \begin{pmatrix} g \\ f \end{pmatrix}, \quad (\text{A.27})$$

where

$$\kappa = \begin{cases} -(l+1) & , j = l + \frac{1}{2} \\ l & , j = l - \frac{1}{2} \end{cases} \quad (\text{A.28})$$

and

$$\Omega_{j,l,m}(\hat{r}) = \sum_{m_l, m_s} (l, \frac{1}{2}, j | m_l, m_s, m) Y_{l, m_l}(\hat{r}) \chi_{m_s} \quad (\text{A.29})$$

is the coupling of Pauli two-spinor, χ_{m_s} , and spherical harmonic, Y_{l, m_l} , to total angular momentum j . From the properties of the Clebsch-Gordan coefficients it follows that $\Omega_{j,l,m}^\dagger \Omega_{j',l',m'} = \delta_{j,j'} \delta_{l,l'} \delta_{m,m'}$ so that the requirement of normalization becomes

$$\int_0^\infty r^2 dr (|g|^2 + |f|^2) = 1. \quad (\text{A.30})$$

For the muon in the 1s atomic orbital the quantum numbers are

$$s = \frac{1}{2}, l = 0 \Rightarrow j = \frac{1}{2}, l' = 2j - 1 = 1, \kappa = -(0 + 1) = -1. \quad (\text{A.31})$$

The explicit forms of the angular parts are thus

$$\Omega_{1/2,0,m} = Y_{0,0}(\hat{r}) \chi_{\text{sign}(m)} \quad (\text{A.32})$$

$$\Omega_{1/2,1,m} = -\sqrt{\frac{3/2-m}{3}} Y_{1,m-1/2}(\hat{r}) \chi_+ + \sqrt{\frac{3/2+m}{3}} Y_{1,m+1/2}(\hat{r}) \chi_-. \quad (\text{A.33})$$

Appendix B

Neutrino Capture Rate Formula

In this appendix we present the approximate relation between the neutrino cross section and the reaction rate at a given radius. The capture reaction rate is given by the product of the cross section of the reaction and the number of neutrinos per unit time per unit area. In the Supernova setting we know the luminosity in neutrinos, L_ν . This gives us the energy released in neutrinos per second. Since we are assuming a spherical flux, we simply have to divide this by the area of a sphere at the given radius to get the neutrino energy per second per area. In order to get the number of neutrinos (the flux) we divide this by the average energy of the neutrinos. Thus

$$\lambda_\nu = \langle \sigma_\nu \rangle \frac{L_\nu}{4\pi r^2 \langle E_\nu \rangle}, \quad (\text{B.1})$$

where r is the radius above the center of the stellar object. The cross section used here is folded with the same neutrino distribution that gives us the average energy $\langle E_\nu \rangle$.

At this point we would like to have a formula that is simple to apply to the Supernova problem. We therefore introduce the characteristic scales for the luminosity ($10^{51} \text{ erg s}^{-1}$), radius (100 km), and neutrino energy (MeV). For the cross section we use the conventional unit of 10^{-41} cm^2 . Upon inserting these quantities we get

$$\lambda_\nu = K \left(\frac{L_\nu}{10^{51} \text{ erg s}^{-1}} \right) \left(\frac{\text{MeV}}{\langle E_\nu \rangle} \right) \left(\frac{100 \text{ km}}{r} \right)^2 \left(\frac{\langle \sigma_\nu \rangle}{10^{-41} \text{ cm}^2} \right), \quad (\text{B.2})$$

where K is a constant that we can easily calculate to get

$$K = \frac{10^{51} \text{ erg s}^{-1} 10^{-41} \text{ cm}^2}{\text{MeV} 100 \text{ km}} = 4.967. \quad (\text{B.3})$$

This is the formula we will be using when turning our calculated neutrino cross sections into reaction rates on the Supernova material. Typically we

APPENDIX B. NEUTRINO CAPTURE RATE FORMULA

will compare to the beta decay half lives and for this we simply take the inverse of this decay rate estimate and multiply by $\ln(2)$.

Appendix C

Nucleosynthesis and Entropy

The entropy per baryon is a commonly used quantity when discussing nucleosynthesis. However, the use can sometimes seem counterintuitive when compared to the general concept of entropy from thermodynamics. This appendix is a brief introduction to the essentials of its use in nucleosynthesis with particular emphasis on the environments treated in the text. The treatment is based on the excellent article by Meyer [187].

The central concept is that of Nuclear Statistical Equilibrium (NSE). Based on the assumption that all nuclear processes take place in equilibrium one can derive an equation for the number of particles with charge Z and mass A , $Y(Z,A)$, by using the principle of maximum entropy. It has the form

$$Y(Z, A) = g(Z, A) \left[\zeta(3)^{A-1} \pi^{(1-A)/2} 2^{(3A-5)/2} \right] A^{3/2} \left(\frac{k_B T}{m_N c^2} \right)^{3(A-1)/2} \times \phi^{(1-A)} Y_p^Z Y_n^{(A-Z)} \exp [B(Z, A)/k_B T], \quad (\text{C.1})$$

where $g(Z, A)$ is the nuclear partition function, $\zeta(3)$ is the zeta function of argument 3, m_N is the nucleon mass, $B(Z, A)$ is the nuclear binding energy, T the temperature, and ϕ is the photon-to-baryon ratio. The latter is given by

$$\phi = Y_\gamma = \frac{2}{\pi^2 (\hbar c)^3} \frac{\zeta(3) (k_B T)^3}{\rho N_A}, \quad (\text{C.2})$$

where ρ is the baryon mass density of the material and N_A is Avagadro's number. The formula is also known as the Law of Mass Action or the Saha equation when discussion chemical processes. The photons enter on account of the assumption that that one photon is released (absorbed) whenever two nucleons combine (or separate), yielding $A - 1$ photons for a system of A nucleons.

In NSE we see that the abundances of nuclei is non-zero. When thinking about the entropy as a measure for the number of ways to share the total energy, this would seem puzzling. Locking nucleons inside nuclei means

that we have them confined and thus have more information about them. However, the combination of nucleons releases photons (since the binding energy is positive). The complex nuclei can also be excited and this can be done in many ways. More photons and excited nuclei will therefore yield more ways to distribute the energy and thus increase the entropy. This also explains why one can only build large abundances of nuclei that release binding energy. Nuclear reactions will operate as long as binding energy can be released to compensate the decrease in free nucleons. To reach the maximum entropy the composition will thus be driven toward the nucleus with the maximum binding energy, which is located in the iron group region (the actual nucleus with largest binding depends on the initial proton-to-neutron ratio).

The actual distribution in NSE depends strongly on S . The total number of states in the system is a product of the baryon states and the photon states (and other relevant components), such that an increase in S gives an increase in each. This means that there will be more states per baryon for larger S . Since a free baryon typically has more states available than one locked inside a nucleus, this entails more free nucleons and lighter nuclei for larger S (at fixed T). This can also be seen from eq.(C.1). The abundance of some heavy nucleus with (Z, A) is proportional to $\phi^{(1-A)}$. Since photon states are proportional to photon number an increase in S will give an increase in ϕ and thus a decrease in the abundance of the heavy nucleus (Z, A) . This, in turn, means more free nucleons and lighter nuclei.

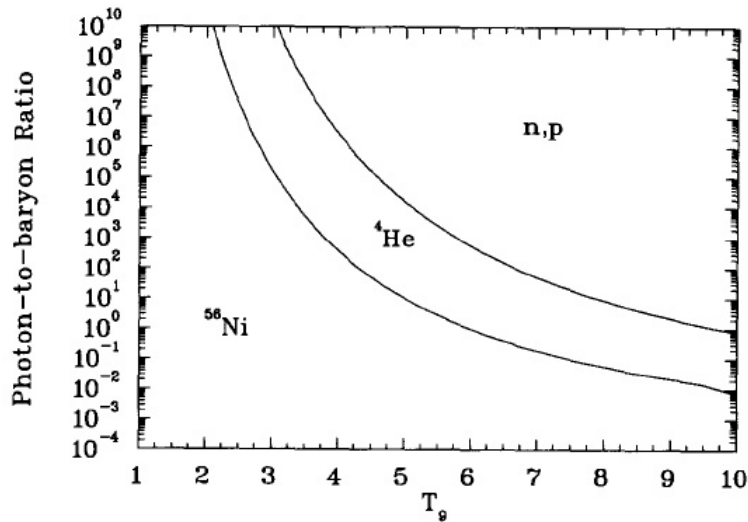


Figure C.1: The dominant species in NSE of a gas containing free nucleons, ${}^4\text{He}$, and ${}^{56}\text{Ni}$ as a function of temperature and photon-to-baryon ratio ϕ for symmetric matter ($N = Z$). Adapted from [187].

The discussion above was at fixed temperature. Varying the temperature moves the abundance peak for fixed ϕ . We illustrate these changes in figure (C.1) where the regions dominated by nucleons, ${}^4\text{He}$, and ${}^{56}\text{Ni}$ are shown as a function of ϕ and T (for symmetric matter $N = Z$). At high T and ϕ we see the dominance of free nucleons. If we fix T and decrease ϕ we see the dominant abundance change to heavier nuclei. The same happens for fixed ϕ with decreasing temperature. The latter is simply due to the $\exp[B(Z, A)/k_B T]$ term in eq. (C.1) which shifts the material to more bound nuclei during expansion and cooling (under adiabatic conditions).

Since the reaction rate of the nuclear processes depend on density and temperature they will decrease as the material expands and cools. When this rate becomes less than the expansion rate of the material, nuclear reactions will shut off in the so-called freeze-out. After this point we have the resulting abundances of NSE nucleosynthesis. Note that the freeze-out is the point where NSE can no longer be maintained (nuclear reactions can still occur out-of-equilibrium, as in the r -process during decay back to stability). The initial entropy of the NSE will determine the amount of free nucleons and nuclei at freeze-out. Therefore it makes sense to characterize different nucleosynthesis processes by the entropy.

It is interesting to consider the influence of the initial proton-to-neutron ratio Y_e on the products of nucleosynthesis. If we have neutron-rich conditions, $Y_e < 0.5$, synthesis of neutron-rich nuclei can take place at fairly low entropy. For extreme conditions with $Y_e < 0.2$ one can even have many neutrons available at freeze-out (since any nucleus can only capture a finite number of neutrons before it hits the drip line). This can give rise to a classical r -process.

For entropies of $S/k_B \sim 10 - 1000$ one can have a so-called α -rich freeze-out. This is a situation where the equilibrium shifts to higher mass nuclei before charged particle reactions shut off. Some ${}^4\text{He}$ will reassemble but not many due to the high entropy. The heavier nuclei formed will then capture these ${}^4\text{He}$ nuclei and produce a distribution of heavy nuclei with α structure. For large entropies there is potential for r -process on this distribution since neutrons are still abundant and will mainly capture on heavy nuclei. This can occur even if the material is only moderately neutron-rich $Y_e \sim 0.35 - 0.45$ with larger entropy allowing larger Y_e .

In proton-rich environments $Y_e > 0.5$ the free nucleons will be predominantly protons. The Coulomb repulsion will then hinder the nucleosynthesis scenarios described above for neutrons since only few protons can be captured on the heavy nuclei. This is why the antineutrino plays a crucial role in the νp -process discussed in chapter (4). It converts protons to neutrons and allows the nucleosynthesis process to continue upward in mass.

Bibliography

- [1] H.A. Bethe, G.E. Brown, J. Applegate and J.M. Lattimer, Nucl. Phys. **A324** (1979) 487.
- [2] A. Heger, S.E. Woosley, G. Martínez-Pinedo and K. Langanke, Astrophys. J. **560** (2001) 307.
- [3] H.-Th. Janka, A. Marek, and F.-S. Kitaura, arXiv:0706.3056v1.
- [4] A. Burrows, E. Livne, L. Dessart, C.D. Ott, and J. Murphy, Astrophys.J. **655** (2007) 416.
- [5] H.E. Suess and H.C. Urey, Rev. Mod. Phys. **28** (1956) 53.
- [6] E.M. Burbidge, G.R. Burbidge, W.A. Fowler, and F. Hoyle, Rev. Mod. Phys. **29** (1957) 547.
- [7] A. G. W. Cameron, P.A.S.P **96** (1957) 201.
- [8] F. Käppeler, H. Beer, and K. Wisshak, Rep. Prog. Phys. **52** (1989) 845.
- [9] Y.-Z. Qian, Prog. Part. Nucl. Phys. **50** (2003) 153.
- [10] J.J. Cowan, C. Sneden, J.E. Lawler, and E.A. Den Hartog, arXiv:astro-ph/0610412v1.
- [11] C. Fröhlich, G. Martínez-Pinedo, M. Liebendörfer, F.-K. Thielemann, E. Bravo, W.R. Hix, K. Langanke and N.T. Zinner, Phys. Rev. Lett. **96** (2006) 142502.
- [12] J. Pruet, R.D. Hoffman, S.E. Woosley, H.-T. Janka and R. Buras, Astrophys. J. **644** (2006) 1028.
- [13] J. Pruet, R. Surman and G.C. McLaughlin, Astrophys. J. **602** (2004) L101.
- [14] F. Käppeler, Prog. Part. Nucl. Phys. **43** (1999) 419.
- [15] K. Langanke and G. Martínez-Pinedo, Rev. Mod. Phys. **75** (2003) 819.

BIBLIOGRAPHY

- [16] E. Fermi, *Z. Physik* **88** (1934) 161.
- [17] W. Greiner and B. Müller *Gauge Theory of Weak Interactions*, Springer-Verlag Berlin Heidelberg 1996.
- [18] J. D. Walecka *Semileptonic Weak Interactions in Nuclei* in *Muon Physics II* edited by Hughes and Wu. Academic Press 1975.
- [19] T. D. Lee and C. N. Yang, *Phys. Rev.* **104** (1956) 254.
- [20] C. S. Wu, E. Ambler, R. Hayward, D. Hoppes, and R. Hudson, *Phys. Rev.* **105** (1957) 1413.
- [21] R. P. Feynmann and M. Gell-Mann, *Phys. Rev.* **109** (1958) 193.
- [22] R. P. Feynmann and M. Gell-Mann, *Phys. Rev.* **111** (1958) 362.
- [23] S. Weinberg, *Phys. Rev.* **112** (1958) 1375.
- [24] M. L. Goldberger and S. B. Treiman, *Phys. Rev.* **111** (1958) 354.
- [25] B. Povh, K. Rith, C. Scholz and F. Zetsche *Particles and Nuclei*, Springer-Verlag Berlin Heidelberg 1999.
- [26] N. Cabibbo, *Phys. Rev. Lett.* **10** (1963) 531.
- [27] J. D. Walecka *Theoretical Nuclear and Subnuclear Physics*, 2nd edition Imperial College Press, London, 2004.
- [28] A. R. Edmonds *Angular Momentum in Quantum Mechanics*, 2nd edition Princeton University Press 1960.
- [29] K. Langanke and E. Kolbe, *At. Data Nucl. Data Tables* **79** (2001) 293.
- [30] P. Möller, J. R. Nix and K.-L. Kratz, *At. Data Nucl. Data Tables* **66** (1997) 131.
- [31] I. N. Borzov, *Phys. Rev.* **C71** (2005) 065801.
- [32] P. Ring and P. Schuck *The Nuclear Many-Body Problem* 2nd printing, Springer-Verlag Berlin Heidelberg, 2000.
- [33] A. Bohr and B. Mottelson *Nuclear Structure*, Vol. I W.A. Benjamin, Inc. New York, 1969.
- [34] N. T. Zinner, K. Langanke, K. Riisager and E. Kolbe, *Eur. Phys. J.* **A17**, (2003) 625.
- [35] E. Kolbe, K. Langanke and P. Vogel, *Phys. Rev.* **C62** (2000) 055502.

BIBLIOGRAPHY

- [36] D. J. Rowe *Nuclear Collective Motion: Models and Theory* Butler & Tanne Ltd, Frome and London, 1970.
- [37] D. Bohm and D. Pines, Phys. Rev. **92** (1957) 609 and 626.
- [38] A. Fetter and J. D. Walecka *Quantum Theory of Many-Particle Systems* McGraw-Hill, New York, 1971.
- [39] L. D. Landau, Sov. Phys. JETP **8** (1959) 70.
- [40] A. B. Migdal *Theory of Finite Fermi Systems and Applications to Atomic Nuclei* Wiley Interscience, New York, 1967.
- [41] G. A. Rinker and J. Speth, Nucl. Phys. **A306** (1978) 360.
- [42] M. R. Plumley *et al.*, Phys. Rev. **C56** (1997) 263.
- [43] F. Grümmer and J. Speth, J.Phys. **G32** (2006) R193.
- [44] E. Kolbe, K. Langanke and P. Vogel, Nucl. Phys. **A652** (1999) 91.
- [45] M. Goldhaber and E. Teller, Phys. Rev. **74** (1948) 1046.
- [46] K. Ikeda, S. Fujii and J. I. Fujita, Phys. Lett. **3** (1963) 271.
- [47] G. M. Fuller and B. S. Meyer, Astrophys. J. **453** (1995) 792.
- [48] N. T. Zinner, Bachelor Thesis Department of Physics and Astronomy, University of Aarhus 2003. Unpublished.
Available at <http://whome.phys.au.dk/~zinner/tekst.ps>.
- [49] G. F. Bertsch and H. Esbensen, Rep. Prog. Phys. **50** (1987) 607.
- [50] H. Sakia, Nucl, Phys. **A690** (2000) 66.
- [51] K. Yako *et al.*, Phys. Lett. **B615** (2005) 193.
- [52] B. H. Wildenthal, Prog. Part. Nucl. Phys. **11** (1984) 5.
- [53] A. Richter, J. Phys.: Conf. Ser. **20** (2005) 13.
- [54] G. F. Bertsch and R. A. Broglia *Oscillations in Finite Quantum Systems* Cambridge University Press, 1994.
- [55] E. Caurier, K. Langanke, G. Martínez-Pinedo, and F. Nowacki, Nucl. Phys. **A653** (1999) 439.
- [56] J.Toivanen, E.Kolbe, K.Langanke, G.Martínez-Pinedo and P.Vogel, Nucl. Phys. **A694** (2001) 395.
- [57] P. E. Hodgson, E. Gadioli, and E. Gadioli Erba *Introductory Nuclear Physics* Clarendon Press, Oxford 1997.

BIBLIOGRAPHY

- [58] V. F. Weisskopf, Phys. Rev. **52** (1937) 295.
- [59] L. G. Moretto, Proc. of the 3rd IAEA symposium on the physics and chemistry of fission, Rochester, New York, 13-17 August 1973, p. 329.
- [60] N. Bohr and J. A. Wheeler, Phys. Rev. **56** (1939) 426.
- [61] A. Gavron *et al.*, Phys. Rev. **C13** (1976) 2374.
- [62] B. Jurado, C. Schmitt, K.-H. Schmidt, J. Benlliure, and A. R. Jung-
hans, Nucl. Phys. **A747** (2005) 14.
- [63] P. Möller and J. R. Nix, At. Data Nucl. Data Tables **39** (1988) 213.
- [64] W. D. Myers and W. J. Swiatecki, Nucl. Phys. **A601** (1996) 141.
- [65] P. Möller, J. R. Nix, W. D. Myers, and W. J. Swiatecki, At. Data
Nucl. Data Tables **59** (1995) 185.
- [66] A. V. Ignatyuk, G. N. Smirenkin, and A. S. Tishin, Sov. J. Nucl. Phys.
21 (1975) 255.
- [67] A. V. Ignatyuk *et al.*, Sov. J. Nucl. Phys. **21** (1975) 519.
- [68] A. V. Ignatyuk *et al.*, Nucl. Phys. **A593** (1995) 519.
- [69] A. R. Junghans *et al.*, Nucl. Phys. **A629** (1998) 635.
- [70] A. V. Karpov *et al.*, J. Phys. **G29** London (2003) 2365.
- [71] A. J. Sierk, Phys. Rev. **C33** (1986) 2039.
- [72] A. Mamdouh, J. M. Pearson, M. Rayet, and F. Tondeur, Nucl. Phys.
A679 (2001) 337.
- [73] A. Kelić and K.-H. Schmidt, Phys. Lett. **B634** (2006) 362.
- [74] W. M. Howard and P. Möller, At. Data Nucl. Data Tables **25** (1980)
219.
- [75] K.-H. Schmidt *et al.*, Nucl. Phys. **A665** (2000) 221.
- [76] M. Bernas *et al.*, Nucl. Phys. **A725** (2003) 213.
- [77] J. Benlliure, A. Grewe, M. de Jong, K.-H. Schmidt, and S. Zhdanov,
Nucl. Phys. **A628** (1998) 458.
- [78] J.-J. Gaimard and K.-H. Schmidt, Nucl. Phys. **A531** (1991) 709.
- [79] F.-K. Thielemann, M. Arnould, and J. Truran, in Advances in Nuclear
Astrophysics, ed. E. Vangioni-Flam (Editions Frontiere, Gif sur Yvette
1987), p. 525.

BIBLIOGRAPHY

- [80] C. Özen, K. Langanke, G. Martinez-Pinéo, and D.J. Dean, arXiv:nucl-th/0703084v1.
- [81] H.-T. Janka and W. Hillebrandt, *Astron. Astrophys. Suppl. Ser.* **78** (1989) 375.
- [82] H.-T. Janka and W. Hillebrandt, *Astron. Astrophys.* **224** (1989) 49.
- [83] M. Liebendörfer, M. Rampp, H.-Th. Janka, and A. Mezzacappa, *Astrophys. J.* **620** (2005) 840.
- [84] A. Burrows, arXiv:astro-ph/0405427v1.
- [85] M. Th. Keil, G.G. Raffelt, and H.-Th. Janka, *Astrophys. J.* **590** (2003) 971.
- [86] S. Wanajo, *Astrophys. J.* **650** (2006) L79.
- [87] G. M. Fuller, R. Mayle, B. S. Meyer, and J. R. Wilson, *Astrophys. J.* **389** (1992) 517.
- [88] G. M. Fuller, R. Mayle, J. R. Wilson, and D. N. Schramm, *Astrophys. J.* **322** (1987) 795.
- [89] T. Yoshida *et al.*, *Phys. Rev. Lett.* **96** (2006) 091101.
- [90] G. C. McLaughlin, J. M. Fetter, A. B. Balantekin, and G. M. Fuller, *Phys. Rev.* **C59** (1999) 2873.
- [91] J. Fetter, G. C. McLaughlin, A. B. Balantekin, and G. M. Fuller, *Astropart.Phys.* **18** (2003) 433.
- [92] The MiniBooNE Collaboration, arXiv:0704.1500v1.
- [93] D. F. Measday, *Phys. Rep.* **354** (2001) 243.
- [94] N. C. Mukhopadhyay, *Phys. Rep.* **30C** (1977) 1.
- [95] N. Auerbach and A. Klein, *Nucl. Phys.* **A422** (1984) 480.
- [96] N. Auerbach, N. Van Giai and O. K. Vorov, *Phys. Rev. C* **56** (1997) R2368.
- [97] H. W. Fearing and M. S. Welsh, *Phys. Rev. C* **46** (1992) 2077.
- [98] H. C. Chiang, E. Oset and P. Fernández de Córdoba, *Nucl. Phys.* **A510** (1990) 591.
- [99] J. Nieves, J. E. Amaro, and M. Valverde, *Phys. Rev. C* **70** (2000) 05503.

BIBLIOGRAPHY

- [100] J. E. Amaro, C. Maieron, J. Nieves, and M. Valverde, *Eur.Phys. J* **A24** (2005) 343.
- [101] E. Kolbe, K. Langanke, and P. Vogel, *Phys. Rev. C* **50** (1994) 2576.
- [102] T. Suzuki, D. F. Measday, and J. P. Roalsvig, *Phys. Rev.* **C35** (1987) 2212.
- [103] K.W. Ford and J.G. Wills, *Nucl. Phys.* **35** (1962) 295.
- [104] E.Kolbe, K.Langanke, and K.Riisager, *Eur. Phys. J. A* **11** (2001) 39.
- [105] M. Morita and A. Fujii, *Phys. Rev.* **118** (1960) 606.
- [106] W. Greiner, *Relativistic Wave Equations*,
3rd English edition (Springer-Verlag, Berlin/Heidelberg,2000).
- [107] M. E. Rose, *Elementary Theory of Angular Momentum*, John Wiley
& Sons, Inc., New York 1957.
- [108] B. H. Wildenthal, *Prog. Part. Nucl. Phys.* **11** (1984) 5.
- [109] E. Caurier, A. Poves, and A. P. Zuker, *Phys. Rev. Lett.* **74** (1995) 1517.
- [110] C. D. Goodman and S. B. Bloom, in *Spin excitation in nuclei*, F. Petrovich *et al.* eds., (Plenum, NY 1983).
G. F. Bertsch and H. Esbensen, *Rep. Prog. Phys.* **50**, 607 (1987).
O. Häusser *et al.*, *Phys. Rev. C* **43** (1991) 230.
K. Langanke, D.J. Dean, P.B. Radha, Y. Alhassid and S.E. Koonin,
Phys. Rev. **C52** (1995) 718.
G. Martinez-Pinedo, A. Poves, E. Caurier and A.P. Zuker, *Phys. Rev.*
C53 (1996) R2602.
- [111] H. Hänscheid *et. al.*, *Z. Phys. A - Atomic Nuclei* **335** (1990) 1.
- [112] H. O. U. Fynbo *et. al.*, *Nucl. Phys.* **A724** (2003) 493.
- [113] P. David *et. al.* *Z. Phys. A - Atomic Nuclei* **330** (1988) 397.
- [114] H. Primakoff, *Rev. Mod. Phys.* **31** (1959) 802.
- [115] M. Arnould and S. Goriely, *Phys. Rep.* **384** (2003) 1.
- [116] V. Costa *et al.*, *Astron. Astrophys.* **358** (2000) L67.
- [117] T. Hayakawa *et al.*, *Phys. Rev. Lett.* **93** (2004) 161102.
- [118] C. Sneden and J.J. Cowan, *Science* **299** (2003) 70.
- [119] C. Travaglio *et al.*, *Astrophys. J.* **601** (2004) 864.

BIBLIOGRAPHY

- [120] J.J. Cowan *et al.*, *Astrophys. J.* **627** (2005) 238.
- [121] N. Dauphas *et al.*, *Nucl. Phys.* **A719** (2003) C287.
- [122] A. Frebel *et al.*, *Nature (London)* **434** (2005) 871.
- [123] R. Buras *et al.*, *Astron. Astrophys.* **447** (2006) 1049.
- [124] M. Liebendörfer *et al.*, *Phys. Rev. D* **63** (2001) 103004.
- [125] T.A. Thompson, E. Quataert, and A. Burrows, *Astrophys. J.* **620** (2005) 861.
- [126] G.V. Domogatskii and D.K. Nodyozhin, *Sov. Astr.* **22** (1978) 297.
- [127] S.E. Woosley and W.C. Haxton, *Nature* **334** (1988) 45.
- [128] S.E. Woosley, D.H. Hartmann, R.D. Hoffman, and W.C. Haxton, *Astrophys. J.* **356** (1990) 272.
- [129] C. Fröhlich *et al.*, *Astrophys. J.* **637** (2006) 415.
- [130] S.W. Bruenn, *Astrophys. J. Suppl.* **58** (1985) 771.
- [131] Y.-Z. Qian and S.E. Woosley, *Astrophys. J.* **471** (1996) 331.
- [132] K. Nomoto and M. Hashimoto, *Phys. Rep.* **163** (1988) 13.
- [133] J. Pruet, S.E. Woosley, R. Buras, H.-T. Janka, and R.D. Hoffman, *Astrophys. J.* **623** (2005) 325.
- [134] C. Fröhlich *et al.*, *Phys. Rev. Lett.* **96** (2006) 142502.
- [135] K. Lodders, *Astrophys. J.* **591** (2003) 1220.
- [136] G.C. Jordan and B.S. Meyer, *Astrophys. J.* **617** (2004) L131.
- [137] H. Schatz *et al.*, *Phys. Rev. Lett.* **86** (2001) 3471.
- [138] F.-K. Thielemann, K. Nomoto, and M. Hashimoto, *Astrophys. J.* **460** (1996) 408.
- [139] R.G. Gratton and C. Sneden, *Astron. Astrophys.* **241** (1991) 501.
- [140] R. Cayrel *et al.*, *Astron. Astrophys.* **416** (2004) 1117.
- [141] B.S. Meyer, *Phys. Rev. Lett.* **89** (2002) 231101.
- [142] R.D. Hoffman, S.E. Woosley, G.M. Fuller, and B.S. Meyer, *Astrophys. J.* **460** (1996) 478.
- [143] N. Iwamoto *et al.*, *Science* **309** (2005) 451.

BIBLIOGRAPHY

- [144] S.E. Woosley and R.D. Hoffman, *Astrophys. J.* **395** (1992) 202.
- [145] B.S. Meyer *et al.*, *Astrophys. J.* **399** (1992) 656.
- [146] R.D. Hoffman, S.E. Woosley, and Y.-Z. Qian, *Astrophys. J.* **482** (1997) 951.
- [147] A.B. Balantekin and G.M. Fuller, *J.Phys.* **G29** (2003) 2513.
- [148] W.C. Haxton, K. Langanke, Y.-Z. Qian, and P. Vogel, *Phys. Rev. Lett.* **78** (1997) 2694.
- [149] Y.-Z. Qian, W.C. Haxton, K. Langanke, and P. Vogel, *Phys. Rev. C* **55** (1997) 1532.
- [150] C. Sneden *et al.*, *Astrophys. J.* **533** (2000) L139.
- [151] C. Arlandini *et al.*, *Astrophys. J.* **525** (1999) 886.
- [152] P.A. Seeger, W.A. Fowler, and D.D. Clayton, *Astrophys. J. Suppl.* **11** (1965) 121.
- [153] T. Rauscher *et al.*, *Astrophys. J.* **429** (1994) 499.
- [154] A.G.W. Cameron, *Astrophys. J.* **562** (2001) 456.
- [155] C. Freiburghaus, S. Rosswog, and F.-K. Thielemann, *Astrophys. J.* **525** (1999) L121.
- [156] Y.-Z. Qian, *Astrophys. J.* **569** (2002) L103.
- [157] S.E. Woosley *et al.*, *Astrophys. J.* **433** (1994) 229.
- [158] E. Kolbe, K. Langanke, and G.M. Fuller, *Phys. Rev. Lett.* **92** (2004) 111101.
- [159] A. Kélic, N.T. Zinner, K. Langanke, and K.-H. Schmidt, *Phys. Lett.* **B616** (2005) 48.
- [160] J. J. Cowan, F.-K. Thielemann and J. W. Truran, *Phys. Rep.* **208** (1991) 267.
- [161] S. Bjørnholm and J.E. Lynn, *Rev. Mod. Phys.* **52** (1980) 725.
- [162] M. Dahlinger, D. Vermeulen and K.-H. Schmidt, *Nucl. Phys.* **A376** (1982) 94.
- [163] I.V. Panov, E. Kolbe, B. Pfeiffer, T. Rauscher, K.-L. Kratz and F.-K. Thielemann, *Nucl. Phys.* **A747** (2005) 633.

BIBLIOGRAPHY

- [164] A. Hektor, E. Kolbe, K. Langanke, and J. Toivanen, Phys. Rev. **C61** (2001) 055803.
- [165] I.V. Panov, C. Freiburghaus, and F.-K. Thielemann, Nucl. Phys. **A688** (2001) 587.
- [166] J. Duflo and A.P. Zuker, Phys. Rev. C **52** (1995) R23.
- [167] Y. Aboussir, J.M. Pearson, A.K. Dutta, and F. Tondueur, Nucl. Phys. **A549** (1992) 155 and At. Data Nucl. Data Tables **61** (1995) 127.
- [168] J.M. Pearson, R.C. Nayak, and S. Goriely, Phys. Lett. **B387** (1996) 455.
- [169] P. Möller, B. Pfeiffer, and K.-L. Kratz, Phys. Rev. C **60** (2003) 055802.
The data is available at the URL:
<http://t16web.lanl.org/Moller/publications/tpnff.dat>.
- [170] W.D. Myers and W.J. Swiatecki, Phys. Rev. C **60** (1999) 014606.
- [171] T. Kodama and K. Takahashi, Nucl. Phys. **A239** (1975) 489.
- [172] F.X. Timmes and D. Arnett, Astrophys. J. Suppl. **125** (1999) 277.
- [173] S. Goriely *et al.*, Nucl. Phys. **A758** (2005) 587.
- [174] I.N. Borzov *et al.*, EXON 2006 International Symposium on Exotic Nuclei, Khanty-Mansiysk, Russia, 17-22 July, 2006.
- [175] I.N. Borzov *et al.*, NIC-IX, International Symposium on Nuclear Astrophysics - Nuclei in the Cosmos - IX, CERN, Geneva, Switzerland, 25-30 June, 2006.
- [176] J.J. Cowan *et al.*, Astrophys. J. **521** (1999) 194.
- [177] B.S. Meyer, Astrophys. J. **449** (1995) L55.
- [178] J.J. Cowan and C. Sneden, Nature **440** (2006) 1151
- [179] V. Hill *et al.*, Astron. Astrophys. **387** (2002) 560.
- [180] J.J. Cowan *et al.*, Astrophys. J. **572** (2002) 861.
- [181] S. Goriely and B. Clerbaux, Astron. Astrophys. **346** (1999) 798.
- [182] S. Wanajo, Astrophys. J. **647** (2006) 1323.
- [183] G.J. Wasserburg and Y.-Z. Qian, Astrophys. J. **529** (2000) L21
- [184] K.-L. Kratz *et al.*, arXiv:astro-ph/0703091v1.

BIBLIOGRAPHY

- [185] C. Travaglio *et al.*, *Astrophys. J.* **601** (2004) 864.
- [186] W. Greiner: *Relativistic Wave Equations*, English Edition, Springer (1996).
- [187] B.S. Meyer, *Phys. Rep.* **227** (1993) 257.